

Transition Metal Oxide Materials for Electrocatalytic and Photocatalytic Water  
Splitting

by

Jeremy Adrian Bau

A thesis submitted in partial fulfillment of the requirements for the degree of

Doctor of Philosophy

Department of Chemistry  
University of Alberta

© Jeremy Adrian Bau, 2015

# Abstract

As the developing world industrializes, humanity needs to produce a greater fraction of its energy via renewable resources in order to alleviate the scarcity of fossil fuels as well as environmental damage from the exhaust of these fuels. However, renewable sources of energy tend to be intermittent in nature and therefore require a method to store generated energy for use at a later time. Hydrogen gas is a promising potential fuel because it can be produced from water with oxygen gas as a byproduct, resulting in an environmentally-friendly production-consumption cycle with water as the product upon combustion. This thesis presents two different approaches to hydrogen generation from water – using light and electricity – with earth-abundant metal oxide catalysts.

A dual-semiconductor photocatalyst consisting of  $\alpha$ -Fe<sub>2</sub>O<sub>3</sub> and CuFe<sub>2</sub>O<sub>4</sub> semiconductor materials in close contact was prepared by first templating iron oxide precursors on sugarcane leaf followed by functionalization of the resulting  $\alpha$ -Fe<sub>2</sub>O<sub>3</sub> surface with copper nanoparticles and high-temperature annealing. Nanoparticle catalysts were further loaded onto the surface of the combined  $\alpha$ -Fe<sub>2</sub>O<sub>3</sub>/CuFe<sub>2</sub>O<sub>4</sub> heterostructure. Investigation of the CuFe<sub>2</sub>O<sub>4</sub> material revealed that it was a poor semiconductor that could evolve hydrogen independently but at low rates.

A novel nickel-iron oxide phase with rock-salt structure was synthesized via thermal decomposition of mixed nickel and iron oleate complexes. Despite the natural instability of bivalent iron in rock-salt crystal structures, the single-crystal

[Ni,Fe]O nanoparticles were stable even under ambient conditions for long periods of time, even upon thermal treatment at 200 °C. Shape control of the nanoparticles could be achieved via modification of the synthetic conditions, resulting in a variety of shapes including cubes, stars, and spheres. The composition of the nanoparticles could also be controlled yielding a wide composition range of nickel iron oxide rock-salt nanocrystals. The surface of the nanoparticles was determined to contain trivalent iron and an amorphous structure unique from the bulk.

The nickel-iron oxide nanoparticles were applied for water oxidation after integration onto tin-doped indium oxide and fluorine-doped tin oxide electrode surfaces. The functionalization was accomplished using UV light irradiation, which resulted in the formation of durable nanoparticle films that withstood the stresses of water oxidation. Electrochemical studies suggested that catalytic activity arose from the surface of the nanoparticles, suggesting that the [Ni,Fe]O phase did not participate in water oxidation. Nonetheless, by giving rise to the catalytic surface layer, [Ni,Fe]O was found to be important for water oxidation as activity was reduced when the phase was lost via heating.

# Preface

Chapter 3 is based on the publication “Nickel/Iron Oxide Nanocrystals with a Nonequilibrium Phase: Controlling Size, Shape, and Composition”, *Chemistry of Materials*, volume 26, issue 16, pages 4796–4804 with authors Jeremy A. Bau, Peng Li, Armando J. Marengo, Dr. Simon Trudel, Brian C. Olsen, Dr. Erik J. Lubert, and Dr. Jillian M. Buriak. Peng Li facilitated the STEM, EELS, and nanoparticle EDX imaging. Acknowledged in the manuscript as well are Mr. Akira Yasuhara of JEOL Ltd. and Dr. Masahiro Kawasaki of JEOL USA Inc. for obtaining STEM images and EDX data as well as Dr. Eric Flaim from the University of Alberta nanoFAB for microscopy consulting. Armando Marengo and Dr. Trudel performed the magnetometry experiments at the University of Calgary. Brian Olsen and Dr. Lubert helped with data analysis and manuscript writing. Dr. Buriak was the supervisor and assisted with manuscript writing. I performed the rest of the data collection, analysis, and writing.

*In loving memory of Van-Tse Shu Chin (September 17, 1923 – July 21, 2014)  
and Van Kong Nee (January 18, 1923 – February 28, 2015)*

*Most of us can, as we choose, make of this world either a palace or a prison.*

*- John Lubbock*

# Acknowledgements

I would like to start by thanking my supervisor, Dr. Jillian Buriak, for her seemingly unconditional support and enduring patience over the last five years. She has given me a great deal of freedom in order to explore science on my own and I am grateful for her help and assistance.

I would also like to thank my committee – Dr. Richard McCreery, Dr. Steven Bergens, Dr. Xihua Wang, and Dr. Robert Campbell, for providing me guidance over the course of my PhD and for taking the time to read over and review this thesis. I would also like to thank Dr. Zhifeng Ding for agreeing to be my external examiner.

Special thanks goes to the members of the Buriak lab for their assistance and friendship. In particular, Dr. Kenneth Harris, Dr. Hosnay Mobarok, Dr. Erik Lubert, Dr. Tonggang Jiu, Shuai Chen and Brian Olsen generously offered particular knowledge that assisted with this dissertation. I would also like to thank and acknowledge other experts who kindly lent me their time to teach me about their fields; in particular, Dr. Sayed Nagy and Dr. Adam Bergren. And of course, no acknowledgement would be complete without thanking Dr. Lawrence Huck for his wisdom, knowledge and support, especially through difficult periods.

I would like to acknowledge funding from the following agencies: Alberta Innovates Tech Futures and the Natural Sciences and Engineering Research Council of Canada.

On a final note, I would like to thank my various friends for their friendship and help. And last but far from least, I would like to thank my parents, Andrew Bau and Renata Van, and of course my brother, Jason Bau, and his wife, Ting Li, for their love and support over the last five years.

# Table of Contents

Abstract.....	ii
Preface.....	iv
Dedication.....	v
Acknowledgements.....	vi
Table of Contents.....	viii
List of Tables.....	xii
List of Figures.....	xiii
List of Symbols and Abbreviations.....	xxiii
<b>1. General Introduction.....</b>	<b>1</b>
1.1 Overview.....	1
1.2 The Need for Renewable Energy.....	1
1.3 Energy Storage and the Potential for H <sub>2</sub> as a Fuel.....	5
1.4 H <sub>2</sub> Production.....	8
1.4.1 Electrochemical Water Splitting.....	11
1.4.2 Photocatalytic Water Splitting.....	15
1.5 First-row Transition Metal Oxides for Water Oxidation.....	20
1.6 Synthesis of Nanostructured metal oxides.....	23
1.7 Overview of the Thesis.....	27
1.8 References.....	29
<b>2. Biotemplated <math>\alpha</math>-Fe<sub>2</sub>O<sub>3</sub>/CuFe<sub>2</sub>O<sub>4</sub> Leaves for Z-Scheme Water Splitting ..</b>	<b>46</b>

2.1	Introduction.....	46
2.1.1	Potential of $\alpha$ -Fe <sub>2</sub> O <sub>3</sub> for Photocatalytic Water Oxidation.....	46
2.1.2	Water Splitting in Nature.....	47
2.1.2	Inorganic Z-Schemes Based on Ferrites .....	48
2.2	Results.....	50
2.2.1	Synthesis of Nanostructured Leaf.....	50
2.2.2	Synthesis of $\alpha$ -Fe <sub>2</sub> O <sub>3</sub> /CuFe <sub>2</sub> O <sub>4</sub> Heterojunction.....	55
2.2.3	Functionalization of $\alpha$ -Fe <sub>2</sub> O <sub>3</sub> /CuFe <sub>2</sub> O <sub>4</sub> Z-Scheme with Catalyst Particles .....	63
2.2.4	Studies on CuFe <sub>2</sub> O <sub>4</sub> .....	66
2.3	Conclusions.....	68
2.4	Experimental.....	69
2.5	References.....	75
<b>3.</b>	<b>Synthesis and Characterization of [Ni,Fe]O Nanoparticles.....</b>	<b>83</b>
3.1	Introduction.....	83
3.1.1	Overview of Metal Oxides and their Applications .....	83
3.1.2	Overview of the Chapter .....	84
3.2	Results.....	85
3.2.1	Synthesis and Characterization of [Ni,Fe]O Nanoparticles.....	85
3.2.2	Effect of Modifying $t_d$ .....	93
3.2.3	Effect of Modifying $t_r$ .....	95
3.2.4	Effect of Initial Precursor Metal Composition.....	97
3.2.5	Magnetic Characterization of Nanoparticles .....	104
3.3	Conclusions.....	109

3.4	Experimental .....	110
3.5	Contributions.....	114
3.6	References.....	114
<b>4.</b>	<b>[Ni,Fe]O Nanoparticles as Water Oxidation Electrocatalysts .....</b>	<b>122</b>
4.1	Introduction.....	122
4.1.1	Overview of the Chapter.....	122
4.1.2	Material Constraints of Current Water Splitting Electrocatalysts .....	122
4.1.3	First-Row Transition Metal Oxides as Water Oxidation Catalysts .....	123
4.1.4	Compositional and Structural Considerations for Catalyst Design .....	124
4.2	Results.....	125
4.2.1	Functionalization of Electrode Surfaces with Nanoparticles.....	125
4.2.2	Understanding Differences in Nanoparticle Composition.....	138
4.2.3	Characterization of Water Oxidation Kinetics.....	142
4.2.4	Effect of Temperature on Catalyst Activity.....	147
4.3	Conclusions.....	151
4.4	Experimental.....	151
4.5	References.....	156
<b>5.</b>	<b>Conclusions.....</b>	<b>163</b>
5.1	Chapter Summaries.....	163
5.1.1	Chapter 1.....	163
5.1.2	Chapter 2.....	164

5.1.3 Chapter 3 .....	165
5.1.3 Chapter 4 .....	165
5.2 Proposed Research Directions .....	166
5.2.1 Biotemplating of Other Metal Oxides.....	166
5.2.2 Exploring the Potential of $\text{CuFe}_2\text{O}_4$ for Electrode Applications .	168
5.2.3 Mechanism of Metal Oleate Decomposition During Formation of Metastable $[\text{Ni,Fe}]\text{O}$ Nanoparticles.....	170
5.2.4 Synthesis of Non-Oxides Utilizing Nickel and Iron Oleate.....	171
5.2.5 Conformal Functionalization of High-Surface Area Electrodes to Increase Activity.....	172
5.2.6 Understanding detailed catalytic properties of $[\text{Ni,Fe}]\text{O}$ nanoparticles, including effect of shape and surface composition .....	173
5.2.7 Acid vs. Base Catalysts .....	174
5.3 References.....	175

# List of Tables

<b>Table 3.1</b>	Characteristics of nanoparticles synthesized from the mixed metal oleate precursor with nickel to iron molar ratios of 33:66 by changing decomposition time ( $t_d$ ).....	88
<b>Table 3.2</b>	Characteristics of nanoparticles synthesized from metal oleates with nickel to iron molar ratios of 33:66 by changing drying time ( $t_r$ )...	97
<b>Table 3.3</b>	Characteristics of nanoparticles synthesized by changing initial ratio of metals. $t_d = 30$ minutes, $t_r = 1$ hour for all samples .....	99
<b>Table 4.1</b>	Tafel slopes of nanoparticle electrodes at different current densities .....	145

# List of Figures

<b>Figure 1.1</b>	Cost per kWh of selected energy sources, as compiled from the US EIA report, “Levelized Cost and Levelized Avoided Cost of New Generation Resources in the Annual Energy Outlook, 2014” .....3
<b>Figure 1.2</b>	Distribution of annual solar energy on the surface of the earth. Reprinted with permission from reference. Reprinted with permission from reference <sup>23</sup> . Copyright (2011) Elsevier .....5
<b>Figure 1.3</b>	Diagram of photosynthetic pathways utilized by algae to produce H <sub>2</sub> and O <sub>2</sub> gases.....10
<b>Figure 1.4</b>	Diagram illustrating the difference between conductors, insulators, and semiconductors.....17
<b>Figure 1.5</b>	Examples of semiconductor bandgap configurations that cannot carry out photocatalytic water splitting because of bad positioning (left, center) compared to a bandgap that can carry out water splitting ....18
<b>Figure 1.6</b>	Band diagrams of single and dual z-scheme absorber water splitting semiconductor systems .....19
<b>Figure 1.7</b>	Diagram of the manganese-cubane catalytic site responsible for water oxidation associated with photosystem II during photosynthesis. Reprinted with permission from reference <sup>106</sup> . Copyright (2011) Nature Publishing Group. ....21
<b>Figure 1.8</b>	Scanning electron micrograph of [Ni,Fe]O nanoparticles formed via decomposition of metal oleate complexes. The composition of these nanoparticles was Ni:Fe 51:49.....24
<b>Figure 1.9</b>	Electron micrograph of an $\alpha$ -Fe <sub>2</sub> O <sub>3</sub> photoelectrode prepared by APCVD. Reprinted with permission from reference <sup>148</sup> . Copyright (2006) American Chemical Society.....25

<b>Figure 1.10</b>	Electron micrograph of an $\alpha$ -Fe <sub>2</sub> O <sub>3</sub> nanotube array prepared by anodization of iron foil. Reprinted with permission from reference <sup>168</sup> . Copyright (2009) American Chemical Society .....	26
<b>Figure 2.1</b>	Diagram of proposed Z-scheme. The $\alpha$ -Fe <sub>2</sub> O <sub>3</sub> , templated from a sugarcane leaf, carries out photocatalytic water oxidation and is directly in contact with CuFe <sub>2</sub> O <sub>4</sub> . The CuFe <sub>2</sub> O <sub>4</sub> uses the separated electrons from the $\alpha$ -Fe <sub>2</sub> O <sub>3</sub> and light to reduce protons to H <sub>2</sub> gas. The $\alpha$ -Fe <sub>2</sub> O <sub>3</sub> and CuFe <sub>2</sub> O <sub>4</sub> are functionalized with iridium oxide and platinum nanoparticle catalysts, respectively .....	49
<b>Figure 2.2</b>	(a) Photograph of the leaf at different stages; from left to right, fixed, HCl-soaked, FeCl <sub>3</sub> -soaked, and final calcined metal oxide leaves. (b) Electron micrograph of a fixed, organic leaf. (c-f) Scanning electron micrographs of final iron oxide leaves at increasing magnifications to show preserved vein structures, including constituent nanoparticles of these features .....	52
<b>Figure 2.3</b>	(a) Scanning electron micrograph of a leaf synthesized with anhydrous FeCl <sub>3</sub> precursor. (b) Scanning electron micrograph of a leaf synthesized with Fe(NO <sub>3</sub> ) <sub>3</sub> •6H <sub>2</sub> O precursor. The region shown in both leaves is believed to be a xylem channel .....	54
<b>Figure 2.4</b>	XPS survey scan of an iron oxide leaf mounted on a silicon substrate with major peaks and complexes labeled .....	55
<b>Figure 2.5</b>	Schematic for synthesis of $\alpha$ -Fe <sub>2</sub> O <sub>3</sub> /CuFe <sub>2</sub> O <sub>4</sub> leaf. The $\alpha$ -Fe <sub>2</sub> O <sub>3</sub> leaf is first exposed to 3 mM 16-MHA, resulting in a leaf with exposed thiol groups. The thiols bind the copper nanoparticles when exposed to a solution of said particles. Finally, the entire structure is heated at 850°C for 3 hours to form CuFe <sub>2</sub> O <sub>4</sub> .....	56
<b>Figure 2.6</b>	(a) Transmission electron micrograph of copper nanoparticles synthesized by thermolysis of copper (II) acetylacetonate. (b) XPS spectra of the Cu 2p <sub>3/2</sub> region of copper nanoparticles dropped on a	

	silicon slide. (c) XPS spectra of the Cu LLM Auger electron region as an identifier of Cu valence state .....	57
<b>Figure 2.7</b>	Scanning electron micrographs of $\alpha$ -Fe <sub>2</sub> O <sub>3</sub> slides functionalized with different linkers followed by copper nanoparticles. (a) 16-MHA; (b) 16-MHA, high-resolution; (c) no linker; (d) no linker, high-resolution; (e) oleic acid; (f) oleic acid, high-resolution.....	58
<b>Figure 2.8</b>	Diffuse reflectance infrared spectra of the $\nu$ (CH <sub>x</sub> ) and $\nu$ (OH) regions of (a) bare iron oxide leaves, (b) 16-MHA functionalized iron oxide leaves, and (c) copper nanoparticle/16-MHA functionalized leaves on a silicon substrate.....	59
<b>Figure 2.9</b>	(a) Cu 2p <sub>3/2</sub> XPS of (top to bottom) 16-MHA/copper nanoparticle-functionalized leaf, copper nanoparticle-functionalized leaf with no 16-MHA linker, and 16-MHA/copper nanoparticle-functionalized leaf heated to 850°C for 3 hours. Red trace corresponds to metallic copper, while blue corresponds to Cu <sup>2+</sup> . (b) Close-up of Cu 2p <sub>3/2</sub> XPS for heated leaf .....	60
<b>Figure 2.10</b>	Auger electron mapping of an $\alpha$ -Fe <sub>2</sub> O <sub>3</sub> slide functionalized with copper nanoparticles and heated to 850°C for 3 hours. (a) Scanning electron micrograph of region of interest, (b) signal map for iron Auger electrons, and (c) signal map for copper Auger electrons .....	62
<b>Figure 2.11</b>	(a) Powder x-ray diffraction patterns of iron oxide leaves (red) and 16-MHA/copper functionalized and heated (850 °C, 3 hours) leaves (orange). (b) Close up of the 29° < 2θ < 37° region where the CuFe <sub>2</sub> O <sub>4</sub> peaks can be seen.....	63
<b>Figure 2.12</b>	(a) Transmission electron micrograph of oleylamine-coated platinum nanoparticles. (b) Scanning electron micrograph of iron oxide slide functionalized with platinum nanoparticles. (c) Pt 4f XPS spectra of leaf functionalized with 16-MHA and platinum nanoparticles (blue) vs. leaf functionalized only with platinum nanoparticles (black). The	

- other coloured curves are peaks for metallic Pt (red), Pt(II) (maroon), and Pt(IV) (orange).....65
- Figure 2.13** (a) Transmission electron microscopy of IrO<sub>2</sub> nanoparticles; (b) Ir 4f XPS spectra of CuFe<sub>2</sub>O<sub>4</sub>/α-Fe<sub>2</sub>O<sub>3</sub> leaf functionalized with IrO<sub>2</sub> nanoparticles (black). Blue peaks correspond to Ir<sup>4+</sup> .....66
- Figure 2.14** Cyclic voltammetry of CuFe<sub>2</sub>O<sub>4</sub> powder on platinum disc electrode in 0.1 M tetrabutylammonium hexafluorophosphate in acetonitrile. Reference electrode is Ag/Ag<sup>+</sup>. The intercepts of the orange lines correspond to the position of the band edges of CuFe<sub>2</sub>O<sub>4</sub> .....67
- Figure 2.15** H<sub>2</sub> evolution studies of CuFe<sub>2</sub>O<sub>4</sub> powder suspended via stirring in 10% v/v triethanolamine. Irradiation time: 1 hour. Light source: 500 W Xe bulb. Catalyst concentration: 1 g/mL. Solution volume: 1 mL .....68
- Figure 3.1** Synthetic Scheme of [Ni,Fe]O Nanoparticles. Reprinted with permission from the reference <sup>53</sup>. Copyright (2014) American Chemical Society. ....86
- Figure 3.2** (a) High-resolution HAADF-STEM micrograph of nanoparticles synthesized with a nickel to iron precursor ratio of 33:67 and decomposition time of 20 min (inset: FFT diffractogram). (b,c) EDX maps of (b) nickel and (c) iron of nanoparticles produced via the same synthesis. Reprinted with permission from the reference <sup>53</sup>. Copyright (2014) American Chemical Society .....87
- Figure 3.3** (a) TEM micrograph and (b) XRD spectrum of [Ni,Fe]O nanocubes where nickel and iron oleate were refluxed separately and combined only after reflux. Reprinted with permission from the reference <sup>53</sup>. Copyright (2014) American Chemical Society .....88
- Figure 3.4** FTIR spectra of individual nickel and iron metal oleate precursors, and the mixed metal oleate precursor derived from the combined reflux of nickel and iron salts with sodium oleate. Reprinted with

	permission from the reference <sup>53</sup> . Copyright (2014) American Chemical Society .....	89
<b>Figure 3.5</b>	(a) Electron diffraction pattern of [Ni,Fe]O nanocubes (right) and simulated electron diffraction pattern of a rocksalt crystal structure (left). (b) XRD spectrum of nanocubes with spectra of bulk NiO and Fe <sub>x</sub> O overlaid. Reprinted with permission from the reference <sup>53</sup> . Copyright (2014) American Chemical Society .....	90
<b>Figure 3.6</b>	(a) Fe EELS spectrum of nanocubes showing L <sub>2</sub> and L <sub>3</sub> peaks. Corresponding (b) Fe 2p <sup>3/2</sup> and (c) Ni 2p XPS spectra. Reprinted with permission from the reference <sup>53</sup> . Copyright (2014) American Chemical Society .....	92
<b>Figure 3.7</b>	TEM micrographs (left) and size distributions (right) of [Ni,Fe]O nanoparticles synthesized by heating the precursor for (a) 15, (b) 20, (c) 25, and (d) 30 min. The composition of the precursor was Ni:Fe 33:66. Reprinted with permission from the reference <sup>53</sup> . Copyright (2014) American Chemical Society.....	94
<b>Figure 3.8</b>	(a) TEM micrograph and corresponding size distribution of nanoparticles synthesized from a 33:67 precursor ratio, 20 min decomposition time and 12 hour drying time. (b) High-resolution HAADF-STEM image of a nanoparticle (inset: FFT diffractogram). (c) Corresponding electron diffraction pattern of the nanoparticles (right) and simulated electron diffraction pattern of a rocksalt crystal structure (left). (d,e) EDX maps of nanoparticles for (d) nickel and (e) iron. Reprinted with permission from the reference <sup>53</sup> . Copyright (2014) American Chemical Society.....	96
<b>Figure 3.9</b>	FTIR spectra of metal oleate precursors with different t <sub>r</sub> (listed top right). The composition of the precursors for this FTIR was Ni:Fe 33:66. Reprinted with permission from the reference <sup>53</sup> . Copyright (2014) American Chemical Society.....	97

<b>Figure 3.10</b>	XRD spectra of nanoparticles synthesized with different compositions of metals in the initial precursor solution with $t_d = 30$ min. All ratios are listed as nickel:iron. Reprinted with permission from the reference <sup>53</sup> . Copyright (2014) American Chemical Society.....	98
<b>Figure 3.11</b>	(a) TEM micrographs of nanoparticles synthesized from pure (a) iron oleate and (b) pure nickel oleate. Size analysis was not performed on nickel nanoparticles due to the fact that nanoparticles were aggregated into clusters. Reprinted with permission from the reference <sup>53</sup> . Copyright (2014) American Chemical Society .....	99
<b>Figure 3.12</b>	TEM micrographs (left) and corresponding size distribution (right) of [Ni,Fe]O nanoparticles synthesized when metal compositions in precursor oleate were modified before synthesis at $t_d = 30$ min. Metal ratios are listed as nickel:iron. (a) 83:17, (b) 66:33, (c) 50:50, (d) 17:83. Reprinted with permission from the reference <sup>53</sup> . Copyright (2014) American Chemical Society.....	101
<b>Figure 3.13</b>	Phase diagram of resultant nanoparticle shapes as a function of nickel to iron precursor ratio and decomposition time. Reprinted with permission from the reference <sup>53</sup> . Copyright (2014) American Chemical Society.....	103
<b>Figure 3.14</b>	Magnetic characterization of [Ni,Fe]O 51:49 cubes, 57:43 stars, and 33:66 spheres. (a) ZFC and FC curves and magnetic hysteresis loops taken at (b) 300 K and (c) 1.9 K. (d) Proposed scheme of Fe and Ni atoms [Ni,Fe]O nanoparticles. Reprinted with permission from the reference <sup>53</sup> . Copyright (2014) American Chemical Society.....	107
<b>Figure 3.15</b>	Effects of thermal annealing [Ni,Fe]O nanoparticles synthesized with a nickel to iron precursor ratio of 33:67 and decomposition time of 20 min. XRD spectra in (a) air and (b) argon. Reprinted with permission from the reference <sup>53</sup> . Copyright (2014) American Chemical Society .....	108

<b>Figure 4.1</b>	Functionalization scheme of transparent conductive electrodes with [Ni,Fe]O nanoparticles.....	125
<b>Figure 4.2</b>	(a) UV-vis spectra of Ni:Fe 51:49 [Ni,Fe]O-functionalized ITO electrodes fabricated by spin-coating followed by 254 nm UV irradiation, air plasma, or no further treatment. (b) UV-vis spectra of a 2 mg/mL solution of Ni:Fe 51:49 [Ni,Fe]O dissolved in hexane .....	126
<b>Figure 4.3</b>	Cyclic voltammograms (first 10 cycles) of ITO electrodes functionalized with Ni:Fe 51:49 [Ni,Fe]O nanoparticles via spin-coating, followed by (a) no further treatment (untreated), (b) air plasma for 10 seconds, and (c) 1 hour of UV irradiation with 254 nm light, repeated until traces have become stable. The electrolyte was 0.1 M KOH. Green traces represent the first of ten cycles, red traces represent the tenth cycle .....	127
<b>Figure 4.4</b>	(a) Voltammograms of ITO electrodes functionalized with Ni:Fe 51:49 [Ni,Fe]O nanoparticles via spin-coating, followed by 1 hour of UV irradiation with 254 nm light (UV-treated), air plasma for 10 seconds (plasma-treated), and no further treatment (untreated), as well as a nanoparticle-free ITO control, in 0.1 M KOH. (b) UV-vis spectra of UV-treated, plasma-treated, and untreated [Ni,Fe]O electrodes before and after voltammetry in (a). (c) Chronopotentiometry trace of UV-treated [Ni,Fe]O electrodes held at a current density of 10 mA/cm <sup>2</sup> for 2 hours in 0.1 M KOH .....	129
<b>Figure 4.5</b>	SEM micrographs of a Ni:Fe 51:49 [Ni,Fe]O-functionalized ITO electrode with no further treatment procedure (a) before and (b) after voltammetry; a plasma-treated electrode (10 seconds, air) (c) before and (d) after voltammetry; and a UV-treated electrode (254 nm, 1 hour) (e) before and (f) after voltammetry. (g) Micrograph of blank ITO.....	131

- Figure 4.6** (a) SEM micrograph of the surface of a catalyst electrode formed by the UV decomposition (254 nm, 1 hour) of a 1:1 nickel:iron oleate mixture dissolved in hexane and spin-cast on ITO. (b) Voltammogram of the metal-oleate UV-treated ITO electrode in 0.1 M KOH.....133
- Figure 4.7** (a)  $\text{Fe}_{2p}$  and (b)  $\text{Ni}_{2p}^{3/2}$  XPS spectra of UV-treated a Ni:Fe 51:49 [Ni,Fe]O nanoparticle-functionalized electrode before and after UV irradiation, after 2 hours in electrolyte (0.1 M KOH), and post-chronopotentiometry in 0.1 M KOH (10 mA/cm<sup>2</sup>, 2 hours).....135
- Figure 4.8** FTIR spectra of a Ni:Fe 51:49 [Ni,Fe]O nanoparticle film spun on high resistivity Si (~10 Ω·cm) after different periods of irradiation with 254 nm UV light, as well as after placement in 0.1 M KOH for 2 hours. The scans were collected in transmission mode .....137
- Figure 4.9** Voltammograms of Ni:Fe 51:49 [Ni,Fe]O nanoparticle-functionalized electrodes in 0.1 M KOH after irradiation with 254 nm UV light for different lengths of time.....138
- Figure 4.10** (a) Voltammograms of [Ni,Fe]O nanoparticle-functionalized electrodes with one layer of nanoparticles of different compositions recorded in 0.1 M KOH. (b) Relationship of thickness based on number of layers and overpotential at 10 mA/cm<sup>2</sup> in 0.1 M KOH of different nanoparticle compositions. All ratios in Ni:Fe .....139
- Figure 4.11** (a) UV-vis spectra of [Ni,Fe]O nanoparticle-functionalized electrodes with increasing numbers of layers. The composition of nanoparticles used in this graph was Ni:Fe 51:49. The electrodes were fabricated irradiation with 254 nm UV light. (b) Relationship between thickness (determined via contact profilometry) and number of layers of [Ni,Fe]O nanoparticle-functionalized electrodes. All ratios in Ni:Fe .....141
- Figure 4.12** SEM micrographs of 1 layer (left) and 2 layer (right) nanoparticle electrodes with different compositions of nanoparticles. From top to

	bottom, the nanoparticle Ni:Fe compositions are 24:76 (a,b), 51:49 (c,d), 73:27 (e,f), and 88:12 (g,h). The electrodes were fabricated irradiation with 254 nm UV light .....	141
<b>Figure 4.13</b>	Tafel curves of [Ni,Fe]O nanoparticle electrodes of different compositions acquired in 0.1 M KOH with 50 second step times. Ratios represented are in Ni:Fe. The electrodes were fabricated irradiation with 254 nm UV light .....	144
<b>Figure 4.14</b>	Proposed mechanism of water oxidation on [Ni,Fe]O nanoparticle surfaces .....	147
<b>Figure 4.15</b>	X-ray diffraction patterns of Ni:Fe 51:49 [Ni,Fe]O nanoparticles drop-cast on silicon substrates and heated for 2 hours in air at 200 °C, 400 °C, and 600 °C .....	148
<b>Figure 4.16</b>	SEM micrographs of Ni:Fe 51:49 [Ni,Fe]O nanoparticle-coated FTO electrodes functionalized via irradiation with 254 nm UV light, followed by heating for 2 hours in air at (a) 200 °C, (b) 400 °C, and (c) 600 °C.....	149
<b>Figure 4.17</b>	(a) Measurements of the water oxidation overpotential at 10 mA/cm <sup>2</sup> in 0.1 M KOH and (b) charge transfer measurements of Ni:Fe 51:49 [Ni,Fe]O nanoparticle electrodes fabricated via irradiation with 254 nm UV light, followed by no heating or heating for 2 hours at 200 °C, 400 °C, and 600 °C. Charge transfer measurements were acquired by functionalizing electrodes with 1,1'-ferrocenedicarboxylic acid followed by linear sweep voltammetry across the 0.45 V vs. Ag/Ag <sup>+</sup> peak corresponding to ferrocenedicarboxylic acid binding and integrating the area of the resultant peak .....	150
<b>Figure 5.1</b>	SiO <sub>2</sub> grown using CVD on DNA templates deposited on (a) mica and (b) gold surfaces. (c) TiO <sub>2</sub> grown using CVD of DNA templates on silicon substrate. Reprinted with permission from reference <sup>3</sup> . Copyright (2013) American Chemical Society .....	167

**Figure 5.2** (a) Optical image of  $\text{CuFe}_2\text{O}_4$  layers spin-coated on quartz (right) and  $\text{CuFe}_2\text{O}_4$  powder prepared via combustion method. (b) UV-vis spectra of  $\text{CuFe}_2\text{O}_4$  on quartz electrode .....169

**Figure 5.3** Electron micrograph of nickel-iron sulfide wires prepared via decomposition of nickel and iron oleate in the presence of 1-octadecanethiol .....172

# List of Symbols

AAO	Anodized Aluminum Oxide
AES	Auger Electron Spectroscopy
BSCF	Barium-Strontium-Cobalt-Iron Oxide
CBM	Conduction Band Minimum
CTAB	Cetyl Trimethylammonium Bromide
CV	Cyclic Voltammetry
CVD	Chemical Vapour Deposition
DNA	Deoxyribonucleic Acid
DRIFTS	Diffuse Reflectance Infrared Fourier Transform Spectroscopy
EDX	Energy Dispersive X-ray Spectroscopy
EELS	Electron Energy Loss Spectroscopy
FC	Field Cooled Magnetization
fcc	Face-center cubic
FE-SEM	Field Emission Scanning Electron Microscope
FTIR	Fourier Transform Infrared Spectroscopy
FTO	Fluorine-doped Tin Oxide
HAADF-STEM	High-Angle Annular Dark Field-Scanning Transmission Electron Microscopy
hcp	Hexagonal close-packed
ITO	Indium Tin Oxide
LMCT	Ligand-to-Metal Charge Transfer
16-MHA	16-Mercaptohexadecanoic Acid
MAP	Modified Auger Parameter
MMO	Mixed Metal Oxide
PBS	Phosphate-Buffered Saline Solution
PVD	Physical Vapour Deposition
PXRD	Powder X-ray Diffraction
SEM	Scanning Electron Microscopy
TEM	Transmission Electron Microscopy

T <sub>B</sub>	Blocking Temperature
t <sub>d</sub>	Decomposition Time
t <sub>r</sub>	Drying Time
UV	Ultraviolet
VBM	Valence Band Maximum
XPS	X-ray Photoelectron Spectroscopy
XRD	X-ray Diffraction
ZFC	Zero Field Cooling Magnetization

# 1 General Introduction

## 1.1 Overview

The goal of this thesis is to investigate methods for synthesizing nanostructures consisting of earth-abundant metal oxides for the photocatalysis and electrocatalysis of water into hydrogen (H<sub>2</sub>) and oxygen (O<sub>2</sub>) gases. Two separate overall projects are reported within; the first project involves the biotemplating of  $\alpha$ -Fe<sub>2</sub>O<sub>3</sub>/CuFe<sub>2</sub>O<sub>4</sub> Z-scheme photoelectrodes for overall photocatalytic water splitting, while the second project involves the synthesis of a [Ni,Fe]O for electrocatalytic water splitting.

In this chapter, a general overview of rationale for water splitting, as well as the choice of metal oxides for material applications will be discussed. Chapter 2 will discuss the biotemplated leaf Z-scheme. Chapters 3 and 4 will discuss the synthesis and electrocatalytic properties of [Ni,Fe]O. Future directions and conclusions will be presented in Chapter 5.

## 1.2 The Need for Renewable Energy

Since the Industrial Revolution, the exploitation of cheap, energy-dense hydrocarbon fossil fuels, namely coal, oil, and natural gas, has allowed humanity to undertake faster travel, manufacture wares of greater quality and quantity, and raise our standard of living to a previously unachieved level. According to the

International Energy Agency, 81.7% of the world's energy needs in 2012 were supplied by coal, oil, and natural gas.<sup>1</sup> However, this reliance on fossil fuels has several disadvantages. Firstly, fossil fuels, as non-renewable resources, suffer from an availability problem as they do not replenish at a fast enough rate to satisfy eternal demand. Based on current consumption rates and reserves, typical estimates for the remaining amount of fossil fuels in the world lie around a half century each for oil and natural gas, and one to three centuries for coal.<sup>2,3</sup> Furthermore, most of the world's fossil fuel deposits are unevenly distributed in both geography and quality.<sup>2-4</sup> In the case of oil, as high quality, low cost oil deposits deplete, the shift to low quality, high cost deposits becomes inevitable, threatening to raise energy costs which in turn will hinder long-term economic development.<sup>4,5</sup>

Over-reliance on fossil fuels is also responsible for generating a variety of by-products, ranging from particulate matter to carbon dioxide (CO<sub>2</sub>). The role of particulate matter in various health issues, including respiratory, cardiac, immunological, and developmental disorders is well documented, especially in the industrializing world.<sup>6-9</sup> Although CO<sub>2</sub> does not have the same medical implications, the generation of this gas via large-scale industrial processes like power generation also has a consequential effect on the world in the form of global warming, which has the potential to affect our lives through rising sea levels due to polar ice cap melt, desertification, and reduced agricultural yields.<sup>10,11</sup> Further complicating matters is that, by 2050, there will be at least 9 billion humans on the earth, and those in the developing world will likely be striving to achieve a Western standard of living based on the model of economic development fuelled by cheap

energy, which will further increase energy demand even as environmental effects become more apparent.<sup>3,10</sup> In order to offset these circumstances, it is critical to develop alternate energy systems while potential disaster can still be averted. However, replacing the fossil fuel regime is an uncertain prospect. In 2014, the U.S. Energy Information Administration (EIA) reported that the capital cost of most conventional grid-based fossil fuel energy systems ranged from \$0.01/kWh to \$0.06/kWh, making fossil fuels, and especially natural gas, the cheapest and most reliable source of energy currently available (Figure 1.1).<sup>12</sup> Recent revolutionary developments in the extraction of natural gas via fracking, as well as the use of combined cycle setups where waste energy generated in an initial combustion reaction is used to drive the combustion of subsequent fuel molecules, has further pushed the cost of natural gas as an energy source down.<sup>13</sup>

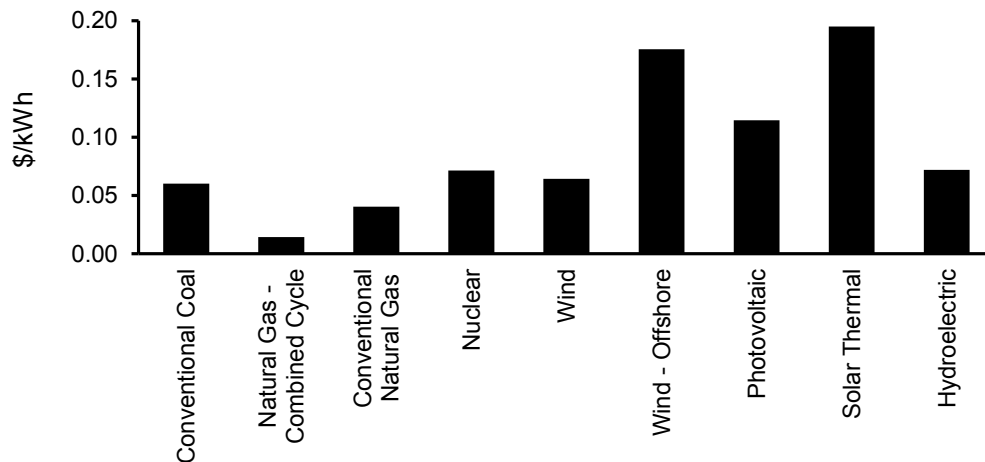


Figure 1.1 Cost per kWh of selected energy sources, as compiled from the US EIA report, “Levelized Cost and Levelized Avoided Cost of New Generation Resources in the Annual Energy Outlook, 2014”.

Therefore, not only must any replacement for fossil fuels be carbon-neutral and abundant; it must also be inexpensive. Two commonly cited alternatives are solar and wind power. Wind power is technically and conceptually simple and has vast theoretical potential. Independent estimates of the full potential for wind power have concluded that the harnessing of all of the potential wind power in the world would fulfill anywhere from 7 to 40 times the earth's annual electricity consumption.<sup>14,15</sup> Although these numbers seem promising and the technology seems readily available, wind power is also beset by a variety of social and geographical problems, including the typical distance of such resources from population centers and extremely uneven distributions between countries, unwillingness by local populations to host generating windmills, and the unpredictability and intermittency of power generation.<sup>16-18</sup> As a result, the potential for wind power to replace fossil fuels is extremely limited.

Solar energy also has great energy potential; the amount of energy stored in all the light from the sun that strikes the surface of the earth in one hour is equivalent to the amount of energy that humanity uses in a single year, or about 9000 times the earth's annual electricity consumption.<sup>10,19</sup> Sunlight, whether direct or indirect, provides the energy needs of every living organism on earth as even fossil fuels are derived from the remains of photosynthetic organisms. Yet despite the potential for solar energy, direct solar conversion has not yet been widely implemented for several reasons. Firstly, although strides have been made towards developing materials that are simultaneously economic to produce and efficient at solar energy conversion, costs for solar materials are still prohibitive compared to those for fossil

fuels.<sup>20-22</sup> Secondly, as with wind power, sunlight can be highly variable, being limited by local environmental conditions such as nighttime, cloud cover or even latitude (Figure 1.2). As a result, mismatches between peak generation and usage periods prevent the full and efficient utilization of solar energy and the development of a storage medium is required.<sup>10,19,23,24</sup>

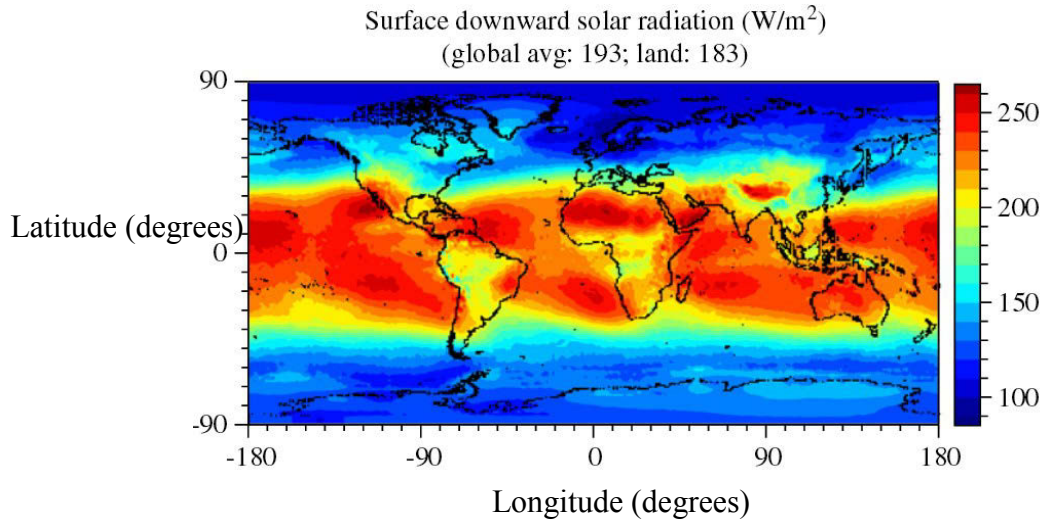


Figure 1.2 Distribution of annual solar energy on the surface of the earth.<sup>24</sup> Reprinted with permission from Elsevier.

### 1.3 Energy Storage and the Potential for H<sub>2</sub> as a Fuel

The quest for an energy storage system appropriate for solar energy is challenged by many of the same problems as the quest for a renewable energy system – ultimately, for large-scale implementation, the energy storage system will need to be economic and environmentally friendly at the same time. Furthermore, any system would need to allow for off-grid access so that mobile applications would be able to access this stored energy. Off-grid access is a special factor because the vast majority of oil product usage is as a fuel for transportation – in its Annual Energy Outlook for 2014, the U.S. Energy Information Administration

reported that over 70% petroleum consumed in the U.S. is for transportation purposes.<sup>25</sup> Yet off-grid applications present their own challenges, requiring convenience and miniaturization so that stored energy can be easily transported and accessed. As a result, two dominant approaches have evolved towards powering next-generation vehicles focus on the ways in which this energy is stored – namely, electrochemical storage and fuels.<sup>26–28</sup> Electrochemical storage-based approaches focus on the development of high-density capacitors or batteries for energy storage. Although electrochemical storage systems have superior specific power performances, meaning that they can generate power very quickly when required (such as in car brakes), they lack the specific energy and energy densities of fuel-based approaches – in essence, electrochemical storage-based approaches are not compact or lightweight enough to store large amounts of energy.<sup>26–28</sup>

Fuels, whether gasoline or H<sub>2</sub>, have higher specific energies and energy densities than electrochemical storage systems.<sup>26–28</sup> Fuel materials are expended in a chemical reaction to release energy, typically generating by-products. While today's fuels – coal, oil, and natural gas – generate carbon by-products, a carbon-free, or at least carbon-neutral synthetic fuel may be able to satisfy the demand for cheap, non-polluting energy storage in the 21<sup>st</sup> century. H<sub>2</sub> has been suggested as fuel because it has both a high specific energy and is carbon-neutral, making it an potential fuel.<sup>28–30</sup> However, the problems of H<sub>2</sub> consumption, storage, and production must be addressed for H<sub>2</sub> fuel to become widespread. In the case of H<sub>2</sub> storage, even though H<sub>2</sub> has a high specific energy (energy per unit mass), the storage of H<sub>2</sub> is difficult because it has a low energy density (energy per unit

volume), therefore requiring significant infrastructure for cooling and/or compression. To circumvent these problems, two approaches towards hydrogen storage have been pursued.<sup>31-34</sup> The first approach involves forming intermediate chemicals that can be formed from H<sub>2</sub> gas (metal hydrides, liquid hydrides) that can, under certain conditions, revert to their dehydrogenated form to yield the reusable storage material and H<sub>2</sub> gas.<sup>31,32</sup> In the second approach, high-surface area nanomaterials such as metal-organic frameworks adsorb large volumes of H<sub>2</sub> gas onto their structures, which can be induced to release H<sub>2</sub> when needed.<sup>33,34</sup> Both of these approaches seek to allow for the high-density storage of H<sub>2</sub> under safer and more ambient conditions.

In the realm of H<sub>2</sub> conversion to energy, there is a great deal of interest in the development of efficient fuel cells.<sup>27,35-37</sup> Fuel cells are appealing because of their high ideal efficiencies; even today's mostly prototypical systems maintain energy conversion efficiencies of close to 60%, compared to the 20% usually achieved by standard gasoline-based internal combustion engines.<sup>36</sup> However, widespread usage of fuel cells is limited by cost, performance and durability.<sup>35,37</sup> As with H<sub>2</sub> storage, much of this arises from material constraints: platinum remains the most commonly used material for fuel cell catalysis, despite its cost and sensitivity to environmental pollutants like CO and H<sub>2</sub>S.<sup>35-37</sup> There is a great deal of research focused on developing inexpensive novel catalytic materials, and candidates that have recently shown promise include conducting polymers, transition metal alloys (with and without platinum), and even various nanoparticle-based structures.<sup>35-38</sup>

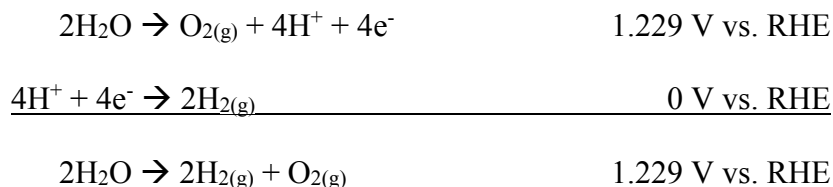
## 1.4 H<sub>2</sub> Production

Presently, hydrocarbon reforming is the most utilized approach to H<sub>2</sub> production, accounting for over 90% of all H<sub>2</sub> produced today.<sup>39,40</sup> Although there are several variations of hydrocarbon reforming, the ultimate approach is the same: hydrocarbons are oxygenated on catalytic metal surfaces at high temperatures (typically group 8, 9 and 10 elements such as platinum and palladium) before decomposing into a mixture of CO or CO<sub>2</sub> and H<sub>2</sub> gas.<sup>39,41-43</sup> It is even possible to start with oxygenated hydrocarbons like biomass or ethanol.<sup>40,41</sup> The H<sub>2</sub> that is separated from this synthetic gas, or syngas, can be subsequently used for other purposes. This reaction can generate large volumes of H<sub>2</sub> gas with a 67% molar yield, explaining its popularity with the chemical industry.<sup>41-43</sup> However, hydrocarbon reforming still generates CO<sub>2</sub> as a by-product, meaning that any H<sub>2</sub> gas generated is not truly carbon-neutral.<sup>39</sup>

H<sub>2</sub> can also be generated by the decomposition of water molecules into H<sub>2</sub> and O<sub>2</sub> gases, generally referred to as water splitting. The major approaches to water splitting that are currently being studied fall into four categories: thermochemical, electrochemical, photocatalytic, and biological.<sup>44,45</sup> Thermochemical water splitting is similar in setup to hydrocarbon reforming in that catalytic surfaces in the presence of high temperatures will naturally decompose water into H<sub>2</sub> and O<sub>2</sub> gases.<sup>46-48</sup> It is even possible to utilize direct, focused solar energy to generate the high temperatures needed to carry out this reaction.<sup>46,47</sup> However, temperatures around 1000 °C are often required for the thermolytic decomposition of water to

proceed in an entropically favourable manner, placing serious constraints on the materials used for reactors.<sup>46,48</sup>

The remaining three major approaches to hydrogen production can be grouped into a single general category of low temperature, electrochemically based reactions. Photocatalytic and biological H<sub>2</sub> production also fall into this category because these remaining approaches ultimately all rely on some variation of the same water oxidation and hydrogen evolution electrochemical half-reactions:



Under standard conditions (all reactant concentrations are 1 M, gas species are present at a partial pressure of 1 atm, and the temperature is 298 K), the reaction depicted above takes place under acidic conditions as the concentration of protons is 1 M – equivalent to a pH of 1. The most direct method to produce H<sub>2</sub> from these reactions is to, as the reaction would suggest, apply a potential across two electrodes in a container of water. In the photocatalytic variation, the potential required to drive the reaction is provided by electron-hole charge separation caused by the absorption of light by one or more semiconductors.<sup>23</sup> Biological H<sub>2</sub> production in turn is arguably a further variation of photocatalytic H<sub>2</sub> production whereby two sets of light-absorbing proteins in photosynthetic algae, called photosystems, deliver oxidizing power to water oxidizing catalytic sites in proteins (Figure

1.3).<sup>49,50</sup> After the photocatalytic oxidation of water at Photosystem II, the excited electrons are then shuttled to Photosystem I where light is used to reduce organic electron acceptors that serve as energy sources in the cell. While this system remains identical in higher-level plants, green algae and cyanobacteria are capable of expressing hydrogenase or nitrogenase enzymes under anaerobic conditions, which utilize transition metal-sulfide cores (usually iron) to reduce protons to H<sub>2</sub>. Widespread biological H<sub>2</sub> production is currently unfeasible owing to the difficulties of developing large-scale bioreactors.<sup>51</sup> Furthermore, the theoretical efficiencies achievable by biological H<sub>2</sub> production are low (13% theoretical max.)<sup>49</sup> compared to semiconductor systems (41% theoretical max. for a dual absorber system analogous to photosynthesis, 30% theoretical maximum for a single absorber system).<sup>23</sup>

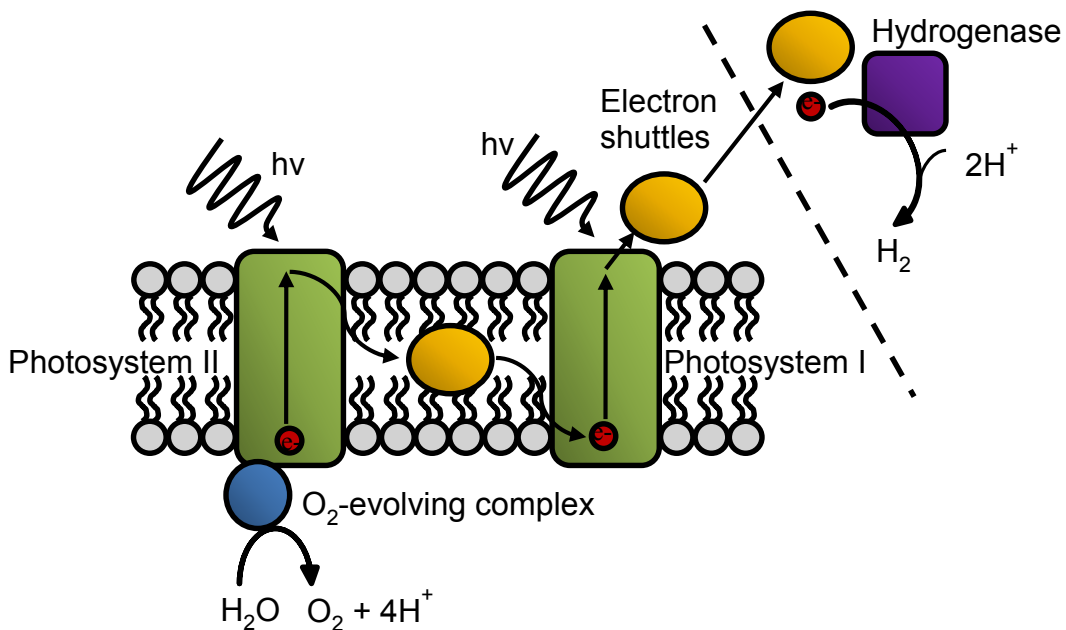


Figure 1.3 Diagram of photosynthetic pathways utilized by algae to produce H<sub>2</sub> and O<sub>2</sub> gases.

### 1.4.1 Electrochemical Water Splitting

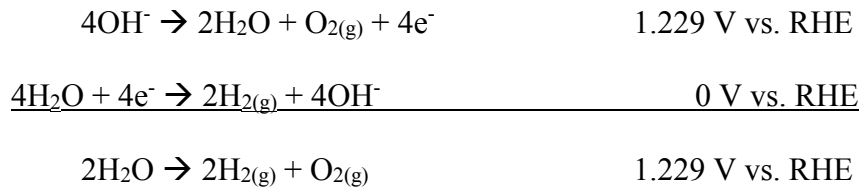
The remaining two major approaches, electrochemical and photocatalytic water splitting, deserve separate treatment as they are the focus of this thesis. Electrochemical water splitting, or water electrolysis, was first reported in 1789 by two Dutchmen, Adriaan Paets van Troostwijk and Johan Rudolph Deiman, when two gold electrodes connected to an electrostatic generator placed in water were observed to evolve bubbles.<sup>52</sup> Although the results were reported initially only in French, German, and Dutch, by 1797 word of the discovery crossed the English Channel where William Nicholson and Anthony Carlisle repeated the work by powering their device with a replication of Alessandro Volta's voltaic pile, a simple early battery powered by redox reactions of conjoined metals.<sup>53</sup> At that time, the discovery of the electrolysis of water was of great interest to the scientific community because it demonstrated that elements could be isolated from their respective natural compounds. Electrolysis was further augmented in 1888, when Dmitry Lachinov developed the first industrial scale electrolyzer for water, which remained the primary method for producing hydrogen until the advent of industrial-scale hydrocarbon reforming in 1962.<sup>43</sup>

The idea of water electrolysis has changed little from its first observations; two electrodes are placed into a common container of water and a sufficiently large potential is applied across the electrodes, resulting in the oxidation of water and evolution of O<sub>2</sub> on the anode and the reduction of protons and evolution of H<sub>2</sub> on the cathode. Yet several challenges have hindered electrolysis from becoming the dominant H<sub>2</sub> production method. The electrochemical overpotential for water

splitting and especially the water oxidation half-reaction is considerably large, reducing the potential efficiency of the system.<sup>23,54,55</sup> The overpotential of an electrochemical reaction is the additional cost required to drive the reaction at an appreciable rate, usually represented by an increased potential above the nominal voltage required to carry out the reaction.<sup>56</sup> Because there are various definitions of what constitutes an appreciable rate, the overpotential reaction can vary not only based on the catalyst, but also on the rate that is determined as the benchmark.<sup>57</sup> Commonly cited performance measures for water oxidation are an overpotential of 400 mV at a current density of 10 mA/cm<sup>2</sup>, while the overpotential for H<sub>2</sub> evolution at 10 mA/cm<sup>2</sup> is typically around 50 mV.<sup>58</sup> H<sub>2</sub> evolution tends to proceed with a smaller overpotential than water oxidation because water oxidation requires a two-step, four electron transfer as opposed to the single-step, two electron transfer required for hydrogen evolution.<sup>23</sup> The multi-step evolution of oxygen is considerably more difficult to carry out than the evolution of hydrogen as the presence of additional steps is associated with additional activation energies and intermediates in the reaction.<sup>59</sup> Furthermore, another consequence of multi-step reactions is that parasitic reactions can take place. In the case of water oxidation, peroxide can also be generated,<sup>60,61</sup> hence the existence of the terms “oxygen evolution reaction” (where the main product is oxygen) and “water oxidation” (which refers to the oxidation of water to all products – mostly peroxide and oxygen).

In addition to considerations of overpotential, water electrolysis catalysts are also limited by the conditions under which the electrolysis of water takes place.

Pure water is a poor system for electrolysis because of its limited conductivity, necessitating the addition of ions to the electrolytic solution. Most commonly used electrolyte ions have the potential to react under electrolytic conditions, making the use of protons and hydroxides preferred to prevent parasitic reactions. However, protons and hydroxides must be added at such high concentrations that the pH becomes extremely corrosive. For example, most alkaline electrolyzers require the use of 15 – 35% KOH (by weight).<sup>44,62</sup> Nonetheless, for most catalyst materials currently used for water splitting, alkaline environments are less corrosive than acidic ones, making alkaline electrolysis the standard electrolytic method.<sup>54</sup> The water splitting reactions in basic conditions become modified to:



This modification in equation also results in a change in the potentials according to the Nernst Equation, which dictates that changes in concentration of the oxidized and reduced species will result in changes in the reaction potential:<sup>56</sup>

$$E = E^0 + (RT/zF)\ln([\text{ox}]/[\text{red}])$$

Where E is the observed potential of the reaction, E<sup>0</sup> is the standard electrode potential of the reaction, R is the universal gas constant (8.3145 J/Kmol), T is the

absolute temperature,  $z$  is the number of electrons transferred in the reaction,  $F$  is Faraday's constant (96485 C/mol), and  $[ox]$  and  $[red]$  represent the concentration of the oxidized and reduced species, respectively. Under ambient temperature (298 K), this equation can further be simplified using base ten logs to:

$$E = E^0 + (0.05916/z)\log([ox]/[red])$$

The derived equation is especially useful because pH is the direct base ten value of the proton concentration. This final equation suggests that the potential of the reaction increases by 59.16 mV for every unit of pH. However, since this equation affects both the water oxidation and H<sub>2</sub> evolution half-reactions identically, the reaction potentials remain separated by 1.229 V. Both acidic and alkaline systems have their benefits; alkaline water oxidation catalysts are abundant but there are no effective membrane systems to separate hydrogen and oxygen gases while acidic systems benefit from developed proton exchange membrane technology and yet have few earth-abundant catalysts.<sup>54,63,64</sup>

A final consideration for electrode material design is economy. The materials that are currently used for efficient water splitting tend to be noble metals in elemental groups 8 through 10, namely rhodium, ruthenium, platinum, and iridium.<sup>44,54</sup> While these metals tend to have high catalytic activities and stabilities in acidic and basic solutions, it would be economically unfeasible to implement these catalysts on any significant scale due to their raw material costs.<sup>54,65</sup> To summarize, in designing electrochemical water splitting catalysts, materials must

(a) have low overpotentials for each water splitting half-reaction, (b) be able to maintain their activities for extended periods of time under the desired (typically harsh pH) conditions, and (c) be able to be mass produced at reasonable prices.

#### **1.4.2 Photocatalytic Water Splitting**

Although plants and algae have been catalyzing the photolysis of water for one billion years, the modern conception of water splitting dates back to 1972, when Akira Fujishima and Kenichi Honda of the University of Tokyo discovered that titanium dioxide ( $\text{TiO}_2$ ) electrodes placed in water would spontaneously evolve bubbles of  $\text{H}_2$  and  $\text{O}_2$  gas when irradiated with UV light.<sup>66</sup> Since then, the promise of a water splitting photoelectrode – a catalytic material or combined set of materials that can simultaneously absorb the solar spectrum and catalyze water splitting – has become a “holy grail” for the scientific community.<sup>23,67</sup> Although  $\text{TiO}_2$  does not fulfill this requirement due to its need for UV light, other reported materials have proven prone to corrosion. Silicon, the dominant semiconductor for photovoltaic electricity production, has been functionalized with  $\text{H}_2$  and  $\text{O}_2$  evolution catalysts, yielding efficient photoelectrodes.<sup>68,69</sup> However, silicon always corrodes in solution. Likewise, group III/V semiconductors – catalyst-functionalized gallium and indium-containing compounds such as  $\text{GaN}:\text{ZnO}$ ,  $\text{GaAs}$ , and  $\text{GaInP}_2$  – have also been reported as “holy grails”, but each has stability issues during irradiation.<sup>70–73</sup> Furthermore, gallium and indium usage is limited by the relative rarity of these two elements. Stability and bandgap requirements severely limit the materials that can be used for the photocatalysis of water.

To more clearly explain these issues, a review on the nature and properties of bandgaps and semiconductor materials is required. A semiconductor is, as the name suggests, a material that conducts electricity better than an insulator but not as well as a conductor. When examined from a molecular orbital perspective, the conductivity of a material can be determined by the presence and size of the material's bandgap. The bandgap is a region in the orbital diagram of a material where no molecular orbitals exist. Typically, at the top of the bandgap exist a series of unoccupied electron orbitals, the lowest in energy of which is known as the conduction band minimum (CBM), while at the bottom of the bandgap are the occupied electron orbitals, the highest in energy of which is known as the valence band maximum (VBM). Conductors do not have bandgaps, meaning that electrons move with ease into the conduction band (Figure 1.4). Insulators have extremely large bandgaps and therefore conductivity is difficult to achieve because a large potential must be applied to allow electrons to move from the VBM to the CBM. Semiconductors have a sufficiently small bandgap that when excited by a photon with sufficiently high enough energy, an electron in the VBM can be promoted to the CBM. The excited electron leaves behind a positively charged hole which can be spatially separated to derive electrical energy, or in the case of photolysis, perform electrochemical reactions.

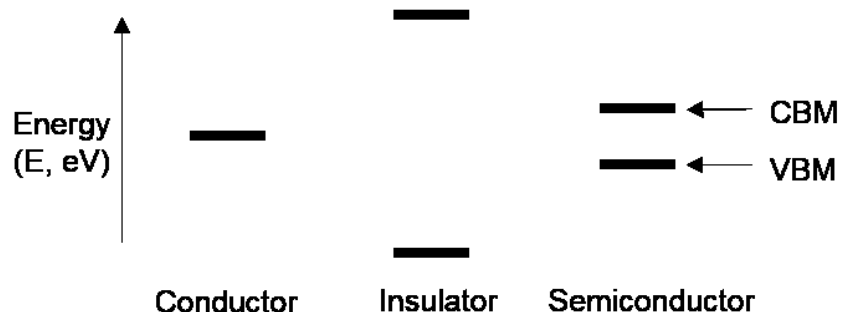


Figure 1.4 Diagram illustrating the difference between conductors, insulators, and semiconductors from a molecular orbital viewpoint.

In order to carry out an electrochemical reaction via semiconductor photo-absorption, several criteria must be met. Firstly, the VBM and CBM positions of the semiconductor device must overlay the potentials of the two corresponding electrochemical half-reactions (Figure 1.5). Secondly, the semiconductor must be excited by a photon of sufficient energy. The energy value of the photon  $E$  is reported in eV. If the energy of the photon  $E$  is greater than the energy of the bandgap (which is also a value with units eV), then the photon has enough energy to induce electron-hole separation. The second criterion explains why water splitting on  $\text{TiO}_2$  has never become commercially viable – with bandgap values of 3.0 and 3.2 (for rutile and anatase  $\text{TiO}_2$ , respectively), the longest wavelength of light that can be utilized for photocatalysis is  $\sim 410$  nm, corresponding to 4% of the solar spectrum. Developing single-absorber materials for photocatalytic water splitting is therefore limited by the necessity of finding and synthesizing materials that can absorb larger portions of the solar spectrum, but also have band edge

positions that overlay half-reaction potentials such that there is sufficient overpotentials to drive both reactions.

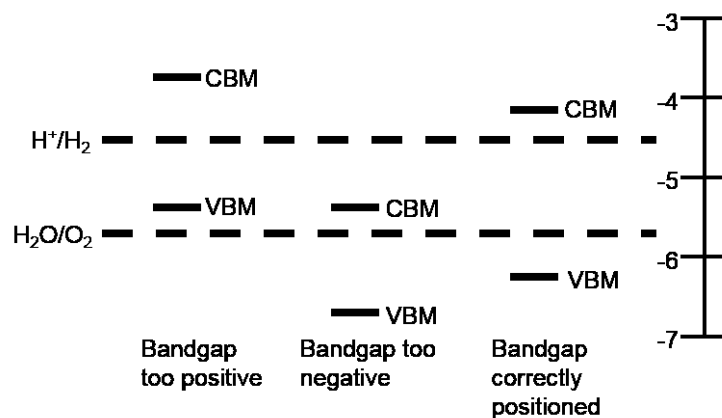


Figure 1.5 Examples of semiconductor bandgap configurations that cannot carry out photocatalytic water splitting because of bad positioning (left, center) compared to a bandgap that can carry out water splitting.

Two-absorber Z-scheme approaches based on inorganic semiconductors would not require a semiconductor with ideally positioned energy band levels, instead opting for two different semiconductors with different bandgaps and band positions, each carrying out one of the water-splitting half reactions. As an additional requirement, the two materials would need overlapping bandgaps and Fermi levels in order to be able to transfer electrons between each other. The Fermi level of a material represents the average energy of states present and in semiconductors exists between the CBM and VBM.<sup>74-76</sup> When two semiconductors are placed in contact with each other, their Fermi levels equalize, possibly accompanied by electron transfer. At that point, an electron from the more energetically positive semiconductor can perform  $H_2$  evolution while the hole from the more energetically negative semiconductor oxidizes water. Meanwhile, the

unused electron and hole recombine where the semiconductors make physical contact. The movement of electrons has caused this type of approach to be dubbed a “Z-scheme”.<sup>77,78</sup> Z-scheme-style dual semiconductor devices can allow for a greater range of semiconductors to be used as the bandgap requirements are not as specific – in particular, the semiconductors of interest do not need to simultaneously have favourable energy positions for both H<sub>2</sub> and O<sub>2</sub> evolution (Figure 1.6). Notably, the use of two complementary smaller bandgap materials can increase the portion of the solar spectrum that can be used. As a result, the ideal maximum theoretical conversion efficiency increases from 30% to 41% when dual absorbers are used instead of single absorbers.<sup>23</sup>

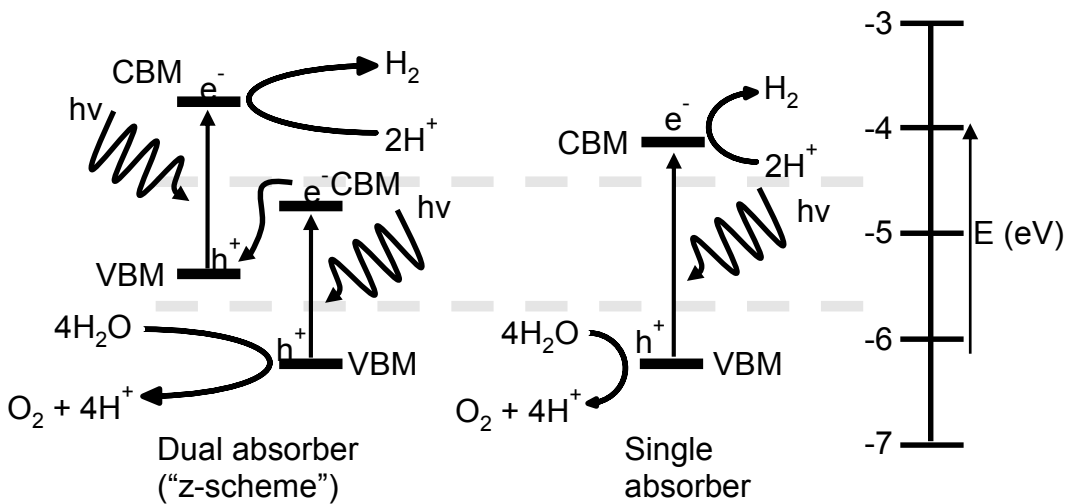


Figure 1.6 Band diagrams of single and dual z-scheme absorber water splitting semiconductor systems.

The requirement of stability under photocatalytic conditions is important to both single and dual absorber systems. Although many nanoparticle-based photocatalytic water splitting systems do not require the same ionic conditions as

used for electrochemical water splitting due to the localized generation of electron-hole pairs, some common semiconductor materials, especially sulfides, are vulnerable to oxidation due to the generation and separation of electron-hole pairs.<sup>79</sup> For example, CdS has band gap edges that overlap the water oxidation and hydrogen evolution potentials, but will nonetheless decompose into cadmium ions and sulfate ions under irradiation in water.<sup>80,81</sup> Decomposition takes place partially due to the poor catalytic activity for water oxidation, as CdS in the presence of effective hole scavengers<sup>82,83</sup> or functionalized with water oxidation catalysts<sup>84,85</sup> will not undergo the same fate, or at least will undergo photo-corrosion at a reduced pace. In contrast, metal oxide semiconductors tend to be more stable due to their intrinsic catalytic activity and the high electronegativity of oxygen.<sup>23,79,80</sup> Ultimately, successful photocatalytic water splitting materials will need to (1) withstand electron-hole induced decomposition during water splitting, (2) have the ideal and appropriate band configurations possible, including a small bandgap for maximal light absorption as well as properly aligned band positions, and (3) be capable of being produced economically and in large quantities.

## **1.5 First-Row Transition Metal Oxides for Water Oxidation**

As with inorganic photovoltaic energy conversion, currently known ideal catalyst materials for electrocatalytic and photocatalytic water splitting are either uneconomical, and/or unstable in water. In order to achieve large-scale deployment of such systems, the ideal approach would be to focus on optimizing earth-abundant elements for catalysis. There is evidence in nature itself that such materials do exist,

primarily in the form of the cubic manganese-calcium oxide clusters that carry out oxygen evolution in photosynthesis (Figure 1.7).<sup>50,86</sup> Inspired by this example, a series of artificial manganese-based systems have been synthesized and pioneered for water oxidation ranging from analogous oxide clusters to simple manganese oxide films.<sup>65,87–91</sup> Various systems based on cobalt and iron have also demonstrated that oxides of these metals can also be catalytic for water oxidation, with commonly reported overpotentials lying between 0.40 and 0.60 V at 10 mA/cm<sup>2</sup>.<sup>92–96</sup> Nickel oxide has the lowest known overpotential of any first row transition metal oxide, with typical overpotentials at 10 mA/cm<sup>2</sup> typically recorded between 0.30 and 0.40 V depending on preparation.<sup>97–102</sup> As a reference, it is common to report overpotentials for similar current densities for RuO<sub>2</sub> and IrO<sub>2</sub> between 0.10 and 0.20 V.<sup>103–105</sup>

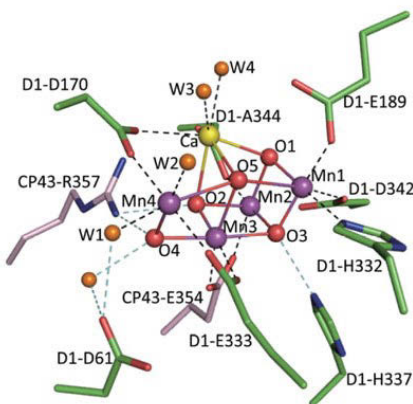


Figure 1.7 Diagram of the manganese-cubane catalytic site responsible for water oxidation associated with photosystem II during photosynthesis. Reprinted with permission from Nature Publishing Group.<sup>106</sup>

In order to further reduce the water oxidation overpotentials of first row transition metal oxides, the synthesis of multi-metallic catalysts is of interest. This strategy has been successful in improving the catalytic activity of nickel oxide,

which appears to have improved catalytic activity when doped with various quantities of iron,<sup>102,107–109</sup> although combining nickel oxide with other metals results in similar (if not quite as effective) improvements in catalytic activity.<sup>57</sup> This synergy can be further optimized through controlling the composition of the electrode systems in addition to factors like electrode feature size and catalyst layer thickness.<sup>102,108,110</sup> Furthermore, the crystal phase of the constituent elements in the catalyst can also have a significant effect on activity. The discovery of non-crystalline materials as effective water oxidation catalysts, beginning with an amorphous cobalt phosphate material in 2008,<sup>92</sup> has spurred the development of materials that are structurally amorphous compared to their more well-characterized crystalline cousins, yet appear to have extremely high activities for water oxidation.<sup>104,107</sup> However, crystalline catalysts like the barium-strontium-cobalt-iron (BSCF) perovskite reported by Suntivich et al. acquire their characteristic low overpotentials because of specific structures – in the case of such catalysts, the perovskite crystal structure.<sup>111</sup> Furthermore, considering that the manganese catalytic site of the oxygen evolving complex of photosynthesis maintains a specific cubane structure, the role of crystal structure should not be downplayed. Indeed, some studies have come forth suggesting that these amorphous catalysts achieve high activities because they adopt a cubane structure *in situ*.<sup>86,96,112,113</sup> Given the variety in viewpoints, the development of novel, efficient water oxidation systems based on idealized compositional and structural properties is possible, but only if these characteristics are properly understood.

For photocatalysis, controlling composition and structure is important for optimizing the position of a material's bandgap. For example, there are multiple unique isoforms of iron oxide, many of which have identical oxidation states. Hematite ( $\alpha\text{-Fe}_2\text{O}_3$ ) has especially significant potential for development as a photocatalyst because it is economic to produce, stable under neutral and basic conditions,<sup>114,115</sup> and has a bandgap of 2.2 eV, allowing for an ideal 13% efficiency when converting sunlight to  $\text{H}_2$ .<sup>115,116</sup> However, the CBM of  $\alpha\text{-Fe}_2\text{O}_3$  is not closer to vacuum level than the required potential for  $\text{H}_2$  evolution, so  $\alpha\text{-Fe}_2\text{O}_3$  cannot evolve  $\text{H}_2$  independently and electrons must leave the anode to reduce protons. Maghemite ( $\gamma\text{-Fe}_2\text{O}_3$ ) is the second most common polymorph of  $\text{Fe}_2\text{O}_3$  (after  $\alpha\text{-Fe}_2\text{O}_3$ ), has a defective spinel structure, similar bandgap to  $\alpha\text{-Fe}_2\text{O}_3$  and high magnetic susceptibility,<sup>117-119</sup> but is not suitable for photocatalysis because it is thermodynamically unstable.<sup>120,121</sup> However, other iron spinels, such as  $\text{CaFe}_2\text{O}_4$  and  $\text{CuFe}_2\text{O}_4$ , are known to function as  $\text{H}_2$  evolution catalysts.<sup>122,123</sup> Therefore, variations in composition and structure can bestow drastic differences in properties, making the search for earth abundant metal oxide catalysts both possible and intensive. Combinatorial studies that examine both composition and structure provide a plentiful and ideal toolkit for discovering future water splitting electrocatalysts and photocatalysts.<sup>110,124,125</sup>

## 1.6 Synthesis of Nanostructured Metal Oxides

In addition to crystal and molecular structure, nanostructuring can also be used to improve catalytic activity on the larger (nanometer) scale. By increasing the

surface area of catalytic materials, more reaction sites can be made available.<sup>126,127</sup> In particular, nanoparticle-based structures are effective methods to create larger-scale catalyst materials because the constituent nanoparticles already have high surface area to volume ratios.<sup>128</sup> While it is common in industrial applications to simply load nanoparticles on inert supports,<sup>126</sup> nanoparticle structures can also be assembled with minimal support.<sup>128–131</sup> Nanoparticle-based nanostructuring routes also benefit from the ability to control the shape, size, and composition of the constituent nanoparticles during the initial synthesis. These features can in turn, when used for nanostructures, impart their novel properties to entire devices and structures.<sup>128</sup> Multiple effective routes for the synthesis of transition metal oxide nanoparticles have been reported, including the thermal decomposition of metal-organic precursors,<sup>132–135</sup> sol-gel hydrolysis and condensation,<sup>136–139</sup> and hydrothermal synthesis.<sup>140–143</sup>

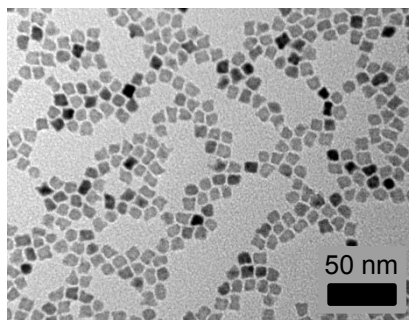


Figure 1.8 Electron micrograph of  $[\text{Ni,Fe}]\text{O}$  nanoparticle formed via decomposition of metal oleate complexes.

There are also a wide variety of non-nanoparticle approaches for synthesizing metal oxide nanostructures. Physical and chemical deposition, electrochemical deposition and anodization, and templating are some of the most commonly used techniques that have been used to synthesize high surface area nanostructured

catalysts.<sup>144</sup> Physical vapour deposition (PVD) includes a wide variety of techniques where atoms are placed directly onto substrate surfaces. In the case of metal oxides, a pure metal oxide or metal source can be bombarded into vapour which then condenses on a substrate surface.<sup>145–147</sup> Chemical vapour deposition (CVD) in contrast utilizes unreacted precursors typically in liquid phase that are easy to vaporize and easily decompose into the desired material upon substrate contact via chemical reaction. One example of successful CVD metal oxide nanostructures was the  $\text{Fe}(\text{CO})_5$ -based system utilized for the synthesis of state-of-the-art  $\alpha\text{-Fe}_2\text{O}_3$  water oxidation electrodes (Figure 1.8).<sup>148</sup> This system was notable for its high surface area as well as the ease of doping during synthesis. Other forms of CVD have been used to prepare  $\alpha\text{-Fe}_2\text{O}_3$  photoelectrodes for water oxidation including spray pyrolysis<sup>149,150</sup> and atomic layer deposition.<sup>151,152</sup> CVD for transition other nanostructured transition metal oxide electrodes and photoelectrodes that have been reported include  $\text{TiO}_2$ ,<sup>153–155</sup>  $\text{BiVO}_4$ ,<sup>156</sup>  $\text{WO}_3$ ,<sup>157,158</sup> and  $\text{CoO}$ ,<sup>153,159</sup> highlighting the ability of CVD to produce conformal, high surface area nanostructures of a variety of metal oxides for electro- and photocatalytic applications.

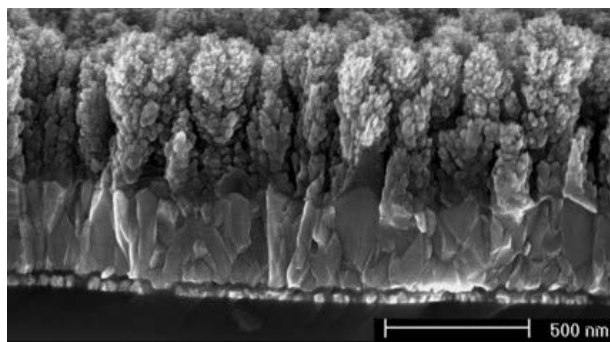


Figure 1.9 Electron micrograph of an  $\alpha\text{-Fe}_2\text{O}_3$  photoelectrode prepared by APCVD.<sup>148</sup> Reprinted with permission from the American Chemical Society.

In addition to vapour deposition, electrochemical and template-based syntheses offer unique avenues to nanostructure synthesis. In particular, the synthesis of tubular nanomaterials via anodization, first pioneered on  $\text{TiO}_2$ ,<sup>160</sup> has the ability to create nanowire and nanotube arrays for a variety of materials. Nanotubes and nanowires are especially desirable because of their high surface area to volume ratios and potential for array-based devices, allowing for easy electrode production.<sup>160</sup> Nanowire and nanotube arrays of a variety of transition metal oxides have been reported, including  $\text{TiO}_2$ ,<sup>161–163</sup>  $\text{WO}_3$ ,<sup>164,165</sup> and  $\alpha\text{-Fe}_2\text{O}_3$  (Figure 1.9).<sup>166–168</sup> Anodization can also be used to form templates, usually made of aluminum oxide, which are then filled in before the template is destroyed.<sup>169</sup> Using this approach, metal oxide structures similar to those produced by direct anodization have been reported,<sup>170–172</sup> although nanostructures that cannot be synthesized by direct anodization such as metals and sulfides have also been demonstrated.<sup>173–175</sup>

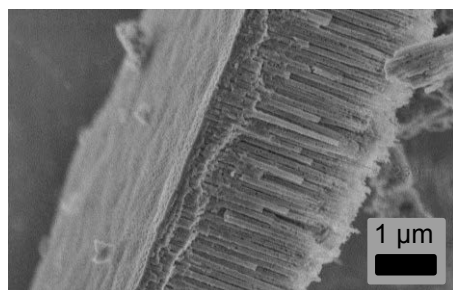


Figure 1.10 Electron micrograph of an  $\alpha\text{-Fe}_2\text{O}_3$  nanotube array prepared by anodization of iron foil.<sup>168</sup> Reprinted with permission from the American Chemical Society.

Anodization can also be used to make templates for nanowire arrays, allowing for the fabrication of a new structure.<sup>176</sup> In most forms of templating, the template

is exposed to a precursor that coats the original template. Afterwards, the template can be removed using chemical or thermal processes that destroy the original template, leaving the new material intact. The field of templating is vast because almost of the diversity of materials that can be optimized as templates.<sup>176</sup> Biotemplating is especially interesting because of the intricate structures of biological systems. Templates that have been demonstrated to produce effective nanostructures of inorganic materials can be as small as DNA,<sup>177,178</sup> proteins,<sup>179,180</sup> and viruses<sup>181–183</sup> but can also be as large as plant leaves.<sup>184,185</sup> Biotemplating is possible because of the dominating presence of common atoms in biological structures; sulfides, hydroxides, and amines all have specific interactions with metals that can be exploited to create metallic copies of structures.<sup>186</sup> As long as the template material can be removed post-templating without destroying the material cast, templating can be a very simple way to produce nanostructured materials.

## 1.7 Overview of the Thesis

This thesis consists of three chapters that discuss different aspects of electrocatalytic and photocatalytic water splitting, with the catalytic material in each case being a metal oxide or mixed metal oxide of an earth-abundant metal.

Chapter 2 discusses the biotemplating of sugarcane leaf species with an iron oxide precursor to form a high-surface area  $\alpha$ -Fe<sub>2</sub>O<sub>3</sub> superstructure that can absorb most of the solar spectrum. Following biotemplating, the structure was functionalized with copper nanoparticles and heated in order to form a second

semiconductor material,  $\text{CuFe}_2\text{O}_4$ . Because these two materials are in intimate contact, the entire structure comprised a Z-scheme – a system with two photoelectrodes. Afterwards, catalyst nanoparticles were integrated in an attempt to harness photocatalytic activity. Since the Z-scheme was not successful at water splitting, reasons for the inability of these semiconductors to carry out water splitting is explored.

Chapter 3 discusses the synthesis of  $[\text{Ni,Fe}]\text{O}$  nanoparticles synthesized by the decomposition of metal oleates at high-temperature. These nanoparticles possessed a metastable structure and yet remained stable for long periods of time under atmospheric conditions. Furthermore, aspects like shape and composition could be easily tuned by modifying the synthetic conditions. Chapter 3 was reproduced in part with permission from:

- a) J.A. Bau, P. Li, A.J. Marenco, S. Trudel, B.C. Olsen, E.J. Lubber, J.M. Buriak, *Chem. Mater.* **2014**, 26(16), 4796-4804. Copyright © 2014 American Chemical Society.

Chapter 4 discusses the functionalization and use of the  $[\text{Ni,Fe}]\text{O}$  nanoparticles synthesized in chapter 3 for electrocatalytic water oxidation. The functionalization of electrode materials with these nanoparticles, and formation into durable electrode structures, was important to developing proper systems under which these nanoparticles could be properly used. Several different techniques, including

simple drop-casting, plasma treatment, and UV irradiation were utilized to make these electrodes.

Chapter 5 will summarize what was learned from this thesis and discuss future directions for this work.

## 1.8 References

- (1) International Energy Agency. Key World Energy Statistics 2014. 2014.
- (2) British Petroleum. BP Statistical Review of World Energy. British Petroleum June 2014.
- (3) Shafiee, S.; Topal, E. When Will Fossil Fuel Reserves Be Diminished? *Energy Policy* **2009**, *37* (1), 181–189.
- (4) Simmons, M. R. *Twilight in the Desert: The Coming Saudi Oil Shock and the World Economy*; Wiley, 2006.
- (5) Hamilton, J. D. Oil and the Macroeconomy since World War II. *J. Polit. Econ.* **1983**, *91* (2), 228–248.
- (6) Gong, P.; Liang, S.; Carlton, E. J.; Jiang, Q.; Wu, J.; Wang, L.; Remais, J. V. Urbanisation and Health in China. *The Lancet* **2012**, *379* (9818), 843–852.
- (7) Baccarelli, A.; Bollati, V. Epigenetics and Environmental Chemicals. *Curr. Opin. Pediatr.* **2009**, *21* (2), 243–251.
- (8) Zhang, J.; Smith, K. R. Household Air Pollution from Coal and Biomass Fuels in China: Measurements, Health Impacts, and Interventions. *Environ. Health Perspect.* **2007**, *115* (6), 848–855.
- (9) Brook, R. D.; Rajagopalan, S.; Pope, C. A.; Brook, J. R.; Bhatnagar, A.; Diez-Roux, A. V.; Holguin, F.; Hong, Y.; Luepker, R. V.; Mittleman, M. A.; et al. Particulate Matter Air Pollution and Cardiovascular Disease An Update to the Scientific Statement From the American Heart Association. *Circulation* **2010**, *121* (21), 2331–2378.
- (10) Lewis, N. S.; Nocera, D. G. Powering the Planet: Chemical Challenges in Solar Energy Utilization. *Proc. Natl. Acad. Sci.* **2006**, *103* (43), 15729–15735.

- (11) Solomon, S.; Plattner, G.-K.; Knutti, R.; Friedlingstein, P. Irreversible Climate Change due to Carbon Dioxide Emissions. *Proc. Natl. Acad. Sci.* **2009**, *106* (6), 1704–1709.
- (12) U.S. Energy Information Administration. Levelized Cost and Levelized Avoided Cost of New Generation Resources in the Annual Energy Outlook 2014. April 2014.
- (13) Lu, X.; Salovaara, J.; McElroy, M. B. Implications of the Recent Reductions in Natural Gas Prices for Emissions of CO<sub>2</sub> from the US Power Sector. *Environ. Sci. Technol.* **2012**, *46* (5), 3014–3021.
- (14) Lu, X.; McElroy, M. B.; Kiviluoma, J. Global Potential for Wind-Generated Electricity. *Proc. Natl. Acad. Sci.* **2009**, *106* (27), 10933–10938.
- (15) Archer, C. L.; Jacobson, M. Z. Evaluation of Global Wind Power. *J. Geophys. Res. Atmospheres* **2005**, *110* (D12), D12110.
- (16) Georgilakis, P. S. Technical Challenges Associated with the Integration of Wind Power into Power Systems. *Renew. Sustain. Energy Rev.* **2008**, *12* (3), 852–863.
- (17) Albadi, M. H.; El-Saadany, E. F. Overview of Wind Power Intermittency Impacts on Power Systems. *Electr. Power Syst. Res.* **2010**, *80* (6), 627–632.
- (18) Toke, D.; Breukers, S.; Wolsink, M. Wind Power Deployment Outcomes: How Can We Account for the Differences? *Renew. Sustain. Energy Rev.* **2008**, *12* (4), 1129–1147.
- (19) Blankenship, R. E.; Tiede, D. M.; Barber, J.; Brudvig, G. W.; Fleming, G.; Ghirardi, M.; Gunner, M. R.; Junge, W.; Kramer, D. M.; Melis, A.; et al. Comparing Photosynthetic and Photovoltaic Efficiencies and Recognizing the Potential for Improvement. *Science* **2011**, *332* (6031), 805–809.
- (20) Wadia, C.; Alivisatos, A. P.; Kammen, D. M. Materials Availability Expands the Opportunity for Large-Scale Photovoltaics Deployment. *Environ. Sci. Technol.* **2009**, *43* (6), 2072–2077.
- (21) Ramasamy, K.; Malik, M. A.; Revaprasadu, N.; O'Brien, P. Routes to Nanostructured Inorganic Materials with Potential for Solar Energy Applications. *Chem. Mater.* **2013**, *25* (18), 3551–3569.
- (22) Mishra, A.; Bäuerle, P. Small Molecule Organic Semiconductors on the Move: Promises for Future Solar Energy Technology. *Angew. Chem. Int. Ed.* **2012**, *51* (9), 2020–2067.

- (23) Walter, M. G.; Warren, E. L.; McKone, J. R.; Boettcher, S. W.; Mi, Q.; Santori, E. A.; Lewis, N. S. Solar Water Splitting Cells. *Chem. Rev.* **2010**, *110* (11), 6446–6473.
- (24) Jacobson, M. Z.; Delucchi, M. A. Providing All Global Energy with Wind, Water, and Solar Power, Part I: Technologies, Energy Resources, Quantities and Areas of Infrastructure, and Materials. *Energy Policy* **2011**, *39* (3), 1154–1169.
- (25) U.S. Energy Information Administration. Annual Energy Outlook 2014 with Projections to 2040. 2014.
- (26) Chan, C. C. The State of the Art of Electric, Hybrid, and Fuel Cell Vehicles. *Proc. IEEE* **2007**, *95* (4), 704–718.
- (27) Winter, M.; Brodd, R. J. What Are Batteries, Fuel Cells, and Supercapacitors? *Chem. Rev.* **2004**, *104* (10), 4245–4270.
- (28) Pearson, R. J.; Eisaman, M. D.; Turner, J. W. G.; Edwards, P. P.; Jiang, Z.; Kuznetsov, V. L.; Littau, K. A.; di Marco, L.; Taylor, S. R. G. Energy Storage via Carbon-Neutral Fuels Made From CO, Water, and Renewable Energy. *Proc. IEEE* **2012**, *100* (2), 440–460.
- (29) Crabtree, G. W.; Dresselhaus, M. S.; Buchanan, M. V. The Hydrogen Economy. *Phys. Today* **2004**, *57* (12), 39–44.
- (30) Balat, M. Potential Importance of Hydrogen as a Future Solution to Environmental and Transportation Problems. *Int. J. Hydrog. Energy* **2008**, *33* (15), 4013–4029.
- (31) Grochala, W.; Edwards, P. P. Thermal Decomposition of the Non-Interstitial Hydrides for the Storage and Production of Hydrogen. *Chem. Rev.* **2004**, *104* (3), 1283–1316.
- (32) Orimo, S.; Nakamori, Y.; Eliseo, J. R.; Züttel, A.; Jensen, C. M. Complex Hydrides for Hydrogen Storage. *Chem. Rev.* **2007**, *107* (10), 4111–4132.
- (33) Suh, M. P.; Park, H. J.; Prasad, T. K.; Lim, D.-W. Hydrogen Storage in Metal–Organic Frameworks. *Chem. Rev.* **2011**, *112* (2), 782–835.
- (34) Thomas, K. M. Adsorption and Desorption of Hydrogen on Metal–organic Framework Materials for Storage Applications: Comparison with Other Nanoporous Materials. *Dalton Trans.* **2009**, No. 9, 1487–1505.

- (35) Debe, M. K. Electrocatalyst Approaches and Challenges for Automotive Fuel Cells. *Nature* **2012**, *486* (7401), 43–51.
- (36) Pollet, B. G.; Staffell, I.; Shang, J. L. Current Status of Hybrid, Battery and Fuel Cell Electric Vehicles: From Electrochemistry to Market Prospects. *Electrochimica Acta* **2012**, *84*, 235–249.
- (37) Eberle, U.; Müller, B.; Helmolt, R. von. Fuel Cell Electric Vehicles and Hydrogen Infrastructure: Status 2012. *Energy Environ. Sci.* **2012**, *5* (10), 8780–8798.
- (38) Chen, Z.; Higgins, D.; Yu, A.; Zhang, L.; Zhang, J. A Review on Non-Precious Metal Electrocatalysts for PEM Fuel Cells. *Energy Environ. Sci.* **2011**, *4* (9), 3167–3192.
- (39) Muradov, N. Z.; Veziroğlu, T. N. From Hydrocarbon to Hydrogen–carbon to Hydrogen Economy. *Int. J. Hydrog. Energy* **2005**, *30* (3), 225–237.
- (40) Haryanto, A.; Fernando, S.; Murali, N.; Adhikari, S. Current Status of Hydrogen Production Techniques by Steam Reforming of Ethanol: A Review. *Energy Fuels* **2005**, *19* (5), 2098–2106.
- (41) Rostrup-Nielsen, J. R. Conversion of Hydrocarbons and Alcohols for Fuel Cells. *Phys. Chem. Chem. Phys.* **2001**, *3* (3), 283–288.
- (42) Simpson, A. P.; Lutz, A. E. Exergy Analysis of Hydrogen Production via Steam Methane Reforming. *Int. J. Hydrog. Energy* **2007**, *32* (18), 4811–4820.
- (43) Rostrup-Nielsen, J. Steam Reforming of Hydrocarbons. A Historical Perspective. In *Studies in Surface Science and Catalysis*; Xu, X. B. and Y., Ed.; Natural Gas Conversion VII Proceedings of the 7th Natural Gas Conversion Symposium; Elsevier, 2004; Vol. 147, pp 121–126.
- (44) Holladay, J. D.; Hu, J.; King, D. L.; Wang, Y. An Overview of Hydrogen Production Technologies. *Catal. Today* **2009**, *139* (4), 244–260.
- (45) Turner, J.; Sverdrup, G.; Mann, M. K.; Maness, P.-C.; Kroposki, B.; Ghirardi, M.; Evans, R. J.; Blake, D. Renewable Hydrogen Production. *Int. J. Energy Res.* **2008**, *32* (5), 379–407.
- (46) Kodama, T.; Gokon, N. Thermochemical Cycles for High-Temperature Solar Hydrogen Production. *Chem. Rev.* **2007**, *107* (10), 4048–4077.
- (47) Rosen, M. A. Advances in Hydrogen Production by Thermochemical Water Decomposition: A Review. *Energy* **2010**, *35* (2), 1068–1076.

- (48) E. Funk, J. Thermochemical Hydrogen Production: Past and Present. *Int. J. Hydrog. Energy* **2001**, *26* (3), 185–190.
- (49) Ghirardi, M. L.; Dubini, A.; Yu, J.; Maness, P.-C. Photobiological Hydrogen-Producing Systems. *Chem. Soc. Rev.* **2009**, *38* (1), 52.
- (50) Yachandra, V. K.; Sauer, K.; Klein, M. P. Manganese Cluster in Photosynthesis: Where Plants Oxidize Water to Dioxygen. *Chem. Rev.* **1996**, *96* (7), 2927–2950.
- (51) Das, D.; Veziroglu, T. N. Advances in Biological Hydrogen Production Processes. *Int. J. Hydrog. Energy* **2008**, *33* (21), 6046–6057.
- (52) de Levie, R. The Electrolysis of Water. *J. Electroanal. Chem.* **1999**, *476* (1), 92–93.
- (53) Kreuter, W.; Hofmann, H. Electrolysis: The Important Energy Transformer in a World of Sustainable Energy. *Int. J. Hydrog. Energy* **1998**, *23* (8), 661–666.
- (54) Cook, T. R.; Dogutan, D. K.; Reece, S. Y.; Surendranath, Y.; Teets, T. S.; Nocera, D. G. Solar Energy Supply and Storage for the Legacy and Nonlegacy Worlds. *Chem. Rev.* **2010**, *110* (11), 6474–6502.
- (55) Rossmeisl, J.; Logadottir, A.; Nørskov, J. K. Electrolysis of Water on (oxidized) Metal Surfaces. *Chem. Phys.* **2005**, *319* (1–3), 178–184.
- (56) Bard, A. J.; Faulkner, L. R. *Electrochemical Methods: Fundamentals and Applications.*; Wiley: New York, 1980; Vol. 2.
- (57) McCrory, C. C. L.; Jung, S.; Peters, J. C.; Jaramillo, T. F. Benchmarking Heterogeneous Electrocatalysts for the Oxygen Evolution Reaction. *J. Am. Chem. Soc.* **2013**, *135* (45), 16977–16987.
- (58) Weber, M. F.; Dignam, M. J. Efficiency of Splitting Water with Semiconducting Photoelectrodes. *J. Electrochem. Soc.* **1984**, *131* (6), 1258–1265.
- (59) Matsumoto, Y.; Sato, E. Electrocatalytic Properties of Transition Metal Oxides for Oxygen Evolution Reaction. *Mater. Chem. Phys.* **1986**, *14* (5), 397–426.
- (60) Izgorodin, A.; Izgorodina, E.; MacFarlane, D. R. Low Overpotential Water Oxidation to Hydrogen Peroxide on a MnO<sub>x</sub> Catalyst. *Energy Environ. Sci.* **2012**, *5* (11), 9496–9501.

- (61) Rüttinger, W.; Dismukes, G. C. Synthetic Water-Oxidation Catalysts for Artificial Photosynthetic Water Oxidation. *Chem. Rev.* **1997**, *97* (1), 1–24.
- (62) Dutta, S. Technology Assessment of Advanced Electrolytic Hydrogen Production. *Int. J. Hydrog. Energy* **1990**, *15* (6), 379–386.
- (63) Zeng, K.; Zhang, D. Recent Progress in Alkaline Water Electrolysis for Hydrogen Production and Applications. *Prog. Energy Combust. Sci.* **2010**, *36* (3), 307–326.
- (64) McCrory, C. C. L.; Jung, S.; Ferrer, I. M.; Chatman, S. M.; Peters, J. C.; Jaramillo, T. F. Benchmarking Hydrogen Evolving Reaction and Oxygen Evolving Reaction Electrocatalysts for Solar Water Splitting Devices. *J. Am. Chem. Soc.* **2015**, *137* (13), 4347–4357.
- (65) Gorlin, Y.; Jaramillo, T. F. A Bifunctional Nonprecious Metal Catalyst for Oxygen Reduction and Water Oxidation. *J. Am. Chem. Soc.* **2010**, *132* (39), 13612–13614.
- (66) Fujishima, A.; Honda, K. Electrochemical Photolysis of Water at a Semiconductor Electrode. *Nature* **1972**, *238* (5358), 37–38.
- (67) Bard, A. J.; Fox, M. A. Artificial Photosynthesis: Solar Splitting of Water to Hydrogen and Oxygen. *Acc Chem Res* **1995**, *28* (3), 141–145.
- (68) Rocheleau, R. E.; Miller, E. L.; Misra, A. High-Efficiency Photoelectrochemical Hydrogen Production Using Multijunction Amorphous Silicon Photoelectrodes. *Energy Fuels* **1998**, *12* (1), 3–10.
- (69) Reece, S. Y.; Hamel, J. A.; Sung, K.; Jarvi, T. D.; Esswein, A. J.; Pijpers, J. J. H.; Nocera, D. G. Wireless Solar Water Splitting Using Silicon-Based Semiconductors and Earth-Abundant Catalysts. *Science* **2011**, *334* (6056), 645–648.
- (70) Kocha, S. S.; Montgomery, D.; Peterson, M. W.; Turner, J. A. Photoelectrochemical Decomposition of Water Utilizing Monolithic Tandem Cells. *Sol. Energy Mater. Sol. Cells* **1998**, *52* (3–4), 389–397.
- (71) Khaselev, O.; Bansal, A.; Turner, J. A. High-Efficiency Integrated Multijunction Photovoltaic/electrolysis Systems for Hydrogen Production. *Int. J. Hydrog. Energy* **2001**, *26* (2), 127–132.
- (72) Khaselev, O.; Turner, J. A. A Monolithic Photovoltaic-Photoelectrochemical Device for Hydrogen Production via Water Splitting. *Science* **1998**, *280* (5362), 425–427.

- (73) Maeda, K.; Domen, K. Solid Solution of GaN and ZnO as a Stable Photocatalyst for Overall Water Splitting under Visible Light†. *Chem. Mater.* **2010**, *22* (3), 612–623.
- (74) Tersoff, J. Schottky Barrier Heights and the Continuum of Gap States. *Phys. Rev. Lett.* **1984**, *52* (6), 465–468.
- (75) Tersoff, J. Theory of Semiconductor Heterojunctions: The Role of Quantum Dipoles. *Phys. Rev. B* **1984**, *30* (8), 4874–4877.
- (76) Zur, A.; McGill, T. C.; Smith, D. L. Fermi-Level Position at a Semiconductor-Metal Interface. *Phys. Rev. B* **1983**, *28* (4), 2060–2067.
- (77) Grätzel, M. Photoelectrochemical Cells. *Nature* **2001**, *414* (6861), 338–344.
- (78) Maeda, K. Z-Scheme Water Splitting Using Two Different Semiconductor Photocatalysts. *ACS Catal.* **2013**, *3* (7), 1486–1503.
- (79) Osterloh, F. E. Inorganic Materials as Catalysts for Photochemical Splitting of Water. *Chem. Mater.* **2008**, *20* (1), 35–54.
- (80) Kudo, A.; Miseki, Y. Heterogeneous Photocatalyst Materials for Water Splitting. *Chem. Soc. Rev.* **2008**, *38* (1), 253–278.
- (81) Meissner, D.; Memming, R.; Kastening, B.; Bahnemann, D. Fundamental Problems of Water Splitting at Cadmium Sulfide. *Chem. Phys. Lett.* **1986**, *127* (5), 419–423.
- (82) Davis, A. P.; Huang, C. P. The Photocatalytic Oxidation of Sulfur-Containing Organic Compounds Using Cadmium Sulfide and the Effect on CdS Photocorrosion. *Water Res.* **1991**, *25* (10), 1273–1278.
- (83) Yun, H. J.; Lee, H.; Kim, N. D.; Lee, D. M.; Yu, S.; Yi, J. A Combination of Two Visible-Light Responsive Photocatalysts for Achieving the Z-Scheme in the Solid State. *ACS Nano* **2011**, *5* (5), 4084–4090.
- (84) Kalyanasundaram, K.; Borgarello, E.; Duonghong, D.; Grätzel, M. Cleavage of Water by Visible-Light Irradiation of Colloidal CdS Solutions; Inhibition of Photocorrosion by RuO<sub>2</sub>. *Angew. Chem. Int. Ed. Engl.* **1981**, *20* (11), 987–988.
- (85) Tseng, H.-W.; Wilker, M. B.; Damrauer, N. H.; Dukovic, G. Charge Transfer Dynamics between Photoexcited CdS Nanorods and Mononuclear Ru Water-Oxidation Catalysts. *J. Am. Chem. Soc.* **2013**, *135* (9), 3383–3386.

- (86) Dismukes, G. C.; Brimblecombe, R.; Felton, G. A. N.; Pryadun, R. S.; Sheats, J. E.; Spiccia, L.; Swiegers, G. F. Development of Bioinspired  $\text{Mn}_4\text{O}_4$ -Cubane Water Oxidation Catalysts: Lessons from Photosynthesis. *Acc. Chem. Res.* **2009**, *42* (12), 1935–1943.
- (87) Brimblecombe, R.; Swiegers, G. F.; Dismukes, G. C.; Spiccia, L. Sustained Water Oxidation Photocatalysis by a Bioinspired Manganese Cluster. *Angew. Chem. Int. Ed.* **2008**, *47* (38), 7335–7338.
- (88) Karlsson, E. A.; Lee, B.-L.; Åkermark, T.; Johnston, E. V.; Kärkäs, M. D.; Sun, J.; Hansson, Ö.; Bäckvall, J.-E.; Åkermark, B. Photosensitized Water Oxidation by Use of a Bioinspired Manganese Catalyst. *Angew. Chem.* **2011**, *123* (49), 11919–11922.
- (89) Boppana, V. B. R.; Jiao, F. Nanostructured  $\text{MnO}_2$ : An Efficient and Robust Water Oxidation Catalyst. *Chem. Commun.* **2011**, *47* (31), 8973–8975.
- (90) Iyer, A.; Del-Pilar, J.; King'ondy, C. K.; Kissel, E.; Garces, H. F.; Huang, H.; El-Sawy, A. M.; Dutta, P. K.; Suib, S. L. Water Oxidation Catalysis Using Amorphous Manganese Oxides, Octahedral Molecular Sieves (OMS-2), and Octahedral Layered (OL-1) Manganese Oxide Structures. *J. Phys. Chem. C* **2012**, *116* (10), 6474–6483.
- (91) Najafpour, M. M.; Ehrenberg, T.; Wiechen, M.; Kurz, P. Calcium Manganese(III) Oxides ( $\text{CaMn}_2\text{O}_4 \cdot x \text{H}_2\text{O}$ ) as Biomimetic Oxygen-Evolving Catalysts. *Angew. Chem. Int. Ed.* **2010**, *49* (12), 2233–2237.
- (92) Kanan, M. W.; Nocera, D. G. In Situ Formation of an Oxygen-Evolving Catalyst in Neutral Water Containing Phosphate and  $\text{Co}^{2+}$ . *Science* **2008**, *321* (5892), 1072–1075.
- (93) Chemelewski, W. D.; Lee, H.-C.; Lin, J.-F.; Bard, A. J.; Mullins, C. B. Amorphous  $\text{FeOOH}$  Oxygen Evolution Reaction Catalyst for Photoelectrochemical Water Splitting. *J. Am. Chem. Soc.* **2014**, *136* (7), 2843–2850.
- (94) Seabold, J. A.; Choi, K.-S. Efficient and Stable Photo-Oxidation of Water by a Bismuth Vanadate Photoanode Coupled with an Iron Oxyhydroxide Oxygen Evolution Catalyst. *J. Am. Chem. Soc.* **2012**, *134* (4), 2186–2192.
- (95) Yin, Q.; Tan, J. M.; Besson, C.; Geletii, Y. V.; Musaev, D. G.; Kuznetsov, A. E.; Luo, Z.; Hardcastle, K. I.; Hill, C. L. A Fast Soluble Carbon-Free Molecular Water Oxidation Catalyst Based on Abundant Metals. *Science* **2010**, *328* (5976), 342–345.

- (96) McCool, N. S.; Robinson, D. M.; Sheats, J. E.; Dismukes, G. C. A Co<sub>4</sub>O<sub>4</sub> “Cubane” Water Oxidation Catalyst Inspired by Photosynthesis. *J. Am. Chem. Soc.* **2011**, *133* (30), 11446–11449.
- (97) Miller, E. L.; Rocheleau, R. E. Electrochemical and Electrochromic Behavior of Reactively Sputtered Nickel Oxide. *J. Electrochem. Soc.* **1997**, *144* (6), 1995–2003.
- (98) Sadiq, I. M.; Mohammad, A. M.; El-Shakre, M. E.; El-Deab, M. S. Electrocatalytic Activity of Nickel Oxide Nanoparticles-Modified Electrodes: Optimization of the Loading Level and Operating pH towards the Oxygen Evolution Reaction. *Int. J. Hydrog. Energy* **2012**, *37* (1), 68–77.
- (99) Dincă, M.; Surendranath, Y.; Nocera, D. G. Nickel-Borate Oxygen-Evolving Catalyst That Functions under Benign Conditions. *Proc. Natl. Acad. Sci.* **2010**, *107* (23), 10337–10341.
- (100) Sun, K.; Park, N.; Sun, Z.; Zhou, J.; Wang, J.; Pang, X.; Shen, S.; Noh, S. Y.; Jing, Y.; Jin, S.; et al. Nickel Oxide Functionalized Silicon for Efficient Photo-Oxidation of Water. *Energy Environ. Sci.* **2012**, *5* (7), 7872–7877.
- (101) Godwin, I. J.; Lyons, M. E. G. Enhanced Oxygen Evolution at Hydrous Nickel Oxide Electrodes via Electrochemical Ageing in Alkaline Solution. *Electrochem. Commun.* **2013**, *32*, 39–42.
- (102) Trotochaud, L.; Ranney, J. K.; Williams, K. N.; Boettcher, S. W. Solution-Cast Metal Oxide Thin Film Electrocatalysts for Oxygen Evolution. *J. Am. Chem. Soc.* **2012**, *134* (41), 17253–17261.
- (103) Yeo, R. S.; Orehotsky, J.; Visscher, W.; Srinivasan, S. Ruthenium-Based Mixed Oxides as Electrocatalysts for Oxygen Evolution in Acid Electrolytes. *J. Electrochem. Soc.* **1981**, *128* (9), 1900–1904.
- (104) Smith, R. D. L.; Sporinova, B.; Fagan, R. D.; Trudel, S.; Berlinguette, C. P. Facile Photochemical Preparation of Amorphous Iridium Oxide Films for Water Oxidation Catalysis. *Chem. Mater.* **2014**, *26* (4), 1654–1659.
- (105) Lyons, M. E. G.; Floquet, S. Mechanism of Oxygen Reactions at Porous Oxide Electrodes. Part 2—Oxygen Evolution at RuO<sub>2</sub>, IrO<sub>2</sub> and Ir<sub>x</sub>Ru<sub>1-x</sub>O<sub>2</sub> Electrodes in Aqueous Acid and Alkaline Solution. *Phys. Chem. Chem. Phys.* **2011**, *13* (12), 5314–5335.
- (106) Umena, Y.; Kawakami, K.; Shen, J.-R.; Kamiya, N. Crystal Structure of Oxygen-Evolving Photosystem II at a Resolution of 1.9 Å. *Nature* **2011**, *473* (7345), 55–60.

- (107) Smith, R. D. L.; Prévot, M. S.; Fagan, R. D.; Zhang, Z.; Sedach, P. A.; Siu, M. K. J.; Trudel, S.; Berlinguette, C. P. Photochemical Route for Accessing Amorphous Metal Oxide Materials for Water Oxidation Catalysis. *Science* **2013**, *340* (6128), 60–63.
- (108) Landon, J.; Demeter, E.; İnoğlu, N.; Keturakis, C.; Wachs, I. E.; Vasić, R.; Frenkel, A. I.; Kitchin, J. R. Spectroscopic Characterization of Mixed Fe–Ni Oxide Electrocatalysts for the Oxygen Evolution Reaction in Alkaline Electrolytes. *ACS Catal.* **2012**, *2* (8), 1793–1801.
- (109) Song, F.; Hu, X. Ultrathin Cobalt–Manganese Layered Double Hydroxide Is an Efficient Oxygen Evolution Catalyst. *J. Am. Chem. Soc.* **2014**, *136* (47), 16481–16484.
- (110) Smith, R. D. L.; Prévot, M. S.; Fagan, R. D.; Trudel, S.; Berlinguette, C. P. Water Oxidation Catalysis: Electrocatalytic Response to Metal Stoichiometry in Amorphous Metal Oxide Films Containing Iron, Cobalt, and Nickel. *J. Am. Chem. Soc.* **2013**, *135* (31), 11580–11586.
- (111) Suntivich, J.; Gasteiger, H. A.; Yabuuchi, N.; Nakanishi, H.; Goodenough, J. B.; Shao-Horn, Y. Design Principles for Oxygen-Reduction Activity on Perovskite Oxide Catalysts for Fuel Cells and Metal–air Batteries. *Nat. Chem.* **2011**, *3* (7), 546–550.
- (112) Kanan, M. W.; Yano, J.; Surendranath, Y.; Dincă, M.; Yachandra, V. K.; Nocera, D. G. Structure and Valency of a Cobalt–Phosphate Water Oxidation Catalyst Determined by in Situ X-Ray Spectroscopy. *J. Am. Chem. Soc.* **2010**, *132* (39), 13692–13701.
- (113) Risch, M.; Klingan, K.; Ringleb, F.; Chernev, P.; Zaharieva, I.; Fischer, A.; Dau, H. Water Oxidation by Electrodeposited Cobalt Oxides—Role of Anions and Redox-Inert Cations in Structure and Function of the Amorphous Catalyst. *ChemSusChem* **2012**, *5* (3), 542–549.
- (114) Itoh, K.; Bockris, J. O. Thin Film Photoelectrochemistry: Iron Oxide. *J. Electrochem. Soc.* **1984**, *131* (6), 1266–1271.
- (115) Sivula, K.; Le Formal, F.; Grätzel, M. Solar Water Splitting: Progress Using Hematite ( $\alpha$ -Fe<sub>2</sub>O<sub>3</sub>) Photoelectrodes. *ChemSusChem* **2011**, *4* (4), 432–449.
- (116) Murphy, A. B.; Barnes, P. R. F.; Randeniya, L. K.; Plumb, I. C.; Grey, I. E.; Horne, M. D.; Glasscock, J. A. Efficiency of Solar Water Splitting Using Semiconductor Electrodes. *Int. J. Hydrog. Energy* **2006**, *31* (14), 1999–2017.

- (117) Beydoun, D.; Amal, R.; Low, G.; McEvoy, S. Occurrence and Prevention of Photodissolution at the Phase Junction of Magnetite and Titanium Dioxide. *J. Mol. Catal. Chem.* **2002**, *180* (1–2), 193–200.
- (118) Cornell, R. M.; Schwertmann, U. *The Iron Oxides: Structure, Properties, Reactions, Occurrences and Uses*; John Wiley & Sons, 2003.
- (119) Cabot, A.; Puentes, V. F.; Shevchenko, E.; Yin, Y.; Balcells, L.; Marcus, M. A.; Hughes, S. M.; Alivisatos, A. P. Vacancy Coalescence during Oxidation of Iron Nanoparticles. *J. Am. Chem. Soc.* **2007**, *129* (34), 10358–10360.
- (120) Yang, S.; Xu, Y.; Cao, Y.; Zhang, G.; Sun, Y.; Gao, D. Zn(II)-Doped  $\gamma$ -Fe<sub>2</sub>O<sub>3</sub> Single-Crystalline Nanoplates with High Phase-Transition Temperature, Superparamagnetic Property and Good Photocatalytic Property. *RSC Adv.* **2013**, *3* (44), 21994–22001.
- (121) Tsuzuki, T.; Schäffel, F.; Muroi, M.; McCormick, P. G. Magnetic Properties of Mechanochemically Synthesized  $\gamma$ -Fe<sub>2</sub>O<sub>3</sub> Nanoparticles. *J. Alloys Compd.* **2011**, *509* (17), 5420–5425.
- (122) Ida, S.; Yamada, K.; Matsunaga, T.; Hagiwara, H.; Matsumoto, Y.; Ishihara, T. Preparation of P-Type CaFe<sub>2</sub>O<sub>4</sub> Photocathodes for Producing Hydrogen from Water. *J. Am. Chem. Soc.* **2010**, *132* (49), 17343–17345.
- (123) Yang, H.; Yan, J.; Lu, Z.; Cheng, X.; Tang, Y. Photocatalytic Activity Evaluation of Tetragonal CuFe<sub>2</sub>O<sub>4</sub> Nanoparticles for the H<sub>2</sub> Evolution under Visible Light Irradiation. *J. Alloys Compd.* **2009**, *476* (1–2), 715–719.
- (124) Rowley, J. G.; Do, T. D.; Cleary, D. A.; Parkinson, B. A. Combinatorial Discovery Through a Distributed Outreach Program: Investigation of the Photoelectrolysis Activity of P-Type Fe, Cr, Al Oxides. *ACS Appl. Mater. Interfaces* **2014**, *6* (12), 9046–9052.
- (125) Wang, L.; Lin, C.; Huang, D.; Zhang, F.; Wang, M.; Jin, J. A Comparative Study of Composition and Morphology Effect of Ni<sub>x</sub>Co<sub>1-x</sub>(OH)<sub>2</sub> on Oxygen Evolution/Reduction Reaction. *ACS Appl. Mater. Interfaces* **2014**, *6* (13), 10172–10180.
- (126) Shiju, N. R.; Guliants, V. V. Recent Developments in Catalysis Using Nanostructured Materials. *Appl. Catal. Gen.* **2009**, *356* (1), 1–17.
- (127) Bell, A. T. The Impact of Nanoscience on Heterogeneous Catalysis. *Science* **2003**, *299* (5613), 1688–1691.

- (128) Nie, Z.; Petukhova, A.; Kumacheva, E. Properties and Emerging Applications of Self-Assembled Structures Made from Inorganic Nanoparticles. *Nat. Nanotechnol.* **2010**, *5* (1), 15–25.
- (129) Kameyama, T.; Osaki, T.; Okazaki, K.; Shibayama, T.; Kudo, A.; Kuwabata, S.; Torimoto, T. Preparation and Photoelectrochemical Properties of Densely Immobilized  $\text{Cu}_2\text{ZnSnS}_4$  Nanoparticle Films. *J. Mater. Chem.* **2010**, *20* (25), 5319–5324.
- (130) Hoertz, P. G.; Chen, Z.; Kent, C. A.; Meyer, T. J. Application of High Surface Area Tin-Doped Indium Oxide Nanoparticle Films as Transparent Conducting Electrodes. *Inorg. Chem.* **2010**, *49* (18), 8179–8181.
- (131) Popczun, E. J.; McKone, J. R.; Read, C. G.; Biacchi, A. J.; Wiltrout, A. M.; Lewis, N. S.; Schaak, R. E. Nanostructured Nickel Phosphide as an Electrocatalyst for the Hydrogen Evolution Reaction. *J. Am. Chem. Soc.* **2013**, *135* (25), 9267–9270.
- (132) Park, J.; An, K.; Hwang, Y.; Park, J.-G.; Noh, H.-J.; Kim, J.-Y.; Park, J.-H.; Hwang, N.-M.; Hyeon, T. Ultra-Large-Scale Syntheses of Monodisperse Nanocrystals. *Nat. Mater.* **2004**, *3* (12), 891–895.
- (133) Bao, N.; Shen, L.; Wang, Y.; Padhan, P.; Gupta, A. A Facile Thermolysis Route to Monodisperse Ferrite Nanocrystals. *J. Am. Chem. Soc.* **2007**, *129* (41), 12374–12375.
- (134) Sun, S.; Zeng, H.; Robinson, D. B.; Raoux, S.; Rice, P. M.; Wang, S. X.; Li, G. Monodisperse  $\text{MFe}_2\text{O}_4$  (M = Fe, Co, Mn) Nanoparticles. *J. Am. Chem. Soc.* **2004**, *126* (1), 273–279.
- (135) Lee, J.; Zhang, S.; Sun, S. High-Temperature Solution-Phase Syntheses of Metal-Oxide Nanocrystals. *Chem. Mater.* **2013**, *25* (8), 1293–1304.
- (136) Pinna, N.; Niederberger, M. Surfactant-Free Nonaqueous Synthesis of Metal Oxide Nanostructures. *Angew. Chem. Int. Ed.* **2008**, *47* (29), 5292–5304.
- (137) Tang, X.; Choo, E. S. G.; Li, L.; Ding, J.; Xue, J. Synthesis of ZnO Nanoparticles with Tunable Emission Colors and Their Cell Labeling Applications. *Chem. Mater.* **2010**, *22* (11), 3383–3388.
- (138) Jagadale, T. C.; Takale, S. P.; Sonawane, R. S.; Joshi, H. M.; Patil, S. I.; Kale, B. B.; Ogale, S. B. N-Doped  $\text{TiO}_2$  Nanoparticle Based Visible Light Photocatalyst by Modified Peroxide Sol–Gel Method. *J. Phys. Chem. C* **2008**, *112* (37), 14595–14602.

- (139) Dong, Y.; He, K.; Yin, L.; Zhang, A. A Facile Route to Controlled Synthesis of  $\text{Co}_3\text{O}_4$  Nanoparticles and Their Environmental Catalytic Properties. *Nanotechnology* **2007**, *18* (43), 435602.
- (140) Yan, L.; Yu, R.; Chen, J.; Xing, X. Template-Free Hydrothermal Synthesis of  $\text{CeO}_2$  Nano-Octahedrons and Nanorods: Investigation of the Morphology Evolution. *Cryst. Growth Des.* **2008**, *8* (5), 1474–1477.
- (141) Tian, H.; Ma, J.; Li, K.; Li, J. Hydrothermal Synthesis of S-Doped  $\text{TiO}_2$  Nanoparticles and Their Photocatalytic Ability for Degradation of Methyl Orange. *Ceram. Int.* **2009**, *35* (3), 1289–1292.
- (142) Ge, S.; Shi, X.; Sun, K.; Li, C.; Uher, C.; Baker, J. R.; Banaszak Holl, M. M.; Orr, B. G. Facile Hydrothermal Synthesis of Iron Oxide Nanoparticles with Tunable Magnetic Properties. *J. Phys. Chem. C* **2009**, *113* (31), 13593–13599.
- (143) Yu, J.; Yu, X. Hydrothermal Synthesis and Photocatalytic Activity of Zinc Oxide Hollow Spheres. *Environ. Sci. Technol.* **2008**, *42* (13), 4902–4907.
- (144) Devan, R. S.; Patil, R. A.; Lin, J.-H.; Ma, Y.-R. One-Dimensional Metal-Oxide Nanostructures: Recent Developments in Synthesis, Characterization, and Applications. *Adv. Funct. Mater.* **2012**, *22* (16), 3326–3370.
- (145) Wolcott, A.; Smith, W. A.; Kuykendall, T. R.; Zhao, Y.; Zhang, J. Z. Photoelectrochemical Water Splitting Using Dense and Aligned  $\text{TiO}_2$  Nanorod Arrays. *Small* **2009**, *5* (1), 104–111.
- (146) Dai, Z. r.; Pan, Z. w.; Wang, Z. l. Novel Nanostructures of Functional Oxides Synthesized by Thermal Evaporation. *Adv. Funct. Mater.* **2003**, *13* (1), 9–24.
- (147) Hahn, N. T.; Ye, H.; Flaherty, D. W.; Bard, A. J.; Mullins, C. B. Reactive Ballistic Deposition of  $\alpha\text{-Fe}_2\text{O}_3$  Thin Films for Photoelectrochemical Water Oxidation. *ACS Nano* **2010**, *4* (4), 1977–1986.
- (148) Kay, A.; Cesar, I.; Grätzel, M. New Benchmark for Water Photooxidation by Nanostructured  $\alpha\text{-Fe}_2\text{O}_3$  Films. *J. Am. Chem. Soc.* **2006**, *128* (49), 15714–15721.
- (149) Duret, A.; Grätzel, M. Visible Light-Induced Water Oxidation on Mesoscopic  $\alpha\text{-Fe}_2\text{O}_3$  Films Made by Ultrasonic Spray Pyrolysis. *J. Phys. Chem. B* **2005**, *109* (36), 17184–17191.

- (150) Jorand Sartoretti, C.; Alexander, B. D.; Solarska, R.; Rutkowska, I. A.; Augustynski, J.; Cerny, R. Photoelectrochemical Oxidation of Water at Transparent Ferric Oxide Film Electrodes. *J. Phys. Chem. B* **2005**, *109* (28), 13685–13692.
- (151) Lin, Y.; Zhou, S.; Sheehan, S. W.; Wang, D. Nanonet-Based Hematite Heteronanostructures for Efficient Solar Water Splitting. *J. Am. Chem. Soc.* **2011**, *133* (8), 2398–2401.
- (152) Lin, Y.; Xu, Y.; Mayer, M. T.; Simpson, Z. I.; McMahon, G.; Zhou, S.; Wang, D. Growth of P-Type Hematite by Atomic Layer Deposition and Its Utilization for Improved Solar Water Splitting. *J. Am. Chem. Soc.* **2012**, *134* (12), 5508–5511.
- (153) Ngo, T. Q.; Posadas, A.; Seo, H.; Hoang, S.; McDaniel, M. D.; Utesh, D.; Triyoso, D. H.; Mullins, C. B.; Demkov, A. A.; Ekerdt, J. G. Atomic Layer Deposition of Photoactive CoO/SrTiO<sub>3</sub> and CoO/TiO<sub>2</sub> on Si(001) for Visible Light Driven Photoelectrochemical Water Oxidation. *J. Appl. Phys.* **2013**, *114* (8), 084901.
- (154) Hwang, Y. J.; Hahn, C.; Liu, B.; Yang, P. Photoelectrochemical Properties of TiO<sub>2</sub> Nanowire Arrays: A Study of the Dependence on Length and Atomic Layer Deposition Coating. *ACS Nano* **2012**, *6* (6), 5060–5069.
- (155) Kafizas, A.; Noor, N.; Carmichael, P.; Scanlon, D. O.; Carmalt, C. J.; Parkin, I. P. Combinatorial Atmospheric Pressure Chemical Vapor Deposition of F:TiO<sub>2</sub>; the Relationship between Photocatalysis and Transparent Conducting Oxide Properties. *Adv. Funct. Mater.* **2014**, *24* (12), 1758–1771.
- (156) Rao, P. M.; Cai, L.; Liu, C.; Cho, I. S.; Lee, C. H.; Weisse, J. M.; Yang, P.; Zheng, X. Simultaneously Efficient Light Absorption and Charge Separation in WO<sub>3</sub>/BiVO<sub>4</sub> Core/Shell Nanowire Photoanode for Photoelectrochemical Water Oxidation. *Nano Lett.* **2014**, *14* (2), 1099–1105.
- (157) Sivula, K.; Formal, F. L.; Grätzel, M. WO<sub>3</sub>–Fe<sub>2</sub>O<sub>3</sub> Photoanodes for Water Splitting: A Host Scaffold, Guest Absorber Approach. *Chem. Mater.* **2009**, *21* (13), 2862–2867.
- (158) Rettie, A. J. E.; Klavetter, K. C.; Lin, J.-F.; Dolocan, A.; Celio, H.; Ishiekwene, A.; Bolton, H. L.; Pearson, K. N.; Hahn, N. T.; Mullins, C. B. Improved Visible Light Harvesting of WO<sub>3</sub> by Incorporation of Sulfur or Iodine: A Tale of Two Impurities. *Chem. Mater.* **2014**, *26* (4), 1670–1677.

- (159) Yang, J.; Walczak, K.; Anzenberg, E.; Toma, F. M.; Yuan, G.; Beeman, J.; Schwartzberg, A.; Lin, Y.; Hettick, M.; Javey, A.; et al. Efficient and Sustained Photoelectrochemical Water Oxidation by Cobalt Oxide/Silicon Photoanodes with Nanotextured Interfaces. *J. Am. Chem. Soc.* **2014**, *136* (17), 6191–6194.
- (160) Mor, G. K.; Varghese, O. K.; Paulose, M.; Shankar, K.; Grimes, C. A. A Review on Highly Ordered, Vertically Oriented TiO<sub>2</sub> Nanotube Arrays: Fabrication, Material Properties, and Solar Energy Applications. *Sol. Energy Mater. Sol. Cells* **2006**, *90* (14), 2011–2075.
- (161) Wang, J.; Lin, Z. Freestanding TiO<sub>2</sub> Nanotube Arrays with Ultrahigh Aspect Ratio via Electrochemical Anodization. *Chem. Mater.* **2008**, *20* (4), 1257–1261.
- (162) Feng, X.; Shankar, K.; Varghese, O. K.; Paulose, M.; Latempa, T. J.; Grimes, C. A. Vertically Aligned Single Crystal TiO<sub>2</sub> Nanowire Arrays Grown Directly on Transparent Conducting Oxide Coated Glass: Synthesis Details and Applications. *Nano Lett.* **2008**, *8* (11), 3781–3786.
- (163) Mor, G. K.; Shankar, K.; Paulose, M.; Varghese, O. K.; Grimes, C. A. Use of Highly-Ordered TiO<sub>2</sub> Nanotube Arrays in Dye-Sensitized Solar Cells. *Nano Lett.* **2006**, *6* (2), 215–218.
- (164) Su, J.; Feng, X.; Sloppy, J. D.; Guo, L.; Grimes, C. A. Vertically Aligned WO<sub>3</sub> Nanowire Arrays Grown Directly on Transparent Conducting Oxide Coated Glass: Synthesis and Photoelectrochemical Properties. *Nano Lett.* **2011**, *11* (1), 203–208.
- (165) Cristino, V.; Caramori, S.; Argazzi, R.; Meda, L.; Marra, G. L.; Bignozzi, C. A. Efficient Photoelectrochemical Water Splitting by Anodically Grown WO<sub>3</sub> Electrodes. *Langmuir* **2011**, *27* (11), 7276–7284.
- (166) Pradhan, G. K.; Parida, K. M. Fabrication, Growth Mechanism, and Characterization of  $\alpha$ -Fe<sub>2</sub>O<sub>3</sub> Nanorods. *ACS Appl. Mater. Interfaces* **2011**, *3* (2), 317–323.
- (167) Mohapatra, S. K.; John, S. E.; Banerjee, S.; Misra, M. Water Photooxidation by Smooth and Ultrathin  $\alpha$ -Fe<sub>2</sub>O<sub>3</sub> Nanotube Arrays. *Chem. Mater.* **2009**, *21* (14), 3048–3055.
- (168) LaTempa, T. J.; Feng, X.; Paulose, M.; Grimes, C. A. Temperature-Dependent Growth of Self-Assembled Hematite ( $\alpha$ -Fe<sub>2</sub>O<sub>3</sub>) Nanotube Arrays: Rapid Electrochemical Synthesis and Photoelectrochemical Properties. *J. Phys. Chem. C* **2009**, *113* (36), 16293–16298.

- (169) Li, F.; Zhang, L.; Metzger, R. M. On the Growth of Highly Ordered Pores in Anodized Aluminum Oxide. *Chem. Mater.* **1998**, *10* (9), 2470–2480.
- (170) Cochran, R. E.; Shyue, J.-J.; Padture, N. P. Template-Based, near-Ambient Synthesis of Crystalline Metal-Oxide Nanotubes, Nanowires and Coaxial Nanotubes. *Acta Mater.* **2007**, *55* (9), 3007–3014.
- (171) Dickey, M. D.; Weiss, E. A.; Smythe, E. J.; Chiechi, R. C.; Capasso, F.; Whitesides, G. M. Fabrication of Arrays of Metal and Metal Oxide Nanotubes by Shadow Evaporation. *ACS Nano* **2008**, *2* (4), 800–808.
- (172) Zhou, H.; Wong, S. S. A Facile and Mild Synthesis of 1-D ZnO, CuO, and  $\alpha$ -Fe<sub>2</sub>O<sub>3</sub> Nanostructures and Nanostructured Arrays. *ACS Nano* **2008**, *2* (5), 944–958.
- (173) Borissov, D.; Isik-Uppenkamp, S.; Rohwerder, M. Fabrication of Iron Nanowire Arrays by Electrodeposition into Porous Alumina. *J. Phys. Chem. C* **2009**, *113* (8), 3133–3138.
- (174) Xu, C. W.; Wang, H.; Shen, P. K.; Jiang, S. P. Highly Ordered Pd Nanowire Arrays as Effective Electrocatalysts for Ethanol Oxidation in Direct Alcohol Fuel Cells. *Adv. Mater.* **2007**, *19* (23), 4256–4259.
- (175) Dang, H.; Singh, V.; Rajaputra, S.; Guduru, S.; Chen, J.; Nadimpally, B. Cadmium Sulfide Nanowire Arrays for Window Layer Applications in Solar Cells. *Sol. Energy Mater. Sol. Cells* **2014**, *126*, 184–191.
- (176) Liu, Y.; Goebel, J.; Yin, Y. Templated Synthesis of Nanostructured Materials. *Chem. Soc. Rev.* **2013**, *42* (7), 2610–2653.
- (177) Surwade, S. P.; Zhou, F.; Wei, B.; Sun, W.; Powell, A.; O'Donnell, C.; Yin, P.; Liu, H. Nanoscale Growth and Patterning of Inorganic Oxides Using DNA Nanostructure Templates. *J. Am. Chem. Soc.* **2013**, *135* (18), 6778–6781.
- (178) Carter, J. D.; LaBean, T. H. Organization of Inorganic Nanomaterials via Programmable DNA Self-Assembly and Peptide Molecular Recognition. *ACS Nano* **2011**, *5* (3), 2200–2205.
- (179) Li, Z.; Xu, Z.; Wang, H.; Ding, J.; Zahiri, B.; Holt, C. M. B.; Tan, X.; Mitlin, D. Colossal Pseudocapacitance in a High Functionality–high Surface Area Carbon Anode Doubles the Energy of an Asymmetric Supercapacitor. *Energy Environ. Sci.* **2014**, *7* (5), 1708–1718.
- (180) Fei, X.; Li, W.; Shao, Z.; Seeger, S.; Zhao, D.; Chen, X. Protein Biomaterialized Nanoporous Inorganic Mesocrystals with Tunable

Hierarchical Nanostructures. *J. Am. Chem. Soc.* **2014**, *136* (44), 15781–15786.

- (181) Nam, K. T.; Kim, D.-W.; Yoo, P. J.; Chiang, C.-Y.; Meethong, N.; Hammond, P. T.; Chiang, Y.-M.; Belcher, A. M. Virus-Enabled Synthesis and Assembly of Nanowires for Lithium Ion Battery Electrodes. *Science* **2006**, *312* (5775), 885–888.
- (182) Royston, E.; Ghosh, A.; Kofinas, P.; Harris, M. T.; Culver, J. N. Self-Assembly of Virus-Structured High Surface Area Nanomaterials and Their Application as Battery Electrodes. *Langmuir* **2008**, *24* (3), 906–912.
- (183) Tsukamoto, R.; Muraoka, M.; Seki, M.; Tabata, H.; Yamashita, I. Synthesis of CoPt and FePt<sub>3</sub> Nanowires Using the Central Channel of Tobacco Mosaic Virus as a Biotemplate. *Chem. Mater.* **2007**, *19* (10), 2389–2391.
- (184) Schnepf, Z.; Yang, W.; Antonietti, M.; Giordano, C. Biotemplating of Metal Carbide Microstructures: The Magnetic Leaf. *Angew. Chem. Int. Ed.* **2010**, *49* (37), 6564–6566.
- (185) Li, X.; Fan, T.; Zhou, H.; Chow, S.-K.; Zhang, W.; Zhang, D.; Guo, Q.; Ogawa, H. Enhanced Light-Harvesting and Photocatalytic Properties in Morph-TiO<sub>2</sub> from Green-Leaf Biotemplates. *Adv. Funct. Mater.* **2009**, *19* (1), 45–56.
- (186) Behrens, S. S. Synthesis of Inorganic Nanomaterials Mediated by Protein Assemblies. *J. Mater. Chem.* **2008**, *18* (32), 3788–3798.

# 2 Biotemplated $\alpha$ -Fe<sub>2</sub>O<sub>3</sub>/CuFe<sub>2</sub>O<sub>4</sub> Leaves for Z-Scheme Water Splitting

## 2.1 Introduction

### 2.1.1 Potential of $\alpha$ -Fe<sub>2</sub>O<sub>3</sub> for photocatalytic water oxidation

In the search for ideal metal oxide semiconductors for photocatalytic water oxidation, hematite ( $\alpha$ -Fe<sub>2</sub>O<sub>3</sub>) appears, at least in theory, to be an ideal semiconductor. Unlike the UV-only semiconductors commonly studied for photocatalysis (TiO<sub>2</sub>, ZnO), it has an indirect bandgap reported around 2.1–2.2 eV,<sup>1–3</sup> meaning that it can achieve a theoretical solar-to-hydrogen conversion efficiency of 12.9% under AM1.5 sunlight, when linked in tandem with another photoelectrode for hydrogen evolution,<sup>4,5</sup> equivalent to a photocurrent density of 12.6 mA/cm<sup>2</sup>. Furthermore,  $\alpha$ -Fe<sub>2</sub>O<sub>3</sub> is stable under basic photocatalytic conditions and will not degrade when used for water oxidation.<sup>5,6</sup> Finally iron is plentiful, making the mass production and implementation of any potential  $\alpha$ -Fe<sub>2</sub>O<sub>3</sub> electrode system economical. However,  $\alpha$ -Fe<sub>2</sub>O<sub>3</sub> also has severe limitations that have thus far prevented it from being fully developed as a photoelectrode material.<sup>5</sup> Specifically, (1) it has poor kinetics for water splitting, now believed to be due to surface states;<sup>7–9</sup> (2) it has poor charge carrier conductivity, preventing the efficient separation of electron-hole pairs;<sup>10,11</sup> (3) it has a short exciton diffusion length of 2–4 nm, meaning that excitons must be generated within an extremely short

distance of a water molecule for successful catalytic transformation;<sup>2</sup> (4) it has an indirect bandgap, meaning that it requires a greater volume of material to absorb light;<sup>1-3</sup> and finally, (5) the conduction band position of  $\alpha$ -Fe<sub>2</sub>O<sub>3</sub> is not sufficiently negative to be able to reduce protons to H<sub>2</sub>, requiring that a second photoelectrode be used in tandem with  $\alpha$ -Fe<sub>2</sub>O<sub>3</sub> electrodes.<sup>4,5</sup> While the last problem could be solved in conjunction with a tandem second semiconductor, the first four problems are more fundamental in nature and attempts to work around such deficiencies have focused on nanostructuring,<sup>10,12-16</sup> doping,<sup>12,16-20</sup> surface treatments,<sup>8,12,21-25</sup> and catalyst functionalization.<sup>26-28</sup>

### **2.1.2 Water Splitting in Nature**

In the design of efficient water splitting systems, one source of inspiration is nature itself. Photosynthetic organisms use photocatalytic water oxidation to generate free electrons to store energy in the form of glucose.<sup>29</sup> This process, which has been described as a “Z-scheme”,<sup>30</sup> involves the photo-excitation of electrons in two spatially separated reaction complexes called photosystems that are then used to reduce biological electron carriers. These electron carriers move between photosystems before eventually being stored in the form of carbohydrates for energy storage. Similar to natural Z-schemes, inorganic heterojunctions composed of two different semiconductors in direct contact have been demonstrated across a wide variety of materials, with the main difference from their biological counterparts being that the second photoelectrochemical reaction is the reduction of protons to hydrogen gas as opposed to the reduction of organic molecules.<sup>31-36</sup>

In addition to basic photosynthetic pathways, certain plants, known as C4 plants, have evolved chemical pathways and specialized physical structures to carry out specific tasks during photosynthesis as well as increase the amount of light absorbed, improving the efficiency of this process.<sup>37,38</sup> Despite the fact that most plant leaves are typically microns thick, there is nonetheless enough transparency to allow most light to reach the reaction centers. The biotemplating of TiO<sub>2</sub> onto a leaf structure has already been reported using sugarcane, a model C4 plant species, suggesting that other semiconductor materials could also utilize this approach.<sup>38,39</sup>

### **2.1.3 Inorganic Z-schemes based on ferrites**

A z-scheme-style dual light absorber approach holds promise for photocatalytic water splitting because a dual absorber system can absorb a greater portion of the solar spectrum, raising ideal efficiencies from 30% for a single absorber to 41% for a dual absorber.<sup>40</sup> This approach is especially important for semiconductor materials like  $\alpha$ -Fe<sub>2</sub>O<sub>3</sub>, which cannot carry out photocatalytic water splitting given its insufficiently positive conduction band. For such materials, a form of electron drain is required, either to utilize the free electrons in a corresponding reaction or to remove the electrons to a secondary electrode where they can be used within another reaction. One potential class of compounds that are potential H<sub>2</sub> evolution photocatalysis is ferrites, iron-containing compounds with the generic formula MFe<sub>2</sub>O<sub>4</sub>. Currently, calcium, copper, and zinc ferrites have all been tested for potential H<sub>2</sub> evolution activity and each of these compounds have more negative band potentials than  $\alpha$ -Fe<sub>2</sub>O<sub>3</sub>.<sup>25,41,42</sup> In this study, copper ferrite (CuFe<sub>2</sub>O<sub>4</sub>) was

selected as the second Z-scheme absorber due to its relative ease of synthesis and the abundance of copper.<sup>42</sup>  $\text{CuFe}_2\text{O}_4$  can be synthesized by placing copper in close proximity with  $\alpha\text{-Fe}_2\text{O}_3$ , and then heating the copper and  $\alpha\text{-Fe}_2\text{O}_3$  at sufficiently high temperatures.<sup>43</sup> The appeal of ferrites in the case of an  $\alpha\text{-Fe}_2\text{O}_3$ -based Z-scheme is that a ferrite could be potentially synthesized directly from the photoanode material.

This chapter discusses attempts to make a water splitting heterojunction both by nanostructuring  $\alpha\text{-Fe}_2\text{O}_3$  and then subsequently functionalizing the surface of the nanostructure with a second semiconductor,  $\text{CuFe}_2\text{O}_4$ , to accomplish complete water splitting. Catalyst nanoparticles were then applied to the surface of the superstructure. A diagram of the final heterojunction is represented in Figure 2.1.

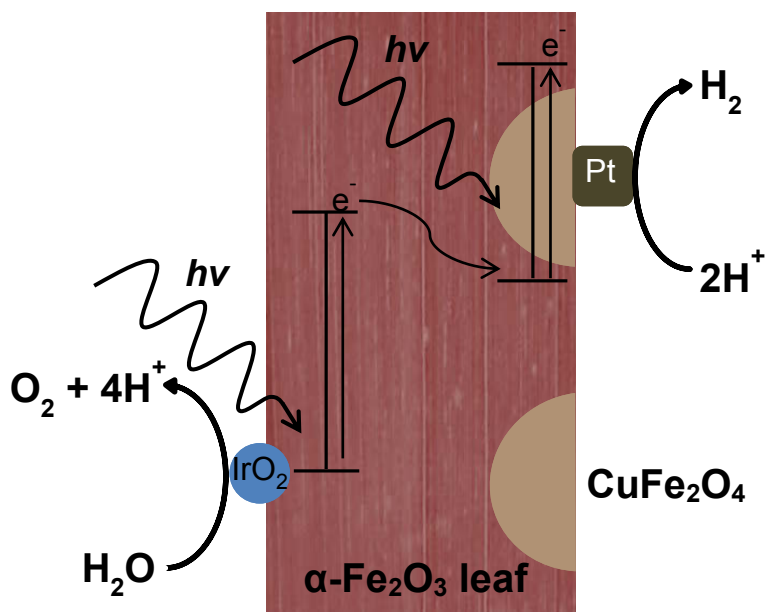


Figure 2.1. Diagram of proposed Z-scheme. The  $\alpha\text{-Fe}_2\text{O}_3$ , templated from a sugarcane leaf, carries out photocatalytic water oxidation and is directly in contact with regions of  $\text{CuFe}_2\text{O}_4$ . The  $\text{CuFe}_2\text{O}_4$  uses the separated electrons from the  $\alpha\text{-Fe}_2\text{O}_3$  and light to reduce protons to hydrogen gas. The  $\alpha\text{-Fe}_2\text{O}_3$  and  $\text{CuFe}_2\text{O}_4$  are functionalized with iridium oxide and platinum nanoparticle catalysts, respectively.

## 2.2 Results

### 2.2.1 Synthesis of nanostructured leaf

The objective of this study was to synthesize biotemplated iron oxide leaves by modifying the strategy demonstrated by Li et al.<sup>38</sup> for making TiO<sub>2</sub> leaves. Most of the steps in the process remained conceptually identical (i.e. selection of sol-gel precursor), but several changes were introduced. First, instead of using a dual-step metallization where metal centers naturally in leaves were replaced by the desired metal followed by infiltration of an iron oxide sol-gel precursor, these two steps were combined into one by soaking leaves in a solution of anhydrous FeCl<sub>3</sub> in ethanol. This change reduced the overall time required for the process. Second, the leaves were first dipped in chloroform to remove the waxy external leaf layer, which was found to improve infiltration of FeCl<sub>3</sub>.<sup>44</sup>

Briefly, the steps are as follows: first, the leaves were preserved by fixation in 2% glutaraldehyde in phosphate buffer (pH 7.2) at 4°C for 12 hours. Afterwards, the leaves were rinsed with and kept in de-ionized water at 4°C for weeks at a time. When the time came for the leaves to be utilized, they were first placed in 5% HCl for 3 hours to remove contaminant metals naturally in leaves, like Mg, Mn, Ca etc. so that they would not dope the final leaf product. As a result, the green leaves turned yellow. Next, the leaves were dehydrated to remove as much water as possible by applying increasing concentrations of ethanol in water for 20 minutes at each concentration. It is important to remove as much water as possible because it is a hydrolysis agent for metal oxide sol-gel precursors.<sup>45,46</sup> Next, the dehydrated leaves were placed in a 0.2 M solution of FeCl<sub>3</sub> in anhydrous ethanol under vacuum

for 18 hours. This solution served as the sol-gel precursor. Finally, the leaves were allowed to hydrolyze in a wet chamber to hydrolyze the sol precursor into a metal oxide network, before calcination under a slow ramp in temperature up to 500°C followed by a rapid heating step at 800°C. The final leaf products were a red-brown colour (Figure 2.2a).

In order to compare the metallized leaves with the original precursor, we performed SEM on the original and final leaf products. In comparing the thicknesses of the leaves before and after metallization, it can be seen that the leaves lost about two thirds of their original thickness after calcination, shrinking from ~200  $\mu\text{m}$  to ~75  $\mu\text{m}$  (Figure 2.2b,c). Despite the considerable shrinkage that took place during processing, the internal structure of the leaves remained intact and individual leaf veins could still be distinguished (Figure 2.2d). Since most of these structures are built around individual cell walls which are in turn composed of structural carbohydrates,<sup>38</sup> it would appear that the cell walls of the original leaves are the main features preserved during the conversion process. Interestingly, when these new iron oxide structures were examined in closer detail, they were found to be porous and composed of multiple smaller iron oxide nanoparticles in contact with each other (Figure 2.2e). The size of these nanoparticles ranges from 50 to 100 nm (Figure 2.2f), which suggests that this process yields larger particle sizes than other processes reported for synthesizing  $\alpha\text{-Fe}_2\text{O}_3$  electrodes.<sup>10,14-16</sup> Based on the physiology of sugarcane leaves, it would appear that these plant channels represent individual plant cells, which form long channels in plant leaves.<sup>38,47,48</sup> Therefore, the use of iron oxide sol-gel precursors has preserved much of the leaf structure.

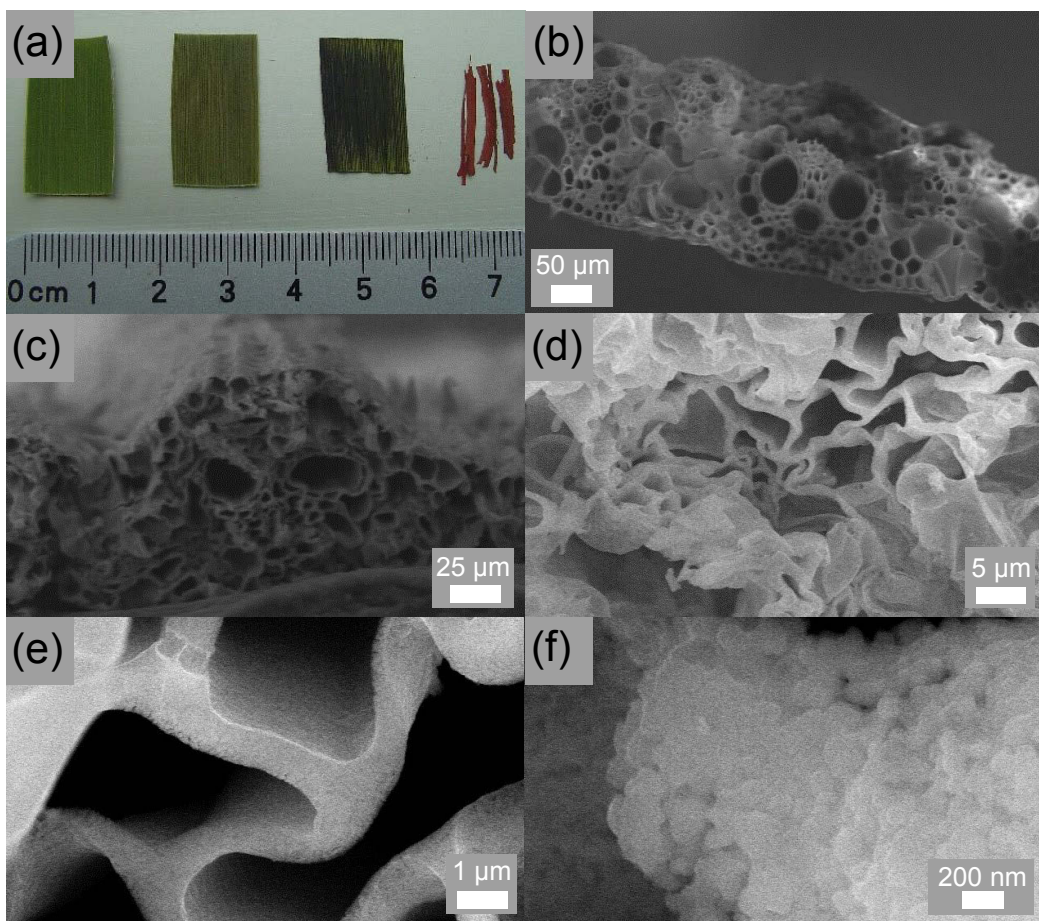


Figure 2.2. (a) Photograph of the leaf at different stages; from left to right, fixed, HCl-soaked, FeCl<sub>3</sub>-soaked, and final calcined metal oxide leaves. (b) Electron micrograph of a fixed leaf. (c-f) Scanning electron micrographs of iron oxide leaves at increasing magnifications to show preserved superstructure as well as lower level structures.

The effectiveness of the biotemplating can be explained by the steps leading to the formation and infiltration of the precursor. When FeCl<sub>3</sub> was added to excess anhydrous ethanol, vapour was instantly formed. When the steam was exposed to pH paper, the pH paper turned red, suggesting that the vapour contained acidic molecules such as HCl. Given that the synthesis of pure iron (III) ethoxide is difficult under ambient conditions, it is unlikely that this alkoxide would be the

product.<sup>49,50</sup> However, it is unlikely that  $\text{Fe}(\text{OH})_6^{3+}$  was the product as the ethanolic  $\text{FeCl}_3$  solution did not condense into a gel when left sealed in air over the course of several months. The presence of any significant amount of water in a sol precursor can limit the stability of the sol due to hydrolysis to form Fe-O-Fe bonds.<sup>45</sup> Therefore, the precursor was likely a mix of ferric iron bound to any mixture of chloride, ethoxide, or hydroxide groups. With insufficient hydroxide to carry out further Fe-O-Fe bond formation, the ultimate hydrolyzing agent in the formation of the leaf must have been derived from the plant structure. As in the case of the  $\text{TiO}_2$  leaf, the ability to form highly reproducible metallic replicas of plant structures is due to the presence of hydroxyl-rich carbohydrates in the structure of the plant.<sup>38</sup>

This hypothesis that pre-hydrolysis affects infiltration and nanoparticle formation can be tested by using a sol-gel precursor that contains large amounts of water. When hydrated iron nitrate ( $\text{Fe}(\text{NO}_3)_3 \cdot 9\text{H}_2\text{O}$ ) was used as the iron precursor, the infiltration of the leaves was heavily concentrated close to either cut edge of the leaf, while the middle of the leaves was a much lighter colour, suggesting poor infiltration. The significantly increased presence of water in the iron precursor solution resulted in the formation of  $\text{Fe}(\text{OH})_6^{3+}$ ,<sup>51</sup> which interacts more strongly with carbohydrate hydroxyl groups through hydrogen bonding and electrostatic interactions than the ethoxide-containing precursor formed in anhydrous conditions, resulting in more limited infiltration. In addition, when these leaves were examined under SEM, they contained notably particulate features compared to leaves prepared from anhydrous precursors (Figure 2.3). Since the major difference between this and previous samples is the presence of water, it is likely

that the precursor molecules prematurely hydrolyze and form Fe-O-Fe bonds between molecules that are not associated with the carbohydrate structure. This hydrolysis results in the formation of nanoparticles, which in turn affects how the metal oxide template is formed. Therefore, the use of an anhydrous ethanolic iron precursor improved infiltration and limited premature hydrolysis of the precursor, resulting in smoother features but also more conformal infiltration.

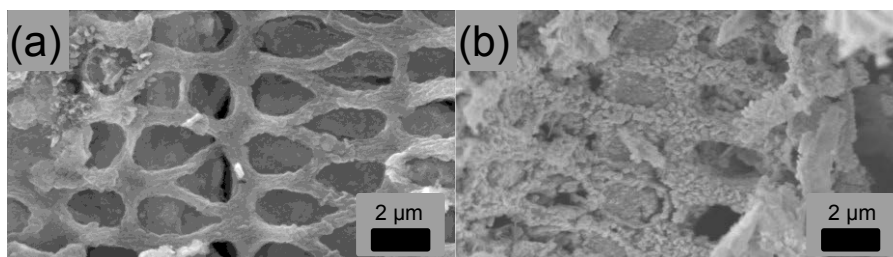


Figure 2.3. (a) Scanning electron micrograph of a leaf synthesized with anhydrous  $\text{FeCl}_3$  precursor. (b) Scanning electron micrograph of a leaf synthesized with  $\text{Fe}(\text{NO}_3)_3 \cdot 6\text{H}_2\text{O}$  precursor. The region shown in both leaves is believed to be a xylem channel.

X-ray photoelectron spectroscopy (XPS) was used to examine the composition of the leaves (Figure 2.4). The main elements detected were iron and oxygen, the former of which corresponded to peak positions for the most oxidized trivalent form of iron.<sup>52</sup> Survey scans on the entire range of binding energies also revealed minimal contamination from elements that would normally be found in large quantities in biological tissue, such as Na, Ca, K, or Cl.<sup>38</sup> The C1s peak could be traced to adventitious carbon, as a combustion analysis demonstrated that the sample had minimal remaining carbon after high temperature calcination. The  $\text{Si}_{2p}$  and  $\text{Si}_{2s}$  peaks were present due to the silicon substrates used for mounting. In

summary, this modified procedure for coating leaves with an iron precursor, followed by calcination, is effective at creating iron oxide copies of plant substrates.

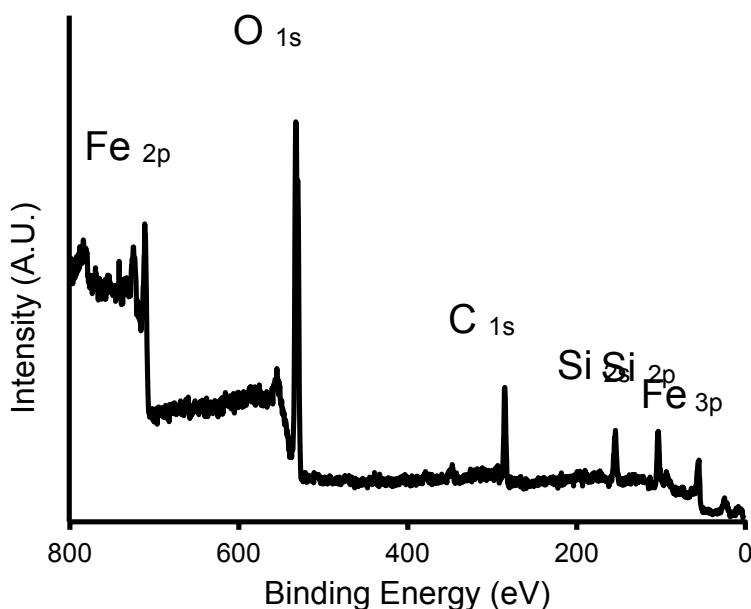


Figure 2.4. XPS survey scan of an iron oxide leaf mounted on a silicon substrate with major peaks and complexes labeled.

### 2.2.2 Synthesis of $\alpha$ - $\text{Fe}_2\text{O}_3$ / $\text{CuFe}_2\text{O}_4$ heterojunction

Having successfully synthesized the iron oxide leaf, the next step was to form a second semiconductor in intimate contact with the iron oxide. The selected approach was to attach copper nanoparticles to the surface of the leaves via organic linker molecule followed by heating at high temperatures to oxidize the copper and sinter it into the iron oxide superstructure (Figure 2.5). The full procedure is as follows: first, the iron oxide is immersed in a solution of 16-mercaptohexadecanoic acid (16-MHA) in chloroform. This simple procedure has been shown to effectively functionalize the  $\gamma$ - $\text{Fe}_2\text{O}_3$  with a monolayer of 16-MHA.<sup>53</sup> The thiol functional group was selected for the high binding affinity of thiols to metals and can

specifically bind copper.<sup>54,55</sup> Once washed with excess chloroform, the iron oxide is placed in a solution of the copper nanoparticles in hexane. After a final hexane wash step, the iron oxide is heated at 850°C for 3 hours to sinter the copper into the iron oxide and form CuFe<sub>2</sub>O<sub>4</sub>.

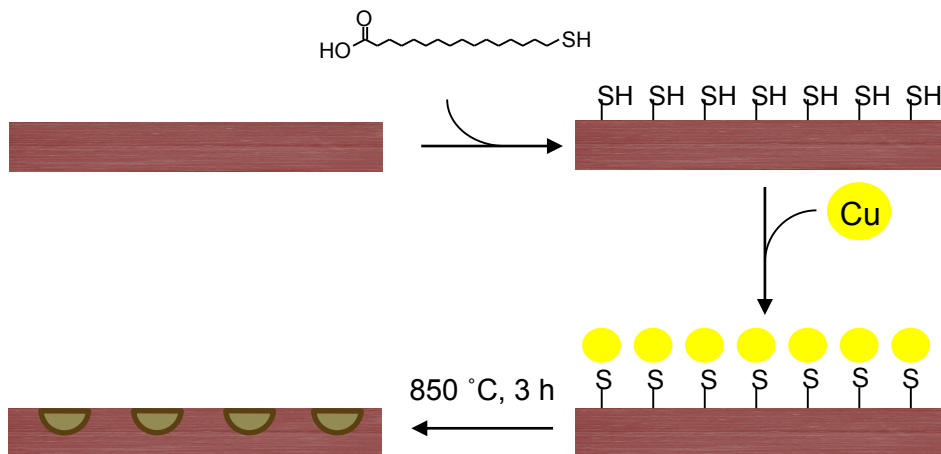
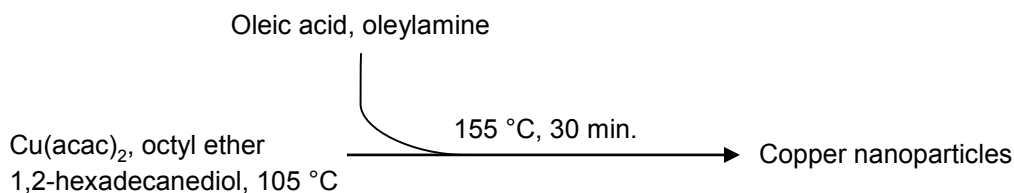


Figure 2.5 Schematic for synthesis of  $\alpha$ -Fe<sub>2</sub>O<sub>3</sub>/CuFe<sub>2</sub>O<sub>4</sub> leaf. The  $\alpha$ -Fe<sub>2</sub>O<sub>3</sub> leaf is first exposed to 3 mM 16-MHA, resulting in a leaf with exposed thiols. The thiols in turn bind the copper nanoparticles. Finally, the entire structure is heated at 850°C for 3 hours to form CuFe<sub>2</sub>O<sub>4</sub>.

The nanoparticles were synthesized via thermolysis of copper acetylacetonate in the presence of reducing and capping agents via the following reaction:



The product, a yellow, hexane-soluble solution of nanoparticles between 10 – 20 nm in diameter (Figure 2.6a), was similar to the nanoparticles previously reported with this procedure.<sup>56</sup> However, XPS analysis of the nanoparticles cast on a silicon surface revealed that, while the Cu 2p spectra was similar to that of metallic copper or Cu<sub>2</sub>O (Figure 2.6b), the position of the LMM Auger emission line was more similar to that of a copper oxide than of metallic copper (Figure 2.6c).<sup>57</sup> Cu<sup>+</sup> and Cu<sup>2+</sup> cannot be distinguished using XPS. Therefore, a modified Auger parameter (MAP) is used, where the MAP is the value of the Cu LMM peak position added to the strongest copper peak position. The MAP of these nanoparticles was found to be 1849.4 eV, closer to the MAP value of Cu<sub>2</sub>O than the values of Cu (1851.3) and CuO (1851.4).<sup>58</sup> Therefore, the copper is partially oxidized, potentially arising from oleic acid capping ligand.<sup>55</sup>

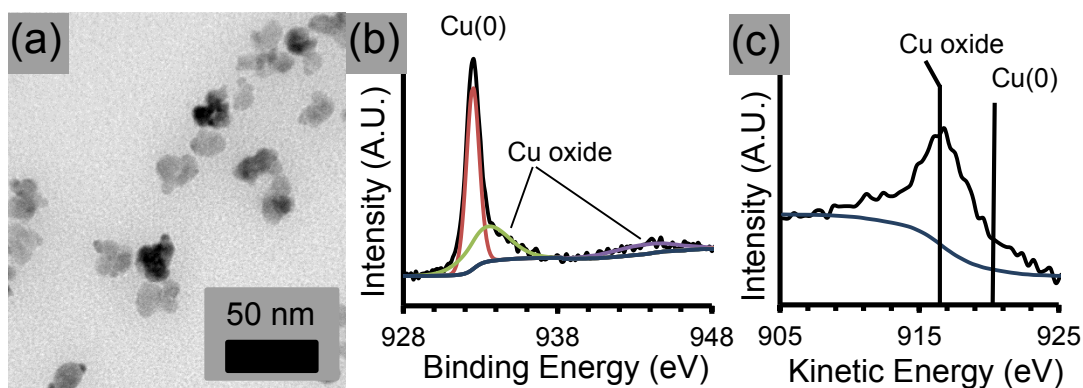


Figure 2.6 (a) Transmission electron micrograph of copper nanoparticles synthesized by thermolysis of copper (II) acetylacetonate. (b) XPS spectra of the Cu 2p<sub>3/2</sub> region of copper nanoparticles dropped on a silicon slide. (c) XPS spectra of the Cu LLM Auger electron region as an identifier of Cu valence state.

Attempts to visualize the copper nanoparticles on the leaf surface via SEM were hindered by the rough surface and poor conductivity of the iron oxide superstructure. Therefore, surface functionalization was first tested on silicon slides of  $\alpha$ -Fe<sub>2</sub>O<sub>3</sub> produced by drop-coating FeCl<sub>3</sub> dissolved in ethanol and heated at 500 °C.<sup>59</sup> This procedure serves as an effective method to generate  $\alpha$ -Fe<sub>2</sub>O<sub>3</sub> surfaces for a variety of characterization purposes. After the functionalization procedure described above, the slides were visualized under SEM, revealing that the entire surface of the  $\alpha$ -Fe<sub>2</sub>O<sub>3</sub> slides was covered with copper nanoparticles (Figures 2.7a, b). Without the use of 16-MHA, copper nanoparticles did not bind as well to the iron oxide surface (Figures 2.7c, d). To confirm that binding was not mediated by interactions between organic groups, oleic acid was used instead of 16-MHA as a linker during the first functionalization step. When exposed to a solution of copper nanoparticles, oleic acid-adhered slides bound the nanoparticles poorly.

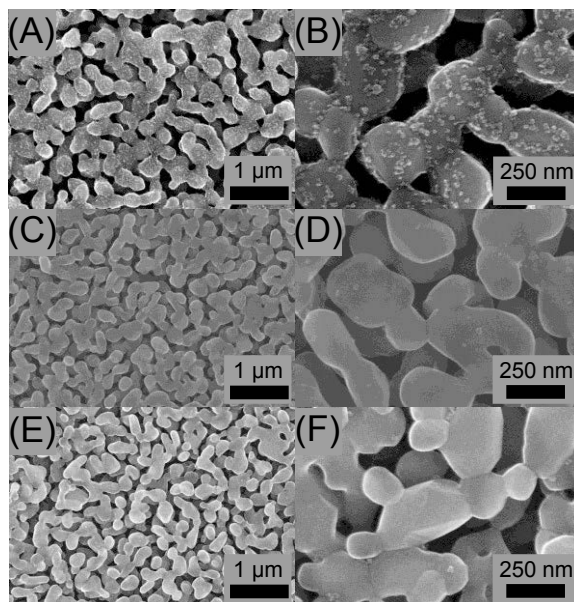


Figure 2.7 Scanning electron micrographs of  $\alpha$ -Fe<sub>2</sub>O<sub>3</sub> slides functionalized with different linkers followed by copper nanoparticles. (a) 16-MHA; (b) 16-MHA, high-resolution; (c) no linker; (d) no linker, high-resolution; (e) oleic acid; (f) oleic acid, high-resolution.

This procedure was repeated on the leaves. To ensure that functionalization proceeded as intended, confirmation of each step was provided using diffuse reflectance infrared fourier transform spectroscopy (DRIFTS) (Figure 2.8). In particular, the increasing presence of organic CH<sub>2</sub> and OH groups was expected to be seen in the FTIR spectrum, due to the strong absorption of these groups as well as their presence as a monolayer on the high surface area iron oxide substrate. Indeed, bare iron oxide leaves had little binding in these regions, as any organics and adsorbed water molecules would be eliminated well below 800°C. Upon 16-MHA functionalization, distinct CH<sub>2</sub> stretching peaks and a broad OH region were noticed, corresponding to the presence of the linker. The FTIR scan of the copper-functionalized leaf included larger CH<sub>2</sub> and OH peaks as well as the appearance of a CH<sub>3</sub> stretching peak due to oleic acid and oleylamine on the surface of the copper nanoparticles. The weak thiol stretch was not seen in any of these experiments.

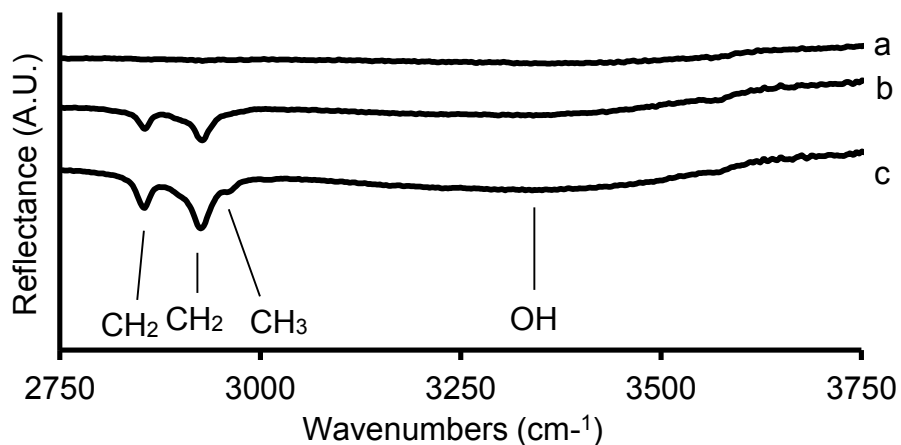


Figure 2.8 DRIFTS spectra of the CH<sub>2</sub>/CH<sub>3</sub> and -OH absorbing regions of (a) bare iron oxide leaves, (b) 16-MHA functionalized iron oxide leaves, and (c) copper nanoparticle/16-MHA functionalized leaves.

To confirm the findings of FTIR, the presence of copper was confirmed using X-ray photoelectron spectroscopy (XPS) (Figure 2.9). Spectra were acquired for leaves with 16-MHA/copper nanoparticle functionalization. The Cu  $2p$  spectra of the copper-containing leaves corresponded to the spectra for metallic Cu<sup>0</sup>, confirming that the copper nanoparticles had been successfully bound onto the iron oxide surface.<sup>60</sup> As a control study, leaves were functionalized with copper nanoparticles without linker molecules. Interestingly, while copper nanoparticle functionalization was still possible without 16-MHA, the amount of copper bound to the surface of the leaf was reduced by half, suggesting that the linker had a critical role in increasing the loading of the nanoparticles on the surface of the leaves. Finally, the leaves were heated at 850°C to remove the linkers, sinter and oxidize the copper, and form CuFe<sub>2</sub>O<sub>4</sub> according to the recommendations of copper-iron-oxygen phase studies.<sup>43</sup> After the heating step had been performed, the presence of copper was found to have been lessened, suggesting that the presence of copper on the surface of the leaves was reduced as a result of the heating step. The reduced presence of Cu limited the ability to collect the LMM peak, but the oxide peaks were sufficiently large that the copper was definitely oxidized.<sup>60</sup>

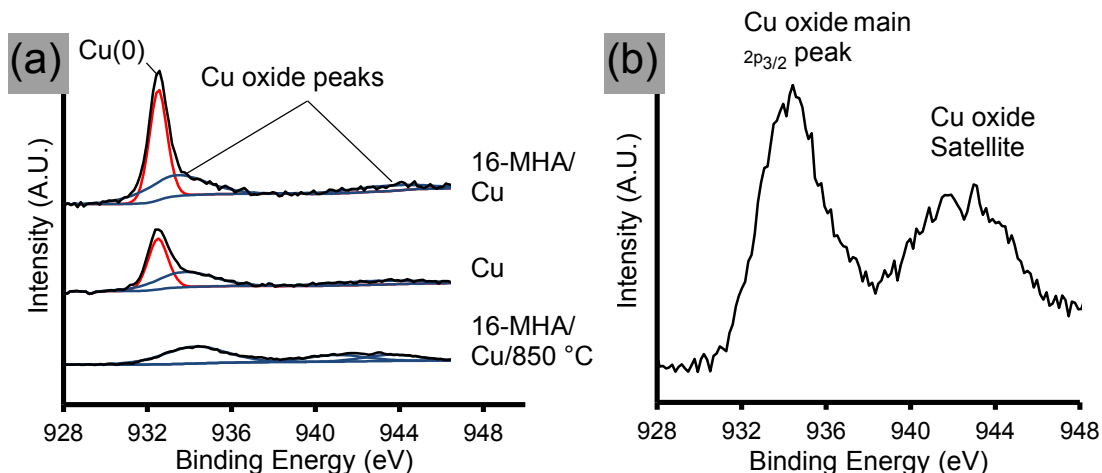


Figure 2.9 (a) Cu  $2p_{3/2}$  XPS of (top to bottom) 16-MHA/copper nanoparticle-functionalized leaf, copper nanoparticle-functionalized leaf with no 16-MHA linker, and 16-MHA/copper nanoparticle-functionalized leaf heated to 850 °C for 3 hours. Red trace corresponds to metallic copper, while blue corresponds to Cu<sup>2+</sup>. (b) Close-up of Cu  $2p_{3/2}$  XPS for heated leaf.

To demonstrate that heating at 850 °C did not result in the removal of copper from the surface of the iron oxide, Auger electron spectroscopy (AES) mapping was performed on iron oxide slides functionalized with 16-MHA and copper nanoparticles and heated to 850 °C for 3 hours (Figure 2.10a, b). Copper was found to be distributed on the surface of the slides, suggesting conformal functionalization and retention (Figure 2.10c). Therefore, it seems unlikely that copper would be somehow removed from the system during heating. Potentially, the reduced XPS presence of copper may be explained by sintering into the structure of the leaves.

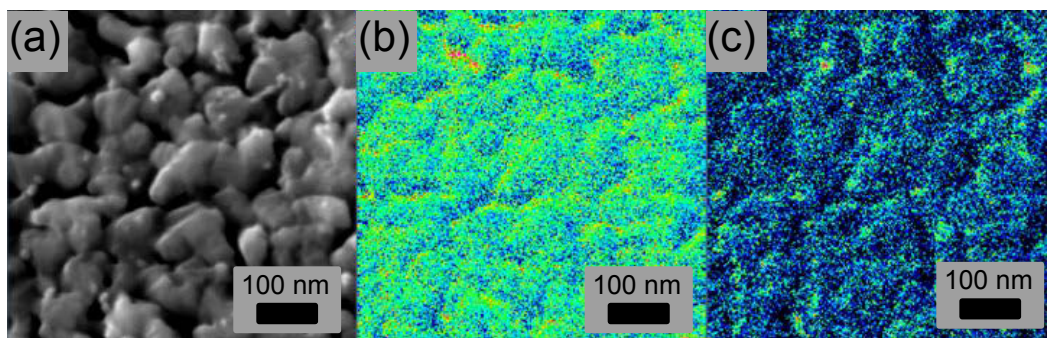


Figure 2.10 Auger electron mapping of an  $\alpha$ -Fe<sub>2</sub>O<sub>3</sub> slide that has been functionalized with copper nanoparticles and heated to 850°C for 3 hours. (a) Micrograph of region of interest, (b) signal map for iron Auger electrons, and (c) signal map for copper Auger electrons.

As the ultimate confirmation of the formation of the phases in the proposed heterojunction, powder X-ray diffraction (PXRD) on both the iron oxide leaves as well as the copper-sintered iron oxide leaf superstructure was performed. Diffraction was also important in confirming that heat had effectively formed the CuFe<sub>2</sub>O<sub>4</sub>, as opposed to simply destroying the linker between the copper and the leaf. Even though phase studies had clearly suggested that this treatment forms  $\alpha$ -Fe<sub>2</sub>O<sub>3</sub>, the XRD, lacking other iron oxide phases, clearly confirms that  $\alpha$ -Fe<sub>2</sub>O<sub>3</sub> is the only present phase of iron oxide (Figure 2.11a). If the original  $\alpha$ -Fe<sub>2</sub>O<sub>3</sub> pattern is overlaid on the pattern of the final structure, there are small diffraction peaks that can be noted in the  $28^\circ \leq 2\theta \leq 42^\circ$  region where CuFe<sub>2</sub>O<sub>4</sub> and  $\alpha$ -Fe<sub>2</sub>O<sub>3</sub> share many of their diffraction peaks (Figure 2.11b). The three most notable differences between the two scans correspond to CuFe<sub>2</sub>O<sub>4</sub>, confirming that the ferrite is present in the leaf. Furthermore, based on the relative peak heights of the two materials, the presence of CuFe<sub>2</sub>O<sub>4</sub> is one-fifth that of the  $\alpha$ -Fe<sub>2</sub>O<sub>3</sub>.

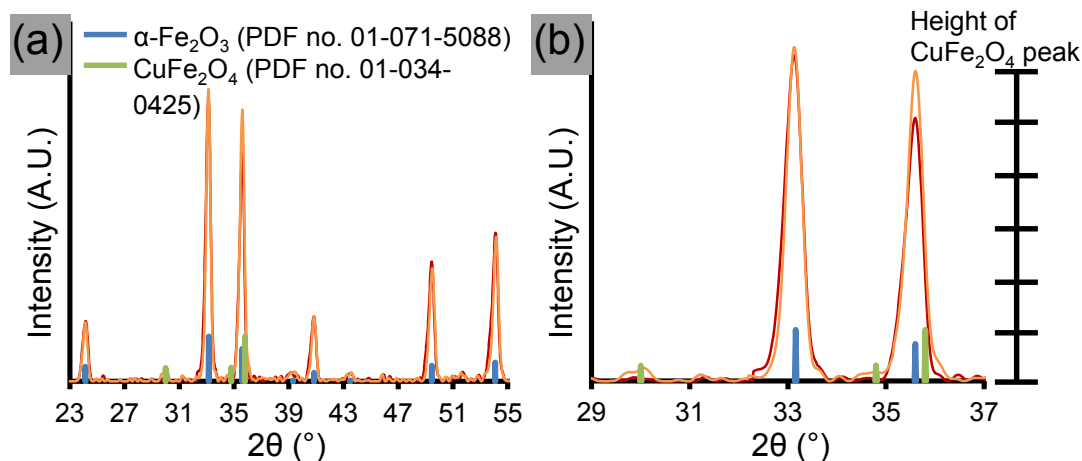


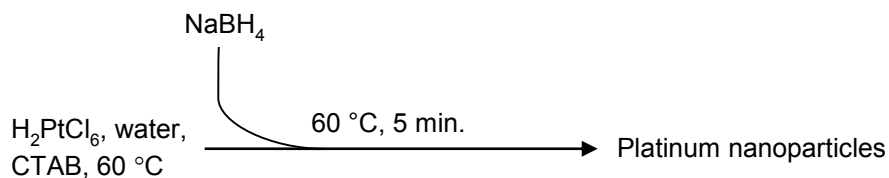
Figure 2.11 (A) Powder x-ray diffraction patterns of iron oxide leaves (red) and 16-MHA/copper functionalized and heated (850 °C, 3 hours) leaves (orange). (B) Close up of the  $29^\circ < 2\theta < 37^\circ$  region where the  $\text{CuFe}_2\text{O}_4$  peaks can be seen.

The final step was to attempt photocatalytic water splitting. The  $\alpha\text{-Fe}_2\text{O}_3/\text{CuFe}_2\text{O}_4$  leaves were suspended at a concentration of 2 mg/mL in a 2 mL non-quartz glass vial of de-ionized water and illuminated under a 500 W Xe chromatography vial while stirring for 8 hours. Gas evolution was measured using headspace injections. No  $\text{H}_2$  was initially detected, suggesting that the leaf had poor activity for overall water splitting. Even when the reaction conditions were varied such that triethanolamine was utilized as a hole scavenger at high concentrations (10% v/v, respectively), no  $\text{H}_2$  was detected.  $\text{O}_2$  detection was not attempted as headspace injections allow for the possibility of atmospheric contamination.

### 2.2.3 Functionalization of $\alpha\text{-Fe}_2\text{O}_3/\text{CuFe}_2\text{O}_4$ Z-scheme with catalyst particles

In an attempt to increase the activity of both oxygen and hydrogen evolution, the surface of the leaf was functionalized with catalysts for both reactions. Iridium oxide nanoparticles are one of the most effective water oxidation catalysts in acid,<sup>61</sup> and platinum has long been used as an effective hydrogen evolution catalyst.<sup>40,62</sup>

Cetyltrimethylammonium bromide (CTAB)-coated platinum nanoparticles were synthesized in water as previously reported.<sup>63</sup> The reaction scheme for the synthesis of platinum nanoparticles is as follows:



To functionalize the leaf with platinum nanoparticles, the copper nanoparticle scheme was modified. First, the CTAB ligands on the platinum nanoparticles were exchanged for oleylamine. The success of the exchange was evident by the separation of the particles into a brown hexane layer that was then washed with water until all white residue had been removed. To confirm that the copper functionalization method works for platinum nanoparticles, the nanoparticles were exposed to a surface of 16-MHA-functionalized iron oxide, resulting in the binding of platinum nanoparticles to the surface of the iron oxide slides (Figure 2.12a). Similarly, binding to the leaf structure was successful based on the strong presence of metallic platinum as assayed by XPS, with minor contribution from oxidized Pt(II) and Pt(IV) species (Figure 2.12b).<sup>64,65</sup> However, in contrast to copper nanoparticles, platinum nanoparticle adhesion to the  $\alpha$ -Fe<sub>2</sub>O<sub>3</sub> leaf surface was much more dependent on the presence of thiol as attempts to functionalize the leaves with platinum without 16-MHA yielded poor functionalization results (Figure 2.12c). Several differences between these two systems may be the reason for this. Firstly, the Pt nanoparticles are much smaller than the copper nanoparticles, allowing

washing to remove these particles much easier when trapped in a high surface area scaffold. Secondly, it may be indicative of the different affinities of thiols and stability of thiolate bonds for these two metals.<sup>66</sup> The platinum remained on the surface of the leaf and in metallic form even after heating at 500 °C to remove 16-MHA.

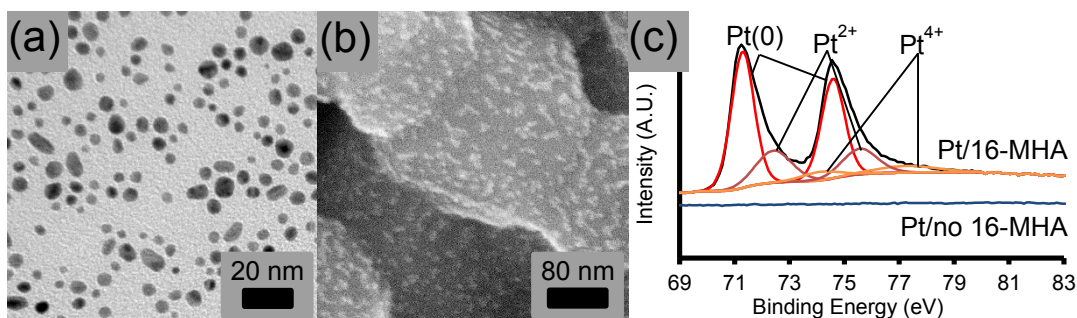
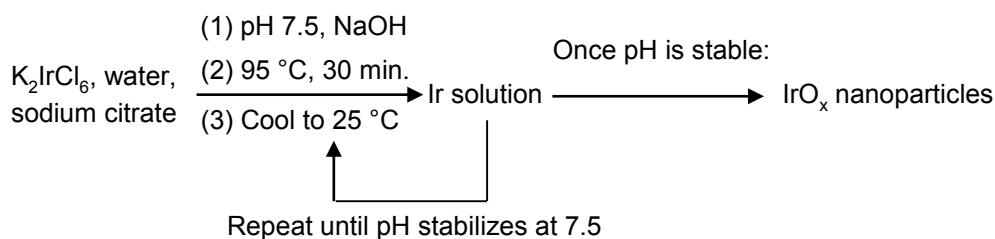


Figure 2.12 (a) Electron micrograph of oleylamine-coated platinum nanoparticles. (b) Electron micrograph of iron oxide slide functionalized with platinum nanoparticles. (c) Pt  $4f$  XPS spectra of leaf functionalized with 16-MHA and platinum nanoparticles (blue) vs. leaf functionalized only with platinum nanoparticles (black). The other coloured curves are peaks for metallic Pt (red), Pt(II) (maroon), and Pt(IV) (orange).

Citrate-capped Iridium oxide nanoparticles were synthesized using a known procedure (Figure 2.13a).<sup>67,68</sup>



Given that the negatively charged citrate should bind a positively charged surface, the pH of the particle solution was adjusted to a pH of 6 so that it was below the isoelectric point of synthetic  $\alpha\text{-Fe}_2\text{O}_3$  (8.0 – 9.0).<sup>69</sup> Imaging of the functionalized surface was even more difficult than for platinum nanoparticles due to the small size of the nanoparticles; therefore, only XPS was used to confirm that iridium oxide nanoparticle functionalization via electrostatic interaction had occurred in the leaves (Figure 2.13b). As with platinum, XPS successfully detected iridium, corresponding to the presence of the nanoparticles on the leaves.<sup>70</sup> Yet despite successful functionalization of both catalysts, photocatalytic  $\text{H}_2$  evolution was still unsuccessful.

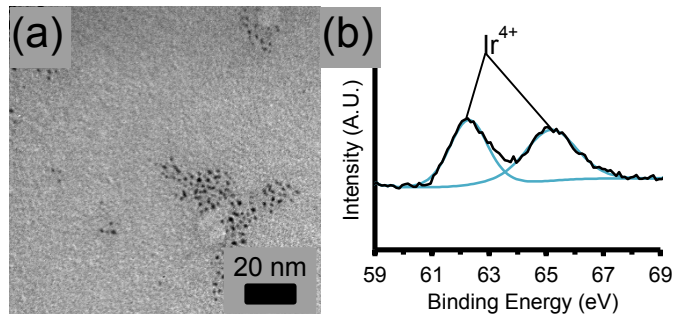


Figure 2.13 (a) Transmission electron microscopy of  $\text{IrO}_2$  nanoparticles; (b)  $\text{Ir}_{4f}$  XPS spectra of  $\text{CuFe}_2\text{O}_4/\alpha\text{-Fe}_2\text{O}_3$  leaf functionalized with  $\text{IrO}_2$  nanoparticles (black). Blue peaks correspond to  $\text{Ir}^{4+}$ .

#### 2.2.4 Studies on $\text{CuFe}_2\text{O}_4$

Since there has been limited work on the semiconductor properties of  $\text{CuFe}_2\text{O}_4$ ,<sup>71,72</sup> experiments were conducted to confirm the band positions and the potential photocatalytic activity of this material.  $\text{CuFe}_2\text{O}_4$  was synthesized via thermal decomposition of a citrate binder containing Cu:Fe ratios of 1:2 at  $850^\circ\text{C}$ .<sup>42</sup> Afterwards, the black powder was suspended in ethanol and dropped onto a

platinum disk electrode. The electrode was scanned in acetonitrile with the electrolyte tetrabutylammonium hexafluorophosphate in order to determine the conduction and valence bands of  $\text{CuFe}_2\text{O}_4$ .<sup>73</sup> These experiments confirmed that the position of the band edges were indeed similar to those previously reported with a conduction band around 3.3 eV and a valence band around 5.1 eV, ultimately corresponding to a band gap of 1.8 eV (Figure 2.14).<sup>72</sup> Therefore,  $\text{CuFe}_2\text{O}_4$  should be able to undertake water reduction resulting in the evolution of  $\text{H}_2$  gas.

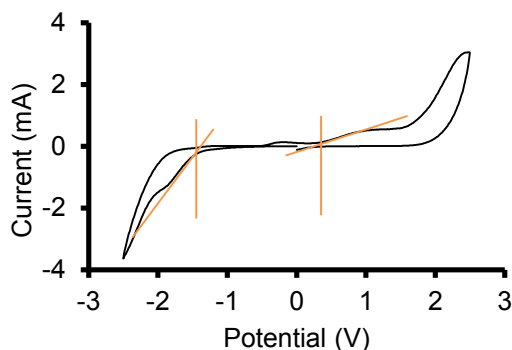


Figure 2.15 Cyclic voltammetry of  $\text{CuFe}_2\text{O}_4$  powder on platinum disc electrode in 0.1 M tetrabutylammonium hexafluorophosphate in acetonitrile. Reference electrode is  $\text{Ag}/\text{Ag}^+$ . The orange lines correspond to the intercepts where band edges would be located.

To confirm that  $\text{CuFe}_2\text{O}_4$  was indeed photocatalytic, the black powder was suspended in aqueous solutions of triethanolamine (10% v/v). The maximum amount of gas produced was 14  $\mu\text{mol}$  of  $\text{H}_2$  at a pH of 3.5 (Figure 2.15).<sup>74</sup> Furthermore, the catalytic activity was pH dependent; the amount of  $\text{H}_2$  evolved fell greatly at pH values greater and lesser than 3.5. In comparison, the  $\text{Pt}/\text{CdS}/\text{Au}/\text{TiO}_2$  system that was synthesized for comparison could generate 75  $\mu\text{mol}/\text{g}/\text{hr}$  with hole scavengers, even under 300 W Xe.<sup>75</sup>

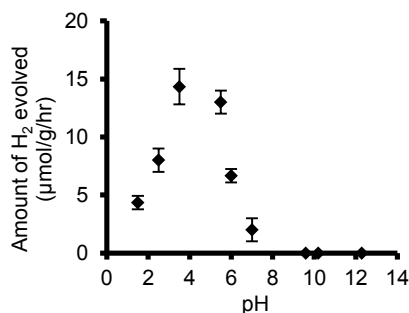


Figure 2.16 H<sub>2</sub> evolution studies of CuFe<sub>2</sub>O<sub>4</sub> powder suspended via stirring in 10% v/v triethanolamine. Irradiation time: 1 hour. Light source: 500 W Xe bulb. Catalyst concentration: 1 g/mL. Solution volume: 1 mL.

When these conditions were applied to the entire leaf, H<sub>2</sub> evolution remained undetectable and even when triethanolamine was added to the reaction solution. Therefore, the Z-scheme was incapable of fulfilling complete water splitting.

## 2.3 Conclusions

The  $\alpha$ -Fe<sub>2</sub>O<sub>3</sub>/CuFe<sub>2</sub>O<sub>4</sub> Z-scheme leaves, while synthetically successful, proved to be unsuccessful for the purpose of water splitting. I propose the following reasons for why this was the case.

Firstly, since the work was begun, several studies have been published suggesting that  $\alpha$ -Fe<sub>2</sub>O<sub>3</sub> has a complicated series of intrinsic surface states that hinder photocatalytic water oxidation,<sup>7-9</sup> even as its other optoelectronic properties can be improved. Secondly, as demonstrated here, CuFe<sub>2</sub>O<sub>4</sub> has promising optoelectronic properties, but has low activity; in comparison to other hydrogen evolution photocatalysts, it does not have high activities (although the values here are similar in magnitude to those recorded for the similar transition metal ferrite, ZnFe<sub>2</sub>O<sub>4</sub>).<sup>74</sup> Thirdly, the loading of CuFe<sub>2</sub>O<sub>4</sub> was much lower than anticipated, and

in conjunction with a relatively inactive but larger  $\alpha$ -Fe<sub>2</sub>O<sub>3</sub>, the ability to carry out water splitting was minimal. In short, the selection of two low activity photocatalysts limited the potential activity for water splitting.

Nonetheless, there are several interesting points to take away from these experiments. Firstly, it is possible to template, with high accuracy, the structure of plants using metals other than titanium with the objective of forming a metal oxide superstructure. In this report, iron was the main constituent material. Furthermore, instead of using a more time-consuming and complicated dual-precursor step as previously reported, only a single precursor step is required. Secondly, the control of hydrolysis of the sol-gel precursor can drastically affect the nanostructure of the final product, with pre-hydrolyzed precursors having rougher features than non-hydrolyzed precursors due to premature nanoparticle formation. Thirdly, using *in situ* ligand exchange and simple electrostatic adsorption, a variety of nanoparticles can be successfully functionalized onto the surface of the leaf for a variety of purposes.

## 2.4 Experimental

**Chemicals. Materials.** Glutaraldehyde (25% wt. in water, Sigma-Aldrich), chloroform (Fisher Scientific), hydrochloric acid (HCl, 36.5-38%, JT Baker), anhydrous ethyl alcohol (Commercial Alcohols), iron(III) chloride (FeCl<sub>3</sub>, reagent grade, 97%, Sigma-Aldrich), copper(II) acetylacetonate (99.99%, Sigma-Aldrich), 1,2-hexadecanediol (TCI America), oleylamine (technical grade, 70%, Sigma-Aldrich), oleic acid (technical grade, 90%, Sigma-Aldrich), n-octyl ether (TCI

America), 16-mercaptohexadecanoic acid (16-MHA, 90%, Sigma-Aldrich), hexane (Fisher-Scientific), potassium hexachloroiridate(IV) (99.99%, Sigma-Aldrich), sodium hydrogen citrate sesquihydrate (99%, Sigma-Aldrich), sodium hydroxide (EMD), DOWEX 1X8-100 (Cl) ion exchange resin (Sigma-Aldrich), chloroplatinic acid hydrate (>99.9%, Sigma-Aldrich), cetyl trimethylammonium bromide (99%, Sigma-Aldrich), and sodium borohydride (98%, EMD) were used as received. Sugarcane leaves were acquired from the University of Alberta Biological Sciences Greenhouse. In the case of the  $\alpha$ -Fe<sub>2</sub>O<sub>3</sub> slides, iron(III) chloride hexahydrate (97%, Sigma-Aldrich) was used as the iron precursor.

**Synthesis of  $\alpha$ -Fe<sub>2</sub>O<sub>3</sub> Leaves.** Procedure for synthesizing  $\alpha$ -Fe<sub>2</sub>O<sub>3</sub> leaves was based on an earlier publication by Li et al. for the synthesis of TiO<sub>2</sub> leaves.<sup>38</sup> To allow for long term storage, leaves were fixed in a solution of 2% glutaraldehyde in phosphate buffer at 4°C for 16 hours. Afterwards, leaves were rinsed with deionized water and stored at 4°C. To prepare  $\alpha$ -Fe<sub>2</sub>O<sub>3</sub> leaves, fixed leaves were first immersed in chloroform for 1 second and wiped clean with a cotton tip to remove the hydrophobic surface cutin layer, washed to remove chloroform, and then added to a solution of 5% HCl for 3 hours, after which the leaves became yellow. Next, the leaves were dehydrated in progressively more concentrated solutions of ethanol in water (v/v); 15%, 30%, 50%, 70%, 90% and 100%. Leaves were left in each solution for 20 minutes. An ethanolic solution of FeCl<sub>3</sub> was prepared by adding anhydrous FeCl<sub>3</sub> to boiling ethanol to a concentration of 0.2 M for FeCl<sub>3</sub>, which was immediately removed from heat. (**Safety Note:** this results in formation of HCl gas). The leaves and FeCl<sub>3</sub> solution were placed into a Schlenk

flask and left under vacuum for 16 hours. Afterwards, the leaves were left in a wet chamber for 2 hours. The infiltrated leaves were finally dried and calcined in a tube furnace under lightly blowing air with the following steps: 40°C, 60°C, 80°C, 105°C, 300°C, and 500°C, each for two hours, followed by a 10 minute high temperature step at 800°C. The ramp speed was 1°C/min. Leaves were lightly clipped between quartz slides.

**$\alpha$ -Fe<sub>2</sub>O<sub>3</sub> control slides for visualizing surface functionalization.** Slides were produced based on procedure detailed by Wang et al.<sup>59</sup> FeCl<sub>3</sub> at a concentration of 0.1 M was drop-cast 10  $\mu$ L at a time onto a silicon wafer and left to dry in air before being heated on a hot plate at 300°C for 5 minutes. This was typically repeated 4 times to get a thick, conformal layer of iron oxide. The slides were then placed in a tube furnace and heated at 800°C for 10 minutes with a ramp of 10°C/minute. Otherwise, these slides were treated as the leaves were in terms of particle functionalization (i.e. incubation times, ligand and nanoparticle concentrations).

**Synthesis and functionalization of copper nanoparticles.** Copper nanoparticles were synthesized via decomposition of copper (II) acetylacetonate in the presence of oleic acid and oleylamine. In a 50 mL three-neck flask, 0.4 mmol of copper (II) acetylacetonate, 1.2 mmol of 1,2-hexadecanediol, and 20 mL of octyl ether were combined. The solution was heated to 105 °C for 10 minutes to dissolve these precursors, before 0.4 mmol of oleic acid and 0.4 mmol of oleylamine were added. The reaction solution was then raised to 155°C and left there for 30 minutes. Subsequently, the reaction was cooled to room temperature before addition of 20 mL of ethanol and centrifugation at 2000 x g. The resulting pellet was resuspended

in hexane at a concentration of 0.2 mg/mL, and contained 10 – 20 nm particles.<sup>56</sup>  $\alpha$ -Fe<sub>2</sub>O<sub>3</sub> leaves were washed with chloroform before being immersed in a 3 mM solution of 16-mercaptohexadecanoic acid (16-MHA) for 10 seconds. The leaves were washed with chloroform twice to remove unbound 16-MHA. Next, the leaves were incubated in a solution of copper nanoparticles for 10 seconds before being washed with hexane to remove unbound particles. Finally, the leaves were heated in an alumina crucible in a tube furnace at 850°C for 30 minutes at a ramp speed of 8°C/min to induce transformation of copper nanoparticles and iron oxide surface to CuFe<sub>2</sub>O<sub>4</sub>.

**Functionalization of Z-scheme with catalyst nanoparticles.** Citrate-capped IrO<sub>2</sub>•xH<sub>2</sub>O nanoparticles were synthesized as reported previously via the hydrolysis of iridium chloride.<sup>67,68</sup> Briefly, a 50 mL aqueous solution of 1.2 mM K<sub>2</sub>IrCl<sub>6</sub> and 3.8 mM sodium citrate was pH-adjusted to 7.5 using NaOH and heated at 95 °C for 30 minutes. The solution was cooled to room temperature and again pH-adjusted to 7.5. The heating and readjustment was repeated until the pH stabilized at 7.5. Finally, the solution was heated at 95 °C for 2 hours to yield nanoparticles. Finally, the solution was stirred with DOWEX 1X8-50 exchange resin beads to remove excess citrate ions. The beads were then filtered to yield purified iridium oxide nanoparticles. To functionalize the surface of the leaf with iridium oxide, the leaf was immersed in a solution of pH 6 citrate-capped IrO<sub>2</sub>•xH<sub>2</sub>O nanoparticles for 10 seconds. This pH was selected because the isoelectric point of  $\alpha$ -Fe<sub>2</sub>O<sub>3</sub> is 8, and so therefore at pH 6, the surface of  $\alpha$ -Fe<sub>2</sub>O<sub>3</sub> would be positively charged while the

citrate ions would be negatively charged, improving electrostatic interactions. The leaf was subsequently heated for 1 minute at 300°C to remove organic ligands.

Platinum nanoparticles were synthesized by reducing a 50 mL aqueous solution of 0.75 M H<sub>2</sub>PtCl<sub>6</sub> and 0.1 M cetylammmonium bromide (CTAB) heated to 60 °C with 1.3 mL of 50 mM NaBH<sub>4</sub>.<sup>63</sup> The particles were mixed with ethanol, oleylamine, and hexane in a 1:2:1:1 ratio. This solution was heated at 40°C for 6 hours before the organic layer was washed with two parts of ethanol and centrifuged at 8000 x g until all white residue was removed. Finally, the particles were resuspended in the original volume of hexane. For functionalization, an α-Fe<sub>2</sub>O<sub>3</sub>/CuFe<sub>2</sub>O<sub>4</sub> leaf was first functionalized with 16-MHA before being placed in the hexane solution of platinum nanoparticles for 10 seconds. The sample was then washed with hexane before heating at 500 °C for 2 hours to remove 16-MHA.

**X-ray Photoelectron Spectroscopy.** X-ray photoelectron spectroscopy (XPS) spectra were collected by Kratos Ultra spectrometer with a base pressure less than  $4 \times 10^{-8}$  Pa. A monochromatic Al K $\alpha$  source ( $h\nu = 1486.6$  eV) was run at a power of 168 W. The analysis spot was 300 x 700  $\mu\text{m}$  and the analyzer resolution was 0.80 eV for Au 4f peaks. The survey scans were collected for binding energies spanning 1100 to 0 eV at constant energy of 160 eV and spectra for narrow regions were collected at pass-energy of 20 eV. Sample charging was compensated by electron flooding. The binding energy (BE) scale was calibrated by assigning C1s peak from surface contamination at 284.8 eV. Relative concentrations of chemical elements were calculated using CasaXPS, using a standard quantification routine, including Scofield sensitivity factors and Shirley background subtraction.

**Synthesis of CuFe<sub>2</sub>O<sub>4</sub> powder.** A previous procedure was followed. Cu(NO<sub>3</sub>)<sub>2</sub>•2.5H<sub>2</sub>O (5 mmol) and Fe(NO<sub>3</sub>)<sub>2</sub>•9H<sub>2</sub>O (10 mmol) in 50 mL of deionized water was added to a 100 mL 0.3 M solution of citric acid and dehydrated on a hot plate at sub-boiling temperature. The resulting brown mass was then heated at 300°C until combustion took place, yielding a black-gray powder. Subsequently, the powder was heated at 850°C for 3 hours to yield a black powder.

**Cyclic Voltammetry.** Cyclic voltammetry was performed using a PARSTAT 2273 potentiostat in a three-electrode configuration. The reference electrode was Ag/Ag<sup>+</sup>. A platinum disc electrode coated with powder and a platinum wire were used as the working and counter electrodes, respectively. The scan rate was 50 mV/s, and the electrolyte was 0.1 M tetrabutylammonium hexafluorophosphate.

**Photocatalytic testing.** H<sub>2</sub> gas evolution studies were performed by loading 1 mg of sample into a 2 mL GC vial with rubber seals. Electrolyte solution (1 mL) consisting of 10% triethanolamine in water was added to the vial before sealing and purging with Ar gas. In cases where pH control was required, the solution was adjusted using HCl. The vials were then illuminated under a 500 W Xe lamp at a distance of 30 cm for 1 hour before testing was performed on a Varian 450 gas chromatogram equipped with thermal conductivity detector and Ar flow gas. Sampling was performed via headspace injection and quantification was done based on standardization to control amounts of H<sub>2</sub> in Ar. In initial testing, 0.1 M KOH was used as the electrolyte.

**Other Characterization.** Scanning electron microscope images of natural and α-Fe<sub>2</sub>O<sub>3</sub> leaves were taken on a Hitachi S-3000 SEM. Some images of the α-Fe<sub>2</sub>O<sub>3</sub>

leaves as well as all images of drop-cast  $\alpha$ -Fe<sub>2</sub>O<sub>3</sub> surfaces were taken with a Hitachi S-4800 FE-SEM. Nanoparticle images were acquired on a JEOL JEM-2100 TEM at an accelerating voltage of 200 kV. Infrared spectroscopy (FTIR) on a Nicolet Nexus 760 Spectrometer with a DRIFTS detector was used to examine the surface of the leaf during 16-MHA and nanoparticle functionalization. X-ray diffraction (XRD) was performed using a Bruker D8 Discover with a Cu K $\alpha$  beam (40 kV, 40 mA,  $\lambda = 1.5406 \text{ \AA}$ ) equipped with a 2D detector. XRD spectra were collected from the 2D ring patterns by radial integration. Samples were prepared by mounting powder on a silicon slide stabilized with isopropanol. Auger electron spectroscopy (AES) was performed on a JEOL JAMP-9500F field emission microprobe.

## 2.5 References

- (1) Gilbert, B.; Frandsen, C.; Maxey, E. R.; Sherman, D. M. Band-Gap Measurements of Bulk and Nanoscale Hematite by Soft X-Ray Spectroscopy. *Phys. Rev. B* **2009**, *79* (3), 035108.
- (2) Kennedy, J. H.; Frese, K. W. Photooxidation of Water at  $\alpha$ -Fe<sub>2</sub>O<sub>3</sub> Electrodes. *J. Electrochem. Soc.* **1978**, *125* (5), 709–714.
- (3) Misho, R. H.; Murad, W. A. Band Gap Measurements in Thin Films of Hematite Fe<sub>2</sub>O<sub>3</sub>, Pyrite FeS<sub>2</sub> and Troilite FeS Prepared by Chemical Spray Pyrolysis. *Sol. Energy Mater. Sol. Cells* **1992**, *27* (4), 335–345.
- (4) Murphy, A. B.; Barnes, P. R. F.; Randeniya, L. K.; Plumb, I. C.; Grey, I. E.; Horne, M. D.; Glasscock, J. A. Efficiency of Solar Water Splitting Using Semiconductor Electrodes. *Int. J. Hydrog. Energy* **2006**, *31* (14), 1999–2017.
- (5) Sivula, K.; Le Formal, F.; Grätzel, M. Solar Water Splitting: Progress Using Hematite ( $\alpha$ -Fe<sub>2</sub>O<sub>3</sub>) Photoelectrodes. *ChemSusChem* **2011**, *4* (4), 432–449.
- (6) Itoh, K.; Bockris, J. O. Thin Film Photoelectrochemistry: Iron Oxide. *J. Electrochem. Soc.* **1984**, *131* (6), 1266–1271.

- (7) Klahr, B.; Gimenez, S.; Fabregat-Santiago, F.; Hamann, T.; Bisquert, J. Water Oxidation at Hematite Photoelectrodes: The Role of Surface States. *J. Am. Chem. Soc.* **2012**, *134* (9), 4294–4302.
- (8) Formal, F. L.; Tétreault, N.; Cornuz, M.; Moehl, T.; Grätzel, M.; Sivula, K. Passivating Surface States on Water Splitting Hematite Photoanodes with Alumina Overlayers. *Chem. Sci.* **2011**, *2* (4), 737–743.
- (9) Iandolo, B.; Hellman, A. The Role of Surface States in the Oxygen Evolution Reaction on Hematite. *Angew. Chem.* **2014**, *126* (49), 13622–13626.
- (10) Wheeler, D. A.; Wang, G.; Ling, Y.; Li, Y.; Zhang, J. Z. Nanostructured Hematite: Synthesis, Characterization, Charge Carrier Dynamics, and Photoelectrochemical Properties. *Energy Environ. Sci.* **2012**, *5* (5), 6682–6702.
- (11) Launay, J. C.; Horowitz, G. Crystal Growth and Photoelectrochemical Study of Zr-Doped  $\alpha$ -Fe<sub>2</sub>O<sub>3</sub> Single Crystal. *J. Cryst. Growth* **1982**, *57* (1), 118–124.
- (12) Kay, A.; Cesar, I.; Grätzel, M. New Benchmark for Water Photooxidation by Nanostructured  $\alpha$ -Fe<sub>2</sub>O<sub>3</sub> Films. *J. Am. Chem. Soc.* **2006**, *128* (49), 15714–15721.
- (13) Lin, Y.; Zhou, S.; Sheehan, S. W.; Wang, D. Nanonet-Based Hematite Heteronanostructures for Efficient Solar Water Splitting. *J. Am. Chem. Soc.* **2011**, *133* (8), 2398–2401.
- (14) Qin, D.-D.; Tao, C.-L.; In, S.; Yang, Z.-Y.; Mallouk, T. E.; Bao, N.; Grimes, C. A. Facile Solvothermal Method for Fabricating Arrays of Vertically Oriented  $\alpha$ -Fe<sub>2</sub>O<sub>3</sub> Nanowires and Their Application in Photoelectrochemical Water Oxidation. *Energy Fuels* **2011**, *25* (11), 5257–5263.
- (15) Cesar, I.; Sivula, K.; Kay, A.; Zboril, R.; Grätzel, M. Influence of Feature Size, Film Thickness, and Silicon Doping on the Performance of Nanostructured Hematite Photoanodes for Solar Water Splitting. *J. Phys. Chem. C* **2009**, *113* (2), 772–782.
- (16) Ling, Y.; Wang, G.; Wheeler, D. A.; Zhang, J. Z.; Li, Y. Sn-Doped Hematite Nanostructures for Photoelectrochemical Water Splitting. *Nano Lett.* **2011**, *11* (5), 2119–2125.
- (17) Hu, Y.-S.; Kleiman-Shwarsstein, A.; Forman, A. J.; Hazen, D.; Park, J.-N.; McFarland, E. W. Pt-Doped  $\alpha$ -Fe<sub>2</sub>O<sub>3</sub> Thin Films Active for Photoelectrochemical Water Splitting. *Chem. Mater.* **2008**, *20* (12), 3803–3805.

- (18) Jang, J. S.; Lee, J.; Ye, H.; Fan, F.-R. F.; Bard, A. J. Rapid Screening of Effective Dopants for Fe<sub>2</sub>O<sub>3</sub> Photocatalysts with Scanning Electrochemical Microscopy and Investigation of Their Photoelectrochemical Properties. *J. Phys. Chem. C* **2009**, *113* (16), 6719–6724.
- (19) Saremi-Yarahmadi, S.; Wijayantha, K. G. U.; Tahir, A. A.; Vaidhyanathan, B. Nanostructured  $\alpha$ -Fe<sub>2</sub>O<sub>3</sub> Electrodes for Solar Driven Water Splitting: Effect of Doping Agents on Preparation and Performance. *J. Phys. Chem. C* **2009**, *113* (12), 4768–4778.
- (20) Kleiman-Shwarsstein, A.; Hu, Y.-S.; Forman, A. J.; Stucky, G. D.; McFarland, E. W. Electrodeposition of  $\alpha$ -Fe<sub>2</sub>O<sub>3</sub> Doped with Mo or Cr as Photoanodes for Photocatalytic Water Splitting. *J. Phys. Chem. C* **2008**, *112* (40), 15900–15907.
- (21) Le Formal, F.; Sivula, K.; Grätzel, M. The Transient Photocurrent and Photovoltage Behavior of a Hematite Photoanode under Working Conditions and the Influence of Surface Treatments. *J. Phys. Chem. C* **2012**, *116* (51), 26707–26720.
- (22) Xi, L.; Bassi, P. S.; Chiam, S. Y.; Mak, W. F.; Tran, P. D.; Barber, J.; Loo, J. S. C.; Wong, L. H. Surface Treatment of Hematite Photoanodes with Zinc Acetate for Water Oxidation. *Nanoscale* **2012**, *4* (15), 4430–4433.
- (23) Hu, Y.-S.; Kleiman-Shwarsstein, A.; Stucky, G. D.; McFarland, E. W. Improved Photoelectrochemical Performance of Ti-Doped  $\alpha$ -Fe<sub>2</sub>O<sub>3</sub> Thin Films by Surface Modification with Fluoride. *Chem. Commun.* **2009**, No. 19, 2652–2654.
- (24) Spray, R. L.; McDonald, K. J.; Choi, K.-S. Enhancing Photoresponse of Nanoparticulate  $\alpha$ -Fe<sub>2</sub>O<sub>3</sub> Electrodes by Surface Composition Tuning. *J. Phys. Chem. C* **2011**, *115* (8), 3497–3506.
- (25) McDonald, K. J.; Choi, K.-S. Synthesis and Photoelectrochemical Properties of Fe<sub>2</sub>O<sub>3</sub>/ZnFe<sub>2</sub>O<sub>4</sub> Composite Photoanodes for Use in Solar Water Oxidation. *Chem. Mater.* **2011**, *23* (21), 4863–4869.
- (26) Tilley, S. D.; Cornuz, M.; Sivula, K.; Grätzel, M. Light-Induced Water Splitting with Hematite: Improved Nanostructure and Iridium Oxide Catalysis. *Angew. Chem.* **2010**, *122* (36), 6549–6552.
- (27) Zhong, D. K.; Sun, J.; Inumaru, H.; Gamelin, D. R. Solar Water Oxidation by Composite Catalyst/ $\alpha$ -Fe<sub>2</sub>O<sub>3</sub> Photoanodes. *J. Am. Chem. Soc.* **2009**, *131* (17), 6086–6087.

- (28) Sivula, K.; Le Formal, F.; Grätzel, M. Solar Water Splitting: Progress Using Hematite ( $\alpha$ -Fe<sub>2</sub>O<sub>3</sub>) Photoelectrodes. *ChemSusChem* **2011**, *4* (4), 432–449.
- (29) Arnold, W.; Azzi, J. R. Chlorophyll Energy Levels and Electron Flow in Photosynthesis. *Proc. Natl. Acad. Sci. U. S. A.* **1968**, *61* (1), 29.
- (30) Grätzel, M. Photoelectrochemical Cells. *Nature* **2001**, *414* (6861), 338–344.
- (31) Sayama, K.; Mukasa, K.; Abe, R.; Abe, Y.; Arakawa, H. A New Photocatalytic Water Splitting System under Visible Light Irradiation Mimicking a Z-Scheme Mechanism in Photosynthesis. *J. Photochem. Photobiol. Chem.* **2002**, *148* (1–3), 71–77.
- (32) Tada, H.; Mitsui, T.; Kiyonaga, T.; Akita, T.; Tanaka, K. All-Solid-State Z-Scheme in CdS–Au–TiO<sub>2</sub> Three-Component Nanojunction System. *Nat. Mater.* **2006**, *5* (10), 782–786.
- (33) Kato, H.; Hori, M.; Kato, R.; Shimodaira, Y.; Kudo, A. Construction of Z-Scheme Type Heterogeneous Photocatalysis Systems for Water Splitting into H<sub>2</sub> and O<sub>2</sub> under Visible Light Irradiation. *Chem. Lett.* **33** (10), 1348–1349.
- (34) Higashi, M.; Abe, R.; Ishikawa, A.; Takata, T.; Ohtani, B.; Domen, K. Z-Scheme Overall Water Splitting on Modified-TaON Photocatalysts under Visible Light ( $\lambda < 500$  nm). *Chem. Lett.* **2008**, *37* (2), 138–139.
- (35) Iwase, A.; Ng, Y. H.; Ishiguro, Y.; Kudo, A.; Amal, R. Reduced Graphene Oxide as a Solid-State Electron Mediator in Z-Scheme Photocatalytic Water Splitting under Visible Light. *J. Am. Chem. Soc.* **2011**, *133* (29), 11054–11057.
- (36) Wang, X.; Liu, G.; Chen, Z.-G.; Li, F.; Wang, L.; Lu, G. Q.; Cheng, H.-M. Enhanced Photocatalytic Hydrogen Evolution by Prolonging the Lifetime of Carriers in ZnO/CdS Heterostructures. *Chem. Commun.* **2009**, No. 23, 3452.
- (37) Sage, R. F. The Evolution of C<sub>4</sub> Photosynthesis. *New Phytol.* **2004**, *161* (2), 341–370.
- (38) Li, X.; Fan, T.; Zhou, H.; Chow, S.; Zhang, W.; Zhang, D.; Guo, Q.; Ogawa, H. Enhanced Light-Harvesting and Photocatalytic Properties in Morph-TiO<sub>2</sub> from Green-Leaf Biotemplates. *Adv. Funct. Mater.* **2009**, *19* (1), 45–56.
- (39) Zhou, H.; Li, X.; Fan, T.; Osterloh, F. E.; Ding, J.; Sabio, E. M.; Zhang, D.; Guo, Q. Artificial Inorganic Leafs for Efficient Photochemical Hydrogen Production Inspired by Natural Photosynthesis. *Adv. Mater.* **2010**, *22* (9), 951–956.

- (40) Walter, M. G.; Warren, E. L.; McKone, J. R.; Boettcher, S. W.; Mi, Q.; Santori, E. A.; Lewis, N. S. Solar Water Splitting Cells. *Chem. Rev.* **2010**, *110* (11), 6446–6473.
- (41) Ida, S.; Yamada, K.; Matsunaga, T.; Hagiwara, H.; Matsumoto, Y.; Ishihara, T. Preparation of P-Type  $\text{CaFe}_2\text{O}_4$  Photocathodes for Producing Hydrogen from Water. *J. Am. Chem. Soc.* **2010**, *132* (49), 17343–17345.
- (42) Yang, H.; Yan, J.; Lu, Z.; Cheng, X.; Tang, Y. Photocatalytic Activity Evaluation of Tetragonal  $\text{CuFe}_2\text{O}_4$  Nanoparticles for the  $\text{H}_2$  Evolution under Visible Light Irradiation. *J. Alloys Compd.* **2009**, *476* (1–2), 715–719.
- (43) Perrot, P.; Arnout, S.; Vrestal, J. Copper - Iron - Oxygen. In *iron systems: phase diagrams, crystallographic and thermodynamic data*; Effenberg, G., Ilyenko, S., Eds.; Materials Science International Team, M., Series Ed.; Landolt-Börnstein - Group IV Physical Chemistry; Springer-Verlag Berlin Heidelberg, 2008; Vol. 11D3.
- (44) Bewick, T. A.; Shilling, D. G.; Querns, R. Evaluation of Epicuticular Wax Removal from Whole Leaves with Chloroform. *Weed Technol.* **1993**, *7* (3), 706–716.
- (45) Gash, A. E.; Tillotson, T. M.; Satcher; Poco, J. F.; Hrubesh, L. W.; Simpson, R. L. Use of Epoxides in the Sol–Gel Synthesis of Porous Iron(III) Oxide Monoliths from Fe(III) Salts. *Chem. Mater.* **2001**, *13* (3), 999–1007.
- (46) Hench, L. L.; West, J. K. The Sol-Gel Process. *Chem. Rev.* **1990**, *90* (1), 33–72.
- (47) Robinson-Beers, K.; Evert, R. F. Ultrastructure of and Plasmodesmatal Frequency in Mature Leaves of Sugarcane. *Planta* **1991**, *184* (3), 291–306.
- (48) Oworu, O. O.; McDavid, C. R.; Maccoll, D. The Anatomy of the Storage Tissue of Sugar-Cane in Relation to Sugar Uptake. *Ann. Bot.* **1977**, *41* (2), 401–404.
- (49) Seisenbaeva, G. A.; Gohil, S.; Suslova, E. V.; Rogova, T. V.; Turova, N. Y.; Kessler, V. G. The Synthesis of Iron (III) Ethoxide Revisited: Characterization of the Metathesis Products of Iron (III) Halides and Sodium Ethoxide. *Inorganica Chim. Acta* **2005**, *358* (12), 3506–3512.
- (50) O’Keefe, B. J.; Monnier, S. M.; Hillmyer, M. A.; Tolman, W. B. Rapid and Controlled Polymerization of Lactide by Structurally Characterized Ferric Alkoxides. *J. Am. Chem. Soc.* **2001**, *123* (2), 339–340.

- (51) Flynn, C. M. Hydrolysis of Inorganic iron(III) Salts. *Chem. Rev.* **1984**, *84* (1), 31–41.
- (52) Grosvenor, A. P.; Kobe, B. A.; Biesinger, M. C.; McIntyre, N. S. Investigation of Multiplet Splitting of Fe 2p XPS Spectra and Bonding in Iron Compounds. *Surf. Interface Anal.* **2004**, *36* (12), 1564–1574.
- (53) Liu, Q.; Xu, Z. Self-Assembled Monolayer Coatings on Nanosized Magnetic Particles Using 16-Mercaptohexadecanoic Acid. *Langmuir* **1995**, *11* (12), 4617–4622.
- (54) Wei, Y.; Chen, S.; Kowalczyk, B.; Huda, S.; Gray, T. P.; Grzybowski, B. A. Synthesis of Stable, Low-Dispersity Copper Nanoparticles and Nanorods and Their Antifungal and Catalytic Properties. *J. Phys. Chem. C* **2010**, *114* (37), 15612–15616.
- (55) Kanninen, P.; Johans, C.; Merta, J.; Kontturi, K. Influence of Ligand Structure on the Stability and Oxidation of Copper Nanoparticles. *J. Colloid Interface Sci.* **2008**, *318* (1), 88–95.
- (56) Mott, D.; Galkowski, J.; Wang, L.; Luo, J.; Zhong, C.-J. Synthesis of Size-Controlled and Shaped Copper Nanoparticles. *Langmuir* **2007**, *23* (10), 5740–5745.
- (57) Espinós, J. P.; Morales, J.; Barranco, A.; Caballero, A.; Holgado, J. P.; González-Elipe, A. R. Interface Effects for Cu, CuO, and Cu<sub>2</sub>O Deposited on SiO<sub>2</sub> and ZrO<sub>2</sub>. XPS Determination of the Valence State of Copper in Cu/SiO<sub>2</sub> and Cu/ZrO<sub>2</sub> Catalysts. *J. Phys. Chem. B* **2002**, *106* (27), 6921–6929.
- (58) Deroubaix, G.; Marcus, P. X-Ray Photoelectron Spectroscopy Analysis of Copper and Zinc Oxides and Sulphides. *Surf. Interface Anal.* **1992**, *18* (1), 39–46.
- (59) Wang, G.; Ling, Y.; Wheeler, D. A.; George, K. E. N.; Horsley, K.; Heske, C.; Zhang, J. Z.; Li, Y. Facile Synthesis of Highly Photoactive  $\alpha$ -Fe<sub>2</sub>O<sub>3</sub>-Based Films for Water Oxidation. *Nano Lett.* **2011**, *11* (8), 3503–3509.
- (60) McIntyre, N. S.; Cook, M. G. X-Ray Photoelectron Studies on Some Oxides and Hydroxides of Cobalt, Nickel, and Copper. *Anal. Chem.* **1975**, *47* (13), 2208–2213.
- (61) Harriman, A.; Pickering, I. J.; Thomas, J. M.; Christensen, P. A. Metal Oxides as Heterogeneous Catalysts for Oxygen Evolution under Photochemical Conditions. *J. Chem. Soc. Faraday Trans. 1 Phys. Chem. Condens. Phases* **1988**, *84* (8), 2795–2806.

- (62) Greeley, J.; Jaramillo, T. F.; Bonde, J.; Chorkendorff, I.; Nørskov, J. K. Computational High-Throughput Screening of Electrocatalytic Materials for Hydrogen Evolution. *Nat. Mater.* **2006**, *5* (11), 909–913.
- (63) Yang, W.; Wang, X.; Yang, F.; Yang, C.; Yang, X. Carbon Nanotubes Decorated with Pt Nanocubes by a Noncovalent Functionalization Method and Their Role in Oxygen Reduction. *Adv. Mater.* **2008**, *20* (13), 2579–2587.
- (64) Şen, F.; Gökağaç, G. Different Sized Platinum Nanoparticles Supported on Carbon: An XPS Study on These Methanol Oxidation Catalysts. *J. Phys. Chem. C* **2007**, *111* (15), 5715–5720.
- (65) Tian, Z. Q.; Jiang, S. P.; Liang, Y. M.; Shen, P. K. Synthesis and Characterization of Platinum Catalysts on Multiwalled Carbon Nanotubes by Intermittent Microwave Irradiation for Fuel Cell Applications. *J. Phys. Chem. B* **2006**, *110* (11), 5343–5350.
- (66) Love, J. C.; Estroff, L. A.; Kriebel, J. K.; Nuzzo, R. G.; Whitesides, G. M. Self-Assembled Monolayers of Thiolates on Metals as a Form of Nanotechnology. *Chem. Rev.* **2005**, *105* (4), 1103–1170.
- (67) Hara, M.; Waraksa, C. C.; Lean, J. T.; Lewis, B. A.; Mallouk, T. E. Photocatalytic Water Oxidation in a Buffered Tris(2,2'-Bipyridyl)ruthenium Complex-Colloidal IrO<sub>2</sub> System. *J. Phys. Chem. A* **2000**, *104* (22), 5275–5280.
- (68) Harriman, A.; Thomas, J. M.; Milward, G. R. Catalytic and Structural Properties of Iridium-Iridium Dioxide Colloids. *New J. Chem.* *11* (11-12), 757–762.
- (69) Parks, G. A. The Isoelectric Points of Solid Oxides, Solid Hydroxides, and Aqueous Hydroxo Complex Systems. *Chem. Rev.* **1965**, *65* (2), 177–198.
- (70) Sanchez Casalongue, H. G.; Ng, M. L.; Kaya, S.; Friebe, D.; Ogasawara, H.; Nilsson, A. In Situ Observation of Surface Species on Iridium Oxide Nanoparticles during the Oxygen Evolution Reaction. *Angew. Chem.* **2014**, *126* (28), 7297–7300.
- (71) Kezzim, A.; Nasrallah, N.; Abdi, A.; Trari, M. Visible Light Induced Hydrogen on the Novel Hetero-System CuFe<sub>2</sub>O<sub>4</sub>/TiO<sub>2</sub>. *Energy Convers. Manag.* **2011**, *52* (8–9), 2800–2806.
- (72) Nasrallah, N.; Kebir, M.; Koudri, Z.; Trari, M. Photocatalytic Reduction of Cr(VI) on the Novel Hetero-System CuFe<sub>2</sub>O<sub>4</sub>/CdS. *J. Hazard. Mater.* **2011**, *185* (2–3), 1398–1404.

- (73) Kucur, E.; Riegler, J.; Urban, G. A.; Nann, T. Determination of Quantum Confinement in CdSe Nanocrystals by Cyclic Voltammetry. *J. Chem. Phys.* **2003**, *119* (4), 2333–2337.
- (74) Chen, X.; Shen, S.; Guo, L.; Mao, S. S. Semiconductor-Based Photocatalytic Hydrogen Generation. *Chem. Rev.* **2010**, *110* (11), 6503–6570.
- (75) Yun, H. J.; Lee, H.; Kim, N. D.; Lee, D. M.; Yu, S.; Yi, J. A Combination of Two Visible-Light Responsive Photocatalysts for Achieving the Z-Scheme in the Solid State. *ACS Nano* **2011**, *5* (5), 4084–4090.

# 3 Synthesis and Characterization of [Ni,Fe]O nanoparticles

## 3.1 Introduction

### 3.1.1 Overview of Metal Oxides and their Applications

Metal oxides and their mixtures have been studied as potential electrode devices for a variety of applications, including Li-ion batteries,<sup>1-3</sup> electrochemical capacitors,<sup>2,4,5</sup> fuel cells,<sup>6,7</sup> gas sensors,<sup>8,9</sup> thin film transistors, electrochemical water oxidation catalysts,<sup>10-12</sup> and photocatalytic materials.<sup>13-15</sup> The attraction of these materials can be explained by the typical stability of metal oxides as well as the relative abundance of many metals oxides compared to traditional catalysts such as platinum, palladium, rhodium etc. since the most common metal oxides discussed and used are often first-row transition metals. Mixtures of these metals can result in novel materials with unique structures and properties, broadening the ultimate potential for the use of metal oxides. Some examples of this tailoring of compositions include improving the sensitivity of gas sensors,<sup>9,16</sup> increasing the absorption range of photocatalysts,<sup>17-20</sup> and changing the activity of catalysts.<sup>21-24</sup>

However, synthetic routes to mixed metal oxides (MMOs) are more difficult than their monometallic equivalents because of the complicating presence of additional metal species.<sup>25</sup> Although numerous synthetic techniques have been reported, including mechanical mixing,<sup>26-28</sup> spray pyrolysis,<sup>29,30</sup> solid-state thermal

decomposition,<sup>11,31–33</sup> and hydrothermal treatment,<sup>23,33–35</sup> each of these techniques has its own downfalls, mostly either polydispersity or phase impurities. Simultaneously controlling the size, shape, homogeneity, composition, and phase of MMO particles is difficult but necessary in order to capture and accurately catalogue the full potential of these materials. In this regard, the high-temperature, atmospherically-controlled decomposition of metal-organic precursors has an advantage over previous methods because it allows for the nucleation and growth of nanoparticles that are homogenous, controllable and yet unachievable by the other listed means due to environmental or entropic considerations.<sup>36,37</sup>

### 3.1.2 Overview of the Chapter

The material reported here, denoted as [Ni,Fe]O, is a MMO that was synthesized via the high-temperature decomposition of metal oleate complexes. In previously reported syntheses of mixed nickel-iron oxide nanoparticles, the two commonly reported phases are spinel nickel ferrite ( $\text{NiFe}_2\text{O}_4$ )<sup>38,39</sup> and rocksalt (i.e. cubic) bunsenite (NiO) with iron in solid solution.<sup>40–44</sup> Although the equilibrium phase diagram of the Ni-Fe-O system predicts negligible solubility of Fe in the rocksalt NiO phase below 800 °C,<sup>41,45</sup> synthetic preparation of phase-pure 10 at% Fe-doped NiO has been previously reported.<sup>44</sup> In contrast, the mixed metal nickel-iron oxide nanoparticles reported here possess a rocksalt crystal structure and are stable under ambient conditions. Furthermore, the nanoparticle products maintain a single-crystal rocksalt structure over almost the entire range of nickel:iron ratios. Several synthetic variables, such as the ratio of nickel to iron in the oleate precursor,

solution decomposition time and the precursor drying time<sup>46</sup> are used to modify the nanoparticle composition, size and shape. The magnetic properties of these nanoparticles are investigated, and it is found that the effective magnetic anisotropy can be tuned by changing particle composition. Lastly, thermal annealing of these metastable nanoparticles demonstrates that they are kinetically stable at elevated temperatures.

## **3.2 Results**

### **3.2.1 Synthesis and Characterization of [Ni,Fe]O Nanoparticles**

Although a wide variety of metal-organic precursors decompose to yield metal oxide nanoparticle products,<sup>47-50</sup> metal oleate precursors present several advantages that include high reaction yields and ease of synthesis.<sup>36,51,52</sup> In this work, metal oleate precursors were prepared by refluxing a mixture of  $\text{NiCl}_2 \cdot 6\text{H}_2\text{O}$  and  $\text{FeCl}_3$  with sodium oleate (Figure 3.1).<sup>36</sup> Throughout this work, a ratio of X:Y Ni:Fe oleate precursor refers to a sample prepared from a X:Y ratio (by metal molarity) of  $\text{NiCl}_2 \cdot 6\text{H}_2\text{O}$  to  $\text{FeCl}_3$ . After the red-brown precursor was separated from the aqueous phase of the reflux, the metal oleate precursor were heated to 305 °C for a given period of time, denoted as the decomposition time ( $t_d$ ), in 1-octadecene under argon to produce nanoparticle products.

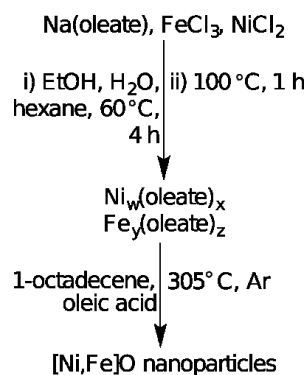


Figure 3.1 Synthetic Scheme of [Ni,Fe]O Nanoparticles

Figure 3.2 shows electron microscopy characterization of nanoparticles formed from the decomposition of 33:67 Ni:Fe oleate precursor in 1-octadecene at 305 °C ( $t_d = 20$  minutes). From these micrographs we see that the nanoparticles have a cubic-like shape with rounded edges and vertices (herein referred to as nanocubes). Moreover, the HAADF-STEM micrograph of these nanocubes (Figure 3.2A) reveals that they are single-crystal nanoparticles with sizes on the order of 8 nm. High-resolution EDX mapping of the nanoparticles (Figures 3.2B-C) reveals that there is no segregation of nickel and iron throughout the nanoparticles, with all of the observed nanoparticles having the same composition. However, the final composition of metal in the nanoparticles varied from that of the nickel and iron precursor ratio; while the starting molar ratio of nickel to iron in the oleate precursor was 33:67, the final molar ratio of metals in the nanoparticles was ~50:50, as determined by EDX (Table 3.1). Modified synthetic reactions where nickel and iron oleate complexes were prepared in separate vessels and then combined yielded nanoparticle products that were identical in appearance and crystal structure, as determined by TEM and XRD (Figure 3.3). Subtle differences in the carbonyl

stretching region of the FTIR spectra,  $\nu(\text{C}=\text{O})$ , of individually prepared iron and nickel oleate complex precursors, and the mixed Fe/Ni complex mixture, suggest that the precursor identities may differ, but the structures of these metal carboxylate complexes have no effect, however, on the resulting nanoparticle products (Figure 3.4). The final yield of metal oxide nanoparticle product was determined to be ~55% based on the remaining metal oxide mass after calcination.

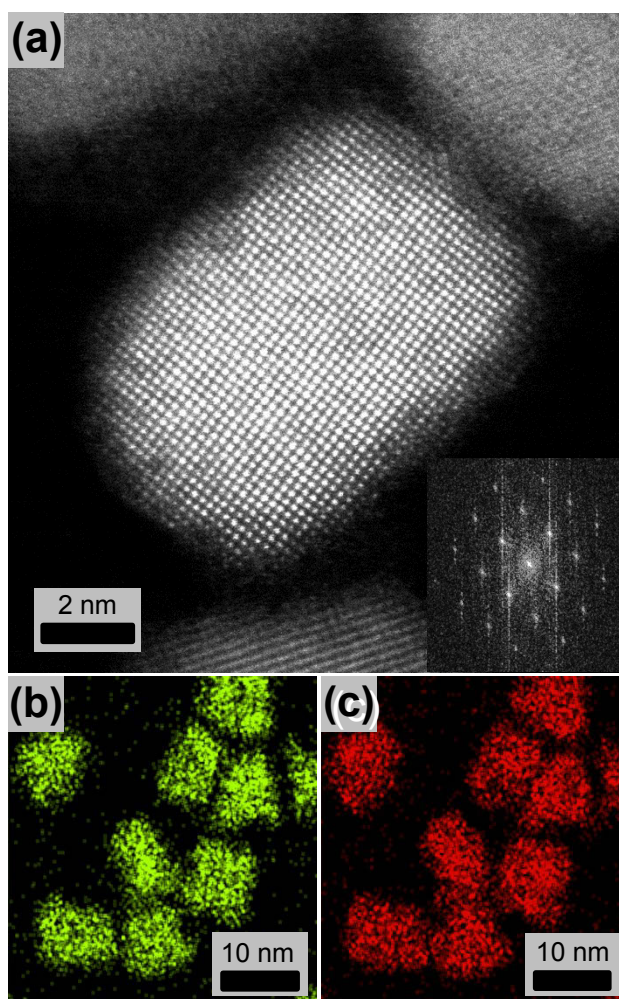


Figure 3.2 (a) High-resolution HAADF-STEM micrograph of nanoparticles synthesized with a nickel to iron precursor ratio of 33:67 and decomposition time of 20 min (inset: FFT diffractogram). (b,c) EDX maps of (b) nickel and (c) iron of nanoparticles produced via the same synthesis.

Table 3.1. Characteristics of nanoparticles synthesized from the mixed metal oleate precursor with nickel to iron molar ratios of 33:66 by changing decomposition time ( $t_d$ ).

$t_d$ , 305°C (min)	Shape	Final Ni:Fe	Size (nm)	Polydispersity (%)
15	Stars	54:46	6.6	11.3
20	Cubes/Stars	51:49	7.9	10.4
25	Cubes	51:49	9.7	9.4
30	Spheres	33:67	9.6	7.1

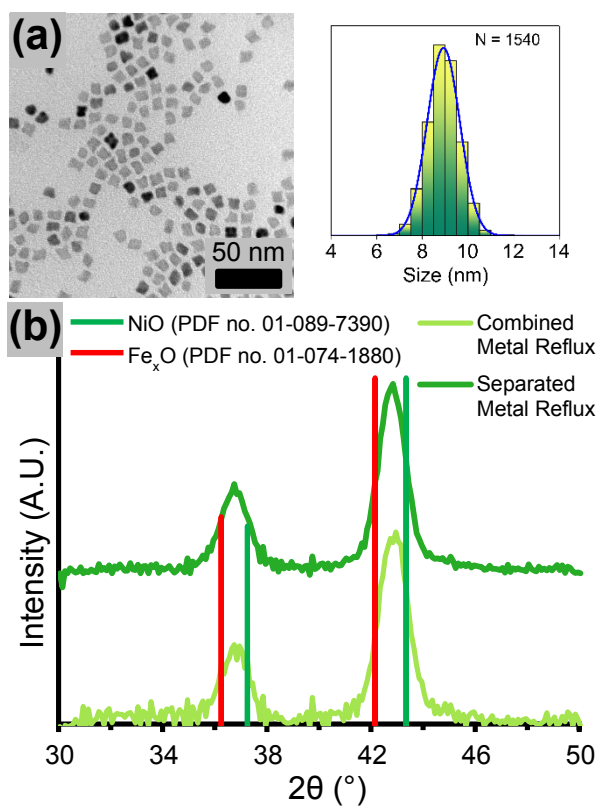


Figure 3.3 (a) TEM micrograph and (b) XRD spectrum of  $[\text{Ni,Fe}]\text{O}$  nanocubes where nickel and iron oleate were refluxed separately and combined only after reflux.

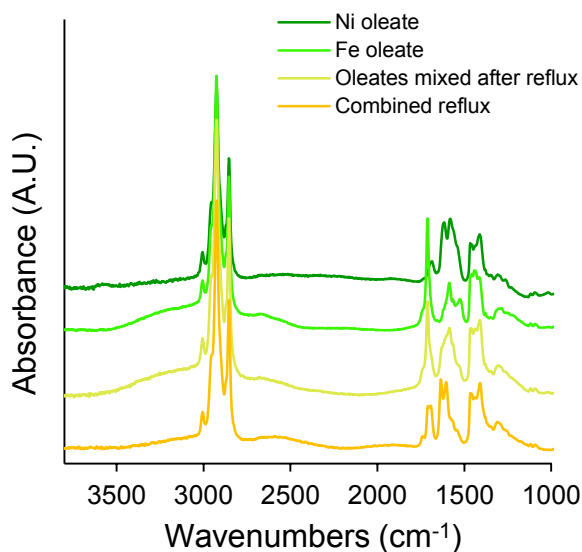


Figure 3.4 FTIR spectra of individual nickel and iron metal oleate precursors, and the mixed metal oleate precursor derived from the combined reflux of nickel and iron salts with sodium oleate.

Shown in Figure 3.5a is the electron diffraction pattern of nanoparticles synthesized with a precursor ratio of 33:67 and decomposition time of 20 min. All of the observed Debye rings can be matched to that of a rocksalt crystal lattice, similar to that found in phase pure NiO and Fe<sub>x</sub>O.<sup>53,54</sup> Furthermore, the XRD spectrum of these nanocubes displays a shift in peak positions relative to pure NiO and Fe<sub>x</sub>O such that the peak positions of the nanocubes lie between the peak positions of pure NiO and Fe<sub>x</sub>O (Figure 3.5b). Using the (200) peak position, the lattice parameter of these nanocubes is calculated to be 4.22 Å, which is roughly halfway between pure Fe<sub>x</sub>O (4.29 Å) and NiO (4.18 Å). This shift in lattice parameter is characteristic of substitutional solid-solutions, where the lattice parameter must change in order to accommodate strain that arises due to the differing atomic sizes of the constituent atoms, as well as attractive and repulsive

forces between the guest and host metal atoms.<sup>55,56</sup> From the HRTEM, EDX mapping, X-ray and electron diffraction data, we propose that the products of the decomposition reaction are single-crystal nanoparticles consisting of a substitutional solid-solution of nickel and iron in rocksalt crystal structure. As short hand, we refer to this phase as  $[\text{Ni,Fe}]\text{O}$ , a non-equilibrium phase under ambient conditions.<sup>41,45</sup>

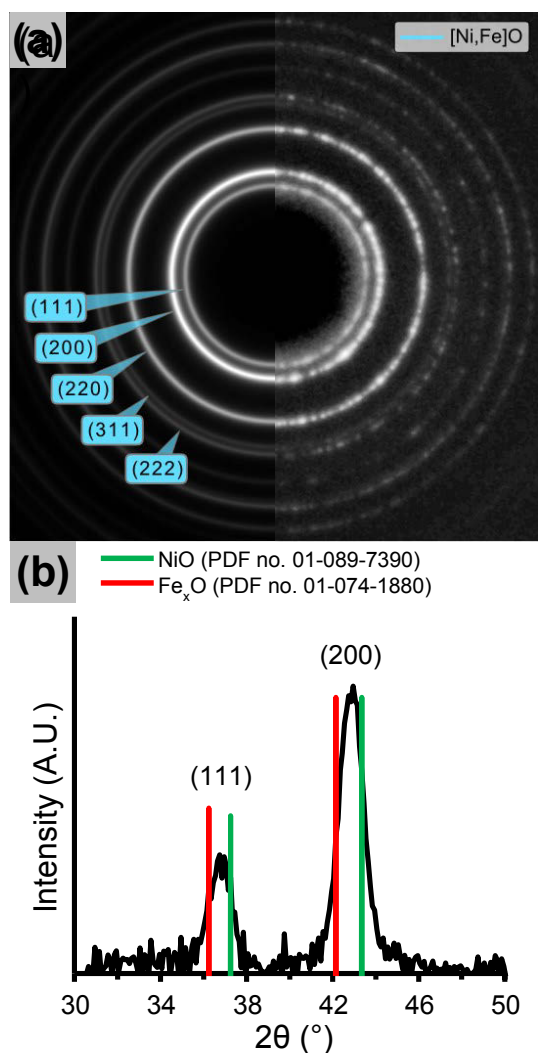


Figure 3.5 (a) Electron diffraction pattern of  $[\text{Ni,Fe}]\text{O}$  nanocubes (right) and simulated electron diffraction pattern of a rocksalt crystal structure (left). (b) XRD spectrum of nanocubes with spectra of bulk NiO and  $\text{Fe}_x\text{O}$  overlaid.

The oxidation states of iron within these nanoparticles (33:67 Ni:Fe precursor ratio, 20 min decomposition time) were studied using EELS and XPS, as shown in Figure 3.6. The shapes and relative areas of the iron  $L_{2,3}$  peaks acquired using EELS (Figure 3.6a) were found to be consistent with those reported for a  $Fe^{2+}$ -containing oxide.<sup>57,58</sup> Further characterization of the iron oxidation states was performed using XPS (Figure 3.6b). The Fe  $2p_{3/2}$  spectrum of the nanocubes displayed a major peak at 710.6 eV, which is consistent with the 710.5 eV Fe  $2p_{3/2}$  peak position of  $Fe_xO$ .<sup>59</sup> Moreover there are no clearly distinguishable satellite peaks, which are characteristic features of pure  $(\alpha,\gamma)-Fe_2O_3$  and  $Fe_3O_4$ .<sup>59</sup> However, it is well known that it is difficult to distinguish iron oxides species from the core-level XPS spectra,<sup>59</sup> since the peak positions of  $Fe_xO$ ,  $Fe_3O_4$  and  $(\alpha,\gamma)-Fe_2O_3$  are all within a 0.5 eV range. Furthermore, there is a significant amount of Ni substitution within the  $Fe_xO$  lattice, which can cause a shift in the peak position. Looking at the Ni 2p XPS spectrum in Figure 3c, we see that the Ni 2p peak positions correspond well with literature values for nickel oxide with a +2 oxidation state.<sup>60,61</sup> From these XPS and EELS data we can conclude that the majority of the Fe and Ni has a +2 oxidation state; however, due to the ambiguity of these XPS scans, the presence of  $Fe^{3+}$  cannot be ruled out.

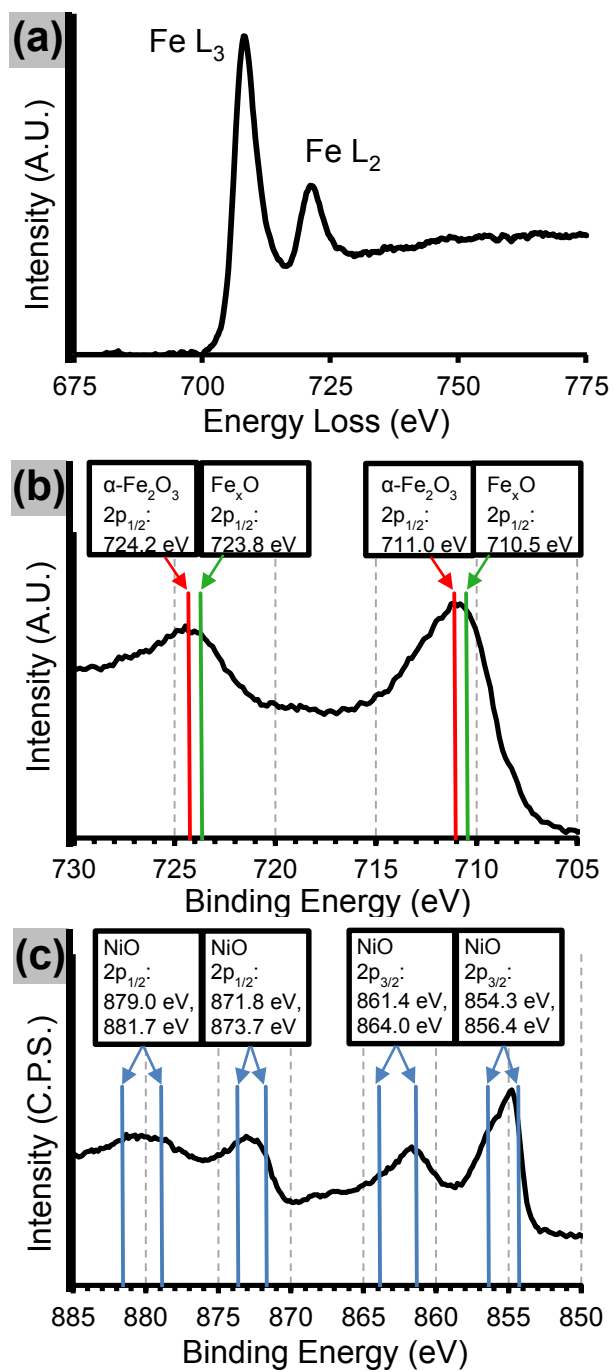


Figure 3.6 (a) Fe EELS spectrum of nanocubes showing L<sub>2</sub> and L<sub>3</sub> peaks. Corresponding (b) Fe 2p<sup>3/2</sup> and (c) Ni 2p XPS spectra.

### 3.2.2 Effect of Modifying Decomposition Time, $t_d$

The shape and composition of the nanocubes were found to be tunable via modifications of the synthetic procedure. For example, when the decomposition time of the 33:67 Ni:Fe metal oleate precursor was varied within the range of 15 to 30 minutes, the nanoparticles underwent a continuous morphological transformation from stars to rounded cubes to spheres (for  $t_d < 15$  min no solid product could be isolated). At  $t_d = 15$  min, the final product was found to be a mixture of concave star-like particles and cubic-like particles with rounded edges and vertices, with an average size of 6.5 nm (Figure 3.7a). As the decomposition time of the reaction is increased ( $t_d = 20, 25$  min) we see that the fraction of cubes increases while the average size also increases up to 9.7 nm (Figures 3.7b,c). Finally at a  $t_d = 30$  min (Figure 3.7d), almost all of the nanoparticles possess a spherical shape, with an average size of 9.6 nm. In addition, an increased decomposition time led to reduced polydispersity, as defined by the standard deviation in size divided by the mean size.<sup>62</sup> As  $t_d$  increased from 15 minutes to 30 minutes, the polydispersity was reduced from 11.3% to 7.1%. This reduction in polydispersity is significant, since sub-10% polydispersity is considered the benchmark value of a highly monodisperse nanoparticle solution.<sup>62</sup> Interestingly it was found that at shorter decomposition times ( $t_d = 15-25$  min), the molar metal ratio of these nanoparticles (as measured by EDX) was  $\sim$  Ni:Fe 50:50, but when  $t_d = 30$  min, the Ni:Fe ratio changed to 33:67.

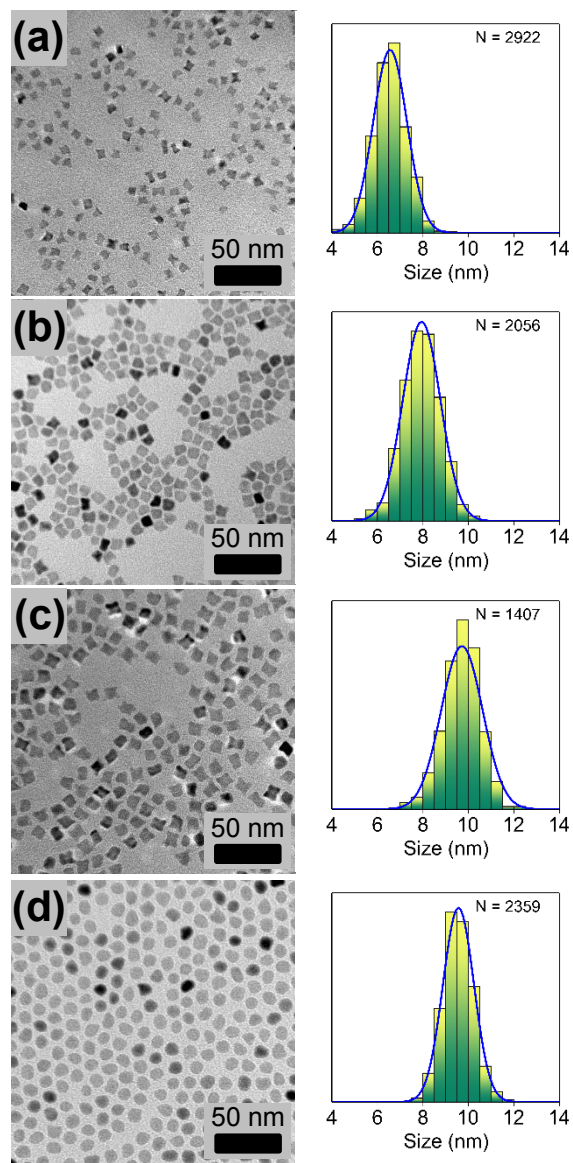


Figure 3.7 TEM micrographs (left) and size distributions (right) of [Ni,Fe]O nanoparticles synthesized by heating the precursor for (a) 15, (b) 20, (c) 25, and (d) 30 min.

### 3.2.3 Effect of Modifying Drying Time, $t_r$

Bronstein and co-workers demonstrated that the structure of the precursor iron oleate complex can have important effects on the resulting iron oxide nanoparticle products.<sup>46</sup> In the work reported here, up to this point, the mixed metal nickel-iron oleate complexes were dried, in air, at 100 °C for 1 h. If the drying time (air, 100 °C) was increased to 3 h or longer, a dramatic change in the resulting nanoparticle products was noted. When a mixed metal oleate precursor with an initial ratio of Ni:Fe of 33:67 ( $t_d = 20$  min) was dried for 12 h, nanoparticles with sizes of ~7-8 nm with an octopod star-like morphology were produced, as shown in Figures 3.8a-b. As with the nanocubes, the stars maintained a single-crystal rocksalt structure as determined by electron diffraction (Figures 3.8b-c). Both nickel and iron were found to be uniformly distributed throughout the stars, as shown by EDX mapping (Figures 3.8e-f). The final compositions of the nanoparticles were relatively unaffected by drying; short drying times (0-1 h) led to final composition ratios of Ni:Fe of ~50:50, while the longer drying times producing slightly Ni-richer (~55:45) nanoparticles (Table 3.2). Using FTIR, it was determined that undried metal oleate precursors had a broad shoulder around 3300  $\text{cm}^{-1}$ , suggestive of residual ethanol or oleic acid dimers.<sup>46</sup> Drying the precursor for a minimum of 3 h resulted in the disappearance of this shoulder (Figure 3.9).

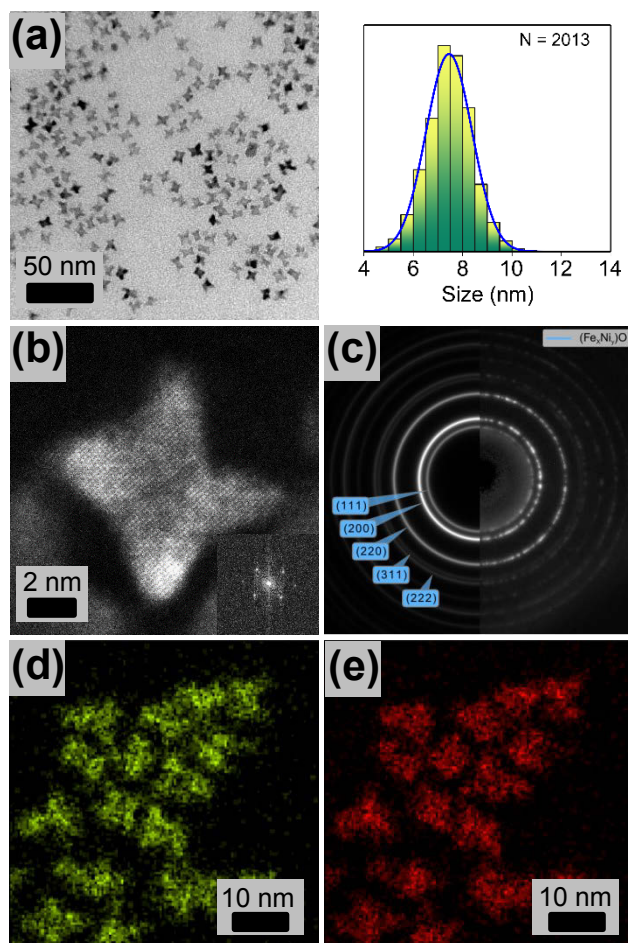


Figure 3.8 (a) TEM micrograph and corresponding size distribution of nanoparticles synthesized from a 33:67 precursor ratio, 20 min decomposition time and 12 hour drying time. (b) High-resolution HAADF-STEM image of a nanoparticle (inset: FFT diffractogram). (c) Corresponding electron diffraction pattern of the nanoparticles (right) and simulated electron diffraction pattern of a rocksalt crystal structure (left). (d,e) EDX maps of nanoparticles for (d) nickel and (e) iron.

Table 3.3 Characteristics of nanoparticles synthesized from metal oleates with nickel to iron molar ratios of 33:66 by changing drying time ( $t_r$ ).

$t_r$ (hrs)	Final Ni:Fe	Size by TEM (nm)
0	52:48	8.1
3	59:41	7.4
6	55:45	8.5
12	57:43	7.5

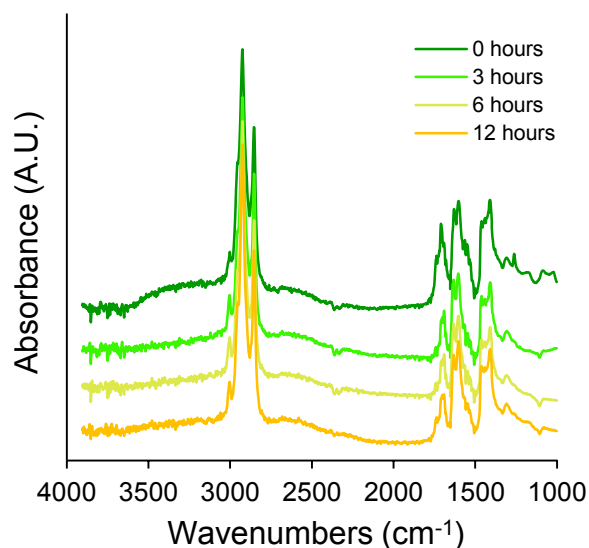


Figure 3.9 FTIR spectra of metal oleate precursors with different  $t_r$  (listed top right).

### 3.2.4 Effect of Initial Precursor Metal Composition

The initial ratios of nickel and iron oleate precursors were varied to further investigate the products of this synthetic approach. Nanoparticles were synthesized from Ni:Fe precursor ratios of 83:17, 67:33, 50:50, 33:67 and 17:83 using a decomposition time of 30 min. The resulting nanoparticle products all exhibited a rocksalt crystal structure as determined by XRD (Figure 3.10), with resulting Ni:Fe product ratios of 88:12, 73:27, 62:38, 33:67, and 24:76, respectively, as determined by EDX (Table 3.3). As expected, there is also a monotonic decrease in the lattice

parameter as the Ni content of the nanoparticles increases. For control purposes, a Ni:Fe ratio of 100:0 (pure nickel oleate) was synthesized using a  $t_d$  of 30 minutes, yielding a black powder that did not re-suspend in hexane; XRD analysis revealed that the powder was composed of both hexagonal and fcc nickel (Figure 3.11a). Under TEM, the powder appeared as  $\sim 25$  nm aggregates of smaller nanoparticles (Figure 3.11b). In contrast, a synthesis of nanoparticles ( $t_d = 30$  min) using 0:100 Ni:Fe (pure iron oleate) yielded  $\sim 21$  nm diameter nanoparticles. From XRD characterization, the dominant crystalline phase was found to be  $Fe_xO$ , however the presence of a very broad peak centered at  $2\theta \sim 35^\circ$  indicates the presence of a secondary iron oxide, likely due to deeper oxidation of the  $Fe_xO$  phase, similarly to previous reports on iron oleate decomposition (Figure 3.11c).<sup>46,63,64</sup>

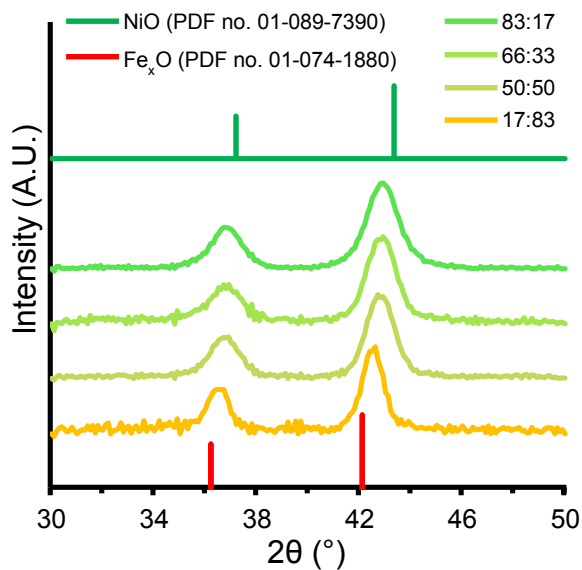


Figure 3.10 XRD spectra of nanoparticles synthesized with different compositions of metals in the initial precursor solution with  $t_d = 30$  min. All ratios are listed as nickel:iron.

Table 3.3 Characteristics of nanoparticles synthesized from metal oleates with nickel to iron molar ratios of 33:66 by changing drying time ( $t_r$ ).

$t_r$ (hrs)	Final Ni:Fe	Size by TEM (nm)
0	52:48	8.1
3	59:41	7.4
6	55:45	8.5
12	57:43	7.5

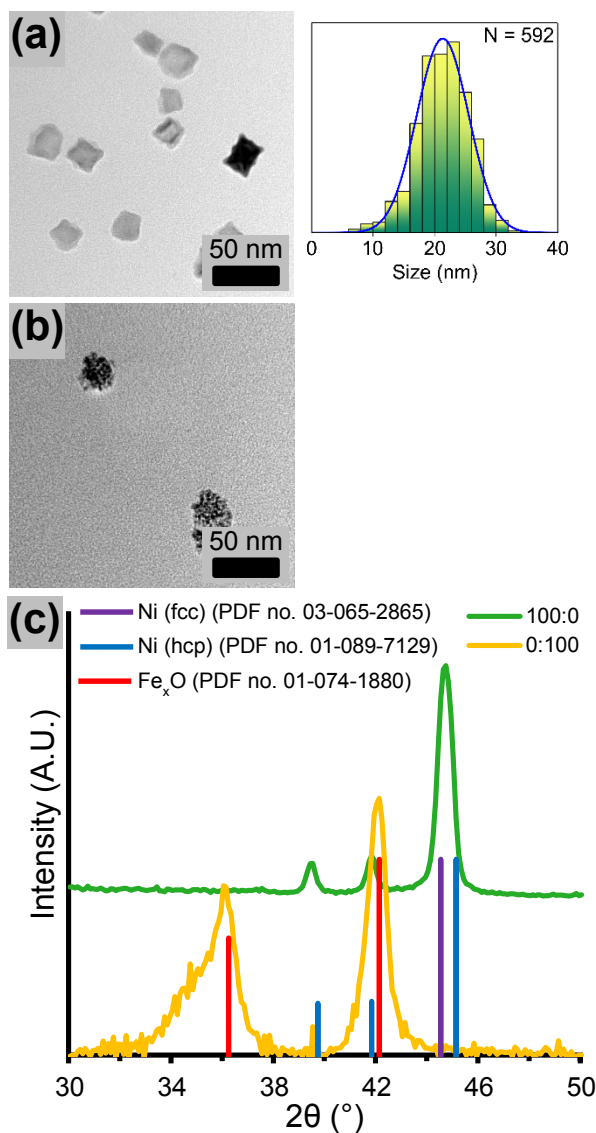


Figure 3.11 TEM micrographs of nanoparticles synthesized from pure (a) iron oleate and (b) pure nickel oleate. Size analysis was not performed on nickel nanoparticles due to the fact that nanoparticles were aggregated into clusters.

Changing the initial metal oleate composition also affected nanoparticle shape, as shown in Figure 3.12. Nanoparticles synthesized from Ni:Fe 83:17 ( $t_d = 30$  minutes for all samples) precursors appeared as irregularly-shaped star-like particles with an average size of 7.3 nm, while nanoparticles synthesized from Ni:Fe 67:33 precursors consisted of a mixture of stars and rounded cubes. The Ni:Fe 50:50 precursors yielded 7.3 nm nanoparticles that appeared to be a mixture of cubes and spheres. Finally, the Ni:Fe 83:17 precursor product was composed of spheres that were 11.0 nm in diameter. While most samples maintained a high degree of monodispersity (9 – 13%), the nanoparticles produced from the Ni:Fe 83:17 precursor had polydispersity values exceeding 15%, and the pure iron oleate sample had a polydispersity value of almost 20%.

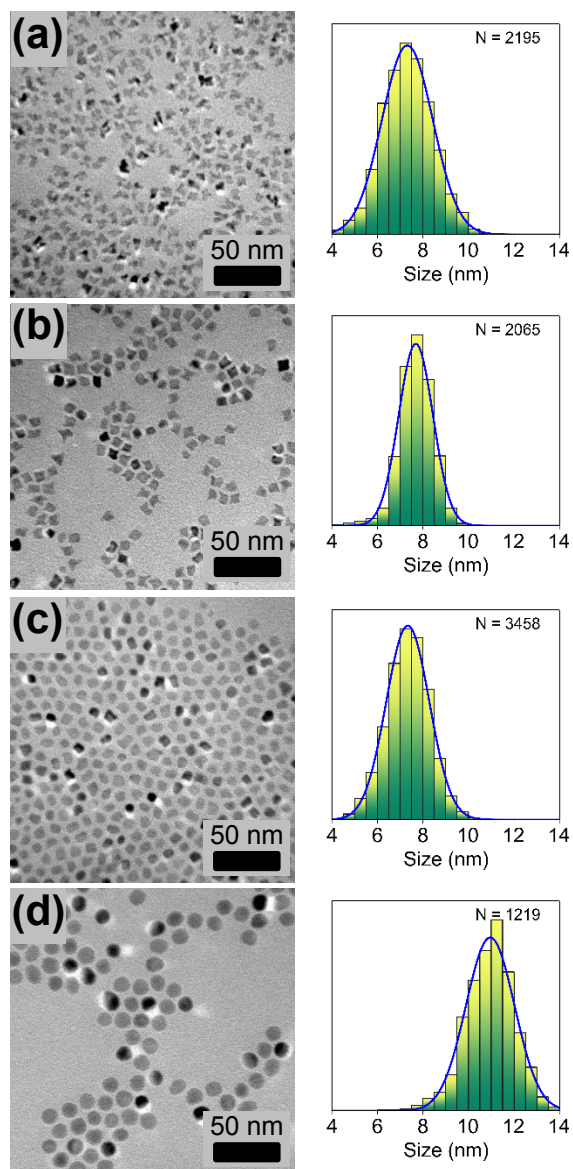


Figure 3.12 TEM micrographs (left) and corresponding size distribution (right) of [Ni,Fe]O nanoparticles synthesized when metal compositions in precursor oleate were modified before synthesis at  $t_d = 30$  min. Metal ratios are listed as nickel:iron. (a) 83:17, (b) 66:33, (c) 50:50, (d) 17:83

By changing the initial precursor ratio of nickel to iron and the decomposition time, we see that a diverse set of nanoparticle shapes can be synthesized; ranging from concave octopod stars, rounded cubes and spherical nanoparticles. The results of these syntheses can be neatly summarized in what can loosely be described as a “phase diagram”, shown in Figure 3.13. In this diagram, two consistent trends emerge. For a fixed precursor ratio, as the decomposition time is increased, the shapes of the resultant nanoparticles evolve in a continuous fashion from star-like concave octopods, to rounded cubes, and finally to spherical nanoparticles. Moreover, the monodispersity of the nanoparticles is found to increase with decomposition time. Alternatively, for a fixed decomposition time, as the nickel to iron precursor ratio is decreased, the same continuous transformation from stars to spheres is observed, with a similar increase in monodispersity. In summary, with a high nickel to iron precursor ratios and at short decomposition times, octopod stars are produced; at intermediate nickel to iron precursor ratios and decomposition times, rounded cubes are produced; at low nickel to iron precursor ratios and long decomposition times, spherical nanoparticles are produced.

In order to understand the evolution of nanoparticle shape shown in Figure 8, we must first understand the origin of star-shaped nanoparticles. In another study of iron oleate decomposition in the presence of oleic acid, varying the ratio of iron oleate to oleic acid allowed for nanoparticle shape control.<sup>65</sup> Specifically, as the ratio of iron oleate to oleic acid was decreased, the shapes of the nanoparticles changed from spheres to stars. The formation of stars was attributed to be a result of uneven growth of the nanoparticles around the nuclei due to increased relative

concentration of strongly adsorbing oleic acid. Given the similarity of our synthetic procedure and nanoparticles shapes to those found in [70], it is proposed that in the initial stages of the reaction (short decomposition times) the nanoparticle growth is kinetically limited, resulting in the formation of stars. However, once the faster growing faces become self-terminated (resulting in a star shape) and the reaction is allowed to continue, the higher energy curved concave surfaces are filled in and the stars transition to cubes and eventually to equilibrium spheres. Furthermore, as summarized in Figure 8, as the iron content of the oleate precursor increases, the reaction proceeds more rapidly. This result suggests that the decomposition of the mixed metal nickel/iron-oleate processed more slowly as the iron content of the mixed metal oleate is increased.

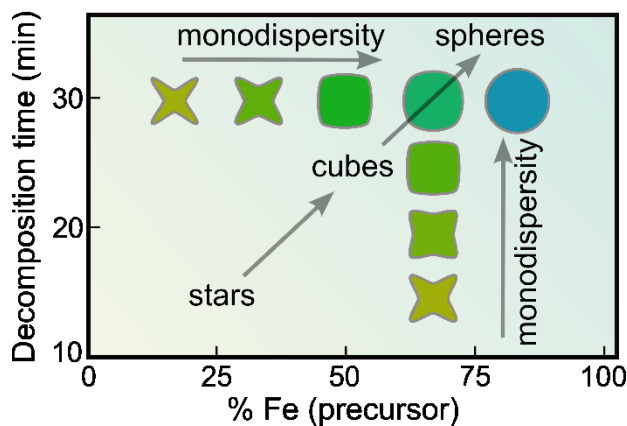


Figure 3.13 Phase diagram of resultant nanoparticle shapes as a function of nickel to iron precursor ratio and decomposition time.

### 3.2.5 Magnetic Characterization of Nanoparticles

Magnetometry was used to examine the magnetic properties of these nanoparticles. Three nanoparticle samples were used for comparison – stars (Ni:Fe 33:67 precursor,  $t_d = 20$  min and dried for 12 hours), nanocubes (Ni:Fe 33:67 precursor,  $t_d = 20$  minutes), and spheres (Ni:Fe 33:67 precursor,  $t_d = 30$  minutes). These samples have similar sizes but different final metal compositions, ranging from 55:45 (stars) to 51:49 (nanocubes) to 33:67 (spheres). Therefore, any variations in magnetic properties should primarily arise from differences in shape and/or composition. In all three samples examined, two magnetic transitions were found in the zero-field cooling (ZFC) curves – a small transition around 50 K and a much larger one that varies in position from 181 K in spheres to 141 K in nanocubes to 111 K in stars (Figure 3.14a). Magnetic transitions observed in FC (field cooling)/ZFC measurements for nanoparticle samples are usually taken to represent the blocking temperature ( $T_B$ ), the point at which the magnetic moment of a nanoparticle is no longer pinned to the nanoparticle's crystalline lattice and the nanoparticle's behaviour switches from being blocked to being superparamagnetic. The convergence of the FC and ZFC curves at the higher transition is consistent with this behaviour. The change in this major transition appears to be influenced by composition and shape; given comparable nanoparticle volumes for the three samples, this shift is most likely a result of a change in the effective magnetic anisotropy constant, which is itself influenced by magnetocrystalline anisotropy (i.e. composition) and shape anisotropy. The position of the minor transition at 50

K does not change significantly and appears to be independent of the major transition.

In order to understand the nature of the major transitions and therefore, the  $T_B$  values of the nanoparticles, magnetic hysteresis loops of these three samples were obtained at 300 K and 1.9 K. None of the samples exhibited any saturation or significant hysteresis at 300 K, even with the application of a 7 T magnetic field strength (Figure 3.14b). This lack of saturation or hysteresis is indicative of antiferromagnetic behaviour at 300 K. In contrast, hysteresis measurements performed at 1.9 K revealed that all three samples showed some degree of hysteresis (Figure 3.14c). Both stars and nanocubes had low coercivities of 5.3 and 5.5 mT, respectively. However, the spheres had a much higher coercivity of 165.2 mT. The magnetization remained low even under a 7 T field (stars: 2.9 emu/g; cubes: 5.4 emu/g; spheres: 5.6 emu/g). This result is interesting because more anisotropic shapes, such as cubes and stars are typically more magnetisable than spheres, which are geometrically isotropic.<sup>66,67</sup> In this system, the opposite trend is observed, suggesting that volume may play a more important role than shape. It is often observed that the surface of magnetic nanoparticles is poorly or even non-magnetic.<sup>68</sup> In going from stars to cubes to spheres, the relative proportion of surface atoms increases, which could explain the decreasing trend in magnetization, as a higher fraction of the nanoparticle is weakly magnetic. Finally, the metallic composition may also play a role in determining the saturation magnetization. Nonetheless, these curves suggest that [Ni,Fe]O is an antiferromagnetic material that exhibits superparamagnetic behaviour, as had been previously observed for

nanoparticles of antiferromagnetic materials.<sup>69–71</sup> Both bulk  $\text{Fe}_x\text{O}$  and  $\text{NiO}$  are considered antiferromagnetic with Néel temperatures of 210 K, and 525 K, respectively,<sup>72,73</sup> so the antiferromagnetic behaviour is in line with that of the parent materials.

The low temperature transition is unusual because it is stable in position and size regardless of variations in bulk nanoparticle properties such as shape and composition. While a similar double peak complex was seen in  $\text{Fe}_x\text{O}$  nanoparticles,<sup>74</sup> it was absent in 10 at% Fe-doped  $\text{NiO}$  nanoparticles,<sup>44</sup> suggesting that the low transition peak is dependent on the increasing presence of  $\text{Fe}^{2+}$ . Given the existence of  $\text{Fe}_3\text{O}_4$  surface states in the  $\text{Fe}_x\text{O}$  nanoparticles,<sup>74</sup> we propose that the low temperature peak arises from the presence and subsequent oxidation of  $\text{Fe}^{2+}$  at the surface of the nanoparticles, resulting in the formation of a surface region with unique magnetic properties. In contrast, surface anisotropy contributions to magnetic properties in pure antiferromagnetic materials usually arise from unpaired surface states.<sup>49</sup> Together with XPS oxidation data, we further propose that  $[\text{Ni,Fe}]\text{O}$  nanoparticles are primarily composed of metal oxides with a +2 oxidation state surrounded by a surface layer of  $\text{Fe}^{3+}$ , as illustrated in Figure 3.14d.

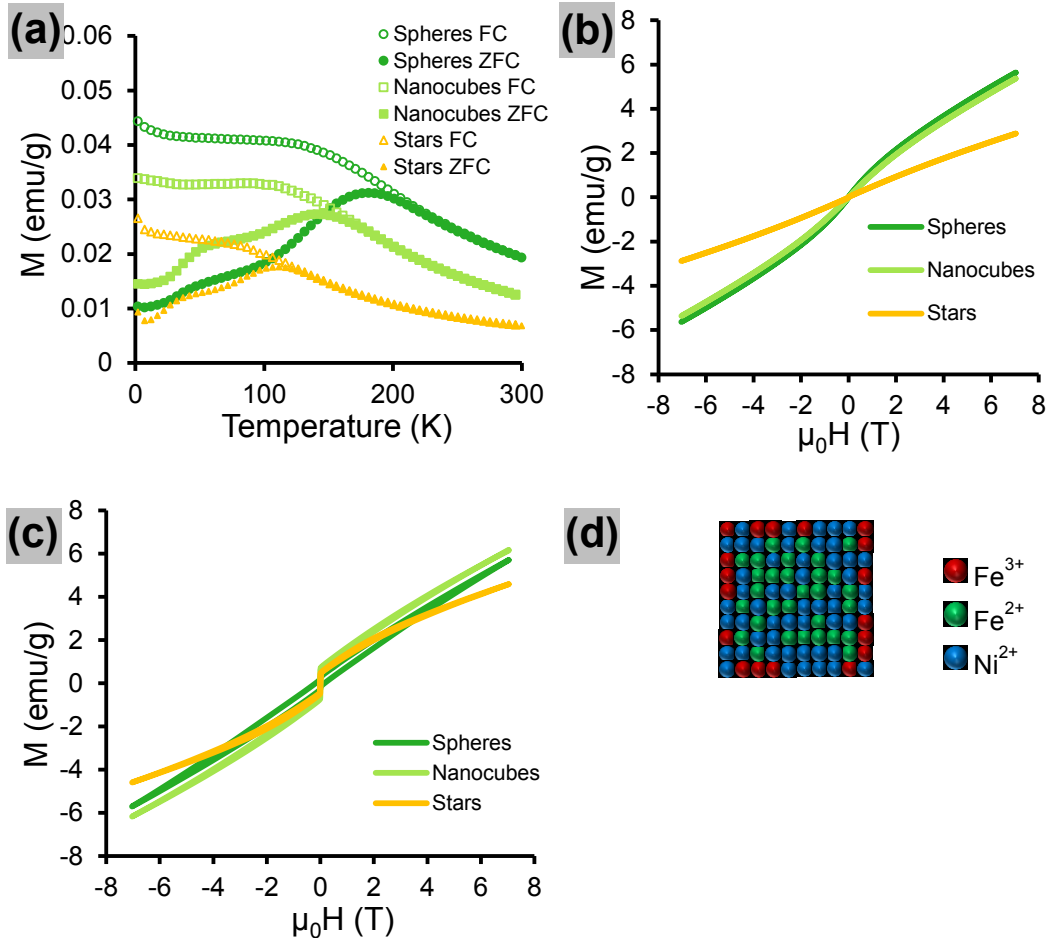


Figure 3.14 Magnetic measurements of differently shaped nanoparticles, including (a) ZFC and FC curves and magnetic hysteresis loops taken at (b) 300 K and (c) 1.9 K. (d) Proposed scheme of Fe and Ni atoms [Ni,Fe]O nanoparticles.

The thermal stability of [Ni,Fe]O nanocubes (33:67 Ni:Fe precursor ratio and  $t_d = 20$  min) was studied by monitoring the XRD spectrum of films heated at three different temperatures (200 °C, 400 °C, 600 °C) for 2 hours under air. The nanocubes demonstrated little structural change when heated to 200 °C in air, as seen in Figure 3.15. At 400 °C, however, the expected equilibrium crystalline NiFe<sub>2</sub>O<sub>4</sub> phase began to appear, eventually becoming the dominant phase (based

on peak heights) at 600 °C. When these experiments were repeated under argon (Figure 3.15b), few differences were observed at 200 °C and 400 °C. However, nanocubes heated to 600 °C in argon exhibited 4 new phases – NiFe<sub>2</sub>O<sub>4</sub>, NiO,  $\alpha$ -Fe<sub>2</sub>O<sub>3</sub>, and metallic nickel. The metastable [Ni,Fe]O phase of the nanoparticles therefore appear to be kinetically persistent up to 200 °C, as it is observed that the [Ni,Fe]O phase does not readily decompose below 200 °C despite the fact that it is not the equilibrium phase at these temperatures.

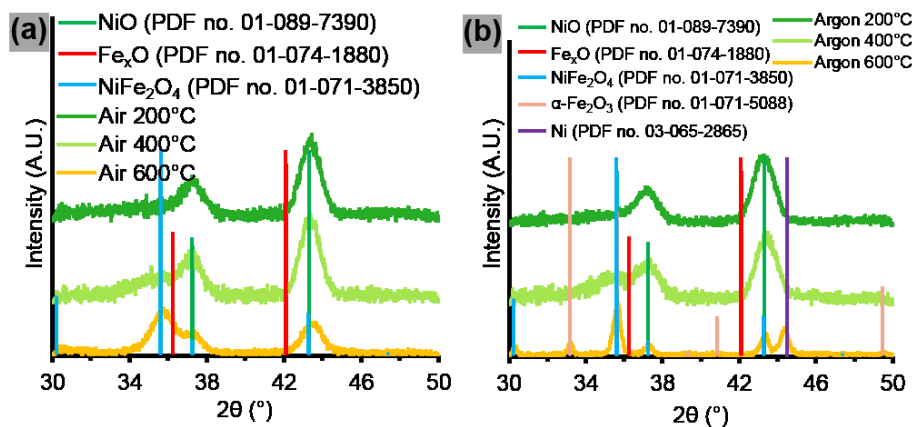


Figure 3.15 Effects of thermal annealing [Ni,Fe]O nanoparticles synthesized with a nickel to iron precursor ratio of 33:67 and decomposition time of 20 min. XRD spectra in (a) air and (b) argon.

On a final note, it is worth speculating why the unique phase was formed. Firstly, a variety of non-equilibrium phases have been reported to form at the nanoscale.<sup>75–77</sup> The most likely explanation for such behaviour is that the size of the crystals permits the stable existence of strained phases. Under larger-scale conditions, these phases would decompose into more thermodynamic structures. Secondly, the synthetic conditions here are reducing. A study on the mechanism of iron oleate-based syntheses suggests that CO derived from the thermal

decomposition of oleate serves as a reducing agent.<sup>63</sup> It has been experimentally demonstrated both here and in the literature that CO can reduce  $\text{Fe}^{3+}$  to  $\text{Fe}^{2+}$  in oleate syntheses, but cannot reduce  $\text{Fe}^{3+}$  to Fe metal.<sup>46,63,78</sup> Therefore, the formation of metallic Ni:Fe nanoparticles is not possible, but the reducing environment prevents the full oxidation of the metals. Under these conditions, the metals form cubic rocksalt nanoparticles, and perhaps the nanoscale environment allows them to preserve this structure upon exposure to ambient atmospheric conditions.

### **3.3 Conclusions**

We have demonstrated the synthesis of monodisperse single-crystal [Ni,Fe]O nanoparticles with a rocksalt crystal structure by thermolysis of a metal oleate precursor. By tuning simple reaction conditions – the decomposition time at 305 °C and the metal ratio within the precursor complex – the shapes and monodispersity could be tuned in a continuous fashion. Specifically, as the nickel to iron precursor ratio is decreased and/or the decomposition time is increased there is a continuous shape transformation from octopod stars, to rounded cubes to spherical nanoparticles, with a subsequent decrease in polydispersity. Moreover, very monodisperse (<10% polydispersity) nanoparticles, less than 10 nm large, could be synthesized. Despite the non-equilibrium phase of the nanoparticles, it is kinetically persistent; evidence of phase changes were not observed after storage under ambient conditions for several months or annealing at 200 °C for 2 h. These nanoparticles also had interesting magnetic properties; the blocking temperature was dependent on the composition and shape of the nanoparticles, but the behaviour

seen in ZFC/FC curves was more reminiscent of  $\text{Fe}_x\text{O}$ . These data, combined with XPS characterization, suggest that the surface of the nanoparticles contains iron in a +3 oxidation state. Together, these data highlight the potential to synthesize a range of solid solution nickel-iron oxide materials with varying properties via a synthetic route that enables access to a metastable phase.

### 3.4 Experimental

**Chemicals.** All chemicals were used as received. Anhydrous  $\text{FeCl}_3$  (98%) was obtained from Strem Chemicals and stored in a  $\text{N}_2$  glovebox.  $\text{NiCl}_2 \cdot 6\text{H}_2\text{O}$  was from ACP Chemicals and sodium oleate (>97%) from Tokyo Chemical Industry. Anhydrous ethanol was obtained from Commercial Alcohols, hexanes and isopropanol from Fisher Chemicals, while oleic acid (technical grade, 90%) and 1-octadecene (technical grade, 90%) were from Sigma-Aldrich.

**Preparation of metal-oleate precursors.** The procedure was based on the previously reported synthesis of ferrite nanoparticles from metal oleates.<sup>36,51</sup> In a typical reaction, 2 mmol of  $\text{NiCl}_2 \cdot 6\text{H}_2\text{O}$ , 4 mmol of  $\text{FeCl}_3$ , and 16 mmol of sodium oleate were dissolved in 10 mL of deionized water, 10 mL of ethanol, and 20 mL of hexane in a 100 mL round bottom flask. The sample was refluxed at 60 °C for 4 hours. After the sample had been cooled to room temperature, the red-brown organic layer containing the metal oleate complex was separated and washed twice with Milli-Q deionized water in a separatory funnel and centrifuged at 3000  $\times g$ .<sup>79</sup> The red-brown liquid was separated and dried in an oven heated to 100 °C under atmospheric pressure for 1 hour to yield a viscous product of metal oleates.<sup>46</sup> For

reactions with varied initial compositions of nickel to iron, the total amount of metal was kept at 6 mmol and 2 mmol of sodium oleate was added for every mmol of nickel and 3 mmol for every mmol of iron, respectively.

**Nanoparticle Synthesis.** The entirety of the preformed metal oleate complex (~4.8 g), as described above, was used as-is and was mixed with 20 mL of 1-octadecene and 0.951 mL of oleic acid in a 250 mL three-neck flask to form a homogenous solution. The flask was evacuated three times using a vacuum Schlenk line and refilled with Ar. The reaction solution was heated to 110 °C and again evacuated three times via the same method. After evacuation, the solution was heated under argon at a heat ramp rate of 3 °C/min to 305 °C, and held at this temperature for 20 min before cooling to room temperature. To isolate the nanoparticles, 40 mL of isopropanol was added. This mixture was then centrifuged at 3000 x g for 10 min. The pellet was re-suspended in 20 mL of hexane, and an equal part of isopropanol was then added before being centrifuged again, in the same manner. Washing was repeated once more. The final pellet was then re-suspended in 20 mL of hexane to form a dark brown solution to yield a concentrated solution of ~15 mg/mL. For yield calculations, thermogravimetric analysis was performed by the University of Alberta Department of Chemistry Analytical and Instrumentation Lab in order to determine the metal oxide portion of the final nanoparticle product.

**Electron Microscopy.** Hexane-diluted nanoparticle solutions of 1 mg/mL were dropped and dried onto 200 mesh copper transmission electron microscope (TEM) grids. Imaging and electron diffraction were performed on a JEOL JEM-

2100 TEM with an accelerating voltage of 200 kV. Selected area electron diffraction (SAED) was acquired on the same system. The distributions of particle area were determined from the TEM micrographs using a thresholding algorithm implemented in Gwyddion.<sup>80</sup> From this, the particle sizes are taken as the square root of particle area.

Further examination of the nanoparticles (bright field images and electron energy loss spectroscopy (EELS)) were acquired on a JEOL JEM-2200FS TEM equipped with a Schottky field-emission gun and an in-column energy filter (Omega filter) and operated at 200 kV accelerating voltage.

Atomic-resolution high-angle annular dark-field scanning TEM (HAADF-STEM) images and energy dispersive X-ray spectroscopy mapping (EDX) were performed on a JEOL JEM-ARM200F spherical aberration corrected STEM/TEM, equipped with a cold-field-emission gun (c-FEG) and operated at 200 kV accelerating voltage.

EDX characterization nanoparticle compositions was performed on a JEOL JSM-6010LA InTouchScope equipped with a Bruker Silicon Drift Detector. Nanoparticle samples were drop-cast on Si wafers. Each composition is the average of three different measurements in separate locations.

**Fourier Transform Infrared Spectroscopy (FTIR).** Scans were collected using a Nicolet Nexus 760 spectrometer with a DTGS detector and a N<sub>2</sub>-purged sample chamber (64 scans, 4 cm<sup>-1</sup> resolution). Metal oleate samples were drop-cast (~10 Ω·cm) Si wafers for data collection in transmission mode.

**X-ray diffraction analysis.** X-ray diffraction (XRD) was performed using a Bruker D8 Discover with a Cu K $\alpha$  beam (40 kV, 40 mA,  $\lambda = 1.5406 \text{ \AA}$ ) equipped with a 2D detector. XRD spectra were collected from the 2D ring patterns by radial integration. Samples were prepared by filling polyethylene terephthalate (PET) capillary tubes with concentrated stock solutions of nanoparticles suspended in hexane. XRD spectra of these samples were then collected in transmission mode. Special care was taken to ensure the samples were correctly aligned to achieve accurate peak positions. Calibration of peak positions was done using a capillary tube filled with a LaB<sub>6</sub> powder. Samples with a planar geometry were prepared by drop-casting nanoparticle solution on silicon (100) substrates. Scans were performed in a grazing incidence configuration with an incident angle of  $\omega = 5^\circ$ . Calibration of peaks was performed with a LaB<sub>6</sub> standard sample. Instrument line broadening was determined to be  $0.28^\circ$ .

**X-ray photoelectron spectroscopy.** X-ray photoelectron spectroscopy (XPS) spectra were collected by Kratos Ultra spectrometer with a base pressure less than  $4 \times 10^{-8} \text{ Pa}$ . A monochromatic Al K $\alpha$  source ( $h\nu = 1486.6 \text{ eV}$ ) was run at a power of 168 W. The analysis spot was  $300 \times 700 \text{ }\mu\text{m}$  and the analyzer resolution was 0.80 eV for Au 4f peaks. The survey scans were collected for binding energies spanning 1100 to 0 eV at constant energy of 160 eV and spectra for narrow regions were collected at pass-energy of 20 eV. Sample charging was compensated by electron flooding. The binding energy (BE) scale was calibrated by assigning C 1s peak from surface contamination at 284.8 eV. Relative concentrations of chemical elements

were calculated using CasaXPS, using a standard quantification routine, including Scofield sensitivity factors and Shirley background subtraction.

**Magnetometry.** Superconducting quantum interference device (SQUID) magnetometry measurements were carried out using a Quantum Design MPMS XL-7S system. Dried powdered samples were loaded into a gelatin capsule, which was sealed with Kapton tape and inserted in a clear diamagnetic plastic straw. Zero field-cooled (ZFC) and field-cooled (FC) measurements were carried out by cooling the samples from 300 to 1.9 K in the absence (ZFC) or presence (FC,  $\mu_0 H = 10$  mT) of an applied magnetic field. A magnetic field strength of 10 mT was applied at 1.9 K, and the magnetization of the sample measured upon warming from 1.9 to 300 K. Isothermal magnetization as a function of field strength measurements were also carried out at temperatures of 1.9 and 300 K by cycling the applied magnetic field strength between 7 and -7 T.

### 3.5 Contributions

Project design, experiments, and analysis were carried out by J.A. Bau. P. Li performed EELS, TEM-EDX, and HAADF-STEM. A.J. Marengo and S. Trudel performed magnetic measurements and helped with analysis of this data. E.J. Lubner and B.C. Olsen assisted with analysis.

### 3.6 References

- (1) Jiang, J.; Li, Y.; Liu, J.; Huang, X.; Yuan, C.; Lou, X. W. (David). Recent Advances in Metal Oxide-Based Electrode Architecture Design for Electrochemical Energy Storage. *Adv. Mater.* **2012**, *24* (38), 5166–5180.

- (2) Liu, C.; Li, F.; Ma, L.-P.; Cheng, H.-M. Advanced Materials for Energy Storage. *Adv. Mater.* **2010**, *22* (8), E28–E62.
- (3) Reddy, M. V.; Subba Rao, G. V.; Chowdari, B. V. R. Metal Oxides and Oxysalts as Anode Materials for Li Ion Batteries. *Chem. Rev.* **2013**, *113* (7), 5364–5457.
- (4) Deng, W.; Ji, X.; Chen, Q.; Banks, C. E. Electrochemical Capacitors Utilising Transition Metal Oxides: An Update of Recent Developments. *RSC Adv.* **2011**, *1* (7), 1171–1178.
- (5) Sassin, M. B.; Chervin, C. N.; Rolison, D. R.; Long, J. W. Redox Deposition of Nanoscale Metal Oxides on Carbon for Next-Generation Electrochemical Capacitors. *Acc. Chem. Res.* **2013**, *46* (5), 1062–1074.
- (6) Suntivich, J.; Gasteiger, H. A.; Yabuuchi, N.; Nakanishi, H.; Goodenough, J. B.; Shao-Horn, Y. Design Principles for Oxygen-Reduction Activity on Perovskite Oxide Catalysts for Fuel Cells and Metal–air Batteries. *Nat. Chem.* **2011**, *3* (7), 546–550.
- (7) Chen, Z.; Higgins, D.; Yu, A.; Zhang, L.; Zhang, J. A Review on Non-Precious Metal Electrocatalysts for PEM Fuel Cells. *Energy Environ. Sci.* **2011**, *4* (9), 3167–3192.
- (8) Wang, C.; Yin, L.; Zhang, L.; Xiang, D.; Gao, R. Metal Oxide Gas Sensors: Sensitivity and Influencing Factors. *Sensors* **2010**, *10* (3), 2088–2106.
- (9) Zakrzewska, K. Mixed Oxides as Gas Sensors. *Thin Solid Films* **2001**, *391* (2), 229–238.
- (10) Kim, M.-G.; Kanatzidis, M. G.; Facchetti, A.; Marks, T. J. Low-Temperature Fabrication of High-Performance Metal Oxide Thin-Film Electronics via Combustion Processing. *Nat. Mater.* **2011**, *10* (5), 382–388.
- (11) Banger, K. K.; Yamashita, Y.; Mori, K.; Peterson, R. L.; Leedham, T.; Rickard, J.; Siringhaus, H. Low-Temperature, High-Performance Solution-Processed Metal Oxide Thin-Film Transistors Formed by a “sol–gel on Chip” Process. *Nat. Mater.* **2011**, *10* (1), 45–50.
- (12) Jeong, S.; Moon, J. Low-Temperature, Solution-Processed Metal Oxide Thin Film Transistors. *J. Mater. Chem.* **2012**, *22* (4), 1243.
- (13) Irie, H.; Watanabe, Y.; Hashimoto, K. Nitrogen-Concentration Dependence on Photocatalytic Activity of  $\text{TiO}_{2-x}\text{N}_x$  Powders. *J. Phys. Chem. B* **2003**, *107* (23), 5483–5486.

- (14) Amano, F.; Yamakata, A.; Nogami, K.; Osawa, M.; Ohtani, B. Visible Light Responsive Pristine Metal Oxide Photocatalyst: Enhancement of Activity by Crystallization under Hydrothermal Treatment. *J. Am. Chem. Soc.* **2008**, *130* (52), 17650–17651.
- (15) Liu, W.; Ye, H.; Bard, A. J. Screening of Novel Metal Oxide Photocatalysts by Scanning Electrochemical Microscopy and Research of Their Photoelectrochemical Properties. *J. Phys. Chem. C* **2009**, *114* (2), 1201–1207.
- (16) Galatsis, K.; Li, Y. X.; Wlodarski, W.; Comini, E.; Sberveglieri, G.; Cantalini, C.; Santucci, S.; Passacantando, M. Comparison of Single and Binary Oxide MoO<sub>3</sub>, TiO<sub>2</sub> and WO<sub>3</sub> Sol–gel Gas Sensors. *Sens. Actuators B Chem.* **2002**, *83* (1–3), 276–280.
- (17) Wang, D.; Kako, T.; Ye, J. Efficient Photocatalytic Decomposition of Acetaldehyde over a Solid-Solution Perovskite (Ag<sub>0.75</sub>Sr<sub>0.25</sub>)(Nb<sub>0.75</sub>Ti<sub>0.25</sub>)O<sub>3</sub> under Visible-Light Irradiation. *J. Am. Chem. Soc.* **2008**, *130* (9), 2724–2725.
- (18) Machida, M.; Yabunaka, J.; Kijima, T. Synthesis and Photocatalytic Property of Layered Perovskite Tantalates, RbLnTa<sub>2</sub>O<sub>7</sub> (Ln = La, Pr, Nd, and Sm). *Chem. Mater.* **2000**, *12* (3), 812–817.
- (19) Toroker, M. C.; Carter, E. A. Transition Metal Oxide Alloys as Potential Solar Energy Conversion Materials. *J. Mater. Chem. A* **2013**, *1* (7), 2474–2484.
- (20) Maeda, K.; Domen, K. Solid Solution of GaN and ZnO as a Stable Photocatalyst for Overall Water Splitting under Visible Light†. *Chem. Mater.* **2010**, *22* (3), 612–623.
- (21) Su, F.-Z.; Liu, Y.-M.; Wang, L.-C.; Cao, Y.; He, H.-Y.; Fan, K.-N. Ga–Al Mixed-Oxide-Supported Gold Nanoparticles with Enhanced Activity for Aerobic Alcohol Oxidation. *Angew. Chem.* **2008**, *120* (2), 340–343.
- (22) Smith, R. D. L.; Prévot, M. S.; Fagan, R. D.; Trudel, S.; Berlinguette, C. P. Water Oxidation Catalysis: Electrochemical Response to Metal Stoichiometry in Amorphous Metal Oxide Films Containing Iron, Cobalt, and Nickel. *J. Am. Chem. Soc.* **2013**, *135* (31), 11580–11586.
- (23) Sadakane, M.; Watanabe, N.; Katou, T.; Nodasaka, Y.; Ueda, W. Crystalline Mo<sub>3</sub>VO<sub>x</sub> Mixed-Metal-Oxide Catalyst with Trigonal Symmetry. *Angew. Chem. Int. Ed.* **2007**, *46* (9), 1493–1496.
- (24) Royer, S.; Duprez, D. Catalytic Oxidation of Carbon Monoxide over Transition Metal Oxides. *ChemCatChem* **2011**, *3* (1), 24–65.

- (25) Dawood, F.; Leonard, B. M.; Schaak, R. E. Oxidative Transformation of Intermetallic Nanoparticles: An Alternative Pathway to Metal/Oxide Nanocomposites, Textured Ceramics, and Nanocrystalline Multimetal Oxides. *Chem. Mater.* **2007**, *19* (18), 4545–4550.
- (26) Wang, Z.; Zhou, L.; (David) Lou, X. W. Metal Oxide Hollow Nanostructures for Lithium-Ion Batteries. *Adv. Mater.* **2012**, *24* (14), 1903–1911.
- (27) Sharma, Y.; Sharma, N.; Subba Rao, G. V.; Chowdari, B. V. R. Nanophase ZnCo<sub>2</sub>O<sub>4</sub> as a High Performance Anode Material for Li-Ion Batteries. *Adv. Funct. Mater.* **2007**, *17* (15), 2855–2861.
- (28) Henkes, A. E.; Bauer, J. C.; Sra, A. K.; Johnson, R. D.; Cable, R. E.; Schaak, R. E. Low-Temperature Nanoparticle-Directed Solid-State Synthesis of Ternary and Quaternary Transition Metal Oxides. *Chem. Mater.* **2006**, *18* (2), 567–571.
- (29) Dunkle, S. S.; Helmich, R. J.; Suslick, K. S. BiVO<sub>4</sub> as a Visible-Light Photocatalyst Prepared by Ultrasonic Spray Pyrolysis. *J. Phys. Chem. C* **2009**, *113* (28), 11980–11983.
- (30) Azurdia, J. A.; Marchal, J.; Shea, P.; Sun, H.; Pan, X. Q.; Laine, R. M. Liquid-Feed Flame Spray Pyrolysis as a Method of Producing Mixed-Metal Oxide Nanopowders of Potential Interest as Catalytic Materials. Nanopowders along the NiO–Al<sub>2</sub>O<sub>3</sub> Tie Line Including (NiO)<sub>0.22</sub>(Al<sub>2</sub>O<sub>3</sub>)<sub>0.78</sub>, a New Inverse Spinell Composition. *Chem. Mater.* **2006**, *18* (3), 731–739.
- (31) Subban, C. V.; Zhou, Q.; Hu, A.; Moylan, T. E.; Wagner, F. T.; DiSalvo, F. J. Sol–Gel Synthesis, Electrochemical Characterization, and Stability Testing of Ti<sub>0.7</sub>W<sub>0.3</sub>O<sub>2</sub> Nanoparticles for Catalyst Support Applications in Proton-Exchange Membrane Fuel Cells. *J. Am. Chem. Soc.* **2010**, *132* (49), 17531–17536.
- (32) Debecker, D. P.; Mutin, P. H. Non-Hydrolytic Sol–gel Routes to Heterogeneous Catalysts. *Chem. Soc. Rev.* **2012**, *41* (9), 3624–3650.
- (33) Chandler, C. D.; Roger, C.; Hampden-Smith, M. J. Chemical Aspects of Solution Routes to Perovskite-Phase Mixed-Metal Oxides from Metal-Organic Precursors. *Chem. Rev.* **1993**, *93* (3), 1205–1241.
- (34) Spooren, J.; Rumblecker, A.; Millange, F.; Walton, R. I. Subcritical Hydrothermal Synthesis of Perovskite Manganites: A Direct and Rapid Route to Complex Transition-Metal Oxides. *Chem. Mater.* **2003**, *15* (7), 1401–1403.

- (35) Nguyen, T.-D.; Dinh, C.-T.; Do, T.-O. A General Procedure to Synthesize Highly Crystalline Metal Oxide and Mixed Oxide Nanocrystals in Aqueous Medium and Photocatalytic Activity of Metal/oxide Nanohybrids. *Nanoscale* **2011**, *3* (4), 1861–1873.
- (36) Bao, N.; Shen, L.; Wang, Y.; Padhan, P.; Gupta, A. A Facile Thermolysis Route to Monodisperse Ferrite Nanocrystals. *J. Am. Chem. Soc.* **2007**, *129* (41), 12374–12375.
- (37) Sun, S.; Zeng, H.; Robinson, D. B.; Raoux, S.; Rice, P. M.; Wang, S. X.; Li, G. Monodisperse  $MFe_2O_4$  ( $M = Fe, Co, Mn$ ) Nanoparticles. *J. Am. Chem. Soc.* **2004**, *126* (1), 273–279.
- (38) Chen, D.-H.; He, X.-R. Synthesis of Nickel Ferrite Nanoparticles by Sol-Gel Method. *Mater. Res. Bull.* **2001**, *36* (7–8), 1369–1377.
- (39) Zhou, J.; Ma, J.; Sun, C.; Xie, L.; Zhao, Z.; Tian, H.; Wang, Y.; Tao, J.; Zhu, X. Low-Temperature Synthesis of  $NiFe_2O_4$  by a Hydrothermal Method. *J. Am. Ceram. Soc.* **2005**, *88* (12), 3535–3537.
- (40) Wang, J.; Cai, J.; Lin, Y.-H.; Nan, C.-W. Room-Temperature Ferromagnetism Observed in Fe-Doped NiO. *Appl. Phys. Lett.* **2005**, *87* (20), 202501–202501 – 3.
- (41) Mallick, P.; Rath, C.; Biswal, R.; Mishra, N. C. Structural and Magnetic Properties of Fe Doped NiO. *Indian J. Phys.* **2009**, *83* (4), 517–523.
- (42) Manna, S.; Deb, A. K.; Jagannath, J.; De, S. K. Synthesis and Room Temperature Ferromagnetism in Fe Doped NiO Nanorods. *J. Phys. Chem. C* **2008**, *112* (29), 10659–10662.
- (43) He, J. H.; Yuan, S. L.; Yin, Y. S.; Tian, Z. M.; Li, P.; Wang, Y. Q.; Liu, K. L.; Wang, C. H. Exchange Bias and the Origin of Room-Temperature Ferromagnetism in Fe-Doped NiO Bulk Samples. *J. Appl. Phys.* **2008**, *103* (2), 023906.
- (44) Moura, K. O.; Lima, R. J. S.; Coelho, A. A.; Souza-Junior, E. A.; Duque, J. G. S.; Meneses, C. T. Tuning the Surface Anisotropy in Fe-Doped NiO Nanoparticles. *Nanoscale* **2014**, *6* (1), 352.
- (45) Rhamdhani, M. A.; Hayes, P. C.; Jak, E. Subsolidus Phase Equilibria of the Fe-Ni-O System. *Metall. Mater. Trans. B* **2008**, *39* (5), 690–701.
- (46) Bronstein, L. M.; Huang, X.; Retrum, J.; Schmucker, A.; Pink, M.; Stein, B. D.; Dragnea, B. Influence of Iron Oleate Complex Structure on Iron Oxide Nanoparticle Formation. *Chem. Mater.* **2007**, *19* (15), 3624–3632.

- (47) Laurent, S.; Forge, D.; Port, M.; Roch, A.; Robic, C.; Vander Elst, L.; Muller, R. N. Magnetic Iron Oxide Nanoparticles: Synthesis, Stabilization, Vectorization, Physicochemical Characterizations, and Biological Applications. *Chem. Rev.* **2008**, *108* (6), 2064–2110.
- (48) Niederberger, M. Nonaqueous Sol–Gel Routes to Metal Oxide Nanoparticles. *Acc. Chem. Res.* **2007**, *40* (9), 793–800.
- (49) Lu, A.-H.; Salabas, E. L.; Schüth, F. Magnetic Nanoparticles: Synthesis, Protection, Functionalization, and Application. *Angew. Chem. Int. Ed.* **2007**, *46* (8), 1222–1244.
- (50) Kwon, S. G.; Hyeon, T. Colloidal Chemical Synthesis and Formation Kinetics of Uniformly Sized Nanocrystals of Metals, Oxides, and Chalcogenides. *Acc. Chem. Res.* **2008**, *41* (12), 1696–1709.
- (51) Park, J.; An, K.; Hwang, Y.; Park, J.-G.; Noh, H.-J.; Kim, J.-Y.; Park, J.-H.; Hwang, N.-M.; Hyeon, T. Ultra-Large-Scale Syntheses of Monodisperse Nanocrystals. *Nat. Mater.* **2004**, *3* (12), 891–895.
- (52) Gu, H.; Soucek, M. D. Preparation and Characterization of Monodisperse Cerium Oxide Nanoparticles in Hydrocarbon Solvents. *Chem. Mater.* **2007**, *19* (5), 1103–1110.
- (53) Jette, E. R.; Foote, F. An X-Ray Study of the Wüstite (FeO) Solid Solutions. *J. Chem. Phys.* **2004**, *1* (1), 29–36.
- (54) Roth, W. L. Multispin Axis Structures for Antiferromagnets. *Phys. Rev.* **1958**, *111* (3), 772–781.
- (55) King, H. W. Quantitative Size-Factors for Metallic Solid Solutions. *J. Mater. Sci.* **1966**, *1* (1), 79–90.
- (56) Castellanos, M.; West, A. R. Deviations from Vegard's Law in Oxide Solid Solutions. The Systems  $\text{Li}_2\text{TiO}_3\text{--MgO}$  and  $\text{Li}_2\text{TiO}_3\text{--Na}_2\text{TiO}_3$ . *J. Chem. Soc. Faraday Trans. 1 Phys. Chem. Condens. Phases* **1980**, *76* (0), 2159.,
- (57) Leapman, R. D.; Grunes, L. A.; Fejes, P. L. Study of the L23 Edges in the 3d Transition Metals and Their Oxides by Electron-Energy-Loss Spectroscopy with Comparisons to Theory. *Phys. Rev. B* **1982**, *26* (2), 614–635.
- (58) Schedel-Niedrig, T.; Weiss, W.; Schlögl, R. Electronic Structure of Ultrathin Ordered Iron Oxide Films Grown onto Pt(111). *Phys. Rev. B* **1995**, *52* (24), 17449–17460.

- (59) Temesghen, W.; Sherwood, P. Analytical Utility of Valence Band X-Ray Photoelectron Spectroscopy of Iron and Its Oxides, with Spectral Interpretation by Cluster and Band Structure Calculations. *Anal. Bioanal. Chem.* **2002**, *373* (7), 601–608.
- (60) Kim, K. S.; Winograd, N. X-Ray Photoelectron Spectroscopic Studies of Nickel-Oxygen Surfaces Using Oxygen and Argon Ion-Bombardment. *Surf. Sci.* **1974**, *43* (2), 625–643.
- (61) Mansour, A. N. Characterization of NiO by XPS. *Surf. Sci. Spectra* **1994**, *3* (3), 231–238.
- (62) Yang, J.; Ling, T.; Wu, W.-T.; Liu, H.; Gao, M.-R.; Ling, C.; Li, L.; Du, X.-W. A Top-down Strategy towards Monodisperse Colloidal Lead Sulphide Quantum Dots. *Nat. Commun.* **2013**, *4*, 1695.
- (63) Hai, H. T.; Yang, H. T.; Kura, H.; Hasegawa, D.; Ogata, Y.; Takahashi, M.; Ogawa, T. Size Control and Characterization of Wüstite (core)/spinel (shell) Nanocubes Obtained by Decomposition of Iron Oleate Complex. *J. Colloid Interface Sci.* **2010**, *346* (1), 37–42.
- (64) Pichon, B. P.; Gerber, O.; Lefevre, C.; Florea, I.; Fleutot, S.; Baaziz, W.; Pauly, M.; Ohlmann, M.; Ulhaq, C.; Ersen, O.; et al. Microstructural and Magnetic Investigations of Wüstite-Spinel Core-Shell Cubic-Shaped Nanoparticles. *Chem. Mater.* **2011**, *23* (11), 2886–2900.
- (65) Bronstein, L. M.; Atkinson, J. E.; Malyutin, A. G.; Kidwai, F.; Stein, B. D.; Morgan, D. G.; Perry, J. M.; Karty, J. A. Nanoparticles by Decomposition of Long Chain Iron Carboxylates: From Spheres to Stars and Cubes. *Langmuir* **2011**, *27* (6), 3044–3050.
- (66) Zhen, G.; Muir, B. W.; Moffat, B. A.; Harbour, P.; Murray, K. S.; Moubaraki, B.; Suzuki, K.; Madsen, I.; Agron-Olshina, N.; Waddington, L.; et al. Comparative Study of the Magnetic Behavior of Spherical and Cubic Superparamagnetic Iron Oxide Nanoparticles. *J. Phys. Chem. C* **2011**, *115* (2), 327–334.
- (67) Kovalenko, M. V.; Bodnarchuk, M. I.; Lechner, R. T.; Hesser, G.; Schäffler, F.; Heiss, W. Fatty Acid Salts as Stabilizers in Size- and Shape-Controlled Nanocrystal Synthesis: The Case of Inverse Spinel Iron Oxide. *J. Am. Chem. Soc.* **2007**, *129* (20), 6352–6353.
- (68) Na, H. B.; Song, I. C.; Hyeon, T. Inorganic Nanoparticles for MRI Contrast Agents. *Adv. Mater.* **2009**, *21* (21), 2133–2148.

- (69) Schuele, W. J.; Deetscreek, V. D. Appearance of a Weak Ferromagnetism in Fine Particles of Antiferromagnetic Materials. *J. Appl. Phys.* **1962**, *33* (3), 1136–1137.
- (70) Kodama, R. H.; Makhlof, S. A.; Berkowitz, A. E. Finite Size Effects in Antiferromagnetic NiO Nanoparticles. *Phys. Rev. Lett.* **1997**, *79* (7), 1393–1396.
- (71) Richardson, J. T.; Yiagas, D. I.; Turk, B.; Forster, K.; Twigg, M. V. Origin of Superparamagnetism in Nickel Oxide. *J. Appl. Phys.* **1991**, *70* (11), 6977–6982.
- (72) Cornell, R. M.; Schwertmann, U. *The Iron Oxides: Structure, Properties, Reactions, Occurrences and Uses*; John Wiley & Sons, 2003.
- (73) Rao, C. N. R.; Raveau, B. *Transition Metal Oxides*; Wiley, 1995.
- (74) Glaria, A.; Kahn, M. L.; Lecante, P.; Barbara, B.; Chaudret, B. Fe<sub>1-y</sub>O Nanoparticles: Organometallic Synthesis and Magnetic Properties. *ChemPhysChem* **2008**, *9* (5), 776–780.
- (75) Kusada, K.; Kobayashi, H.; Yamamoto, T.; Matsumura, S.; Sumi, N.; Sato, K.; Nagaoka, K.; Kubota, Y.; Kitagawa, H. Discovery of Face-Centered-Cubic Ruthenium Nanoparticles: Facile Size-Controlled Synthesis Using the Chemical Reduction Method. *J. Am. Chem. Soc.* **2013**, *135* (15), 5493–5496.
- (76) Dinega, D. P.; Bawendi, M. G. A Solution-Phase Chemical Approach to a New Crystal Structure of Cobalt. *Angew. Chem. Int. Ed.* **1999**, *38* (12), 1788–1791.
- (77) Soriano, R. B.; Wu, J.; Kanatzidis, M. G. Size as a Parameter to Stabilize New Phases: Rock Salt Phases of Pb<sub>m</sub>Sb<sub>2n</sub>Se<sub>m+3n</sub>. *J. Am. Chem. Soc.* **2015**.
- (78) Park, J.; Lee, E.; Hwang, N.-M.; Kang, M.; Kim, S. C.; Hwang, Y.; Park, J.-G.; Noh, H.-J.; Kim, J.-Y.; Park, J.-H.; et al. One-Nanometer-Scale Size-Controlled Synthesis of Monodisperse Magnetic Iron Oxide Nanoparticles. *Angew. Chem.* **2005**, *117* (19), 2932–2937.
- (79) Buck, M. R.; Biacchi, A. J.; Schaak, R. E. Insights into the Thermal Decomposition of Co(II) Oleate for the Shape-Controlled Synthesis of Wurtzite-Type CoO Nanocrystals. *Chem. Mater.* **2014**, *26* (3), 1492–1499.
- (80) Nečas, D.; Klapetek, P. Gwyddion: An Open-Source Software for SPM Data Analysis. *Cent. Eur. J. Phys.* **2012**, *10* (1), 181–188.

# 4 [Ni,Fe]O Nanoparticles as Water Oxidation Electrocatalysts

## 4.1 Introduction

### 4.1.1 Overview

Having synthesized of a novel nickel-iron oxide compound in the previous chapter, the focus now becomes studying what potential electrocatalytic properties that these nanoparticles might have for water oxidation. The surface of these nanoparticles consists of a mixture of bivalent nickel/trivalent iron, forming a unique mixed-valence shell that protects the nanoparticle structure from the decomposition seen in pure  $\text{Fe}_x\text{O}$  nanoparticles.<sup>1</sup> Because of the structural combination of a unique crystal phase surrounded by a less ordered surface, these nanoparticles make an excellent case study for understanding the role of structure in nickel iron oxide catalysis of water oxidation. This chapter has two objectives: firstly, to describe a functionalization method that does not affect the metastable phase of the nanoparticles; and secondly, to understand the electrocatalytic properties of this material, if any.

### 4.1.2 Material constraints of current water splitting electrocatalysts

Although high activity electrocatalysts for water oxidation and hydrogen evolution do exist, such materials are typically limited by cost; platinum, iridium,

and ruthenium and their oxides are three extremely scarce materials that are usually cited as being some of the best water splitting electrocatalysts.<sup>2-4</sup> For the more kinetically challenging water oxidation reaction, such a problem is especially pertinent as the overpotential achievable by iridium and ruthenium oxides at a current density of 10 mA/cm<sup>2</sup> is typically less than 0.20 V,<sup>5-7</sup> whereas the same value for pure nickel oxide (the best monometallic earth abundant material) typically lies around 0.40 V.<sup>8-13</sup> For the reverse hydrogen evolution reaction, the overpotential on platinum group elements is typically 0.05 V, but recent studies have revealed that first row transition metal phosphides of cobalt, nickel, and iron can carry out the same reaction at comparable (though marginally higher) overpotentials compared to platinum.<sup>14-16</sup> Therefore, in the implementation of a hydrogen economy, the development of earth-abundant water oxidation electrocatalysts is a more pressing matter.

#### **4.1.3 First-row transition metal oxides as water oxidation catalysts**

Fortunately, there is a strong suggestion that earth abundant oxides have the potential to carry out water splitting at significant rates in the form of the oxygen-evolving complex of photosystem II, which is responsible for oxygen evolution in photosynthetic organisms such as plants and algae. In this complex, water oxidation is carried out by a unique Mn<sub>3</sub>Ca cubane catalytic site where each metal is surrounded by oxygen in a cubic configuration.<sup>17</sup> This catalytic site has been the source of inspiration for a series of manganese-based artificial molecular and heterogenous systems, ranging from analogous cubanes to simple manganese oxide

films.<sup>18-23</sup> Meanwhile, nickel oxide has long been known as an efficient water oxidation catalyst regardless of differences in preparation method and is the metal oxide behind the 0.40 V overpotential at 10 mA/cm<sup>2</sup> – the lowest recorded for a pure first-row transition metal oxide.<sup>8-10</sup> In addition, various systems based on cobalt oxides and iron oxides have also demonstrated that oxides of these metals can also be catalytic.<sup>24-28</sup>

#### 4.1.4 Compositional and structural considerations for catalyst design

Mixtures of first-row transition metals can also be combined to produce multi-metallic catalysts, some of which have superior catalytic activities compared to monometallic oxides.<sup>13,29-32</sup> This synergy can be further optimized through controlling the composition of the electrode systems, in addition to ordinary controls like electrode feature size and catalyst layer thickness.<sup>13,30,33</sup> Another potential factor to consider is the crystal phase of the constituent elements; while amorphous metal oxides are known to catalyze water oxidation at low overpotentials,<sup>29</sup> other catalysts like the barium strontium cobalt iron (BSCF) perovskite reported by Suntivich et al. acquire their characteristic low overpotentials because of their crystal structures.<sup>28</sup> This picture is further complicated by the possibility that amorphous materials are catalytic because of the *in situ* formation of cubane catalytic sites.<sup>34-37</sup> Given the wide variety of structural and compositional possibilities, the potential for developing novel, efficient water oxidation systems based on compositionally abundant and structurally ideal designs is limitless, but only if these characteristics are properly understood.

## 4.2 Results

### 4.2.1 Functionalization of Electrode Surfaces with Nanoparticles

In order to study the catalytic properties of these nanoparticles for water oxidation, it was necessary to develop a procedure that would allow for the formation of durable films of nanoparticles on electrode surfaces. Since the ultimate goal was to determine what effect, if any, that the [Ni,Fe]O phase had on water oxidation catalysis, it was important that the procedure not destroy the unique structure of the nanoparticles. Three different electrode functionalization approaches were compared – spin-coating (“untreated”), spin-coating followed by a ten second air plasma treatment at 0.2 torr at 18 W (“plasma-treated”), and spin-coating followed by ultraviolet (254 nm) irradiation for 1 hour (“UV-treated”). The films were spun from 2 mg/mL solutions of Ni:Fe 51:49 nanoparticles (Figure 4.1).

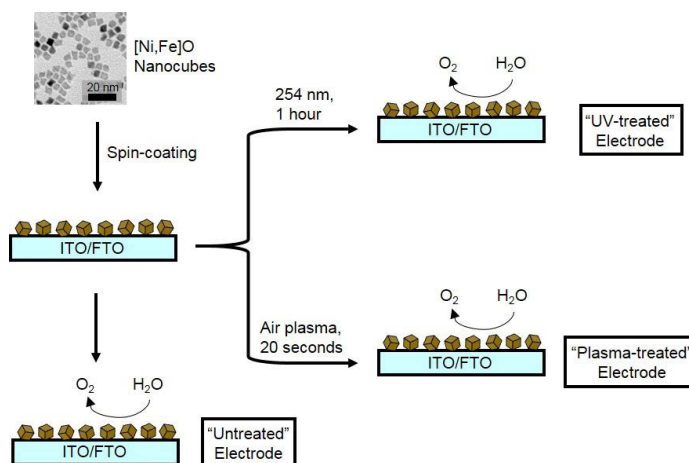


Figure 4.1 Functionalization scheme of transparent conducting oxide electrodes with [Ni,Fe]O nanoparticles

Air plasma treatment was selected as a treatment method because it has been shown to remove organic ligands with minimal changes to inorganic structures and surfaces,<sup>38</sup> while UV treatment was chosen because UV irradiation has been used to convert metal 2-ethylhexanoate precursors into amorphous metal oxide films.<sup>29</sup> Since metal ethylhexanoates and metal oleate bonds share similar carboxylate-metal interactions, irradiation of nanoparticles was expected to yield similarly robust films. Upon each functionalization treatment, all electrodes were optically similar as determined by UV-visible spectrometry (Figure 4.2a), where the presence of nanoparticles could be clearly distinguished by their strong absorption in the 350 – 500 nm range (Figure 4.2b) when compared to bare ITO.

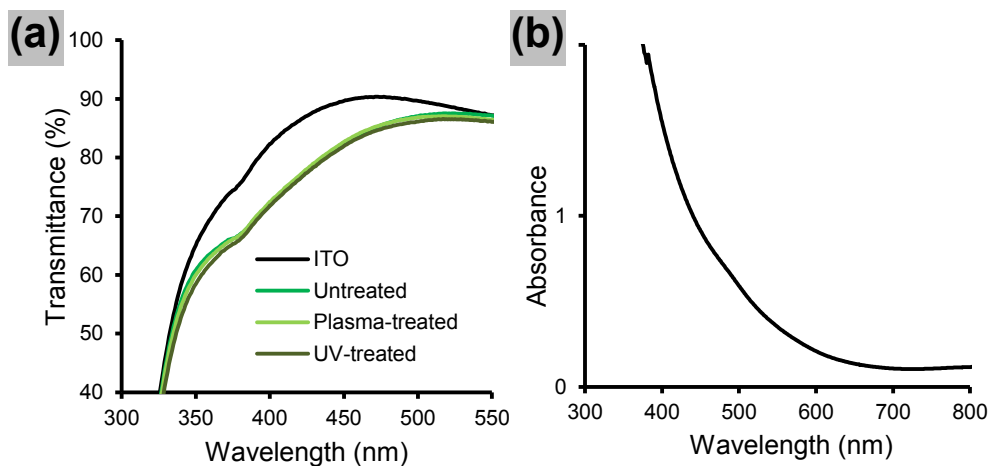


Figure 4.2 (a) UV-vis spectra of differently functionalized ITO electrodes. (b) UV-vis spectra of a concentrated solution of nanoparticles dissolved in hexane.

After functionalization, water oxidation activity was measured in 0.1 M KOH. The potential of the electrodes was scanned positive from open circuit potential until the current density reached 10 mA/cm<sup>2</sup> and then returned to open circuit potential, repeating this cycle until the overpotential ceased to change (Figure 4.3).

The water oxidation overpotential at 10 mA/cm<sup>2</sup> of UV-treated electrodes typically stopped changing after two or three cycles, while the water oxidation overpotential for plasma-treated and untreated electrodes took up to ten cycles to stabilize.

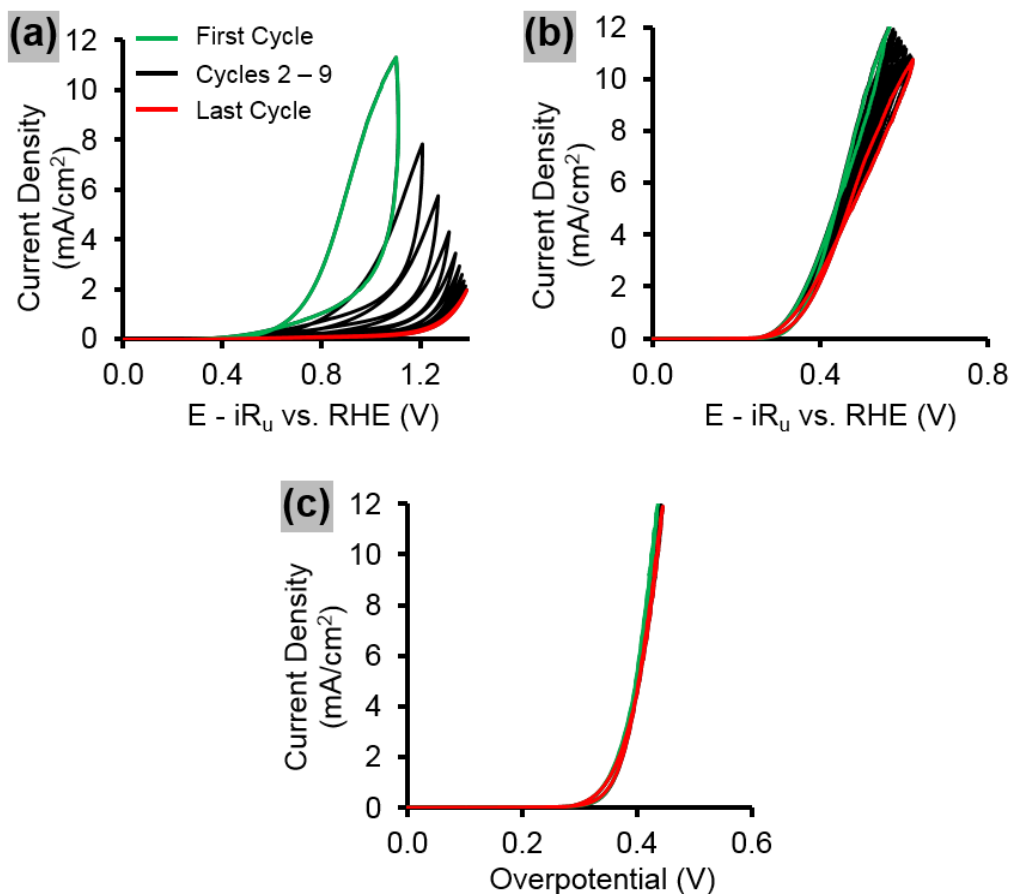


Figure 4.3 Cyclic voltammograms (first 10 cycles, sweep rate 50 mV/s) of ITO electrodes functionalized with Ni:Fe 51:49 [Ni,Fe]O nanoparticles via spin-coating, followed by (a) no further treatment (untreated), (b) air plasma for 10 seconds, and (c) 1 hour of UV irradiation with 254 nm light, repeated until traces became stable. The electrolyte was 0.1 M KOH. Green traces represent the first of ten cycles, red traces represent the tenth cycle.

UV-treated electrodes had the lowest overpotentials for water oxidation (0.43 V) at a current density of 10 mA/cm<sup>2</sup> (Figure 4.4a), while plasma-treated electrodes had overpotentials of 0.60 V at the same current density. However, untreated

electrodes rapidly lost activity such that when the voltammograms finally reached stability, the voltammograms of the untreated electrodes appeared similar in catalytic activity to bare ITO. This trend in overpotentials was reflected by the trend in UV-vis spectra of the electrodes post-voltammetry, where UV-treated electrodes underwent no change in light absorption compared to an untreated electrode not used for voltammetry. In contrast, plasma-treated electrodes and untreated electrodes had reduced absorption and a near-complete loss in absorption in the 350 – 500 nm region, respectively, when compared to an untreated electrode before voltammetry (Figure 4.4b). The stability of UV-treated electrodes was also studied by chronopotentiometry; under the stability testing criteria suggested by McCrory et al. of 10 mA/cm<sup>2</sup> for 2 hours,<sup>31</sup> the UV-treated electrode demonstrated an increase in overpotential by 40 mV (Figure 4.4c). This increase in overpotential exists within the range of increases seen by the wide selection of catalysts studied by McCrory et al.<sup>39</sup>

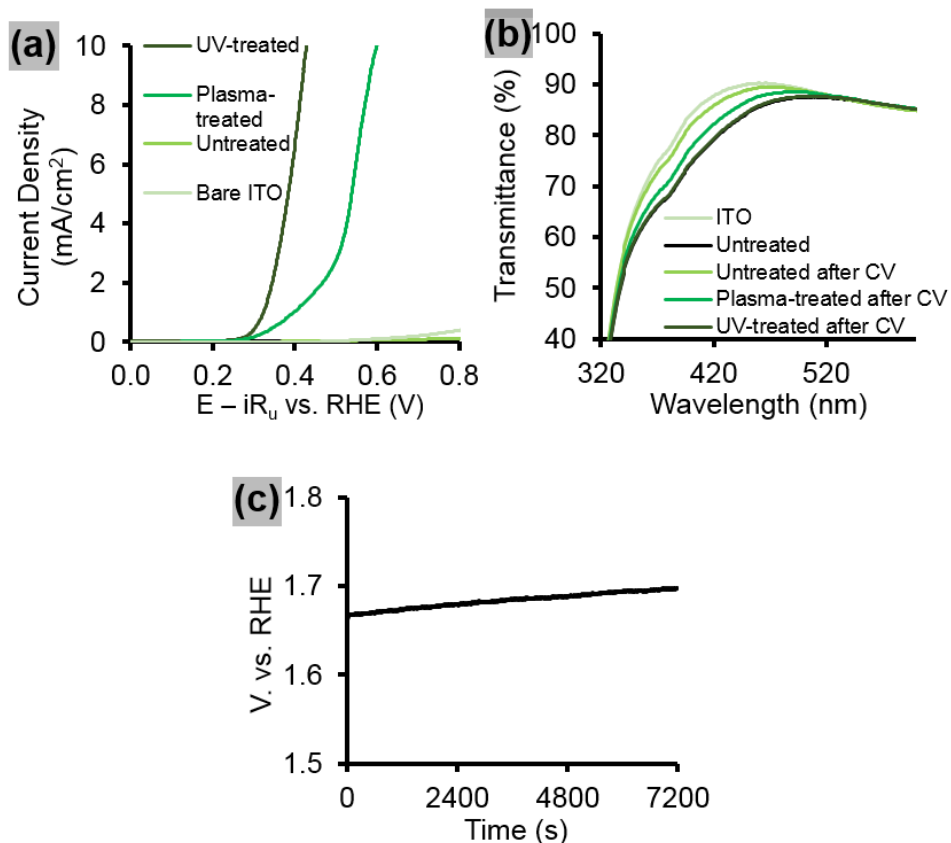


Figure 4.4 (a) Voltammograms of ITO electrodes functionalized with Ni:Fe 51:49 [Ni,Fe]O nanoparticles via spin-coating, followed by 1 hour of UV irradiation with 254 nm light (UV-treated), air plasma for 10 seconds (plasma-treated), and no further treatment (untreated), as well as a nanoparticle-free ITO control, in 0.1 M KOH. (b) UV-vis spectra of UV-treated, plasma-treated, and untreated [Ni,Fe]O electrodes before and after voltammetry in (a). (c) Chronopotentiometry trace of UV-treated [Ni,Fe]O electrodes held at a current density of 10 mA/cm<sup>2</sup> for 2 hours in 0.1 M KOH.

Physical differences between these three electrodes were examined using SEM before and after voltammetry. SEM inspection of untreated nanoparticle electrodes that had not been UV- or plasma-treated appeared as mostly conformal nanoparticle films with some regions of exposed ITO (Figure 4.5a). However, after voltammetry, these electrodes lost much of their nanoparticle coverage to yield mostly bare surfaces (Figure 4.5b). Plasma-treatment did not affect the initial

appearance of electrodes (Figure 4.5c), but upon voltammetry, much of the nanoparticle film was removed from the substrate (Figure 4.5d). Finally, UV-treated nanoparticle films were not visibly affected by the UV treatment (Figure 4.5e) and remained similar in appearance after voltammetry (Figure 4.5f), suggesting that of the functionalization procedures attempted, only UV irradiation was successful at forming films of nanoparticles with stable adhesion to the ITO. A micrograph of bare ITO has been provided for comparison (Figure 4.5g). The data imply that losses in catalytic activity arise primarily from losses in nanoparticle coverage, and that the reduction in UV-vis absorption seen in untreated and plasma-treated electrodes arises from a loss of adhered nanoparticles. In contrast, the superior catalytic activity of UV-treated Ni:Fe nanoparticle electrodes appears to arise from the improved durability and resulting nanoparticle coverage of ITO in these electrodes.

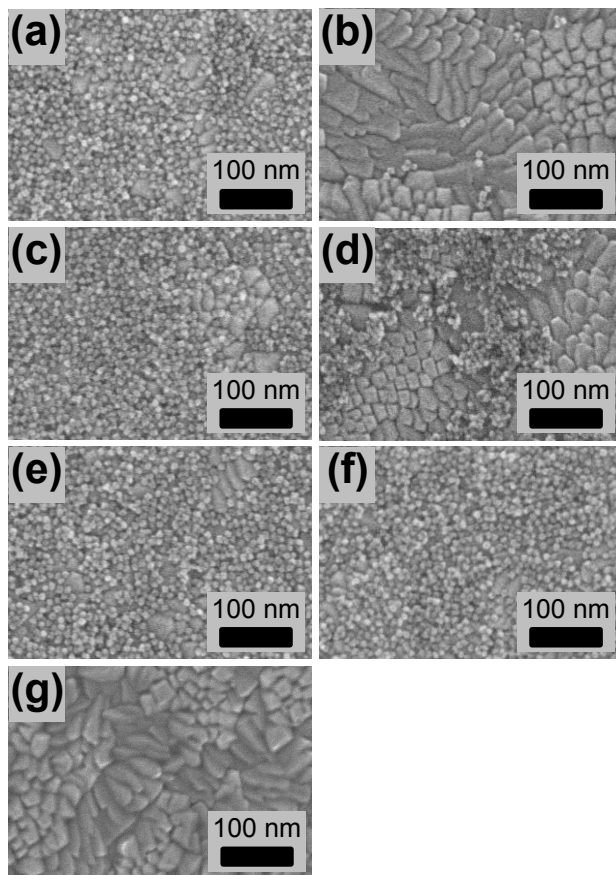


Figure 4.5 SEM micrographs of a Ni:Fe 51:49 [Ni,Fe]O-functionalized ITO electrode with no further treatment procedure (a) before and (b) after voltammetry; a plasma-treated electrode (10 seconds, air) (c) before and (d) after voltammetry; and a UV-treated electrode (254 nm, 1 hour) (e) before and (f) after voltammetry. (g) Micrograph of blank ITO.

It is established that the UV irradiation of metal-organic precursors, specifically of molecular transition metal complexes associated with carboxylate groups, can be used to fabricate amorphous metal oxide films from metal-organic precursors.<sup>29,40</sup> However, analogous behaviour in nanoparticles with organic ligands has not been reported. If the UV-induced decomposition of metal-organic precursors is based on ligand-to-metal charge transfer (LMCT) from carboxylate to metal core,<sup>40</sup> then carboxylate-capped nanoparticles should undergo a similar

process when irradiated by UV light, explaining why UV irradiation of [Ni,Fe]O nanoparticles forms well-adhered films of the nanoparticles. Furthermore, the irradiation of any mixture of carboxylate-bound metals should yield adherent films and metal carboxylates that do not have ethylhexanoate ligands should not be necessary. Therefore, a 1:1 solution of Ni:Fe oleate in hexane prepared by reflux of NiCl<sub>2</sub>, FeCl<sub>3</sub>, and sodium oleate in hexane, ethanol and water was spin-cast on ITO electrodes and irradiated with UV light for 1 hour. Previously, we demonstrated that this oleate precursor mixture is comprised of nickel and iron oleates – and therefore is composed of metal carboxylates.<sup>41</sup> The resulting film was clearly visible under SEM as a thick layer (Figure 4.6a) and maintained a 1:1 composition of Ni:Fe as determined by EDX. The overpotential for water oxidation of these films at 10 mA/cm<sup>2</sup> was 0.26 V, lower than the overpotential of the nanoparticle electrodes reported here but similar to electrodes fabricated using metal ethylhexanoates (Figure 4.6b)<sup>29</sup> despite having the same near-unity composition of Ni:Fe as the nanoparticles. The reduced catalytic activity of the nanoparticles relative to the amorphous films appears to confirm the higher activity of amorphous materials over crystalline ones.<sup>29,33</sup> However, the photolytic decomposition of metal oxide nanoparticles with carboxylate ligands nonetheless yields robust films much like films derived from molecular metal ethylhexanoates.

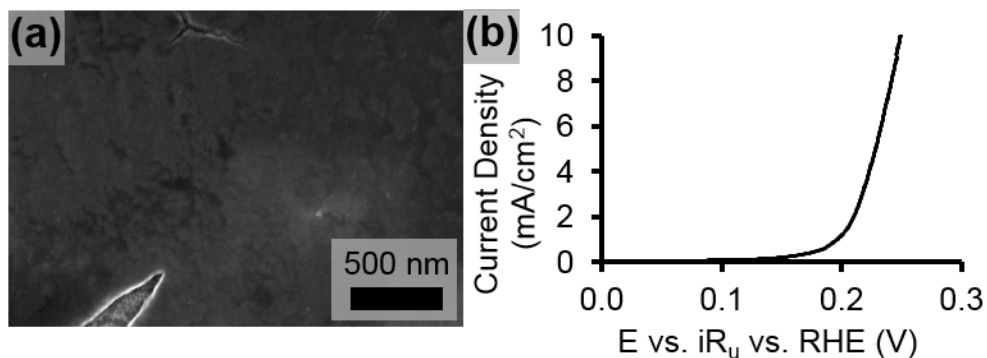


Figure 4.6 (a) SEM micrograph of the surface of a catalyst electrode formed by the UV decomposition (254 nm, 1 hour) of a 1:1 nickel:iron oleate mixture dissolved in hexane and spin-cast on ITO. (b) Voltammogram of the metal-oleate UV-treated ITO electrode in 0.1 M KOH.

The  $\text{Ni}_{2p}$  and  $\text{Fe}_{3p}$  spectra of untreated, UV-treated, UV-treated/0.1 M KOH-treated (2 hours at open circuit potential in 0.1 M KOH), and UV-treated/post-chronopotentiometry ( $10 \text{ mA/cm}^2$ , 2 hours) electrodes were acquired in order to study nanoparticle stability. While no major differences in  $\text{Fe}_{2p}$  peak positions were found after any of these treatments, the shoulder of the main peak at 708 eV decreased after treatment in 0.1 M KOH for two hours despite remaining unchanged during UV irradiation (Figure 4.7a). Since this shoulder is associated with bivalent iron,<sup>42</sup> its reduction in size suggests that some of the bivalent iron is oxidized during the KOH treatment. However, the  $\text{Fe}_{2p}$  satellite peak remained unchanged post-irradiation and did not display the strong bias in position towards  $\text{Fe}^{2+}$  or  $\text{Fe}^{3+}$  typically seen in bivalent or trivalent iron oxides,<sup>42</sup> suggesting that oxidation was limited and that the  $[\text{Ni,Fe}]\text{O}$  valences remained intact even after KOH treatment and electrochemistry. In the  $\text{Ni}_{2p}$  spectra, the shape of the main peak rounded out upon chronopotentiometry (Figure 4.7b). This change in shape appears to be associated with the transformation of nickel oxide to nickel hydroxide that takes

place during water oxidation.<sup>13</sup> However, compared to the 3 eV shift previously reported for fully transformed NiO,<sup>13</sup> the change in NiO peaks reported in this study were minimal, suggesting that any transformation of nickel was limited to a small population. In fact, both nickel and iron XPS spectra remain mostly unchanged by UV irradiation, treatment in basic solution, and electrocatalysis, suggesting that even under harsh oxidizing conditions (0.1M KOH, ~1.7 V vs. RHE), the bivalent nature of the nanoparticles remained intact. Given this data, the reduction in catalytic activity seen in chronopotentiometry may arise from a loss in catalyst material, although further study would be needed to confirm this possibility.

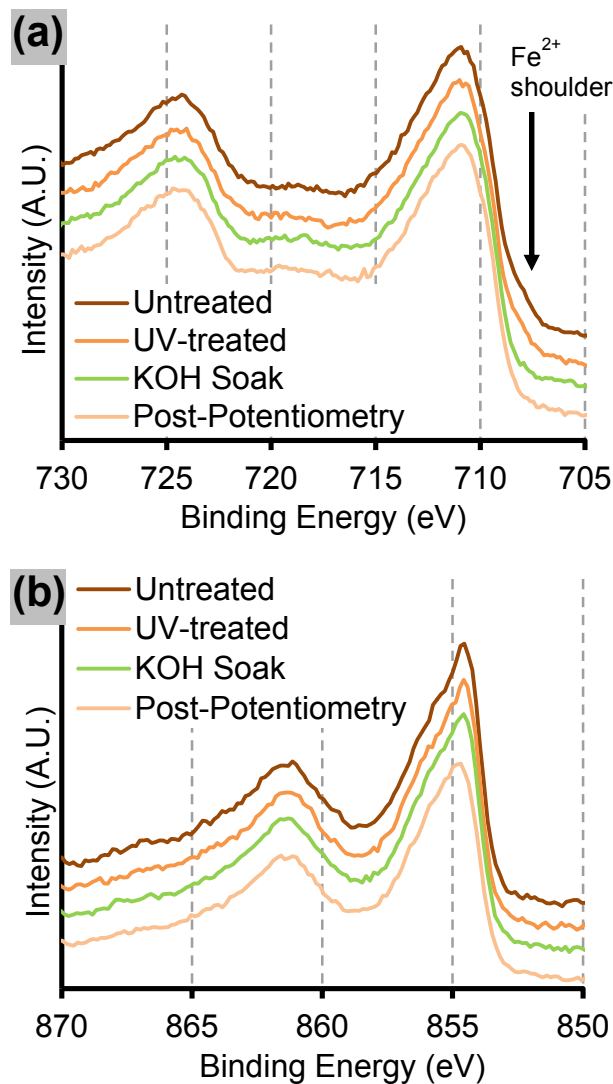


Figure 4.7 (a)  $\text{Fe}_{2p}$  and (b)  $\text{Ni}_{2p}^{3/2}$  XPS spectra of UV-treated a Ni:Fe 51:49 [Ni,Fe]O nanoparticle-functionalized electrode before and after UV irradiation, after 2 hours in electrolyte (0.1 M KOH), and post-chronopotentiometry in 0.1 M KOH (10 mA/cm<sup>2</sup>, 2 hours).

Further surface characterization of the nanoparticle films was performed using FTIR of thin films of nanoparticles spin-cast on high-resistivity Si (Figure 4.8). The strongest absorbing feature was the  $\sim 430\text{ cm}^{-1}$  peak corresponding to the average position of the IR absorption peaks of NiO ( $\sim 450\text{ cm}^{-1}$ )<sup>43,44</sup> and FeO ( $410\text{ cm}^{-1}$ ).<sup>45</sup>

Since the position and size of this peak did not change during irradiation, FTIR further confirmed the high stability of the nanoparticles. In contrast, absorption in the CH<sub>2</sub>/CH<sub>3</sub> region (2800 – 3000 cm<sup>-1</sup>) underwent reduction with UV irradiation, corresponding to the photolytic decomposition of organic ligands. However, traces of the CH<sub>2</sub>/CH<sub>3</sub> complex remained after one hour despite the catalytic stability of electrodes UV-treated for this amount of time, suggesting that complete elimination of ligand was not required for formation of durable films. Furthermore, although broad absorption was present in the 3500 cm<sup>-1</sup> region before UV irradiation, the size of this peak increased after 15 minutes of irradiation and indicates the increasing presence of metal hydroxyl groups.<sup>46,47</sup> Many transition metal oxide water oxidation catalysts appear to involve hydrated metal centers<sup>25,26,48–50</sup> and the presence of these groups on the surface layer of the nanoparticles may be responsible for the catalytic activity of these nanoparticles. Finally, immersion in 0.1 M KOH resulted in the removal of all organic groups, making complete removal of such groups during UV irradiation unnecessary as any groups would be automatically removed upon exposure to the electrolytic solution.

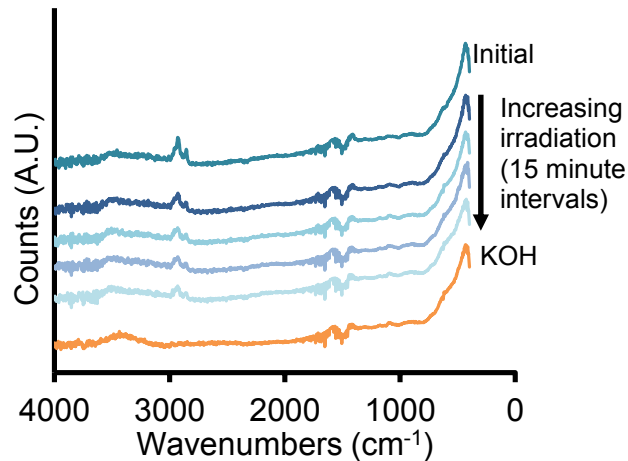


Figure 4.8 FTIR spectra of a Ni:Fe 51:49 [Ni,Fe]O nanoparticle film spun on high resistivity Si ( $\sim 10 \Omega \cdot \text{cm}$ ) after different periods of irradiation with 254 nm UV light, as well as after placement in 0.1 M KOH for 2 hours. The scans were collected in transmission mode.

Since XPS and FTIR results suggested that UV irradiation did not damage the [Ni,Fe]O nanoparticles and that complete ligand removal via irradiation was not required for durable film formation, the kinetics of film formation were studied by irradiating untreated nanoparticle electrodes for 5, 10, 15, and 30 minutes. Stability was determined by the overpotential for water oxidation at  $10 \text{ mA/cm}^2$ . Although the electrodes that had been irradiated for 5 minutes preserved enough catalyst material to have lower overpotentials for water oxidation (0.90 V) than untreated electrodes, the activity of the electrodes irradiated for 5 minutes was still far below that of electrodes that had been UV-irradiated for 1 hour. The overpotential of electrodes irradiated for 10 minutes fell drastically to 0.47 V, and finally after 15 minutes of irradiation electrodes reached the same overpotential as the electrodes irradiated for 1 hour (Figure 4.9). Therefore, in order to form nanoparticle films that withstand water oxidation, the electrodes must be irradiated for at least 15

minutes in order to remove the majority of the organic ligands on the surface of the nanoparticles.

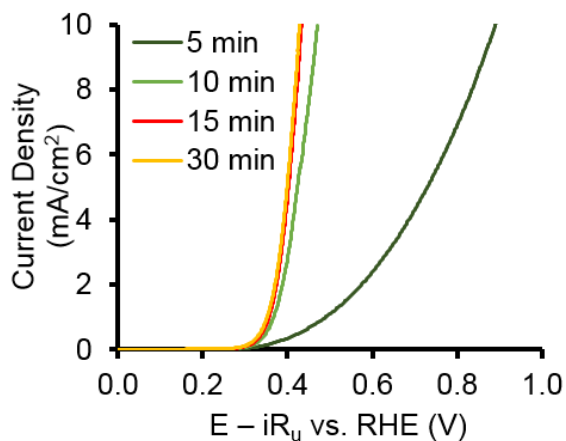


Figure 4.9 Voltammograms of Ni:Fe 51:49 [Ni,Fe]O nanoparticle-functionalized electrodes in 0.1 M KOH after irradiation with 254 nm UV light for different lengths of time.

#### 4.2.2 Understanding Differences in Nanoparticle Composition

The ability of UV irradiation to fabricate films of other nanoparticles was determined next, specifically those previously reported with variable Ni:Fe concentration.<sup>41</sup> Fabricating these electrodes is of interest because the ratio of nickel to iron in oxide catalysts has been considered an important determinant of catalytic activity for water oxidation, although the exact molar ratio of Ni:Fe can range from 10% to 31% depending on the preparation method.<sup>30,33,48,51</sup> Solutions with nanoparticle Ni:Fe ratios of 88:12, 73:27, and 24:76 were spin-cast onto ITO electrodes and irradiated with UV light for 1 hour. Upon testing for water oxidation catalysis in 0.1 M KOH, the electrodes were determined to have overpotentials of 0.32 V, 0.36 V, and 0.50 V, respectively, at a current density of 10 mA/cm<sup>2</sup> (Figure 4.10a). Furthermore, the overpotentials of these electrodes could be improved by

applying a layer-by-layer process of alternating spin-coating and UV irradiation processes to increase the amount of nanoparticles on the electrode surface. A modest reduction in overpotential took place between all electrodes synthesized using 1 and 2 layers of nanoparticle deposition, with the Ni:Fe 24:76 overpotential being reduced from 0.50 V to 0.47 V; the Ni:Fe 51:49 overpotential being reduced from 0.44 V to 0.40 V; the Ni:Fe 73:27 overpotential being reduced from 0.36 V to 0.34 V; and the Ni:Fe 88:12 overpotential being reduced from 0.32 V to 0.30 V (all measured at a current density of 10 mA/cm<sup>2</sup>) (Figure 4.10b). However, further layers did not significantly improve overpotentials. Therefore, the [Ni,Fe]O system reaches a minimal overpotential for water oxidation with lower iron concentrations as the lowest overpotential was acquired from nanoparticles with a Ni:Fe ratio of 88:12 – similar to other nickel iron oxide systems.<sup>30,33,48,51</sup>

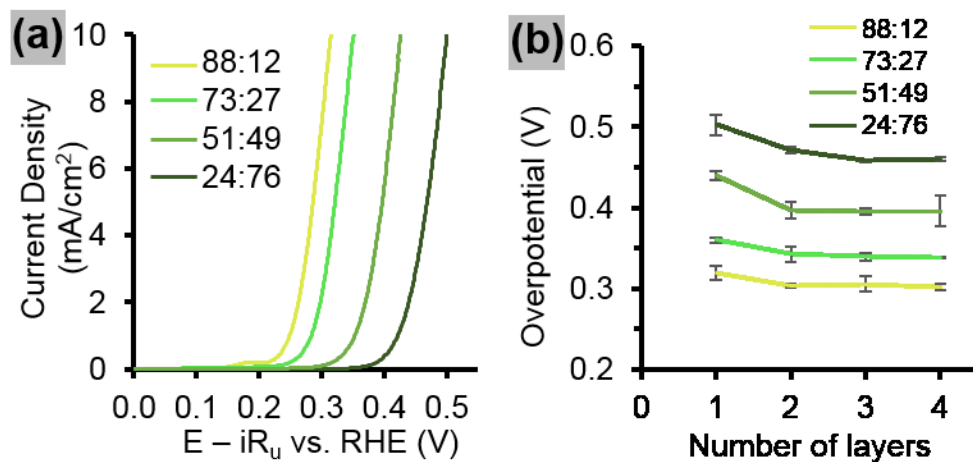


Figure 4.10 (a) Voltammograms of [Ni,Fe]O nanoparticle-functionalized electrodes with one layer of nanoparticles of different compositions recorded in 0.1 M KOH. (b) Relationship of thickness based on number of layers and overpotential at 10 mA/cm<sup>2</sup> in 0.1 M KOH of different nanoparticle compositions. All ratios in Ni:Fe.

The increased loading of nanoparticles significantly changed the optical properties of the nanoparticle films and could be quantified via UV-vis spectroscopy (Figure 4.11a). Using the Ni:Fe 51:49 sample as an example, absorption increased monotonically with increasing layers of nanoparticles, reducing the transmission at 450 nm from 84.5% to 69.3% over the course of 4 layers of nanoparticles. This increase in thickness was confirmed using profilometry, where the measured film thickness increased with the number of layers (Figure 4.11b). Single-layer nanoparticle films were not analyzed via this method because the films were incomplete. Increasing thickness did not necessarily result in improving catalytic activity as improvements stopped after two layers of nanoparticles had been deposited, suggesting that thickness, and by extension, material loading, is not the only determinant of catalytic activity. SEM was performed on each different set of nanoparticle electrodes to determine if there was a noticeable physical difference between the single-layer and multiple-layer electrodes. For all nanoparticles studied, a single cycle of nanoparticle deposition yielded incomplete nanoparticle films where bare ITO could be seen in some regions (Figure 4.12a,c,e,g). However, these regions disappeared after one additional loading cycle, resulting in complete nanoparticle films (Figure 4.12b,d,f,h). Since additional layers did not reduce overpotential, it appears that surface coverage, not electrode thickness, was the most important factor in influencing overpotential. This in turn suggests that water oxidation takes place on the surface of the nanoparticles – and particularly nanoparticle surfaces close to the electrode surface.

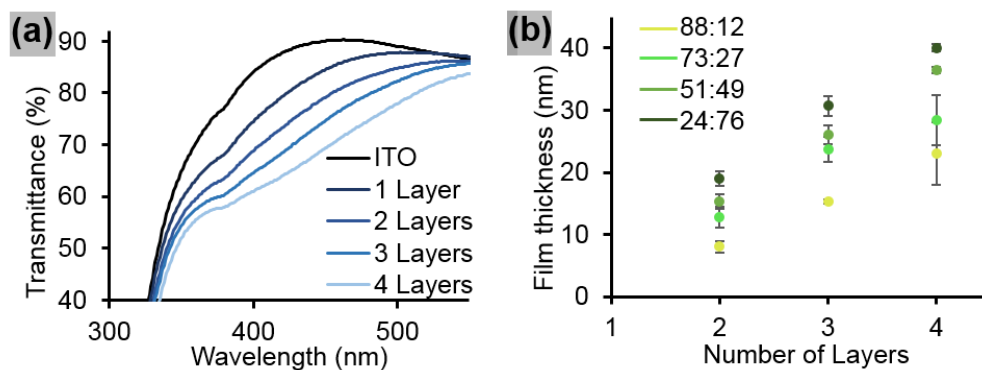


Figure 4.11 (a) UV-vis spectra of [Ni,Fe]O nanoparticle-functionalized electrodes with increasing numbers of layers. The composition of nanoparticles used in this graph was Ni:Fe 51:49. (b) Relationship between thickness (determined via contact profilometry) and number of layers of [Ni,Fe]O nanoparticle-functionalized electrodes. All ratios in Ni:Fe.

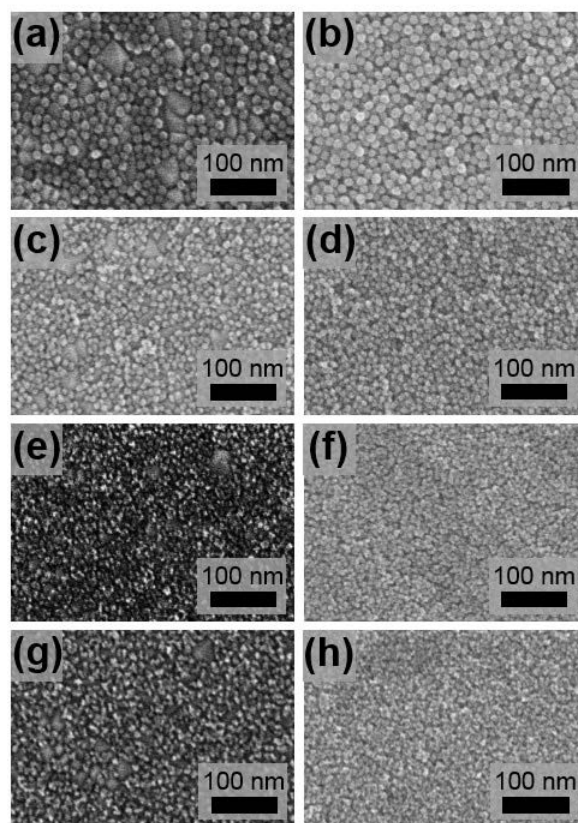


Figure 4.12 SEM micrographs of 1 layer (left) and 2 layer (right) nanoparticle electrodes with different compositions of nanoparticles. From top to bottom, the nanoparticle Ni:Fe compositions are 24:76 (a,b), 51:49 (c,d), 73:27 (e,f), and 88:12 (g,h).

### 4.2.3 Characterization of Water Oxidation Kinetics

Tafel characterization was used to further study overpotentials as well as the kinetics of the water oxidation reaction on electrodes with two layers of nanoparticles, which achieved the lowest overpotentials for water oxidation with the least catalyst material loading. Tafel plots compare the energy input into a system to the catalytic output in the form of current density, and are often linear according to the Butler-Volmer equation:<sup>52</sup>

$$i = i_0 [e^{(-\alpha n F \eta)/(2.3 RT)} - e^{((1 - \alpha) n F \eta)/(2.3 RT)}]$$

Where  $i$  is the current density,  $i_0$  is the exchange current density (the current density when the electrode is at equilibrium),  $F$  is Faraday's constant,  $n$  is the number of electrons transferred in the reaction,  $\alpha$  is the charge transfer coefficient, and  $\eta$  is the overpotential. The entire equation is used to describe the electrochemical kinetics of a two-electrode system (anode and cathode). The second term ( $e^{((1 - \alpha) n F \eta)/(2.3 RT)}$ ) describes the behaviour of the anode such as that seen in water oxidation. Therefore, the slope of a Tafel plot of an electrode catalytic for water oxidation, where exponential, can be described by the relation  $(1 - \alpha) n F \eta / 2.3 RT$ . The charge transfer coefficient is valuable because it is a measure of how effective a catalyst is at transferring electrons; the larger  $\alpha$ , the more efficiently a reaction proceeds.

As found with voltammetry, the overpotentials for water oxidation acquired from [Ni,Fe]O nanoparticle electrodes at 10 mA/cm<sup>2</sup> ranged from 0.30 V for Ni:Fe

88:12 electrodes to 0.50 V for Ni:Fe 24:76 electrodes (Figure 4.13). These water oxidation overpotentials lie in a higher range of values than the water oxidation overpotentials recorded for a similar composition range of amorphous nanoparticles, which existed between 0.27 V and 0.35 V, for Ni:Fe 69:31 and Ni:Fe 25:75 compositions, respectively.<sup>51</sup> In a study of crystalline catalysts, a Ni:Fe 60:40 water oxidation electrode achieved a water oxidation overpotential of 0.43 V at 10 mA/cm<sup>2</sup>, a higher value than the 0.40 V achieved by Ni:Fe 51:49 [Ni,Fe]O nanoparticles in this study,<sup>53</sup> which contain less nickel. Therefore, the [Ni,Fe]O nanoparticles are more similar to crystalline than amorphous catalysts at higher current densities. However, the water oxidation overpotentials achieved by [Ni,Fe]O nanoparticles at lower current densities, specifically 1 mA/cm<sup>2</sup>, lie between 0.24 V and 0.40 V for Ni:Fe 88:12 and Ni:Fe 24:76 compositions, respectively. In particular, the nickel-rich Ni:Fe 88:12 and 73:27 electrodes can reach overpotentials that are low enough to make them as effective as amorphous nickel iron oxide equivalents at 1 mA/cm<sup>2</sup>, many of which have reported water oxidation overpotentials between 0.24 V and 0.27 V.<sup>33,51</sup> The overpotential of crystalline mixed nickel-iron oxide systems at 1 mA/cm<sup>2</sup> has been reported as 0.36 V for Ni:Fe 60:40 electrodes – still higher than the 0.33 V seen here for [Ni,Fe]O Ni:Fe 51:49.<sup>53</sup>

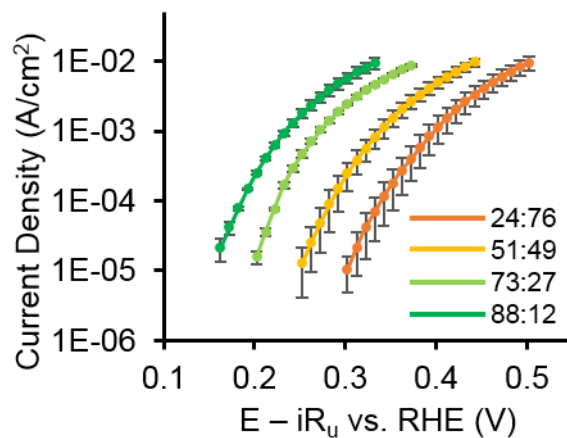


Figure 4.13 Tafel curves of [Ni,Fe]O nanoparticle electrodes of different compositions acquired in 0.1 M KOH with 50 second step times. Ratios represented are in Ni:Fe.

These differences in water oxidation overpotentials arising from composition and crystallinity are reflected in the slopes of the Tafel plots of [Ni,Fe]O nanoparticle electrodes, which exhibit low current density ( $<0.5 \text{ mA/cm}^2$ ) and high current density ( $>2 \text{ mA/cm}^2$ ) regions. In the low current density regime, the Tafel slopes acquired from the [Ni,Fe]O nanoparticle electrodes in order of increasing slope values were 36 mV/decade (Ni:Fe 73:27), 42 mV/decade (Ni:Fe 88:12), 44 mV/decade (Ni:Fe 51:49), and 48 mV/decade (Ni:Fe 24:76) (Table 4.1). These values lie within the range of reported Tafel slopes for nickel iron oxide catalysts whether amorphous or crystalline, which are typically reported to lie between 30 and 50 mV/decade.<sup>33,51,53</sup> Furthermore, the lowest Tafel slope in the [Ni,Fe]O series came from the Ni:Fe 73:27 electrode (36 mV/decade). In comparison, crystalline catalysts tend to reach a minimum in Tafel slope with lower iron concentration, with Ni:Fe 80:20 catalysts maintaining Tafel slopes of 33 mV/decade,<sup>53</sup> and amorphous nickel iron oxide catalysts reaching a minimum Tafel slope (30

mV/decade) when Ni:Fe is close to unity 40:60.<sup>33</sup> Therefore, [Ni,Fe]O nanoparticle electrodes do not appear to follow amorphous or crystalline trends regarding Tafel slope at lower current densities. Above 2 mA/cm<sup>2</sup>, the Tafel slopes increased to over 100 mV/decade. While it is typical for metal oxide water oxidation electrocatalysts to undergo an increase in Tafel slope around this current density due to a change in the rate determining step of water oxidation,<sup>54,55</sup> recent nickel iron oxide catalysts that are amorphous or porous are notable because the Tafel slope remains linear from the low current density regime (at a slope below 50 mV/decade) up to 5 mA/cm<sup>2</sup>.<sup>13,51</sup> In the [Ni,Fe]O system, Tafel slope rapidly increases above 2 mA/cm<sup>2</sup> to over 100 mV/decade by the time current density reaches 10 mA/cm<sup>2</sup>.

Table 4.1 Tafel slopes of nanoparticle electrodes at different current densities

Composition (Ni:Fe)	Tafel slope (mV/decade) (<0.5 mA/cm <sup>2</sup> )	Tafel slope (mV/decade) (>1.5 mA/cm <sup>2</sup> )
88:12	42 ± 3	106 ± 3
73:27	36 ± 3	115 ± 3
51:49	44 ± 4	113 ± 8
24:76	48 ± 1	115 ± 12

Although information on the kinetics of water oxidation on crystalline nickel iron oxide catalysts at high current densities (>2 mA/cm<sup>2</sup>) is limited, much of the Tafel behaviour can be understood through the lens of crystalline catalysts. The bulk volume of crystalline catalysts is typically inaccessible to catalysis due to the poor permeability of reactant molecules.<sup>50,54,56</sup> In the case of [Ni,Fe]O, both the

Tafel behaviour of nanoparticle electrodes during water oxidation and the dependence of catalytic activity of [Ni,Fe]O electrodes on surface coverage as opposed to catalyst loading suggest that the crystalline core of [Ni,Fe]O does not permit the entry of any water molecules. The disordered, hydroxide-rich surface layer that [Ni,Fe]O naturally maintains is likely responsible for carrying out water oxidation. Since the electrochemical data here reflect the behaviour of the surface layer, it can be said that this surface layer behaves more similarly to an amorphous catalyst than a crystalline one, suggesting that it may potentially retain a porous, catalytically active structure. Even if [Ni,Fe]O does not directly participate in catalysis, this phase may nonetheless be the root cause of catalytic activity in the nanoparticles, allowing for the formation of the disordered surface layer due to the latent instability of  $\text{Fe}^{2+}$  oxides. In addition, rock-salt NiO can transform into a porous material under anodic conditions much easier than other phases – another potential source of activity arising from [Ni,Fe]O.<sup>13</sup>

Finally, the small differences in slope at lower current densities between different compositions of electrodes suggests that the mechanism of water oxidation does not largely change between different ratios of Ni:Fe. Specifically, these Tafel slopes suggest that nickel oxide is the primary reaction site for water oxidation as the loss of nickel merely increases the overpotential but not the slope. Similarly, at high overpotentials, the same closeness in Tafel slopes is seen, with similar potential consequences. The role of iron is still unknown but several studies have reported the presence of high oxidation state (+4) nickel atoms in nickel based water oxidation catalysts.<sup>57–60</sup> It has been proposed that such nickel sites, formed

by the presence of a nearby iron atom, are the active sites for water oxidation.<sup>48</sup>

Based on these observations, the following mechanism can be proposed:

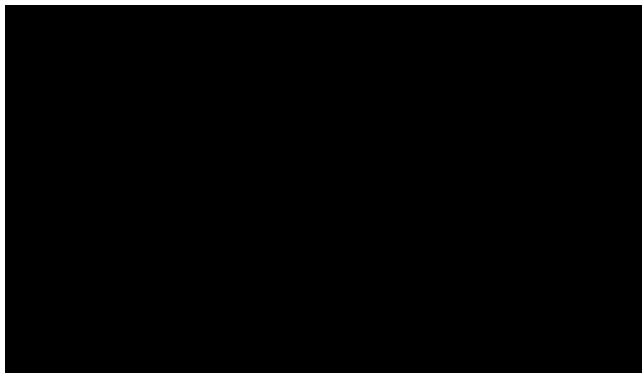


Figure 4.14 Proposed mechanism of water oxidation on [Ni,Fe]O nanoparticle surfaces.

As for which steps would be rate limiting, with these results it is impossible to determine. A specific nickel iron oxide study would be required as has been performed for RuO<sub>2</sub>.<sup>55</sup>

#### 4.2.4 Effect of Temperature on Catalyst Activity

Modification of the crystal phase should demonstrate the importance of the [Ni,Fe]O phase to the water oxidation activity of these nanoparticles. Previously, it was shown that heating [Ni,Fe]O to 400 °C results in the appearance of the spinel NiFe<sub>2</sub>O<sub>4</sub> phase,<sup>41</sup> which is less catalytic for water oxidation than any hydroxylated phases of iron-doped nickel oxide.<sup>49</sup> Spinel phases are also inhibited from transforming into hydroxide phases like rock-salt phases, reducing their potential water oxidation activity.<sup>13</sup> Furthermore, between 200 °C and 400 °C, the structure of the nanoparticles undergoes dehydration from nickel and iron hydroxides to anhydrous oxides,<sup>61-63</sup> although it should be possible to reverse any loss in activity

due to the rapid reversibility of hydration when metal oxides are returned to aqueous environments.<sup>54</sup> Nanoparticle electrodes were fabricated on FTO using five layer-by-layer cycles using Ni:Fe 51:49 nanoparticles. The electrodes were then heated in air for 2 hours at 200 °C, 400 °C, and 600 °C. The crystal structures of heated nanoparticles were as previously reported, with NiFe<sub>2</sub>O<sub>4</sub> beginning to appear in small amounts at 400°C (Figure 4.15). Under SEM, electrodes heated at 200°C appeared similar to unheated electrodes (Figure 4.16a), but at 400°C, the nanoparticles began to agglomerate into large clusters, precluding the possibility of surface area loss (Figure 4.16b). At 600 °C, sintering was highly noticeable and individual nanoparticles lost some of their shape (Figure 4.16c).

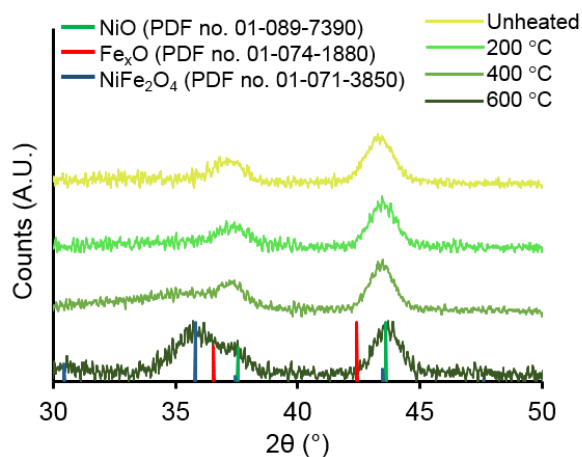


Figure 4.15 X-ray diffraction patterns of Ni:Fe 51:49 [Ni,Fe]O nanoparticles drop-cast on silicon substrates and heated for 2 hours in air at 200 °C, 400 °C, and 600 °C.

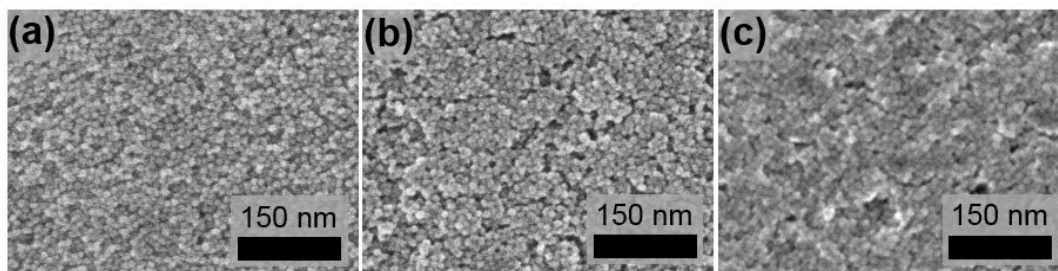


Figure 4.16 SEM micrographs of Ni:Fe 51:49 [Ni,Fe]O nanoparticle-coated FTO electrodes heated for 2 hours in air at (a) 200 °C, (b) 400 °C, and (c) 600 °C.

While the control and 200°C electrodes had water oxidation overpotentials similar to the previously achieved value of 0.40 V, an increase in overpotential of 20 mV was noticed at 400 °C (Figure 4.17a). At 600 °C, the overpotential increased by 60 mV compared to the control sample, marking the only time that the overpotential achieved by Ni:Fe 51:49 [Ni,Fe]O electrodes was greater than the Ni:Fe 60:40 crystalline catalyst reported by Gerken et al.,<sup>53</sup> even though the Ni:Fe 51:49 system reported here had less nickel – and therefore should have had a higher overpotential under all conditions. This finding precludes an important distinction between crystalline nickel iron oxide catalysts. However, since the surface of the electrode was visually confirmed to have changed during heating at high temperatures, it was important to determine what portion of the loss in activity arose from a loss in surface area. Therefore, voltammetry was performed on 1,1'-ferrocenedicarboxylic acid-functionalized films to determine the amount of charge transferred per unit of surface area of the electrodes (Figure 4.17b), which directly correlates with the present electrochemically active surface area (Figure 4.17c).<sup>64</sup> While charge transfer differences were found between the samples, these changes did not correlate directly with changes in overpotential, as the largest reduction in

transferred charge took place between 200 °C and 400 °C, where only a minor increase in overpotential had been noted, and not between 400 °C and 600 °C where the largest increase in overpotential had been seen. Furthermore, despite a significant reduction in transferred charge between electrodes left at room temperature and electrodes heated to 200°C, there was no significant change in overpotential between these samples – suggesting that re-hydration restores pre-heating catalytic activity. Therefore, the loss in catalytic activity on heated nanoparticle electrodes cannot solely arise from a loss of surface area, leaving changes in crystal structure as the most likely reason for reduced catalytic activity at higher temperatures. The unique ability of [Ni,Fe]O to retain higher water oxidation activity than calcined nickel-iron oxides of the same composition emphasizes the importance of structure – and not just composition – in the search for new water oxidation catalysts.

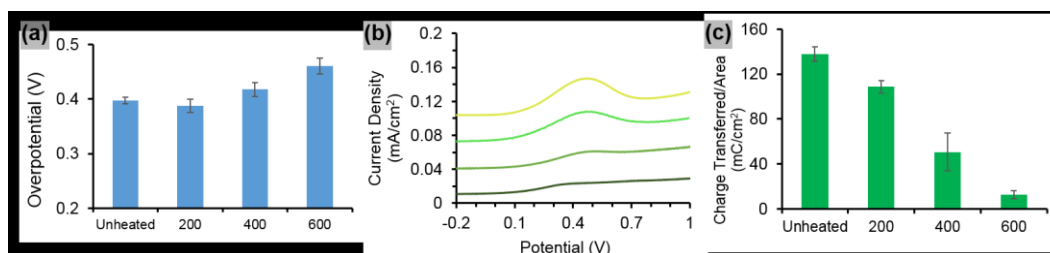


Figure 4.17 (a) Measurements of the water oxidation overpotential at 10 mA/cm<sup>2</sup> in 0.1 M KOH and (b) charge transfer measurements of Ni:Fe 51:49 [Ni,Fe]O nanoparticle electrodes without heating and heated for 2 hours at 200 °C, 400 °C, and 600 °C. Charge transfer measurements were acquired by functionalizing electrodes with 1,1'-ferrocenedicarboxylic acid followed by linear sweep voltammetry across the 0.45 V vs. Ag/Ag<sup>+</sup> peak corresponding to ferrocenedicarboxylic acid binding and integrating the area of the resultant peak.

### 4.3 Conclusions

This study focused on understanding the water oxidation catalytic activity for [Ni,Fe]O nanoparticles. By using a simple UV irradiation procedure, thin, durable films of nanoparticles were formed on surfaces of ITO and FTO, which could then be used for electrochemical testing without affecting the unique crystal structure of the nanoparticles. During electrochemical study, the surface of the nanoparticles was determined to carry out water oxidation, while the bulk structure contributed minimally to catalytic activity. Nonetheless, the underlying [Ni,Fe]O structure was still important for catalysis as introducing NiFe<sub>2</sub>O<sub>4</sub> at the expense of [Ni,Fe]O through heating resulted in a reduction in catalytic activity. Therefore, the unique properties of [Ni,Fe]O underline that studying composition is not enough to build ideal catalysts; structure too must be accounted for and crystalline transition metal oxide catalysts should not be ignored as potential catalysts.

### 4.4 Experimental

**Chemicals.** FeCl<sub>3</sub> (98%) (Strem Chemicals), NiCl<sub>2</sub>•6H<sub>2</sub>O (ACP Chemicals), sodium oleate (>97%) (Tokyo Chemical Industry), ethanol (Commercial Alcohols), hexanes, acetonitrile, isopropanol, and potassium hydroxide (KOH, ACS Certified) (Fisher Chemicals), and 1,1'-ferrocenedicarboxylic acid (96%), oleic acid (technical grade, 90%), tetrabutylammonium hexafluorophosphate (TBAHFP, ≥99.0%), and 1-octadecene (technical grade, 90%) (Sigma-Aldrich) were used as received. Tin-doped indium oxide on glass (SiO<sub>2</sub> passivated, R<sub>s</sub> = 8 – 12 Ω/□, “ITO”) was acquired from Delta Technologies. Fluorine-doped tin oxide on glass

(2 mm thickness,  $R_s \approx 13 \Omega/\square$ , “FTO”) was acquired from Pilkington via Sigma-Aldrich.

**Synthesis of nanoparticles.** All nanoparticles were synthesized as previously reported.<sup>41</sup> Briefly, metal chlorides in ratios of Ni:Fe 1:5, 2:4, 4:2, and 5:1 mmol were refluxed with sodium oleate amounting to 2 mmol of sodium oleate per mmol of Ni and 3 mmol of sodium oleate per mmol of Fe in a mixture of 20 mL hexane, 10 mL ethanol, and 10 mL water at 60°C for 4 hours. After cooling, the hexane portion was separated and washed with water before centrifuging to remove more hydrophilic contaminants and products. The red-brown liquid was dried at 100°C for 1 hour in an oil bath in a fume hood to remove hexane. The waxy product was dissolved in 20 mL of 1-octadecene with 0.951 mL of oleic acid in a 250 mL three neck flask. The flask was degassed by evacuation and refilling 3 times with Ar at room temperature, and then at 110°C. The reaction was then ramped to 305 °C at a rate of 3 °C/min and held at this temperature for 20 minutes. After cooling, 40 mL of isopropanol was added to the reaction mixture, which was then centrifuged and resuspended in hexane. Isopropanol was used to wash this mixture twice more before final storage in hexane under ambient conditions.

**Electrode Fabrication.** ITO and FTO substrates were diced into 2 cm x 2 cm squares, which, were cleaned sequentially via sonication in methylene chloride, Milli-Q water (18.2 M $\Omega$ cm), and isopropanol for 10 minutes each. Nanoparticle solutions in hexane diluted to 2 mg/mL were then spin-cast onto ITO and FTO surfaces 50  $\mu$ L at a time and spun at 1000 rpm for 10 seconds. The nanoparticle-coated electrodes were then either left untreated, plasma-treated for 10 seconds

under air plasma at 0.2 torr (Harrick Plasma, PDC 32G, 18 W), or UV-irradiated for 1 hour using a 254 nm Hg penlamp (UVP) positioned 1 cm away from the surface of the electrode. For electrodes prepared with an oleate precursor without nanoparticles, the precursor reflux solution described above was prepared to a Ni:Fe 3 mmol:3 mmol ratio. The hexane layer was then separated and directly spin-cast onto ITO slides by applying 50  $\mu$ L the oleate mixture at a concentration of 100 mg/mL and spinning at 1000 rpm for 10 seconds. The ITO slides with oleate mixture were then irradiated for 1 hour using 254 nm UV light.

**Electrode Characterization.** Imaging of the electrodes was performed using a Hitachi S-4800 FE-SEM with an accelerating voltage of 20 kV, while thickness measurements were performed using a KLA Tencor P-10 Surface Profilometer. UV-vis measurements were performed using a Perkin Elmer Lambda 1050 UV-vis NIR Spectrophotometer. Energy dispersive x-ray (EDX) analysis of films fabricated from oleate precursors was performed on a JEOL JSM-6010LA InTouchScope.

**Electrochemistry.** All electrochemistry was performed using a Parstat 2273 Potentiostat with Powersuite v 2.58 software using a three-electrode electrochemical cell with an Ag/AgCl (saturated KCl) reference electrode standardized to potassium ferricyanide and platinum wire counter electrode. The working solution used for catalytic testing was 0.1 M KOH. Voltammetry scans from open-circuit potential to a current density of 10 mA/cm<sup>2</sup>, at a scan rate of 20 mV/s were performed on all electrodes to ensure stability of recordings. Open circuit potential before all experiments was determined to lie between 0 and 0.1 V.

The software used was POWERCV. Uncompensated resistance was determined using a Nyquist plot generated with POWERSine based on the left-side zero-intercept of the plot when imaginary resistance reached 0  $\Omega$ . Each point in the voltammogram was then corrected by subtracting from the potential the product of uncompensated resistance and current. Chronopotentiometry was undertaken using POWERStep software at a current density of 10 mA/cm<sup>2</sup>. For Tafel plots, the current interrupt uncompensated resistance function was used as this option was available in the POWERCorr Tafel software. Tafel plots were taken at a rate of 10 mV/s with step times of 50 seconds. This time was determined by chronoamperometry.

Electrochemically active surface area was measured as previously described, based on the electrochemical adsorption of 1,1'-ferrocenedicarboxylic acid to metal oxide surfaces.<sup>64</sup> The electrodes were plasma cleaned in air for 5 minutes to remove potential surface contaminants before immersion in 1 mM of 1,1'-ferrocenedicarboxylic acid in ethanol for 10 minutes. Afterwards, the electrodes were washed with ethanol and acetonitrile. Cyclic voltammetry was then performed on the electrodes using an Ag/Ag<sup>+</sup> reference electrode in 0.1 M TBAHFP in acetonitrile. The scan range used was -0.50 V to 1.75 V, at a rate of 0.10 V/s. The amount of charge transferred was taken by integrating the anodic peak in voltammograms using the Power Suite software and divided by the area of the electrode to acquire the charge transferred per area value.

**Fourier Transform Infrared Spectroscopy (FTIR).** Scans were collected using a Nicolet Nexus 760 spectrometer with a DTGS detector and a N<sub>2</sub>-purged

sample chamber (256 scans,  $4 \text{ cm}^{-1}$  resolution). Nanoparticle samples were drop-cast on undoped, high resistivity ( $\sim 10 \text{ }\Omega\cdot\text{cm}$ ) Si wafers for data collection in transmission mode.

**X-ray Photoelectron Spectroscopy.** X-ray photoelectron spectroscopy (XPS) spectra were collected by Kratos Ultra spectrometer with a base pressure less than  $4 \times 10^{-8}$  Pa. A monochromatic Al  $K\alpha$  source ( $h\nu = 1486.6 \text{ eV}$ ) was run at a power of 168 W. The analysis spot was  $300 \times 700 \text{ }\mu\text{m}$  and the analyzer resolution was 0.80 eV for Au 4f peaks. The survey scans were collected for binding energies spanning 1100 to 0 eV at constant energy of 160 eV and spectra for narrow regions were collected at pass-energy of 20 eV. Sample charging was compensated by electron flooding. The binding energy (BE) scale was calibrated by assigning C 1s peak from adventitious carbon at 284.8 eV. Relative concentrations of chemical elements were calculated using CasaXPS, using a standard quantification routine, including Scofield sensitivity factors and Shirley background subtraction.

**X-ray Diffraction.** X-ray diffraction (XRD) was performed using a Bruker D8 Discover with a Cu  $K\alpha$  beam (40 kV, 40 mA,  $\lambda = 1.5406 \text{ \AA}$ ) equipped with a 2D detector. XRD spectra were collected from the 2D ring patterns by chiral integration. Samples were prepared by drop-casting nanoparticle solution on silicon (100) substrates followed by heat treatment in air at either 200 °C, 400 °C, or 600 °C for two hours in a Lindberg/Blue M tube furnace. Scans were performed in a grazing incidence configuration with an incident angle of  $\omega = 5^\circ$ .

## 4.5 References

- (1) Glaria, A.; Kahn, M. L.; Lecante, P.; Barbara, B.; Chaudret, B. Fe<sub>1-y</sub>O Nanoparticles: Organometallic Synthesis and Magnetic Properties. *ChemPhysChem* **2008**, *9* (5), 776–780.
- (2) Holladay, J. D.; Hu, J.; King, D. L.; Wang, Y. An Overview of Hydrogen Production Technologies. *Catal. Today* **2009**, *139* (4), 244–260.
- (3) Turner, J.; Sverdrup, G.; Mann, M. K.; Maness, P.-C.; Kroposki, B.; Ghirardi, M.; Evans, R. J.; Blake, D. Renewable Hydrogen Production. *Int. J. Energy Res.* **2008**, *32* (5), 379–407.
- (4) Cook, T. R.; Dogutan, D. K.; Reece, S. Y.; Surendranath, Y.; Teets, T. S.; Nocera, D. G. Solar Energy Supply and Storage for the Legacy and Nonlegacy Worlds. *Chem. Rev.* **2010**, *110* (11), 6474–6502.
- (5) Yeo, R. S.; Orehtsky, J.; Visscher, W.; Srinivasan, S. Ruthenium-Based Mixed Oxides as Electrocatalysts for Oxygen Evolution in Acid Electrolytes. *J. Electrochem. Soc.* **1981**, *128* (9), 1900–1904.
- (6) Lyons, M. E. G.; Floquet, S. Mechanism of Oxygen Reactions at Porous Oxide Electrodes. Part 2—Oxygen Evolution at RuO<sub>2</sub>, IrO<sub>2</sub> and Ir<sub>x</sub>Ru<sub>1-x</sub>O<sub>2</sub> Electrodes in Aqueous Acid and Alkaline Solution. *Phys. Chem. Chem. Phys.* **2011**, *13* (12), 5314–5335.
- (7) Smith, R. D. L.; Sporinova, B.; Fagan, R. D.; Trudel, S.; Berlinguette, C. P. Facile Photochemical Preparation of Amorphous Iridium Oxide Films for Water Oxidation Catalysis. *Chem. Mater.* **2014**, *26* (4), 1654–1659.
- (8) Miller, E. L.; Rocheleau, R. E. Electrochemical and Electrochromic Behavior of Reactively Sputtered Nickel Oxide. *J. Electrochem. Soc.* **1997**, *144* (6), 1995–2003.
- (9) Sadiq, I. M.; Mohammad, A. M.; El-Shakre, M. E.; El-Deab, M. S. Electrocatalytic Activity of Nickel Oxide Nanoparticles-Modified Electrodes: Optimization of the Loading Level and Operating pH towards the Oxygen Evolution Reaction. *Int. J. Hydrog. Energy* **2012**, *37* (1), 68–77.
- (10) Dincă, M.; Surendranath, Y.; Nocera, D. G. Nickel-Borate Oxygen-Evolving Catalyst That Functions under Benign Conditions. *Proc. Natl. Acad. Sci.* **2010**, *107* (23), 10337–10341.
- (11) Sun, K.; Park, N.; Sun, Z.; Zhou, J.; Wang, J.; Pang, X.; Shen, S.; Noh, S. Y.; Jing, Y.; Jin, S.; et al. Nickel Oxide Functionalized Silicon for Efficient Photo-Oxidation of Water. *Energy Environ. Sci.* **2012**, *5* (7), 7872–7877.

- (12) Godwin, I. J.; Lyons, M. E. G. Enhanced Oxygen Evolution at Hydrous Nickel Oxide Electrodes via Electrochemical Ageing in Alkaline Solution. *Electrochem. Commun.* **2013**, *32*, 39–42.
- (13) Trotochaud, L.; Ranney, J. K.; Williams, K. N.; Boettcher, S. W. Solution-Cast Metal Oxide Thin Film Electrocatalysts for Oxygen Evolution. *J. Am. Chem. Soc.* **2012**, *134* (41), 17253–17261.
- (14) Popczun, E. J.; McKone, J. R.; Read, C. G.; Biacchi, A. J.; Wiltrout, A. M.; Lewis, N. S.; Schaak, R. E. Nanostructured Nickel Phosphide as an Electrocatalyst for the Hydrogen Evolution Reaction. *J. Am. Chem. Soc.* **2013**, *135* (25), 9267–9270.
- (15) Callejas, J. F.; McEnaney, J. M.; Read, C. G.; Crompton, J. C.; Biacchi, A. J.; Popczun, E. J.; Gordon, T. R.; Lewis, N. S.; Schaak, R. E. Electrocatalytic and Photocatalytic Hydrogen Production from Acidic and Neutral-pH Aqueous Solutions Using Iron Phosphide Nanoparticles. *ACS Nano* **2014**, *8* (11), 11101–11107.
- (16) Tian, J.; Liu, Q.; Asiri, A. M.; Sun, X. Self-Supported Nanoporous Cobalt Phosphide Nanowire Arrays: An Efficient 3D Hydrogen-Evolving Cathode over the Wide Range of pH 0–14. *J. Am. Chem. Soc.* **2014**, *136* (21), 7587–7590.
- (17) Yachandra, V. K.; Sauer, K.; Klein, M. P. Manganese Cluster in Photosynthesis: Where Plants Oxidize Water to Dioxygen. *Chem. Rev.* **1996**, *96* (7), 2927–2950.
- (18) Gorlin, Y.; Jaramillo, T. F. A Bifunctional Nonprecious Metal Catalyst for Oxygen Reduction and Water Oxidation. *J. Am. Chem. Soc.* **2010**, *132* (39), 13612–13614.
- (19) Brimblecombe, R.; Swiegers, G. F.; Dismukes, G. C.; Spiccia, L. Sustained Water Oxidation Photocatalysis by a Bioinspired Manganese Cluster. *Angew. Chem. Int. Ed.* **2008**, *47* (38), 7335–7338.
- (20) Karlsson, E. A.; Lee, B.-L.; Åkermark, T.; Johnston, E. V.; Kärkäs, M. D.; Sun, J.; Hansson, Ö.; Bäckvall, J.-E.; Åkermark, B. Photosensitized Water Oxidation by Use of a Bioinspired Manganese Catalyst. *Angew. Chem.* **2011**, *123* (49), 11919–11922.
- (21) Boppana, V. B. R.; Jiao, F. Nanostructured MnO<sub>2</sub>: An Efficient and Robust Water Oxidation Catalyst. *Chem. Commun.* **2011**, *47* (31), 8973–8975.

- (22) Iyer, A.; Del-Pilar, J.; King'ondeu, C. K.; Kissel, E.; Garces, H. F.; Huang, H.; El-Sawy, A. M.; Dutta, P. K.; Suib, S. L. Water Oxidation Catalysis Using Amorphous Manganese Oxides, Octahedral Molecular Sieves (OMS-2), and Octahedral Layered (OL-1) Manganese Oxide Structures. *J. Phys. Chem. C* **2012**, *116* (10), 6474–6483.
- (23) Najafpour, M. M.; Ehrenberg, T.; Wiechen, M.; Kurz, P. Calcium Manganese(III) Oxides ( $\text{CaMn}_2\text{O}_4 \cdot x \text{H}_2\text{O}$ ) as Biomimetic Oxygen-Evolving Catalysts. *Angew. Chem. Int. Ed.* **2010**, *49* (12), 2233–2237.
- (24) Kanan, M. W.; Nocera, D. G. In Situ Formation of an Oxygen-Evolving Catalyst in Neutral Water Containing Phosphate and  $\text{Co}^{2+}$ . *Science* **2008**, *321* (5892), 1072–1075.
- (25) Chemelewski, W. D.; Lee, H.-C.; Lin, J.-F.; Bard, A. J.; Mullins, C. B. Amorphous  $\text{FeOOH}$  Oxygen Evolution Reaction Catalyst for Photoelectrochemical Water Splitting. *J. Am. Chem. Soc.* **2014**, *136* (7), 2843–2850.
- (26) Seabold, J. A.; Choi, K.-S. Efficient and Stable Photo-Oxidation of Water by a Bismuth Vanadate Photoanode Coupled with an Iron Oxyhydroxide Oxygen Evolution Catalyst. *J. Am. Chem. Soc.* **2012**, *134* (4), 2186–2192.
- (27) Yin, Q.; Tan, J. M.; Besson, C.; Geletii, Y. V.; Musaev, D. G.; Kuznetsov, A. E.; Luo, Z.; Hardcastle, K. I.; Hill, C. L. A Fast Soluble Carbon-Free Molecular Water Oxidation Catalyst Based on Abundant Metals. *Science* **2010**, *328* (5976), 342–345.
- (28) Suntivich, J.; Gasteiger, H. A.; Yabuuchi, N.; Nakanishi, H.; Goodenough, J. B.; Shao-Horn, Y. Design Principles for Oxygen-Reduction Activity on Perovskite Oxide Catalysts for Fuel Cells and Metal–air Batteries. *Nat. Chem.* **2011**, *3* (7), 546–550.
- (29) Smith, R. D. L.; Prévot, M. S.; Fagan, R. D.; Zhang, Z.; Sedach, P. A.; Siu, M. K. J.; Trudel, S.; Berlinguette, C. P. Photochemical Route for Accessing Amorphous Metal Oxide Materials for Water Oxidation Catalysis. *Science* **2013**, *340* (6128), 60–63.
- (30) Landon, J.; Demeter, E.; İnoğlu, N.; Keturakis, C.; Wachs, I. E.; Vasić, R.; Frenkel, A. I.; Kitchin, J. R. Spectroscopic Characterization of Mixed Fe–Ni Oxide Electrocatalysts for the Oxygen Evolution Reaction in Alkaline Electrolytes. *ACS Catal.* **2012**, *2* (8), 1793–1801.
- (31) McCrory, C. C. L.; Jung, S.; Peters, J. C.; Jaramillo, T. F. Benchmarking Heterogeneous Electrocatalysts for the Oxygen Evolution Reaction. *J. Am. Chem. Soc.* **2013**, *135* (45), 16977–16987.

- (32) Song, F.; Hu, X. Ultrathin Cobalt–Manganese Layered Double Hydroxide Is an Efficient Oxygen Evolution Catalyst. *J. Am. Chem. Soc.* **2014**, *136* (47), 16481–16484.
- (33) Smith, R. D. L.; Prévot, M. S.; Fagan, R. D.; Trudel, S.; Berlinguette, C. P. Water Oxidation Catalysis: Electrocatalytic Response to Metal Stoichiometry in Amorphous Metal Oxide Films Containing Iron, Cobalt, and Nickel. *J. Am. Chem. Soc.* **2013**, *135* (31), 11580–11586.
- (34) Dismukes, G. C.; Brimblecombe, R.; Felton, G. A. N.; Pryadun, R. S.; Sheats, J. E.; Spiccia, L.; Swiegers, G. F. Development of Bioinspired Mn<sub>4</sub>O<sub>4</sub>–Cubane Water Oxidation Catalysts: Lessons from Photosynthesis. *Acc. Chem. Res.* **2009**, *42* (12), 1935–1943.
- (35) Kanan, M. W.; Yano, J.; Surendranath, Y.; Dincă, M.; Yachandra, V. K.; Nocera, D. G. Structure and Valency of a Cobalt–Phosphate Water Oxidation Catalyst Determined by in Situ X-Ray Spectroscopy. *J. Am. Chem. Soc.* **2010**, *132* (39), 13692–13701.
- (36) McCool, N. S.; Robinson, D. M.; Sheats, J. E.; Dismukes, G. C. A Co<sub>4</sub>O<sub>4</sub> “Cubane” Water Oxidation Catalyst Inspired by Photosynthesis. *J. Am. Chem. Soc.* **2011**, *133* (30), 11446–11449.
- (37) Risch, M.; Klingan, K.; Ringleb, F.; Chernev, P.; Zaharieva, I.; Fischer, A.; Dau, H. Water Oxidation by Electrodeposited Cobalt Oxides—Role of Anions and Redox-Inert Cations in Structure and Function of the Amorphous Catalyst. *ChemSusChem* **2012**, *5* (3), 542–549.
- (38) Gehl, B.; Frömsdorf, A.; Aleksandrovic, V.; Schmidt, T.; Pretorius, A.; Flege, J.-I.; Bernstorff, S.; Rosenauer, A.; Falta, J.; Weller, H.; et al. Structural and Chemical Effects of Plasma Treatment on Close-Packed Colloidal Nanoparticle Layers. *Adv. Funct. Mater.* **2008**, *18* (16), 2398–2410.
- (39) McCrory, C. C. L.; Jung, S.; Ferrer, I. M.; Chatman, S. M.; Peters, J. C.; Jaramillo, T. F. Benchmarking Hydrogen Evolving Reaction and Oxygen Evolving Reaction Electrocatalysts for Solar Water Splitting Devices. *J. Am. Chem. Soc.* **2015**, *137* (13), 4347–4357.
- (40) Avey, A. A.; Hill, R. H. Solid State Photochemistry of Cu<sub>2</sub>(OH)<sub>2</sub>(O<sub>2</sub>C(CH<sub>2</sub>)<sub>4</sub>CH<sub>3</sub>)<sub>4</sub> in Thin Films: The Photochemical Formation of High-Quality Films of Copper and Copper(I) Oxide. Demonstration of a Novel Lithographic Technique for the Patterning of Copper. *J. Am. Chem. Soc.* **1996**, *118* (1), 237–238.

- (41) Bau, J. A.; Li, P.; Marenco, A. J.; Trudel, S.; Olsen, B. C.; Luber, E. J.; Buriak, J. M. Nickel/Iron Oxide Nanocrystals with a Nonequilibrium Phase: Controlling Size, Shape, and Composition. *Chem. Mater.* **2014**, *26* (16), 4796–4804.
- (42) Grosvenor, A. P.; Kobe, B. A.; Biesinger, M. C.; McIntyre, N. S. Investigation of Multiplet Splitting of Fe <sub>2p</sub> XPS Spectra and Bonding in Iron Compounds. *Surf. Interface Anal.* **2004**, *36* (12), 1564–1574.
- (43) Xia, X. H.; Tu, J. P.; Zhang, J.; Wang, X. L.; Zhang, W. K.; Huang, H. Electrochromic Properties of Porous NiO Thin Films Prepared by a Chemical Bath Deposition. *Sol. Energy Mater. Sol. Cells* **2008**, *92* (6), 628–633.
- (44) Subramanian, B.; Mohamed Ibrahim, M.; Senthilkumar, V.; Murali, K. R.; Vidhya, V.; Sanjeeviraja, C.; Jayachandran, M. Optoelectronic and Electrochemical Properties of Nickel Oxide (NiO) Films Deposited by DC Reactive Magnetron Sputtering. *Phys. B Condens. Matter* **2008**, *403* (21–22), 4104–4110.
- (45) Jasinski, R.; Iob, A. FTIR Measurements of Iron Oxides on Low Alloy Steel. *J. Electrochem. Soc.* **1988**, *135* (3), 551–556.
- (46) Green, S. V.; Watanabe, M.; Oka, N.; Niklasson, G. A.; Granqvist, C. G.; Shigesato, Y. Electrochromic Properties of Nickel Oxide Based Thin Films Sputter Deposited in the Presence of Water Vapor. *Thin Solid Films* **2012**, *520* (10), 3839–3842.
- (47) Li, H.; Li, W.; Zhang, Y.; Wang, T.; Wang, B.; Xu, W.; Jiang, L.; Song, W.; Shu, C.; Wang, C. Chrysanthemum-like  $\alpha$ -FeOOH Microspheres Produced by a Simple Green Method and Their Outstanding Ability in Heavy Metal Ion Removal. *J. Mater. Chem.* **2011**, *21* (22), 7878–7881.
- (48) Trotochaud, L.; Young, S. L.; Ranney, J. K.; Boettcher, S. W. Nickel–Iron Oxyhydroxide Oxygen-Evolution Electrocatalysts: The Role of Intentional and Incidental Iron Incorporation. *J. Am. Chem. Soc.* **2014**, *136* (18), 6744–6753.
- (49) Li, Y.-F.; Selloni, A. Mechanism and Activity of Water Oxidation on Selected Surfaces of Pure and Fe-Doped NiO<sub>x</sub>. *ACS Catal.* **2014**, *4* (4), 1148–1153.
- (50) Trasatti, S. Physical Electrochemistry of Ceramic Oxides. *Electrochimica Acta* **1991**, *36* (2), 225–241.

- (51) Qiu, Y.; Xin, L.; Li, W. Electrocatalytic Oxygen Evolution over Supported Small Amorphous Ni–Fe Nanoparticles in Alkaline Electrolyte. *Langmuir* **2014**, *30* (26), 7893–7901.
- (52) Bard, A. J.; Faulkner, L. R. *Electrochemical Methods: Fundamentals and Applications*.; Wiley: New York, 1980.
- (53) Gerken, J. B.; Shaner, S. E.; Massé, R. C.; Porubsky, N. J.; Stahl, S. S. A Survey of Diverse Earth Abundant Oxygen Evolution Electrocatalysts Showing Enhanced Activity from Ni–Fe Oxides Containing a Third Metal. *Energy Environ. Sci.* **2014**, *7* (7), 2376–2382.
- (54) Doyle, R. L.; Godwin, I. J.; Brandon, M. P.; Lyons, M. E. G. Redox and Electrochemical Water Splitting Catalytic Properties of Hydrated Metal Oxide Modified Electrodes. *Phys. Chem. Chem. Phys.* **2013**, *15* (33), 13737–13783.
- (55) Fang, Y.-H.; Liu, Z.-P. Mechanism and Tafel Lines of Electro-Oxidation of Water to Oxygen on RuO<sub>2</sub>(110). *J. Am. Chem. Soc.* **2010**, *132* (51), 18214–18222.
- (56) Lin, F.; Boettcher, S. W. Adaptive Semiconductor/electrocatalyst Junctions in Water-Splitting Photoanodes. *Nat. Mater.* **2014**, *13* (1), 81–86.
- (57) Bediako, D. K.; Lassalle-Kaiser, B.; Surendranath, Y.; Yano, J.; Yachandra, V. K.; Nocera, D. G. Structure–Activity Correlations in a Nickel–Borate Oxygen Evolution Catalyst. *J. Am. Chem. Soc.* **2012**, *134* (15), 6801–6809.
- (58) Balasubramanian, M.; Melendres, C. A.; Mini, S. X-Ray Absorption Spectroscopy Studies of the Local Atomic and Electronic Structure of Iron Incorporated into Electrodeposited Hydrated Nickel Oxide Films†. *J. Phys. Chem. B* **2000**, *104* (18), 4300–4306.
- (59) Demourgues-Guerlou, L.; Fournès, L.; Delmas, C. On the Iron Oxidation State in the Iron-Substituted  $\gamma$  Nickel Oxyhydroxides. *J. Solid State Chem.* **1995**, *114* (1), 6–14.
- (60) Corrigan, D. A.; Conell, R. S.; Fierro, C. A.; Scherson, D. A. In-Situ Moessbauer Study of Redox Processes in a Composite Hydroxide of Iron and Nickel. *J. Phys. Chem.* **1987**, *91* (19), 5009–5011.
- (61) Sun, X.; Wang, G.; Hwang, J.-Y.; Lian, J. Porous Nickel Oxide Nano-Sheets for High Performance Pseudocapacitance Materials. *J. Mater. Chem.* **2011**, *21* (41), 16581–16588.

- (62) Wang, D.; Song, C.; Hu, Z.; Fu, X. Fabrication of Hollow Spheres and Thin Films of Nickel Hydroxide and Nickel Oxide with Hierarchical Structures. *J. Phys. Chem. B* **2005**, *109* (3), 1125–1129.
- (63) Cornell, R. M.; Schwertmann, U. *The Iron Oxides: Structure, Properties, Reactions, Occurrences and Uses*; John Wiley & Sons, 2006.
- (64) Krause, K. M.; Taschuk, M. T.; Harris, K. D.; Rider, D. A.; Wakefield, N. G.; Sit, J. C.; Buriak, J. M.; Thommes, M.; Brett, M. J. Surface Area Characterization of Obliquely Deposited Metal Oxide Nanostructured Thin Films. *Langmuir* **2009**, *26* (6), 4368–4376.

# 5 Conclusions

This thesis sought to examine approaches to synthesizing and utilizing metal oxides for water splitting via photocatalytic and electrocatalytic means. In this final chapter, each preceding chapter will be summarized and future directions will be provided.

## 5.1 Chapter Summaries

### 5.1.1 Chapter 1

In chapter 1, the field of water splitting was reviewed. There is a strong and important rationale for developing alternative energy storage systems in addition to systems that can convert energy using alternative sources, because many of these sources suffer from intermittent availabilities. The potential for producing hydrogen gas from water is important because water is ubiquitous on the face of the earth and facile. To this effect, the history of producing hydrogen from water was discussed, as well as the other dominant form of hydrogen production currently used, hydrocarbon reforming, which produces hydrogen from hydrocarbons and is therefore not carbon-neutral because of the generation of carbon monoxide and carbon dioxide. Finally, the materials perspective for water splitting was briefly discussed. Specifically, the past reliance of the field on scarce and or UV-absorbing materials has prevented any strong industrial pursuit into the field of water splitting.

### 5.1.2 Chapter 2

Chapter 2 detailed the routes and rationale behind a water splitting z-scheme composed of two earth abundant semiconductors in intimate contact, functionalized with catalysts in order to improve activity. The two materials, hematite ( $\alpha\text{-Fe}_2\text{O}_3$ ) and copper ferrite ( $\text{CuFe}_2\text{O}_4$ ), cannot carry out full water splitting independently and require a second semiconductor or hole or electron scavenger in order to carry out oxygen or hydrogen evolution, making a z-scheme approach ideal for any such system where both of these semiconductors are involved. Given that  $\alpha\text{-Fe}_2\text{O}_3$  has naturally poor activity, a high surface area structure of this material was created using a template of a sugarcane leaf, resulting in an  $\alpha\text{-Fe}_2\text{O}_3$  superstructure. This structure was subsequently functionalized with copper nanoparticles, and upon annealing at high temperature, the copper diffused into the leaf structure and formed  $\text{CuFe}_2\text{O}_4$ . The new heterostructure was then functionalized using linkers and via electrostatic interactions in order to make sure that the semiconductor materials were in contact with catalyst nanoparticles. However, despite catalysts and surface area, water splitting was not possible. Since  $\text{CuFe}_2\text{O}_4$  is a less well-characterized material, further characterization was performed to confirm bandgap positions and photocatalytic activity.  $\text{CuFe}_2\text{O}_4$  indeed had the correct band positions and was catalytically active, but the activity was not very high. Therefore, this approach to water splitting was hindered by poor material properties. Nonetheless, biotemplating was extended beyond  $\text{TiO}_2$  and a variety of approaches to assembling larger-scale materials was demonstrated.

### 5.1.3 Chapter 3

Chapter 3 explored the synthesis of [Ni,Fe]O nanoparticles via the high-temperature decomposition of nickel and iron oleates. These nanoparticles maintained a metastable rock-salt structure, which is unusual considering that such a material ordinarily does not exist under ambient conditions due to the instability of bivalent iron. Nonetheless, these nanoparticles were stable after storage for long periods of time in ambient conditions. Furthermore, it was possible to achieve shape and composition control during the synthetic process by controlling the time that the reaction solution was held at decomposition temperature and the drying state of the metal oleate precursor. Closer examination of the particles using magnetometry demonstrated that the surface of the nanoparticles decomposed into a less stable trivalent iron-containing shell that had unique magnetic properties when compared to the bulk of the nanoparticles. Finally, the metastability of this phase was confirmed by heating of the nanoparticles at high temperature, where the phase did not decompose until up to 400°C. The fact that this phase could be synthesized under specific conditions but does not exist in most conventional phase diagrams underscores the importance of controlled-condition nanoparticle synthetic techniques as means to achieve normally unattainable crystal phases.

### 5.1.4 Chapter 4

Chapter 4 examined the potential of [Ni,Fe]O nanoparticles synthesized in chapter 3 for water oxidation electrocatalysis. A simple method based on photolytic decomposition of metal-organic materials for amorphous oxides was extended to

nanoparticle systems, resulting in durable and catalytically active nanoparticle electrodes. Using this system, it was determined that nanoparticles with greater nickel content were determined to have higher catalytic activities for water oxidation than nanoparticles with lower nickel content. Furthermore, the surface of the nanoparticles was determined to be responsible for the catalytic activity, with little to do with the bulk of the nanoparticles. The surface, home to a unique disordered mixed nickel iron oxide phase, was also determined to be important as the catalytic activity of the nanoparticles could be effectively reduced by heating, but at temperatures that were insufficiently high to destroy the rock-salt bulk nanoparticle structure.

## **5.2 Proposed Research Directions**

### **5.2.1 Biotemplating of other metal oxides**

Since the sol-gel based templating of metal oxides has now been extended from solely  $\text{TiO}_2$  to  $\text{Fe}_2\text{O}_3$ , there is now a potential for extending this technique to allow for not only other pure metal oxides, but also doped or mixed metal oxides. The possibility that any high surface area hydroxyl-rich structure, many of which can be found in the living world, can be replicated and converted to another material with high accuracy makes biotemplating an extremely flexible technique for producing high surface area structures of any material. A further curiosity that was not explored in Chapter 2, but remains unexplored, is the potential for doping using a sol-gel biotemplating technique whereby a small amount of dopant precursor is introduced into a precursor solution. It will be interesting to determine if the

composition of such a dopant material can be controlled in a precise and conformal manner, or if precursors bind to the template with different affinities, resulting in a need to control reaction conditions.

Furthermore, the application of such techniques and knowledge to other carbohydrate structures is interesting because such an approach may mean the eventual tailoring of precision structures composed of hydroxyl-rich molecules. In particular, DNA or protein engineering could be used to develop templates that have no analogue in nature.<sup>1,2</sup> This approach would allow for the high-yield synthesis of inorganic nanostructures that do not exist in nature. On a larger scale, there is always the potential for producing templates based on non-oxide structures as well. The demonstration of an iron carbide leaf using a biotemplating approach highlighted a significant difference: in the iron carbide leaf, only leaf veins were replicated, resulting in a wireframe electrode that was utilized as a water splitting electrocatalyst.<sup>3</sup>

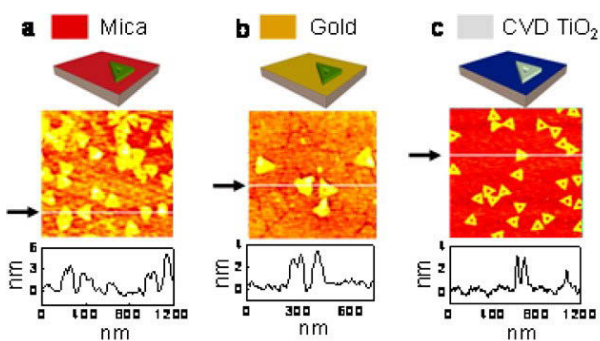


Figure 5.1 SiO<sub>2</sub> grown using CVD on DNA templates deposited on (a) mica and (b) gold surfaces. (c) TiO<sub>2</sub> grown using CVD of DNA templates on silicon substrate. Reprinted with permission from the American Chemical Society.

### 5.2.2 Exploring the potential of $\text{CuFe}_2\text{O}_4$ for electrode applications

These studies demonstrated that the material  $\text{CuFe}_2\text{O}_4$  has a relatively small bandgap that can absorb a large portion of the solar spectrum. However, like many ferrites,  $\text{CuFe}_2\text{O}_4$  is seldom explored because of the high temperature of preparation needed to form the material in a defect-free manner. Typically, a temperature in excess of  $800^\circ\text{C}$  is required.<sup>4</sup> However, the literature lacks a serious characterization of the photo-properties of  $\text{CuFe}_2\text{O}_4$ , or even a strong attempt to optimize the conditions required for photocatalysis. Since most of the reported methods involve a high-temperature combustion scheme, nanoparticles are often aggregated with low surface area.<sup>5-7</sup> However, at  $800^\circ\text{C}$ , it is possible to synthesize electrodes of  $\text{CuFe}_2\text{O}_4$  based on the drop-casting of thin films from solution – as long as the electrode material can withstand the temperature. Materials such as fluorine-tin oxide on quartz or noble metal electrodes could be used to finally explore if  $\text{CuFe}_2\text{O}_4$  has any potential as a solar energy material.

The rationale and pursuit for using  $\text{CuFe}_2\text{O}_4$  as a solar energy material is strong. Apart from the fact that little is known about the potential of this material, the high abundance for copper and iron, the stability of this material, and of course, the band-gap energetics all make the material worth studying. Of course, there is the potential that the material simply has a low activity; however, it should be noted that these problems have not stopped people from examining  $\alpha\text{-Fe}_2\text{O}_3$  in great detail. Furthermore, in comparison to water oxidation photoanodes, there exists a far smaller proportion of earth abundant, low-processing cost photocathode material for hydrogen evolution, making pursuit of new materials desirable.

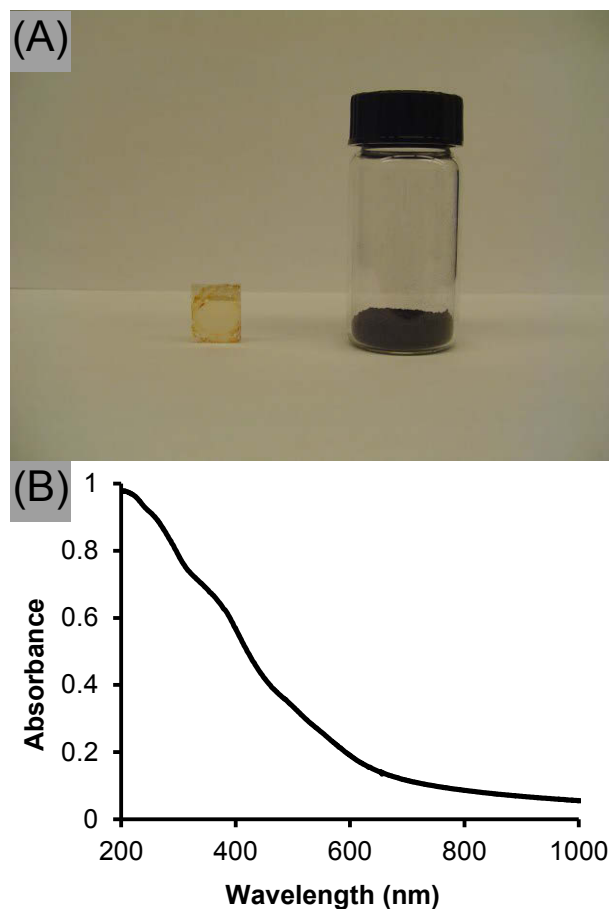


Figure 5.2 (a) Optical image of CuFe<sub>2</sub>O<sub>4</sub> layers spin-coated on quartz (left) and CuFe<sub>2</sub>O<sub>4</sub> powder prepared via combustion method. (b) UV-vis spectra of CuFe<sub>2</sub>O<sub>4</sub> on quartz electrode.

It may also be worth exploring if it is possible to synthesize solutions of CuFe<sub>2</sub>O<sub>4</sub> nanoparticles. If solution-based thermal decomposition can be used to make metastable materials, it may be possible to use the same technique to synthesize materials that require high temperatures to form. Attempts to synthesize CuFe<sub>2</sub>O<sub>4</sub> nanoparticles in solution phase in the past have been unsuccessful due to differences in the decomposition temperatures of the precursors, typically resulting in nanoparticles with variable composition or outright mixtures of copper and ferrite.<sup>8,9</sup> By controlling the proportion of copper in the reaction solution, or

changing the decomposition properties of the precursor, it may be possible to synthesize stoichiometric nanoparticles – recall in Chapter 3 that individual nickel and iron oleates yielded large yields at higher temperatures, but when combined, they decomposed at slower rates and had more limited yields. A potential synergistic effect between a copper precursor and iron oleate may have a similar relationship.

### **5.2.3 Mechanism of metal oleate decomposition during formation of metastable [Ni,Fe]O nanoparticles**

It is worth examining the mechanism of nanoparticle formation in the metal oleate process for several reasons. Firstly, during the synthetic process, a variety of shapes were achieved. This complexity is worth exploring and understanding because it may be possible to achieve further shape control. Secondly, there are several subtleties of the reaction that are not as well understood. In particular, the conversion of  $\text{Fe}^{3+}$  to  $\text{Fe}^{2+}$  in the absence of an obvious reducing agent is worth understanding. Furthermore, the sources of oxygen in the reaction that lead to a metal oxide structure are worth discussing because most of the oxygen in-reaction appears to be derived from hydrocarbons with carboxylate groups. Understanding these subtleties will make it possible to understand how a rock-salt structured nanoparticle was derived while equivalent reactions typically yield ferrite-structured nanoparticles.<sup>9</sup>

Acquiring greater control during the reaction process will increase the potential for shapes, sizes and compositions that can be achieved, and potentially even

phases. It may even be possible to synthesize core-shell nanoparticles by understanding the order of decomposition. Metal oleates have different decomposition temperatures, and as a result, typically in mixtures on metal oleate will decompose before the other. In the case of nickel and iron oleate, it may be possible to control the order of decomposition via control over introduction of the oleate precursors as in a hot injection. Since most of these metal oxides have some sort of magnetic property, the goal of making such core-shell nanoparticles would be interesting for magnetic characterization – and even for application in exchange bias, where core-shell magnetic nanoparticles are desirable for their close contact of two materials with different magnetic properties.<sup>10,11</sup>

#### **5.2.4 Synthesis of non-oxides utilizing nickel and iron oleate**

Understanding the mechanism of nanoparticle formation will also lead the way to using metal oleate decomposition to synthesize non-oxide compounds. The potential for synthesizing mixed metal sulfides and phosphides are of interest because many such compounds have recently been considered as catalysts and photo-conversion materials. Only by understanding the mechanism of formation would it be possible to understand where the source of the anion arises and how it could therefore be incorporated into a reaction solution. This possibility has already been explored for sulfides, but the success has been limited due to a poor understanding of the materials. For metal sulfides, oleic acid was replaced with octadecanethiol, resulting in mixed nickel-iron nanorods with controllable compositions as well as variable phases (Figure 5.2). However, the purification of

these nanorods is currently in question. Nonetheless, nickel and iron sulfides are attractive contenders as future solar energy materials,<sup>12</sup> making the iron oleate method here a potentially effective route to these materials.

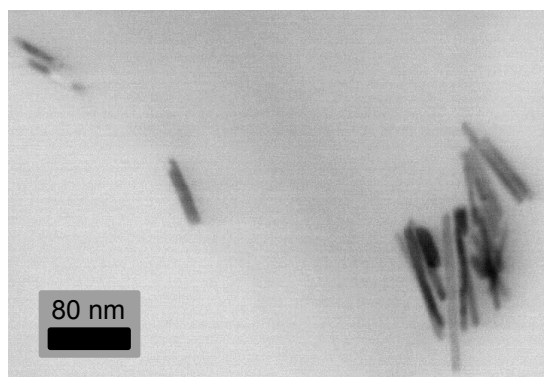


Figure 5.3 Electron micrograph of nickel-iron sulfide wires prepared via decomposition of nickel and iron oleate in the presence of 1-octadecanethiol.

### **5.2.5 Conformal functionalization of high-surface area electrodes to increase activity**

Although much work has been done on developing materials for catalytic electrodes, less work has been performed on optimizing the deposition of these materials such that minimal amounts of material are deposited thus reducing costs and preventing the catalyst layer from absorbing too much light meant for the semiconductor. Therefore, such material systems are often unable to exploit the benefits of using a high surface area electrode, which can ultimately increase the amount of surface area that can be used for catalysis. The benefit of the [Ni,Fe]O nanoparticle system here, as demonstrated via the conformal functionalization of

copper and platinum nanoparticles in Chapter 2, is that it is possible to use a linker based system to produce a conformally functionalized surface using nanoparticle-based methods for producing films. By combining the nanoparticle functionalization work in Chapter 2 with the [Ni,Fe]O nanoparticles, it is possible to produce a high surface area electrode that can carry out water oxidation with a higher current density than other electrode systems. Using a similar linker based system, it is possible to functionalize any electrode surface with these nanoparticles and determine if the increased surface area improves water splitting activity.

### **5.2.6 Understanding detailed catalytic properties of [Ni,Fe]O nanoparticles, including effect of shape and surface composition**

The immediate environment of nickel iron oxide catalysts is of great interest, as it is generally recognized that the nickel serves as the main reaction site while the iron provides a supporting role since nickel oxide alone is far more catalytic for water oxidation than iron oxide.<sup>13-15</sup> It is possible that differences in composition between different studies can be attributed to the local surface environment of nickel oxide. However, the exact mechanism by which iron lowers the catalytic barriers for water oxidation is unknown. An important direction for nickel iron oxide catalysts is understanding the surface environment of these catalysts. Since studies on understanding the surface composition of nanoparticles are published and therefore characterization techniques are well known, nanoparticle surface composition and structure could be tuned and studied before more electrochemistry is performed.<sup>16,17</sup>

Another point of interest is understanding the effect of shape on catalytic activity. Shape can have an important influence on catalytic activity at the nanoscale, primarily because differences in shape can expose different crystal planes or active sites that can have significant differences in catalytic activity.<sup>18-21</sup> Early work was done on determining if star-shaped particles were superior catalysts to cubes. At the time, the effect was found to be negligible, especially compared to the effect on composition that was studied in Chapter 4. However, this work still needs to be confirmed. In addition, since the synthetic results have provided such a variety in nanoparticle shape and size, determining if any of these properties have a significant effect in changing catalytic activity may open up new avenues into understanding their catalytic activity for water oxidation.

### **5.2.7 Acid vs. Base Catalysts**

One issue that was not addressed in this thesis is the difference between acid and alkaline water oxidation catalysts. Both systems have advantages and disadvantages that are widely studied. Alkaline systems benefit from the use of earth-abundant first-row transition metal oxide catalysts such as nickel and iron, while acidic systems tend to require significantly rarer metals such as iridium and ruthenium.<sup>22,23</sup> However, the major benefit to acidic systems is that such systems already have well-developed membrane technology arising from studies on fuel cells, and specifically proton exchange membranes.<sup>24</sup> These membranes allow for the separation of H<sub>2</sub> and O<sub>2</sub> gases in solution, in turn laying the groundwork for compact devices. Membrane technology for alkaline water splitting does not yet

exist. For the development of devices for water splitting, both of these constraints will require resolution although the needs between the two systems are different from each other.

### 5.3 References

- (1) Surwade, S. P.; Zhou, F.; Wei, B.; Sun, W.; Powell, A.; O'Donnell, C.; Yin, P.; Liu, H. Nanoscale Growth and Patterning of Inorganic Oxides Using DNA Nanostructure Templates. *J. Am. Chem. Soc.* **2013**, *135* (18), 6778–6781.
- (2) Carter, J. D.; LaBean, T. H. Organization of Inorganic Nanomaterials via Programmable DNA Self-Assembly and Peptide Molecular Recognition. *ACS Nano* **2011**, *5* (3), 2200–2205.
- (3) Schnepf, Z.; Yang, W.; Antonietti, M.; Giordano, C. Biotemplating of Metal Carbide Microstructures: The Magnetic Leaf. *Angew. Chem. Int. Ed.* **2010**, *49* (37), 6564–6566.
- (4) Perrot, P.; Arnout, S.; Vrestal, J. Copper - Iron - Oxygen. In *iron systems: phase diagrams, crystallographic and thermodynamic data*; Effenberg, G., Ilyenko, S., Eds.; Materials Science International Team, M., Series Ed.; Landolt-Börnstein - Group IV Physical Chemistry; Springer-Verlag Berlin Heidelberg, 2008; Vol. 11D3.
- (5) Zhang, R.; Liu, J.; Wang, S.; Niu, J.; Xia, C.; Sun, W. Magnetic CuFe<sub>2</sub>O<sub>4</sub> Nanoparticles as an Efficient Catalyst for C-O Cross-Coupling of Phenols with Aryl Halides. *ChemCatChem* **2011**, *3* (1), 146–149.
- (6) Bazgir, A.; Hosseini, G.; Ghahremanzadeh, R. Copper Ferrite Nanoparticles: An Efficient and Reusable Nanocatalyst for a Green One-Pot, Three-Component Synthesis of Spirooxindoles in Water. *ACS Comb. Sci.* **2013**, *15* (10), 530–534.
- (7) Yang, H.; Yan, J.; Lu, Z.; Cheng, X.; Tang, Y. Photocatalytic Activity Evaluation of Tetragonal CuFe<sub>2</sub>O<sub>4</sub> Nanoparticles for the H<sub>2</sub> Evolution under Visible Light Irradiation. *J. Alloys Compd.* **2009**, *476* (1–2), 715–719.
- (8) Nakhjavan, B.; Tahir, M. N.; Panthöfer, M.; Gao, H.; Schladt, T. D.; Gasi, T.; Ksenofontov, V.; Branscheid, R.; Weber, S.; Kolb, U.; et al. Synthesis, Characterization and Functionalization of Nearly Mono-Disperse Copper Ferrite Cu<sub>x</sub>Fe<sub>3-x</sub>O<sub>4</sub> Nanoparticles. *J. Mater. Chem.* **2011**, *21* (19), 6909–6915.

- (9) Bao, N.; Shen, L.; Wang, Y.; Padhan, P.; Gupta, A. A Facile Thermolysis Route to Monodisperse Ferrite Nanocrystals. *J. Am. Chem. Soc.* **2007**, *129* (41), 12374–12375.
- (10) Nogués, J.; Sort, J.; Langlais, V.; Skumryev, V.; Suriñach, S.; Muñoz, J. S.; Baró, M. D. Exchange Bias in Nanostructures. *Phys. Rep.* **2005**, *422* (3), 65–117.
- (11) Sun, X.; Frey Huls, N.; Sigdel, A.; Sun, S. Tuning Exchange Bias in Core/Shell FeO/Fe<sub>3</sub>O<sub>4</sub> Nanoparticles. *Nano Lett.* **2012**, *12* (1), 246–251.
- (12) Wadia, C.; Alivisatos, A. P.; Kammen, D. M. Materials Availability Expands the Opportunity for Large-Scale Photovoltaics Deployment. *Environ. Sci. Technol.* **2009**, *43* (6), 2072–2077.
- (13) Hong, D.; Yamada, Y.; Nagatomi, T.; Takai, Y.; Fukuzumi, S. Catalysis of Nickel Ferrite for Photocatalytic Water Oxidation Using [Ru(bpy)<sub>3</sub>]<sup>2+</sup> and S<sub>2</sub>O<sub>8</sub><sup>2-</sup>. *J. Am. Chem. Soc.* **2012**, *134* (48), 19572–19575.
- (14) Trotochaud, L.; Young, S. L.; Ranney, J. K.; Boettcher, S. W. Nickel–Iron Oxyhydroxide Oxygen-Evolution Electrocatalysts: The Role of Intentional and Incidental Iron Incorporation. *J. Am. Chem. Soc.* **2014**, *136* (18), 6744–6753.
- (15) Smith, R. D. L.; Prévot, M. S.; Fagan, R. D.; Trudel, S.; Berlinguette, C. P. Water Oxidation Catalysis: Electrocatalytic Response to Metal Stoichiometry in Amorphous Metal Oxide Films Containing Iron, Cobalt, and Nickel. *J. Am. Chem. Soc.* **2013**, *135* (31), 11580–11586.
- (16) Suntivich, J.; Xu, Z.; Carlton, C. E.; Kim, J.; Han, B.; Lee, S. W.; Bonnet, N.; Marzari, N.; Allard, L. F.; Gasteiger, H. A.; et al. Surface Composition Tuning of Au–Pt Bimetallic Nanoparticles for Enhanced Carbon Monoxide and Methanol Electro-Oxidation. *J. Am. Chem. Soc.* **2013**, *135* (21), 7985–7991.
- (17) Cui, C.; Gan, L.; Li, H.-H.; Yu, S.-H.; Heggen, M.; Strasser, P. Octahedral PtNi Nanoparticle Catalysts: Exceptional Oxygen Reduction Activity by Tuning the Alloy Particle Surface Composition. *Nano Lett.* **2012**, *12* (11), 5885–5889.
- (18) Fang, Y.-H.; Liu, Z.-P. Mechanism and Tafel Lines of Electro-Oxidation of Water to Oxygen on RuO<sub>2</sub>(110). *J. Am. Chem. Soc.* **2010**, *132* (51), 18214–18222.

- (19) Narayanan, R.; El-Sayed, M. A. Shape-Dependent Catalytic Activity of Platinum Nanoparticles in Colloidal Solution. *Nano Lett.* **2004**, *4* (7), 1343–1348.
- (20) Deng, Y.-J.; Tian, N.; Zhou, Z.-Y.; Huang, R.; Liu, Z.-L.; Xiao, J.; Sun, S.-G. Alloy Tetrahedral Pd–Pt Catalysts: Enhancing Significantly the Catalytic Activity by Synergy Effect of High-Index Facets and Electronic Structure. *Chem. Sci.* **2012**, *3* (4), 1157–1161.
- (21) Zhang, H.; Jin, M.; Xiong, Y.; Lim, B.; Xia, Y. Shape-Controlled Synthesis of Pd Nanocrystals and Their Catalytic Applications. *Acc. Chem. Res.* **2013**, *46* (8), 1783–1794.
- (22) McCrory, C. C. L.; Jung, S.; Peters, J. C.; Jaramillo, T. F. Benchmarking Heterogeneous Electrocatalysts for the Oxygen Evolution Reaction. *J. Am. Chem. Soc.* **2013**, *135* (45), 16977–16987.
- (23) McCrory, C. C. L.; Jung, S.; Ferrer, I. M.; Chatman, S. M.; Peters, J. C.; Jaramillo, T. F. Benchmarking Hydrogen Evolving Reaction and Oxygen Evolving Reaction Electrocatalysts for Solar Water Splitting Devices. *J. Am. Chem. Soc.* **2015**, *137* (13), 4347–4357.
- (24) Mauritz, K. A.; Moore, R. B. State of Understanding of Nafion. *Chem. Rev.* **2004**, *104* (10), 4535–4586.